COMENIUS UNIVERSITY IN BRATISLAVA
FACULTY OF MATHEMATICS, PHYSICS AND INFORMATICS

DEVELOPMENT OF THE DOUBLE CASCADE RECONSTRUCTION TECHNIQUES FOR THE BAIKAL-GVD NEUTRINO TELESCOPE

AND

ANALYSIS OF THE KM3NET DIGITAL OPTICAL MODULE PROPERTIES

DOCTORAL THESIS

2025 MGR. ELIŠKA ECKEROVÁ

Comenius University in Bratislava
Faculty of Mathematics, Physics and Informatics

Development of the Double Cascade Reconstruction Techniques for the Baikal-GVD Neutrino Telescope
and
Analysis of the KM3NeT Digital Optical Module Properties

Doctoral Thesis

Study programme:	Nuclear and Subnuclear Physics
Field of study:	Physics
Department:	Department of Nuclear Physics and Biophysics
Supervisor:	prof. RNDr. Fedor Šimkovic, CSc.
Consultants (Baikal-GVD):	Mgr. Rastislav Dvornický, PhD. Mgr. Lukáš Fajt, PhD.
Consultants (KM3NeT):	Dr. Ronald Bruijn Dr. Vladimir Kulikovskiy

Bratislava, 2025
Mgr. Eliška Eckerová

Univerzita Komenského v Bratislave
Fakulta matematiky, fyziky a informatiky

ZADANIE ZÁVEREČNEJ PRÁCE

Meno a priezvisko študenta: Mgr. Eliška Eckerová
Študijný program: jadrová a subjadrová fyzika (Jednoodborové štúdium, doktorandské III. st., denná forma)
Študijný odbor: fyzika
Typ záverečnej práce: dizertačná
Jazyk záverečnej práce: anglický
Sekundárny jazyk: slovenský

Názov: Development of the Double Cascade Reconstruction Techniques for the Baikal-GVD Neutrino Telescope and Analysis of the KM3NeT Digital Optical Module Properties
Vývoj techník na rekonštrukciu dvojitých kaskád pre neutrínový teleskop Baikal-GVD a analýza vlastností digitálneho optického modulu experimentu KM3NeT

Anotácia: Neutrínové teleskopy spolu s teleskopmi na detekciu gama žiarenia a observatóriami gravitačných vĺn nám otvárajú okná do vesmíru. Neutrínové teleskopy sú budované z obrovskej trojrozmernej siete optických senzorov umiestnených v hĺbkach arktického ľadu, Stredozemného mora, Tichého oceánu a jazera Bajkal. Ich úlohou je registrácia Čerenkovovho žiarenia produkovaného pri interakcii vysokoenergetických neutrín s médiom detekčného prostredia. Konštrukcia detektora umožňuje rekonštruovať neutrínové eventy a určiť vôňu, energiu a smer interagujúcich neutrín na základe analýzy miesta a času detekcie signálu v optických moduloch. Predpokladá sa, že detekcia astrofyzikálnych neutrín, môže pomôcť vyriešiť tajomstvo pôvodu ultra-vysokoenergetického kozmického žiarenia vo vesmíre. Pomocou rekonštrukcie trajektórií neutrín sa spätne lokalizujú objekty vo vesmíre, ktoré môžu produkovať kozmické žiarenie s energiami podstatne väčšími aké sa dosiahujú na urýchľovačoch elementárnych častíc, protónov a jadier na Zemi. V súčastnosti sú v prevádzke a ďalšej výstavbe štyri neutrínové teleskopy, IceCube na južnej pologuli a Baikal-GVD, KM3NeT a P-ONE na severnej pologuli. Tieto teleskopy formujú našu prvotnú predstavu o pôvode vysokoenergetických neutrín a poukazujú na potrebu ďalšieho výskumu v tomto smere. Rozlišujeme dve kategórie eventov v neutrínových teleskopoch: treky a kaskády. Treky sú produkované v interakciách miónových neutrín v kanáli cez nabité prúdy, zatiaľ čo kaskády sú výsledkom interakcií cez nabité prúdy pre elektrónové a tau neutrína a taktiež interakcií cez neutrálne prúdy pre všetky vône neutrín. Kaskády umožňujú dostatočne presné určenie energie neutrín, avšak menej presné určenie smeru ich trajektórie. Na druhej strane trekové eventy nám poskytujú kvalitné určenie smeru trajektórie neutrín na úrovni jedného stupňa rozlíšenia, ale určenie ich energie je menej presné. Hlavné ciele dizertačnej práce sú nasledovné:

- Možná detekcia vysokoenergetických tau neutrín v neutrínových teleskopoch by znamenala, že majú astrofyzikálny pôvod, keďže ich produkcia v atmosfére Zeme je zanedbateľná ako aj pravdepodobnosť oscilácie vysokoenergetických atmosferických miónových, resp. elektrónových, neutrín v tau neutrína. V danej súvislosti bude vyvinutý nový algoritmus na rekonštrukciu dvojitých kaskád za účelom detekcie astrofyzikálnych tau neutrín pomocou neutrínového teleskopu Baikal-GVD.

• Hlavnou úlohou neutrínového teleskopu Baikal-GVD je registrácia Čerenkovovo žiarenie z interakcií vysokoenergetických neutrín. Toto unikátne detekčné zariadenie pozoruje tiež rôzne pozaďové procesy včítane tých majúcich pôvod v biologických a chemických komponentoch vody jazera Bajkal. Predmetom výskumu bude analýza svetelnej aktivity vôd jazera Bajkal na základe dát evidovaných v období rokov 2018, 2019 a 2020. Analýzy budú zahrňovať najmä časové a priestorové variácie luminiscenčnej aktivity.

• Kalibrácie detektora KM3NeT a interpretácia registrovaných dát vyžaduje detailné porozumenie vlastností digitálneho optického modulu. Rozpady rádioaktívnych izotopov draslíka-40, uránu-238 a tória-232 prítomné v skle tejto základnej detekčnej jednotky spolu s rádioaktivitou ich dcérskych produktov prispievajú k formovaniu pozaďového signálu detektora. Tento signál digitálneho optického modulu bude po prvýkrát meraný a analyzovaný v prostredí takmer bez miónov v podzemnom laboratóriu v Modane. Taktiež budú realizované simulácie uvedených pozaďových procesov na základe dostupných údajov charakterizujúcich konštrukciu tohto zariadenia a následne budú porovnané s nameranými hodnotami.

Výsledky tohto vedeckého výskumu umožnia zefektívniť využitie neutrínových teleskopov Baikal-GVD a KM3NeT, zdokonaliť spracovanie dát z nich, a celkovo prispejú k pochopeniu procesov vo vesmíre.

Cieľ: Vývoj softvéru a spracovanie údajov z neutrínových teleskopov Baikal-GVD a KM3NeT umiestnených na severnej pologuli.

Literatúra: [1] T. K. Gaisser, R. Engel, E. Resconi: Cosmic Rays and Particle Physics, 2nd Edition, 2016, ISBN-13: 978-0521016469.
[2] Carlo Giunti and Chung W. Kim: Neutrino Physics and Astrophysics, Oxford University Press 2007, ISBN 978–0–19–850871–7.
[3] S.M. Bilenky: Introduction to the Physics of Massive and Mixed Neutrinos. Lecture Notes in Physics 947. Springer-Verlag Berlin Heidelberg 2018.
[4] Baikal-GVD Collaboration, Baikal-GVD: Gigaton Volume Detector in Lake Baikal (Scientific-Technical Report). Moscow (2012).
[5] KM3NeT Collaboration, Letter of intent for KM3NeT 2.0, Journal of Physics G: Nuclear and Particle Physics, 43 (2016) 8, 084001.
Knižné publikácie týkajúce sa fyziky častíc a astronómie ako aj publikácie v recenzovaných časopisoch a arXiv knižnici na internete (https://arxiv.org/).

Kľúčové slová: kozmické žiarenie; neutrínová astronómia; neutrínové teleskopy Baikal-GVD and KM3NeT; neutrínová aróma – elektrónové, miónové a tau neutrína; digitálny optický modul; pozaďové svetelné procesy; podzemné laboratórium

Školiteľ: prof. RNDr. Fedor Šimkovic, CSc.
Konzultant: Mgr. Rastislav Dvornický, PhD.
Konzultant: Mgr. Lukáš Fajt, PhD.
Konzultant: Dr. Ronald Bruijn
Konzultant: Dr. Vladimir Kulikovskiy
Katedra: FMFI.KJFB - Katedra jadrovej fyziky a biofyziky

Univerzita Komenského v Bratislave
Fakulta matematiky, fyziky a informatiky

Vedúci katedry: prof. RNDr. Jozef Masarik, DrSc.

Spôsob sprístupnenia elektronickej verzie práce:
bez obmedzenia

Dátum zadania: 09.01.2020

Dátum schválenia: 13.01.2020

prof. RNDr. Jozef Masarik, DrSc.
garant študijného programu

študent

školiteľ

79746416

Comenius University Bratislava
Faculty of Mathematics, Physics and Informatics

THESIS ASSIGNMENT

Name and Surname: Mgr. Eliška Eckerová
Study programme: Nuclear and Subnuclear Physics (Single degree study, Ph.D. III. deg., full time form)
Field of Study: Physics
Type of Thesis: Dissertation thesis
Language of Thesis: English
Secondary language: Slovak

Title: Development of the Double Cascade Reconstruction Techniques for the Baikal-GVD Neutrino Telescope and Analysis of the KM3NeT Digital Optical Module Properties

Annotation: Neutrino telescopes, with gamma-ray and radio telescopes and gravitational-wave laser interferometers, have played a crucial role in space exploration. These telescopes consist of large arrays of optical sensors placed in transparent mediums, such as water or ice, to detect the Cherenkov light produced when high-energy neutrinos interact with the surrounding material. They are designed to reconstruct various characteristics of neutrino events, including their flavor, energy, and direction, by analyzing the known locations and timing of the optical modules. Detecting ultra-high energy cosmic neutrinos may provide valuable insights into the mystery of the origins of cosmic rays. Researchers aim to trace the paths of these neutrinos back to their sources, which are believed to also produce cosmic rays with energies much higher than those generated by man-made colliders. Four major neutrino telescopes are operational and expanding: IceCube, Baikal-GVD, KM3NeT, and the Pacific Ocean Neutrino Experiment. These telescopes offer an initial glimpse into the high-energy neutrino universe, highlighting the need for further investigation. Detected events fall into two categories: tracks and showers. Tracks are produced by charged-current interactions involving muon neutrinos, while showers result from charged-current interactions with electron and tau neutrinos and all-flavor neutral-current interactions. The cascades associated with shower events provide precise energy estimates within a few percent but are less accurate in determining direction. On the other hand, track events offer excellent directional resolution, typically within one degree, but their energy estimates are less precise. The primary objectives of the PhD thesis are as follows:

- High-energy tau neutrinos are promising for astrophysical neutrino detection due to their negligible atmospheric production and oscillation from muon and electron neutrinos. A new algorithm for reconstructing double cascades will be developed to detect astrophysical tau neutrinos using the Baikal-GVD neutrino telescope.
- The Baikal-GVD neutrino telescope aims to detect Cherenkov radiation from neutrino interactions but also records background noise from ambient light. It is planned to analyze the optical light activity of Baikal water, particularly the time and spatial variations of the luminescence activity, for data collected in 2018, 2019, and 2020.

- Accurate analysis of KM3NeT data and detector calibration depend on a comprehensive understanding of the digital optical module's properties. Radioactive isotopes, such as potassium-40, uranium-238, and thorium-232, present in the glass of the digital optical module contribute to its background signals. The internal noise of the digital optical module will be measured and analyzed in a nearly muon-free environment at the Modane Underground Laboratory.

The findings from the PhD study are expected to be essential to the fields of neutrino telescopes and astronomy.

Aim: Develop software to process and analyze data from the Baikal-GVD and KM3NeT neutrino telescopes located in the Northern Hemisphere.

Literature: [1] T. K. Gaisser, R. Engel, E. Resconi: Cosmic Rays and Particle Physics, 2nd Edition, 2016, ISBN-13: 978-0521016469.
[2] Carlo Giunti and Chung W. Kim: Neutrino Physics and Astrophysics, Oxford University Press 2007, ISBN 978–0–19–850871–7.
[3] S.M. Bilenky: Introduction to the Physics of Massive and Mixed Neutrinos. Lecture Notes in Physics 947. Springer-Verlag Berlin Heidelberg 2018.
[4] Baikal-GVD Collaboration, Baikal-GVD: Gigaton Volume Detector in Lake Baikal (Scientific-Technical Report). Moscow (2012).
[5] KM3NeT Collaboration, Letter of intent for KM3NeT 2.0, Journal of Physics G: Nuclear and Particle Physics, 43 (2016) 8, 084001.
Textbooks on particle physics and astronomy, as well as articles from academic journals and the arXiv library (https://arxiv.org/).

Keywords: cosmic rays; the Baikal-GVD and KM3NeT neutrino telescopes; electron, muon, and tau neutrinos; digital optical module; double cascades; ambient light; underground laboratory

Tutor:	prof. RNDr. Fedor Šimkovic, CSc.
Consultant:	Mgr. Rastislav Dvornický, PhD.
Consultant:	Mgr. Lukáš Fajt, PhD.
Consultant:	Dr. Ronald Bruijn
Consultant:	Dr. Vladimir Kulikovskiy
Department:	FMFI.KJFB - Department of Nuclear Physics and Biophysics
Head of department:	prof. RNDr. Jozef Masarik, DrSc.
Assigned:	09.01.2020
Approved:	13.01.2020

prof. RNDr. Jozef Masarik, DrSc.
Guarantor of Study Programme

....
Student

....
Tutor

I hereby declare that I personally elaborated the study presented here, under leadership of my supervisor and with assistance of my consultants. Literature and sources are listed.

Bratislava, February 2025 ....

Mgr. Eliška Eckerová

Acknowledgments

Firstly, I would like to express my gratitude to my supervisor prof. RNDr. Fedor Šimkovic, CSc., for his support, encouragement, and scientific explanations which helped me to understand neutrino physics better. I greatly appreciate that he provided me with numerous possibilities to attend conferences and internships which were very beneficial for this work.

My sincere gratitude belongs to my consultant Mgr. Rastislav Dvornický, PhD., for his guidance, continuous support, and advice. I am very grateful for discussions, explanations, and his help regarding Baikal-GVD.

Special thanks belong to my consultant Mgr. Lukáš Fajt, PhD., for valuable insights, creative ideas, and enthusiasm that motivated me to work. His support and guidance made this Baikal-GVD double cascade reconstruction algorithm possible.

I would also like to express my gratitude to my consultant Dr. Ronald Bruijn. I greatly appreciate his help with preparation of the LSM experimental setup, willingness to explain everything about the KM3NeT hardware, and also valuable discussions about data analysis.

I would like to thank my consultant Dr. Vladimir Kulikovskiy, for the support regarding the KM3NeT part of the thesis. I am very grateful for fruitful discussions that helped to shape the KM3NeT chapter and also for his guidance during work with Monte Carlo simulations and data analysis.

Further, I would like to extend my gratitude to doc. Ing. Ivan Štekl, CSc., who made the collaboration among KM3NeT, LSM, and NRPI possible. I also appreciate that he provided me with the opportunity to attend many internships in IEAP in Prague which significantly helped me with this work.

I would also like to thank Dr. Yury Shitov, for his advice and help with the measurements in the Modane underground laboratory and also for the realization of the cooperation between KM3NeT and NRPI.

My gratitude belongs to Zuzka, who studied PhD alongside me. I deeply appreciate numerous discussions, continuous support, and also the fact that we could get through difficult times together. Many thanks also belong to Báša for her help and valuable discussions.

Finally, special thanks belong to my family, for their never-ending support, continuous encouragement, and patience.

Abstrakt

Neutrínová astronómia je dôležitá súčasť multi-messenger astronómie. Neutrína sú ideálne častice na výskum procesov v hlbokom vesmíre. Ich vlastnosti im umožňujú precestovať obrovské vzdialenosti vo vesmíre bez prekážok a tak prinášať neporušené informácie o javoch v hlbokom vesmíre. Tieto vlastnosti však robia detekciu neutrín veľmi náročnou.

Táto dizertačná práca sa zaoberá dvomi z hlavných neutrínových teleskopov na svete – Baikal-GVD a KM3NeT. V týchto teleskopoch sa neutrína detegujú nepriamo, pomocou detegovania Čerenkovovho žiarenia emitovaného nabitými časticami, ktoré vznikajú v interakciách neutrín. Hlavným cieľom časti tejto práce, ktorá je zameraná na neutrínový teleskop Baikal-GVD, je vývoj algoritmu na rekonštrukciu dvojitých kaskád. Signatúra dvojitých kaskád môže vznikať v interakcii ν_τ. Keďže produkcia vysokoenergetických ν_τ v atmosfére je zanedbateľná, detekcia vysokoenergetických ν_τ potenciálne umožňuje identifikáciu astrofyzikálnych neutrín. V tejto časti práce je opísaný vývoj prvého algoritmu na rekonštrukciu dvojitých kaskád pre Baikal-GVD, taktiež je vyhodnotená jeho presnosť a efektivita. Ďalej sú prezentované prvé výsledky spracovania experimentálnych dát týmto rekonštrukčným algoritmom. Druhá téma spojená s neutrínovým teleskopom Baikal-GVD je analýza svetla prítomného v jazere Bajkal. Toto svetlo vytvára pozadie k neutrínovým analýzam, preto je podstatné jeho dôkladné štúdium. V tejto časti práce sú prezentované časové a priestorové variácie tohto pozaďového svetla. Časť práce, ktorá je spojená s neutrínovým teleskopom KM3NeT, sa zaoberá štúdiom vnútorného šumu základnej detekčnej jednotky tohto detektora – digitálneho optického modulu. Vnútorný šum zodpovedá signálu, ktorý sa deteguje ak nie sú prítomné žiadne vonkajšie zdroje. Kvôli prirodzenému odtieneniu hlavného zdroja pozadia – atmosferických miónov, boli tieto merania uskutočnené v podzemnom laboratóriu v Modane. Táto časť práce sa zaoberá prípravou experimentálnej aparatúry na tieto merania, následnými experimentálnymi meraniami ako aj vývojom Monte Carlo simulácií zodpovedajúcim aparatúre použitej pri meraniach v laboratóriu v Modane. Ďalej je prezentovaná detailná analýza Monte Carlo simulácii a dát nameraných v podzemnom laboratóriu.

Kľúčové slová: astrofyzikálne neutrína, neutrínové teleskopy, Baikal-GVD, KM3NeT, dvojité kaskády, digitálny optický modul

Abstract

Neutrino astronomy plays a vital role in the broader field of multi-messenger astronomy. Neutrinos are ideal particles for investigation of processes happening in deep space. Their attributes allow them to travel tremendous distances in the universe unimpeded and thus providing undistorted information about deep-space phenomena. Conversely, these characteristics make neutrino detection a challenging endeavor.

This doctoral thesis is focused on two of the main neutrino telescopes in the world – Baikal-GVD and KM3NeT. In these telescopes, neutrinos are detected indirectly, through detection of Cherenkov radiation produced by secondary charged particles originating in neutrino interactions. The main aim of the part of the thesis dedicated to the Baikal-GVD neutrino telescope is the development of the double cascade reconstruction algorithm. Double cascade signature can be created in ν_τ interaction. Since the production of high-energy ν_τ in the atmosphere is negligible, detection of high-energy ν_τ provides a promising way of astrophysical neutrinos identification. In this part of the thesis, development as well as the precision and the efficiency of the first double cascade reconstruction algorithm for the Baikal-GVD neutrino telescope are presented. Moreover, the first results from the processing of the experimental data with the double cascade reconstruction algorithm are given. The second topic related to the Baikal-GVD neutrino telescope is the analysis of the ambient light present in Lake Baikal. Ambient light creates unavoidable background to neutrino identification, hence the systematic study of this light is essential. Time and spatial variations of the ambient light at the Baikal-GVD site are presented. The part of the thesis related to the KM3NeT neutrino telescope describes the study of internal noise of the basic detection unit of this detector – digital optical module. Internal noise corresponds to signals which are detected when no external sources are present. In order to suppress a primary source of background – atmospheric muons, the measurements were performed in the Modane underground laboratory. This part of the thesis includes the preparation of the experimental setup for these measurements, subsequent experimental measurements as well as the development of the Monte Carlo simulations corresponding to the Modane underground laboratory setup. Furthermore, the detailed analysis of Monte Carlo simulations and the data collected in the laboratory is presented.

Keywords: astrophysical neutrinos, neutrino telescopes, Baikal-GVD, KM3NeT, double cascades, digital optical module

Contents

Introduction

Exploration of deep space has always presented challenge to humankind. That is one of the main reasons standing behind the development of the neutrino astrophysics.

Neutrinos can hide a key to many unanswered questions related to the origin and evolution of the universe and processes inside its deepness. They are ideal cosmic probes. Neutrinos do not have electric charge, therefore, their trajectories are not influenced by the electromagnetic fields in the universe. Hence, the direction of the incoming neutrino points directly to the source where this neutrino originated. Secondly, their cross-sections of the interactions with matter are very small, therefore, neutrinos can travel enormous distances and pass through very dense environments without interaction. They can bring us undistorted information about phenomena that happens in the vicinity of black holes, active galactic nuclei, or collisions of black holes, neutron stars, or entire galaxies. However, these attributes make neutrino detection difficult. In order to obtain sufficient statistics, the detectors with huge sensitive volume ($\sim$ km^3) are required.

In 1960 at the Rochester conference, Markov proposed the idea of building neutrino telescopes deep in the lake or sea [1]. Following this idea, the project of the first underwater neutrino telescope called Deep Underwater Muon and Neutrino Detector DUMAND was discussed in 1970s [2]. In 1987, the first string with photomultiplier tubes was installed in the Pacific ocean near Hawaii. However, DUMAND was never fully constructed [3].

The Baikal Gigaton Volume Detector (Baikal-GVD) is the successor of the first completed underwater neutrino telescope in the world – NT-200. The installation of NT-200 was finished in 1998 [4]. Baikal-GVD is still under construction, in 2024 it consists of 3 960 optical modules installed on 110 strings.

The Cubic Kilometre Neutrino Telescope (KM3NeT) is the neutrino telescope under construction in the Mediterranean sea [5]. It is the successor of the Astronomy with a Neutrino Telescope and Abyss environmental RESearch project (ANTARES) [6], which was dismantled in February 2022. KM3NeT consists of two detectors – KM3NeT/ARCA situated nearby Capo Passero, Italy and KM3NeT/ORCA placed in vicinity of the Toulon, France.

In addition to Baikal-GVD and KM3NeT, there are other large-scale neutrino telescopes in the world installed or planned to be built – IceCube installed at the South Pole [7], and future projects like Pacific Ocean Neutrino Experiment (P-ONE) planed to be constructed in the Pacific ocean nearby Vancouver [8], The tRopIcal DEep-sea Neutrino Telescope (TRIDENT) intended to be built in South China Sea [9], Huge Underwater high-energy Neutrino Telescope (HUNT) [10] and NEutrino Observatory in the Nanhai (NEON) [11].

This doctoral thesis is focused on two large-scale water Cherenkov neutrino telescopes – Baikal-GVD and KM3NeT. It is organized into five chapters. The first chapter briefly describes status of the neutrino astrophysics field and gives principles of neutrino detection. In the second chapter, the description of two neutrino telescopes – Baikal-GVD and KM3NeT which are the subjects of this PhD thesis is given. The third chapter is dedicated to the description of the first steps in detailed analysis of the properties of the KM3NeT digital optical module. The analysis is focused on the study of the internal noise of the digital optical module – signal detected by the digital optical module when no external sources are present. To obtain data suitable for this kind of the analysis, measurements were performed in the Modane underground laboratory under Fréjus peak. The description of the experimental setup, Monte Carlo simulations and analysis of the first measured data is given. The fourth chapter is dedicated to the study of ambient light field in Lake Baikal. This light contributes to unavoidable background of the Baikal-GVD neutrino telescope. Time and spatial variations of this light field are described. The fifth chapter presents a description of the development of the first double cascade reconstruction algorithm for the Baikal-GVD neutrino telescope. The double cascade signature is produced in particular type of ν_τ interaction. The registration of the high-energy ν_τ is one of the most promising ways to detect astrophysical neutrinos because the rate of production of high-energy ν_τ in the atmosphere or the probability of the atmospheric neutrinos of other flavor to oscillate to high-energy ν_τ is almost negligible [12]. The efficiency and the precision of the newly developed algorithm are given. Moreover, the estimation of the rates of the ν_τ double cascade background events as well as the results from experimental data processing with double cascade reconstruction algorithm are presented.

Chapter 1

Neutrino astrophysics

Neutrinos are excellent particles for the universe exploration. Their uniqueness stems from the combination of their attributes. They are lightest known elementary particles and they do not have electric charge. Therefore, they can travel through the space without being influenced by electromagnetic fields – their trajectories are directly pointing to their source, thus allowing source identification. This is a great advantage in comparison with charged particles. In their case after deflection by electromagnetic fields, their direction is not correlated with the source, see Fig. 1.1.

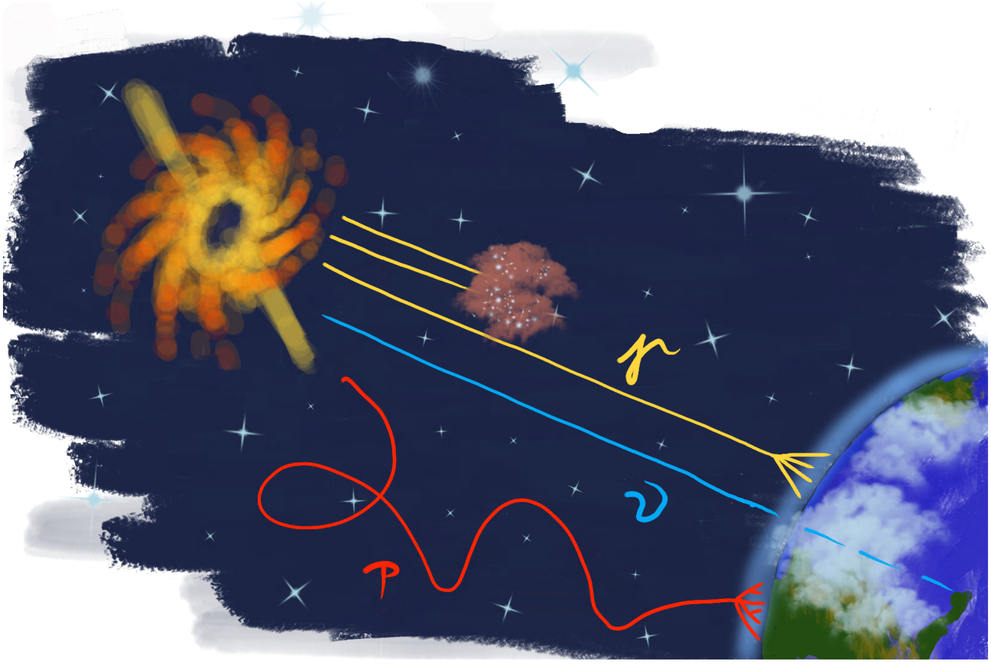

Figure 1.1: Illustration of the trajectories of various particles, propagating through the universe. Paths of neutral particles – photons (yellow color), neutrinos (blue color) are not deflected by electromagnetic fields, while trajectory of charged particles e.g. protons (red color) is curved due to the influence of these fields. Image credit: Barbora Eckerová.

Furthermore, neutrinos are stable particles and interact only via weak interaction (presuming gravitational interaction is negligible in particle physics) with very small cross-sections. These attributes enable them to travel through very dense environments and immense distances without interaction and therefore they can be used as cosmic probes allowing us to study processes in deep space.

Simultaneously, these attributes make their detection a challenging task. To obtain significant statistics, detectors with volume at the level of km^3 are required. For Cherenkov neutrino telescopes sufficient reservoir of clear medium for light propagation is needed. Subsequently, this volume is instrumented with light sensitive detectors – photomultiplier tubes. Currently, several Cherenkov neutrino telescopes are installed or planed to be built in ocean, sea, lake, or ice.

1.1 Astrophysical neutrinos

The observation of neutrinos with extraterrestrial origin dates back to 1960s, when Homestake experiment detected neutrinos produced in the Sun. They used tank filled with liquid tetrachloroethylene to detect neutrinos by counting argon produced in interaction [13]:

$$^{37}Cl + \nu_e \rightarrow e^- +^{37} Ar. \tag{1.1}$$

Approximately 20 years later in 1987, neutrinos from supernova SN1987A were detected by Kamiokande II [14] and Irvine-Michigan-Brookhaven detectors [15]. Moreover, also antineutrinos were detected by Baksan Neutrino Observatory [16]. The energy of detected events was in the range from 7.5 to 40 MeV.

The evidence for high-energy astrophysical neutrinos was reported by IceCube in 2013. The atmospheric origin of detected events was rejected at 4 σ level [17]. In following studies published by IceCube in 2014 and 2016, the atmospheric origin of the observed events was rejected at 5.7 and 5.6 σ, respectively [18], [19]. The next experiment which reported observation of diffuse astrophysical neutrino flux was Baikal-GVD in 2023. The null astrophysical neutrino flux hypothesis was rejected at 3.05 σ level [20].

The isotropic diffuse astrophysical neutrino flux can be parametrized as:

$$\Phi^{\nu+\bar{\nu}}_{astro} = 3 \cdot 10^{-18} \Phi_{astro} \left(\frac{E_\nu}{E_0} \right)^{-\gamma_{astro}} [\mathrm{GeV}^{-1}\mathrm{s}^{-1}\mathrm{sr}^{-1}\mathrm{cm}^{-2}], \tag{1.2}$$

where Φ_{astro} is normalization of one-flavor neutrino flux, γ_{astro} denotes spectral index, E_ν is neutrino energy, and $E_0 = 100$ TeV. Numerical factor of 3 in this equation stands for three neutrino flavors. This model assumes equal neutrino flavors and identical number of neutrinos and antineutrinos at Earth. The parameters from Eq. 1.2 obtained from the fit by various experiments are shown in Fig. 1.2. Measured energy spectrum of diffuse flux of astrophysical neutrinos is displayed in Fig. 1.3.

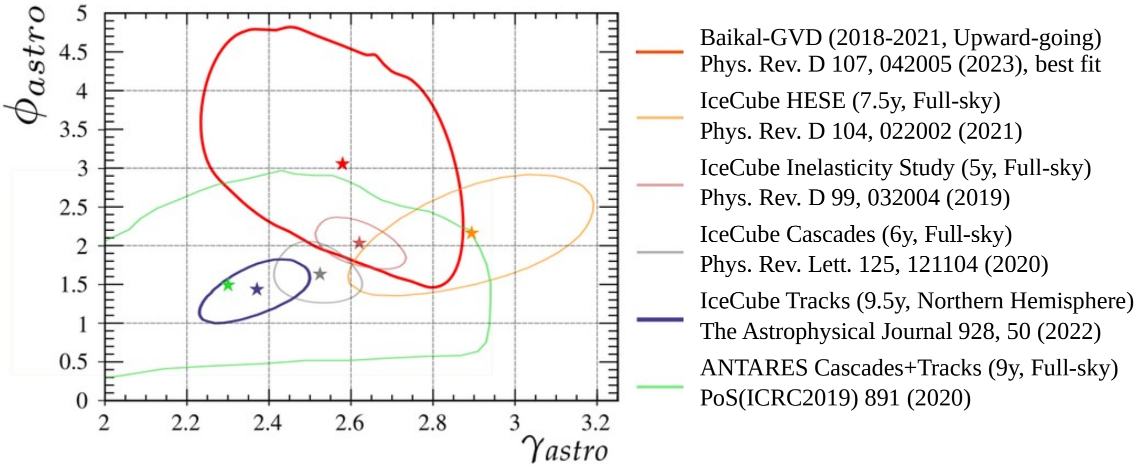

Figure 1.2: Parameters of the astrophysical diffuse neutrino flux – normalization Φ_{astro} and spectral index γ_{astro} from Eq. 1.2 obtained from the fit for the single power law hypothesis. The contours display 68 % confidence regions. Different colors show results from different experiments and various event selections. Taken from [20], legend adapted.

Considering neutrino cross-sections and their flux at the highest energies, detection of the ultra-high energy events is unique. Recently, the detection of the event which could be the most energetic neutrino event ever observed was announced by the KM3NeT Collaboration [22, 23]. The detailed analysis of this event is expected to be published soon.

The sources of high-energy astrophysical neutrinos are still unexplored, so far only small fraction of potential candidates was discovered. As the first potential source of high-energy astrophysical neutrinos, the blazar TXS 0506+056 was identified. In this case, the direction and time of the neutrino event with estimated energy of 290 TeV detected by IceCube was coincident with γ-ray flare from γ-ray blazar TXS 0506+056. Random coincidence of the detected neutrino event with the TXS 0506+056 flare was rejected at 3 σ level [24]. Independent search of the excess of the high-energy neutrinos from the direction of blazar TXS 0506+056 in the IceCube data measured prior to the flare in 2017 resulted in the evidence of the neutrino emission from TXS 0506+056 direction at the level of 3.5 σ [25]. In 2021, Baikal-GVD observed neutrino event with estimated energy of 224 TeV from the blazar TXS 0506+056 direction followed by radio flare detected by RATAN-600 [26].

The next observation of correlation of direction of neutrino events with source was reported in 2022 by IceCube. The excess of detected neutrino events was connected

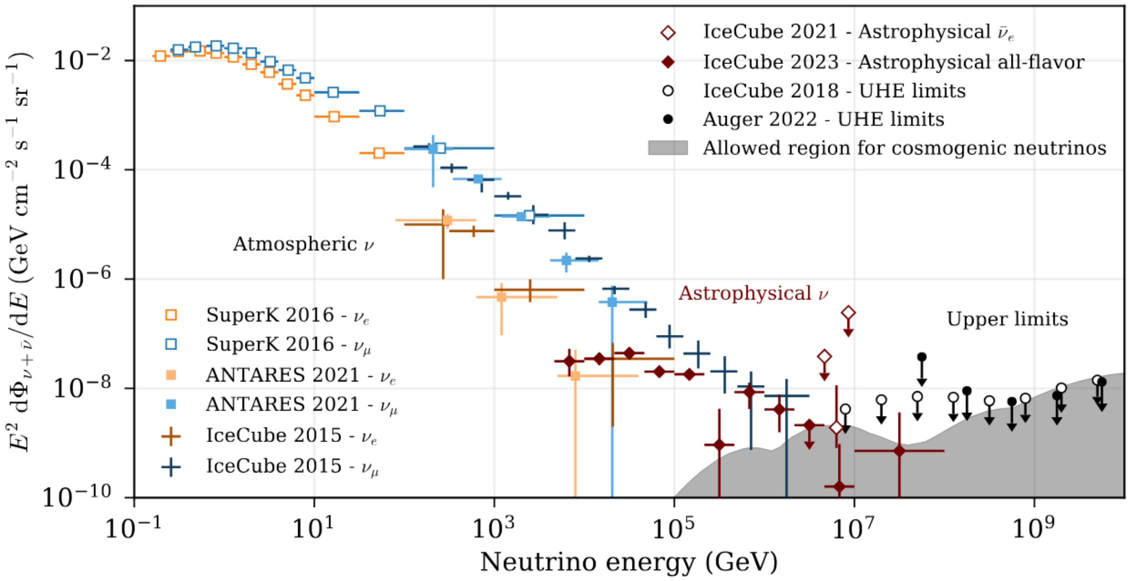

Figure 1.3: Measured energy spectrum of diffuse neutrino flux for astrophysical and atmospheric neutrinos. Measurements from various experiments are shown. For the highest energies, model predictions for cosmogenic neutrinos are compared with experimental limits. Given fluxes are normalized to single flavor of neutrinos and antineutrinos assuming equal ratio of neutrinos and antineutrinos. For astrophysical neutrinos equal flavor ratio at Earth is assumed. Taken from [21].

with active galaxy NGC 1068 at 4.2 σ significance level. However, the fluxes from these two sources – TXS 0506+056 and NGC 1068, in their corresponding energy ranges contribute no more than approximately 1 % to the overall astrophysical neutrino diffuse flux, see Fig. 1.4 [27].

Another possible source of the astrophysical neutrinos is our galaxy, the Milky Way. The IceCube Collaboration reported the observation of neutrinos from the Galactic plane with significance at the level of 4.5 σ [28].

Production of high-energy neutrinos is expected to be connected with the same sites where cosmic rays are accelerated. High-energy neutrinos and also γ can be produced in interactions of accelerated cosmic rays with surrounding matter or radiation fields. There are two main production mechanisms:

- hadronuclear interactions – interactions of cosmic rays with matter

$$\begin{aligned} p+p &\rightarrow p+p+\pi^0, \\ p+p &\rightarrow p+n+\pi^+, \\ p+n &\rightarrow p+n+\pi^0, \\ p+n &\rightarrow p+p+\pi^-. \end{aligned} \tag{1.3}$$

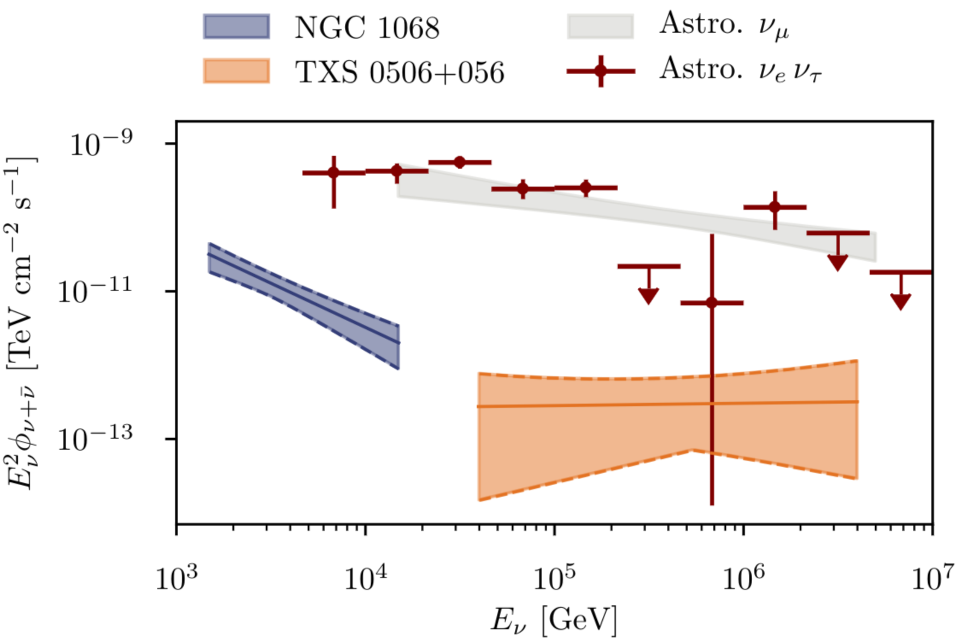

Figure 1.4: Point source fluxes from the sources TXS 0506+056 and NGC 1068 compared with total diffuse flux of astrophysical neutrinos. Presented fluxes correspond to single flavor of neutrinos and antineutrinos assuming equal neutrino flavor ratio. Taken from [27].

- photohadronic interactions – interaction of cosmic rays with photons

$$\begin{aligned} p + \gamma &\to \Delta^+ \to n + \pi^+, \\ p + \gamma &\to \Delta^+ \to p + \pi^0. \end{aligned} \tag{1.4}$$

Dominant decay (branching ratio $\sim$ 98.82 % [21]) of neutral pion is decay into two photons:

$$\pi^0 \to \gamma + \gamma. \tag{1.5}$$

Charged pions subsequently decay into muons with branching ratio $\sim$ 99.99 % [21]:

$$\begin{aligned} \pi^+ &\to \mu^+ + \nu_\mu, \\ \pi^- &\to \mu^- + \bar{\nu}_\mu. \end{aligned} \tag{1.6}$$

Finally, muons decay according to the scheme:

$$\begin{aligned} \mu^- &\to e^- + \nu_\mu + \bar{\nu}_e, \\ \mu^+ &\to e^+ + \bar{\nu}_\mu + \nu_e. \end{aligned} \tag{1.7}$$

In this scenario, flavor ratio of neutrinos at the source is $\nu_e : \nu_\mu : \nu_\tau = 1:2:0$. At the Earth, due to the effect of neutrino oscillations, the expected neutrino flavor ratio is $\nu_e : \nu_\mu : \nu_\tau = 1:1:1$ [29].

1.2 Cosmic rays

Cosmic rays are particles mainly protons less abundantly heavier nuclei propagating through the space. Their sources and acceleration mechanisms are still unclear, but since the neutrinos are expected to be produced at the same sources, combined study of astrophysical neutrinos and cosmic rays is considered to be a promising way how to analyze the origin of cosmic rays.

The energy spectrum of cosmic rays, together with spectra of neutrinos and γ-rays are shown in Fig. 1.5.

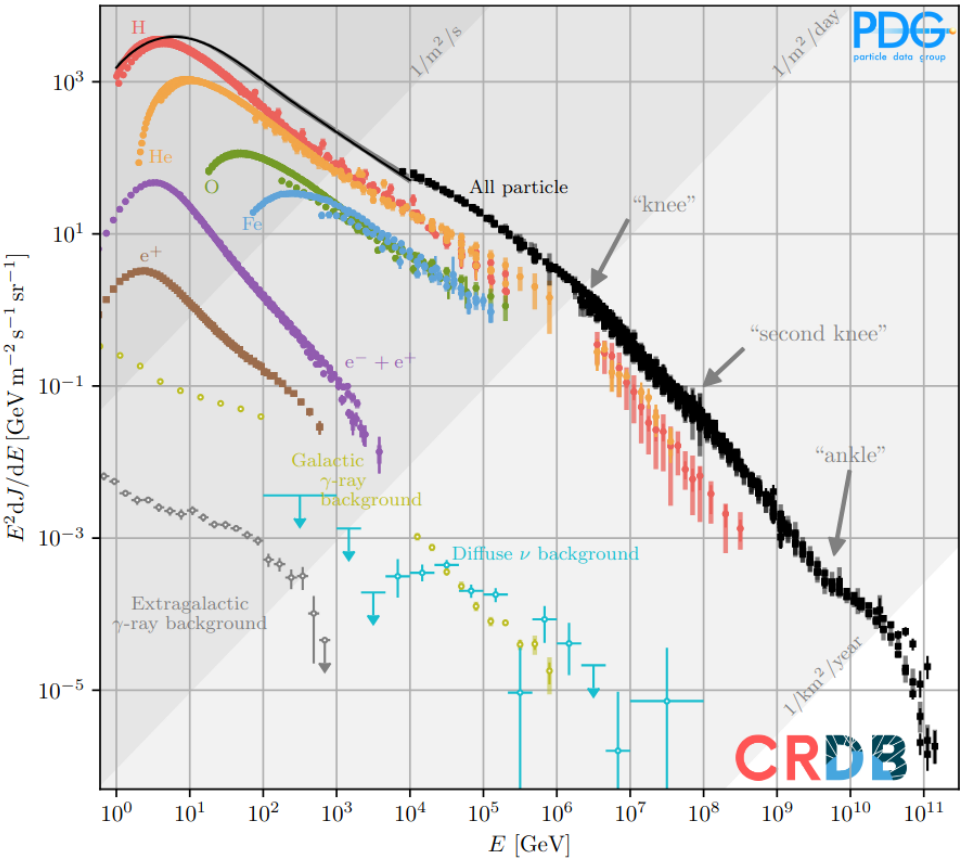

Figure 1.5: Energy spectrum of cosmic rays. Measured diffuse fluxes of the charged cosmic rays, γ rays and neutrinos multiplied by kinetic energy squared as a function of kinetic energy are shown. Diagonal lines illustrate energy integrated fluxes. Taken from [21].

The energy spectrum of cosmic rays can be characterized by a power law dependence:

$$\frac{dN}{dE} \sim E^{-\gamma}. \tag{1.8}$$

The spectral index γ varies from 2.5 to 3.3. The energy spectrum exhibits several features. Up to few PeV range, the spectral index γ equals approximately 2.7, at the few PeV energy there is so called "knee" where energy spectrum become softer with γ at the level of 3. The second feature, the steepening of the spectrum, is the "second knee" at approximately 100 PeV, where γ changes to ~ 3.3. At a few EeV, there is an "ankle" where spectral index changes to ~ 2.5 – spectrum becomes harder again. Finally, the cosmic ray flux is significantly suppressed above few tens of EeV [21].

The possible explanation of the cut-off of the cosmic ray flux at few tens of EeV is the Greisen-Zatsepin-Kuzmin (GZK) effect [30, 31]. It implies that protons with energies higher than few tens of EeV start to interact with cosmic microwave background producing pions through delta resonance, see Eq. 1.4. This interaction limits propagation distance of such protons to approximately 100 Mpc [21]. It might explain the suppression of the flux at EeV energies.

The maximal energy to which a cosmic ray accelerator can accelerate cosmic rays can be estimated using Hillas criterion [32]. It states that a particle can be accelerated while its gyroradius is smaller than the size of the cosmic ray accelerator. The gyroradius also called Larmor radius is the radius of a circular trajectory of charged particle in a homogeneous magnetic field. Consequently, if the particle acquire sufficient energy so its Larmor radius is larger that size of the accelerator, the particle can escape – therefore maximal energy which the particle can accumulate is limited.

1.3 Atmospheric neutrinos

Atmospheric neutrinos are produced in interactions of cosmic rays with the atmosphere. Since they are indistinguishable from astrophysical neutrinos, they are considered as one of the main sources of the background to astrophysical neutrino analyses.

In interactions of cosmic rays with the atmosphere huge amount of secondary particles are created. Among them, pions and less frequently kaons can be produced. Illustration of interaction of cosmic rays with the atmosphere is shown in Fig. 1.6.

These mesons subsequently decay, pions for example according to decay schemes given in Eq. 1.6 and Eq. 1.7. Neutrinos produced in decays of these mesons in the atmosphere belong to so called conventional atmospheric neutrino flux. The energy spectrum of conventional atmospheric neutrinos follows $E^{-3.7}$ power law, this flux dominates in GeV to TeV energy range. The prompt atmospheric neutrinos originate in decay of hadrons, that contain charm or bottom quark. The prompt atmospheric neutrino flux is predicted to dominate at the highest energies, the energy spectrum is expected to be harder $E^{-2.7}$ in comparison with conventional atmospheric neutrino flux [21]. The measured energy spectrum of atmospheric neutrinos is shown in Fig. 1.3.

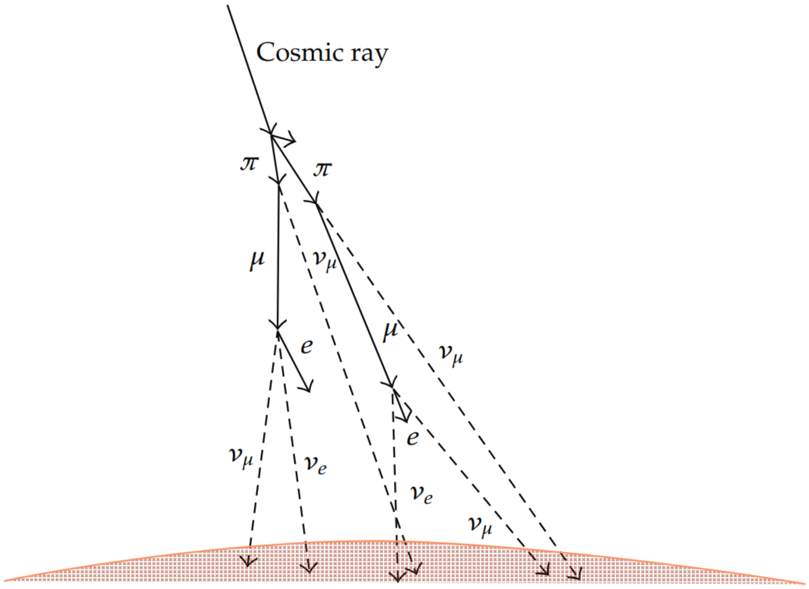

Figure 1.6: Illustration of the atmospheric neutrino production. In interaction of cosmic rays with the atmosphere pions are produced. They subsequently decay following Eq. 1.6 and Eq. 1.7, resulting in the atmospheric neutrino production. Taken from [33].

1.4 Neutrino interactions

Neutrinos interact with matter through weak interaction. According to the type of the exchanged boson, there are two types of interactions – charged current and neutral current.

Charged current (CC) interactions are realized via exchanging W^+ or W^-. In this interaction, incoming neutrino interacts with matter resulting in lepton with the same flavor as interacting neutrino:

$$N + \nu_\ell \rightarrow X + \ell. \tag{1.9}$$

The Feynman diagram of the CC interaction is shown in Fig 1.7a.

At certain energy of electron antineutrino, which is approximately 6.3 PeV, the probability of its interaction with atomic electrons is increased. The phenomenon of this enhancement is referred to as Glashow resonance [34] and the equation of this interaction is following:

$$\overline{\nu}_e + e^- \rightarrow W^- \rightarrow leptons/hadrons. \tag{1.10}$$

In 2021, IceCube reported observation of the event consistent with being created in Glashow resonance [35].

The other type of interaction is Neutral Current interaction (NC). It is mediated by electrically neutral Z^0 boson. In this interaction, neutrino of an arbitrary flavor interacts with matter and in the final state there is neutrino with the same flavor:

$$N + \nu_\ell \rightarrow X + \nu_\ell. \tag{1.11}$$

In Fig. 1.7b corresponding Feynman diagram is displayed. In both equations – Eq. 1.9 and Eq. 1.11, N denotes target nucleon and X symbolizes particles in the final state of the interaction.

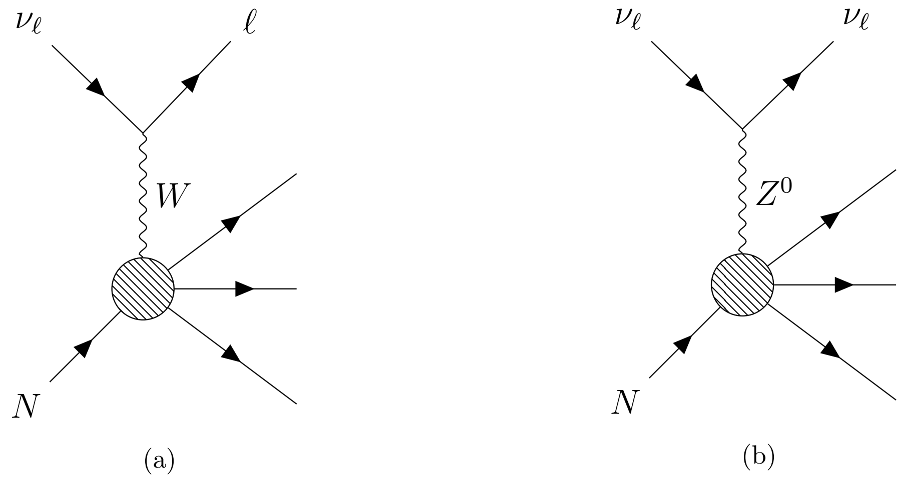

Figure 1.7: Feynman diagrams of deep inelastic scattering process – the neutrino with flavor l scatters off a quark inside the nucleon producing a hadronic cascade and a lepton in the final state. a) Charged current interaction. b) Neutral current interaction.

The total cross-sections for CC interactions of neutrinos and antineutrinos as a function of their energy are shown in Fig. 1.8. Simultaneously, the partial cross-sections for particular processes – quasi-elastic scattering (QE), resonance production (RES), and deep inelastic scattering (DIS) are given. For high-energy neutrinos and antineutrinos deep inelastic scattering dominates. In this process, neutrino interacts with quarks inside nucleons and hadronic cascade is produced [36].

1.5 Cherenkov radiation

When a charged particle is propagating through matter, it polarizes atoms in this medium. After particle passage, these atoms emit photons in order to return to the ground state. If the velocity of this particle is lower than the speed of light in the corresponding medium, interference of these photons is destructive. However, if the velocity of the particle is higher than the velocity of light in the medium, it results in constructive interference of the photons. This effect is called Cherenkov radiation [37].

Illustration of Cherenkov radiation is shown in Fig. 1.9. The angle between direction

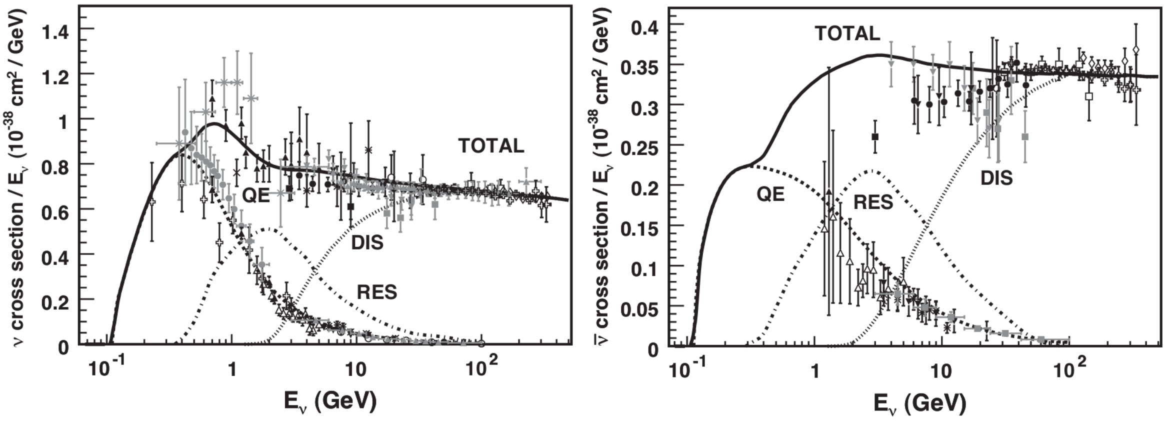

Figure 1.8: Total and partial neutrino (left) and antineutrino (right) per nucleon charged current interactions cross-sections given as a function of energy. Points display different measurements. Dashed and dotted lines show predictions for different contributing processes – quasi-elastic scattering (QE), resonance production (RES), and deep inelastic scattering (DIS). Black line depict prediction for total cross-section. Taken from [36].

of the particle trajectory and Cherenkov light emission is given as:

$$cos(\theta_C) = \frac{1}{\beta n}, \tag{1.12}$$

where θ_C is Cherenkov angle, β denotes ratio between particle velocity and the speed of light in vacuum v/c, and n means refractive index of the material. For a relativistic particle ($\beta \approx 1$) propagating in the water with refractive index $n \approx 1.33$, Cherenkov angle θ_C is approximately 41.2°.

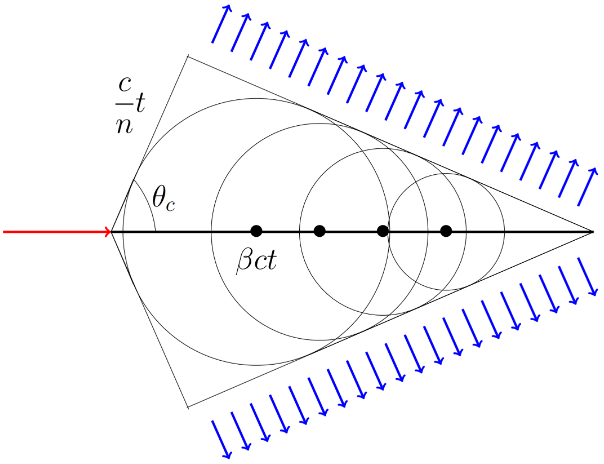

Figure 1.9: Schematic view of Cherenkov radiation propagation. Red arrow represents charged particle, blue arrows depict Cherenkov radiation. Taken from [38].

The number of Cherenkov photons N emitted by the charged particle per wavelength $d\lambda$ and per meter traveled in the matter dz is expressed by the Frank-Tamm equation [39]:

$$\frac{d^2N}{dzd\lambda} = \frac{2\pi\alpha q^2}{\lambda^2}\left(1 - \frac{1}{(\beta n)^2}\right). \tag{1.13}$$

In this equation α is the fine structure constant and q denotes charge of the particle. From Eq. 1.13 it follows, that for relativistic muon with $\beta \approx 1$ traveling in seawater, approximately $3.7 \cdot 10^4$ photons will be emitted per meter of the particle trajectory in the wavelength range 300 - 650 nm. Chosen wavelength range corresponds to the wavelengths in which typical photomultiplier tubes are most efficient.

1.6 Light signatures

In the water Cherenkov neutrino telescopes, neutrinos are detected through the registration of the Cherenkov radiation emitted by the charged particles that originate in the neutrino interactions. There are two main types of the Cherenkov light patterns – *tracks* and *cascades*, see Fig. 1.10. According to the type of the neutrino interaction, there are various light signatures that can be registered in the neutrino telescopes, see Fig. 1.11.

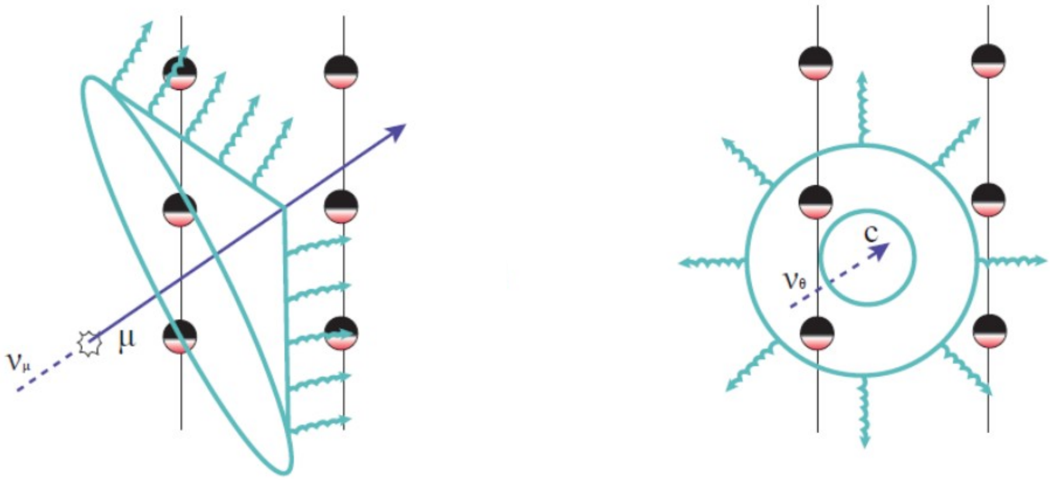

Figure 1.10: Illustration of two types of the Cherenkov light patterns – track (left) and cascade (right). Taken from [40].

In the deep inelastic scattering of the neutrino with nucleon, a hadronic cascade is created. This is mutual feature of CC and NC interactions regardless of the neutrino flavor.

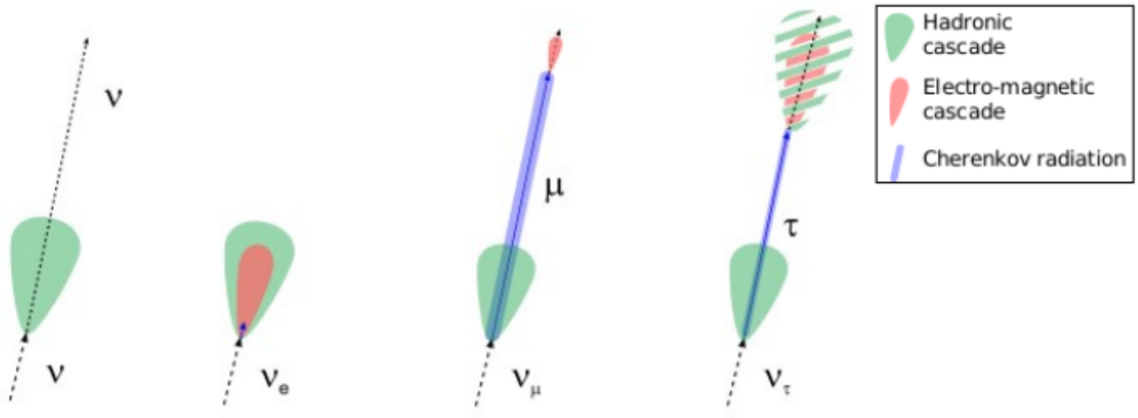

Figure 1.11: Illustration of the signatures created in various types of the neutrino interactions. From left to right, NC interaction resulting in a hadronic cascade for all three types of neutrino flavors, the other three signatures are produced by CC interactions of neutrinos with different flavors. Taken from [41].

Since neutrino originating in the NC interaction can not be registered, the NC interaction is not dependent on the neutrino flavor and only single cascade signature is registered in the detector.

In the CC interaction of electron neutrino, electron is produced. It creates electromagnetic cascade in the same area in which the hadronic cascade from neutrino interaction is formed. Therefore, the resulting signature is single cascade.

The angular distribution of the Cherenkov photon emission for cascades is not completely uniform. The angle between cascade axis and direction of photon emission for electromagnetic and hadronic cascades is shown in Fig. 1.12 [42].

Muon that is produced in the CC interaction of muon neutrino creates track signature. Together with the cascade produced in neutrino interaction, the CC interaction of muon neutrino creates the track starting with the cascade.

Tau lepton originating in the CC interaction of tau neutrino has mean lifetime $\tau = (290.3 \pm 0.5) \cdot 10^{-15}$ s [21]. Due to the relativistic effects its mean lifetime is prolonged in the reference system associated with the detector. Therefore, the mean path that tau lepton travels before it decays can be calculated according to following equation:

$$L = \gamma c \tau = \frac{E}{m_\tau c^2} c\tau \approx 49 \frac{E}{\mathrm{PeV}} \ [\mathrm{m}], \tag{1.14}$$

where γ denotes the Lorentz factor, c marks the speed of light in vacuum, E is the energy of the tau lepton in the detector frame in PeV, and m_τ marks the mass of tau lepton.

According to the decay mode of tau lepton there are two types of signatures. If tau lepton decays into muon, the signature is very similar to signature created in CC

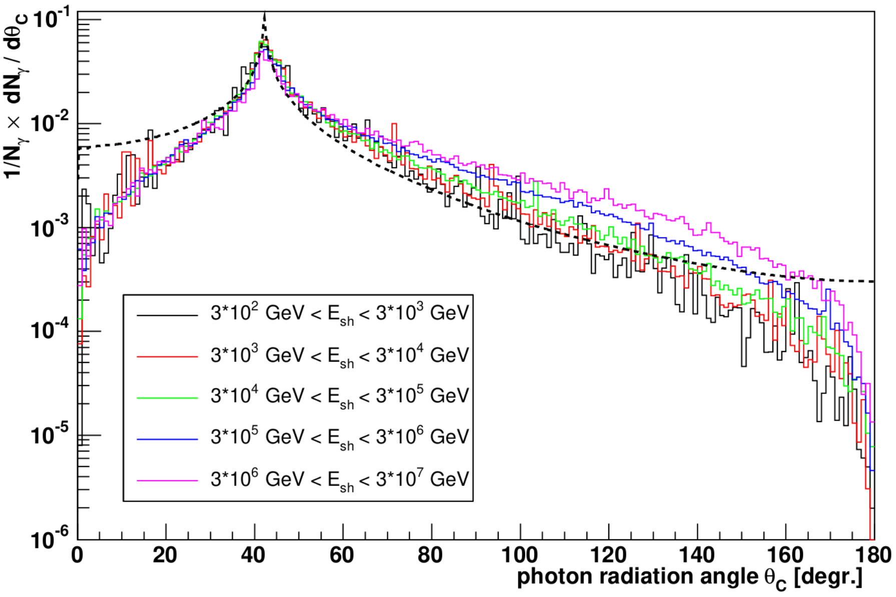

Figure 1.12: Distribution of the angle between cascade axis and photon emission direction. Color lines depict this distribution for hadronic cascades with different energies E_{sh} (ANTARES detector response taken into account). Black dashed line corresponds to the electromagnetic cascade (without detector response simulation). Taken from [42].

interaction of muon neutrino – track starting with the cascade created in the neutrino interaction.

The second type of the signature is created when tau lepton decays into electron or hadrons. In this kind of interaction two cascades are created – one in tau neutrino interaction and one in tau lepton decay. They are connected by the track created by tau lepton. This kind of signature is called double cascade.

Chapter 2

Neutrino telescopes

Detection of neutrinos is challenging task. Due to the tiny neutrino cross-sections, volume of the neutrino telescopes is required to be at the km^3 level in order to obtain sufficient statistics. In the ice and water Cherenkov neutrino telescopes, registration of the neutrinos is based on the detection of the Cherenkov radiation emitted by the charged particles produced in neutrino interactions. Basically, these telescopes are three dimensional grids of the photomultiplier tubes, that register light that was emitted inside or in vicinity of the detector volume. Currently in 2024, there are several neutrino telescopes installed, planed or under construction. Five of them are members of Global Neutrino Network (GNN) [43] – IceCube, KM3NeT and its predecessor ANTARES, Baikal-GVD, and P-ONE, see Fig. 2.1. GNN objective is to develop coherent strategy and ensure closer cooperation among these neutrino telescopes.

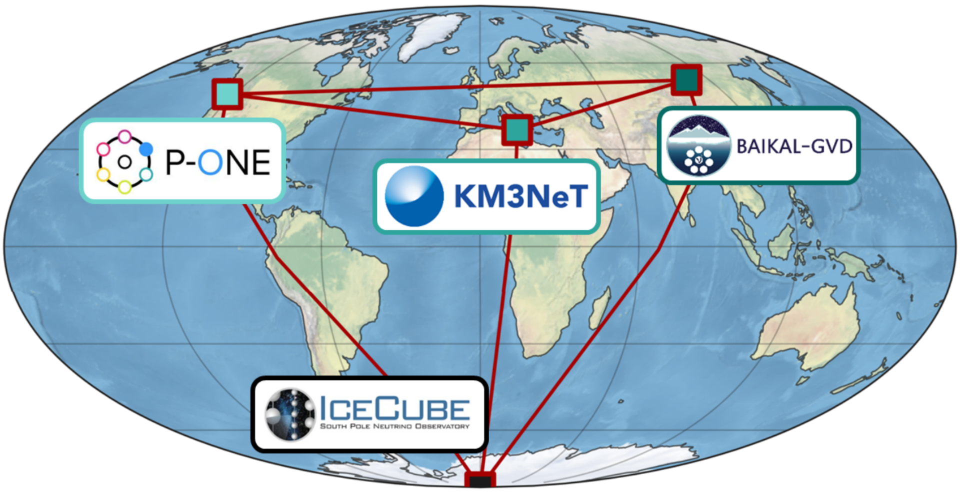

Figure 2.1: Map of the global neutrino network members. Taken from [44].

2.1 Baikal-GVD neutrino telescope

The Baikal Gigaton Volume Detector (Baikal-GVD) [45] is a neutrino telescope under construction in the deepest freshwater lake in the world – Lake Baikal. This neutrino telescope is located in the southern part of the lake approximately 3 - 4 km from the shore at the depths of $\sim$ 750 - 1 275 m. In depths below 750 m the sufficient elimination of sunlight is achieved. The location on the Northern hemisphere provides relatively high sensitivity to observe Galaxy Center.

The main goal of Baikal-GVD is detection of the high-energy astrophysical neutrinos. The purpose of their detection is e.g. to discover sources of astrophysical neutrinos, determine processes in which these neutrinos are produced, and study the integral diffuse flux of neutrinos. Data from Baikal-GVD can also be used for indirect search for dark matter – through detection of the neutrinos originated in annihilation of weakly interacting massive particles (WIMP) [46] in the Sun or in the center of the Earth. There is also a possibility to perform a search for exotic particles like magnetic monopoles [47]. In addition to particle physics analyses, Baikal-GVD data can be used for limnology research.

Lake Baikal offers numerous advantages for deployment of the neutrino telescope. Firstly, Baikal is a freshwater lake thus the additional background from ^{40}K is negligible. The purity of the water ensures good light propagation properties – absorption length (20 - 25 m) and scattering length (30 - 50 m). Expected precision of the reconstruction of the direction of track events is about 0.25° and for cascade events it is approximately 3.5 - 6.5°. Moreover, the flatness of the lakebed in the location where the telescope is deployed allows almost unlimited extension of the detector volume. Next, the lake is frozen during several months (February - April) – the installation and maintenance of the detector is significantly simpler and cheaper than for the other water or ice neutrino telescopes. The next benefit is, that the design of the Baikal-GVD detection units allows rearrangement of the detector geometry according to the requirements of performed studies.

The Baikal-GVD telescope is composed of independently working units called clusters. Cluster is a structure which consists of 8 strings equipped with optical modules. Baikal-GVD is still under construction, the deployment started in 2016 when the first cluster was installed. To enhance the sensitivity of the Baikal-GVD telescope, in addition to the clusters, there are inter-cluster strings [48]. The first inter-cluster string was installed in 2022. They are situated approximately in the geometrical center of three clusters. The configuration of the inter-cluster string is basically identical as for the conventional string. Among clusters, there are also strings equipped with high-power pulsed lasers. These lasers are used for the inter-cluster time calibrations and studies of the light propagation in water. The schematic view of the Baikal-GVD neutrino telescope together with the deployment timeline is shown in Fig. 2.2.

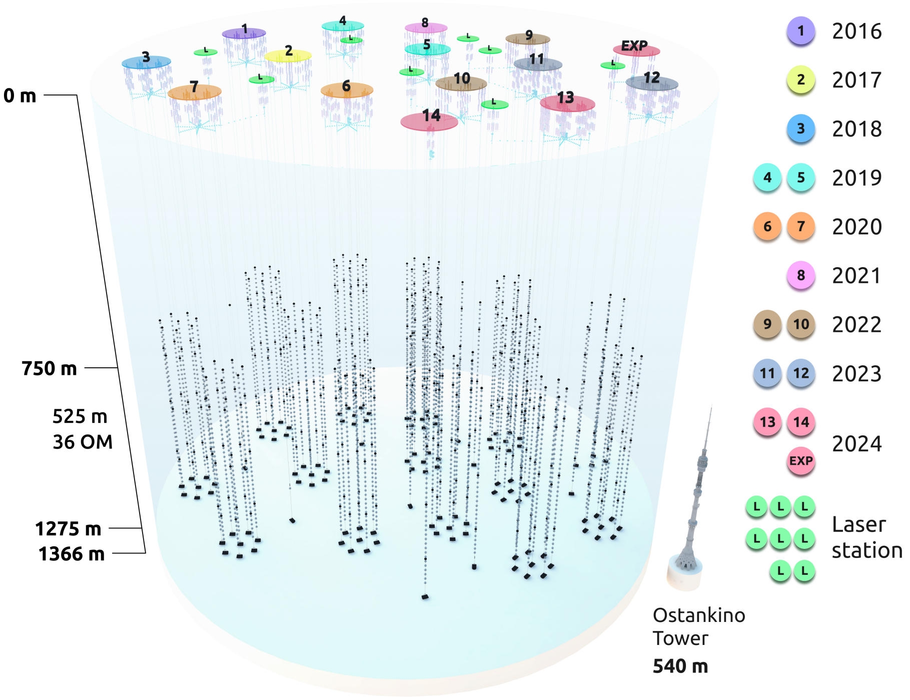

Figure 2.2: Layout of the Baikal-GVD telescope in year 2024. Taken from [49].

Distance between centers of two clusters is approximately 200 - 300 m. One cluster is composed of 288 optical modules, the detector consists of 3 960 optical modules in total in 2024 [49].

Specifications and information about the Baikal-GVD telescope provided in this chapter are taken from [4, 50, 51].

2.1.1 Optical module

An elementary unit of the Baikal-GVD telescope is called Optical Module (OM), see Fig. 2.3. The main component of the OM is photomultiplier tube (PMT) Hamamatsu-R7081HQE enclosed in a pressure-resistant glass sphere VITROVEX with diameter of 42 cm. It is composed of two hemispheres. To hold two hemispheres together, the pressure in OM is reduced to 0.7 atm.

The PMT is attached to the lower hemisphere of the OM with silicon elastic gel. This gel ensures optical contact between the PMT and glass. To reduce influence of the Earth magnetic field, the PMT is surrounded by mu-metal wire cage. Together with PMT, other electronic components are enclosed in OM – a controller, a high voltage unit, a two channel amplifier, and two LEDs for time and charge calibrations. There are also devices for measurements of OM condition – temperature sensor, manometer, accelerometer and compass, see Figs. 2.3b, 2.4.

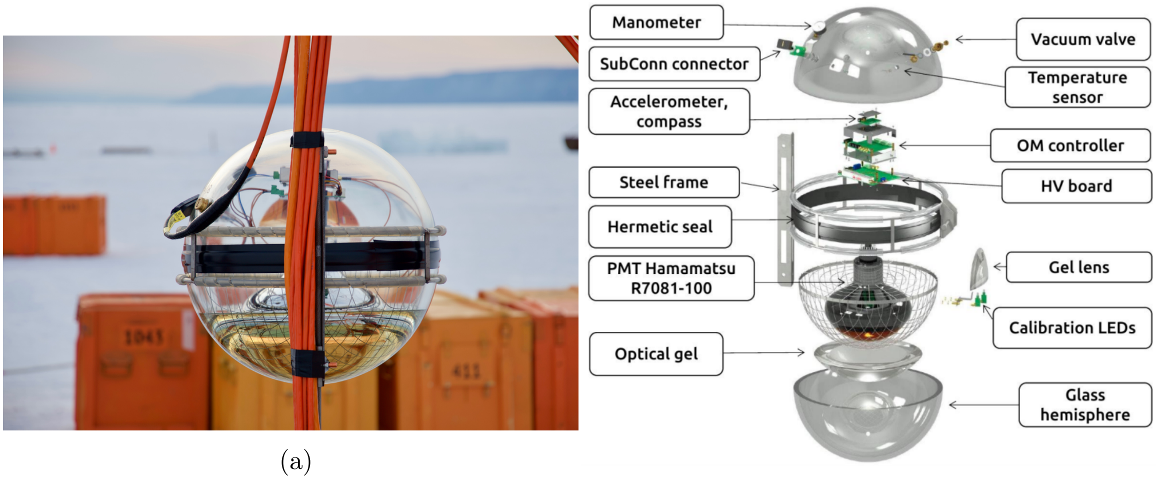

(a)

(b)

Figure 2.3: Optical module of the Baikal-GVD neutrino telescope. a) Photo of the optical module attached to the string. Image credit: Baikal-GVD Collaboration. b) Components of the Baikal-GVD optical module. Taken from [49].

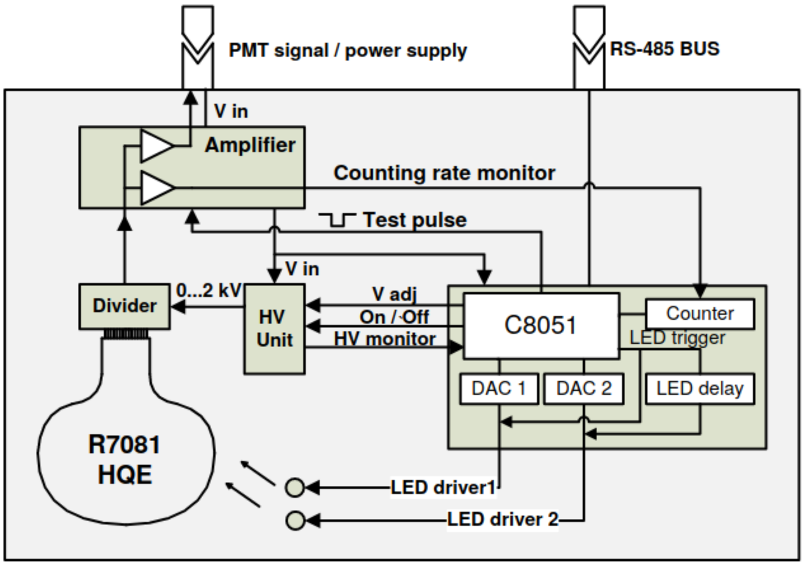

Figure 2.4: A block scheme of an optical module. Taken from [4].

There are several requirements for PMTs – high quantum efficiency (probability that if photon hits the photocathode photoelectron will be emitted), large photocathode area, and high time resolution (several nanoseconds). A Hamamatsu-R7081HQE was chosen with quantum efficiency ~ 35 %, see Fig. 2.5 and photocathode area ~ 500 cm^2.

Working voltage for PMT is provided by high-voltage unit. This value is specific for every PMT and it is determined in laboratory tests before deployment. It is set in the range from 1.3 to 1.8 kV to obtain gain of the PMT at the level of 10^7.

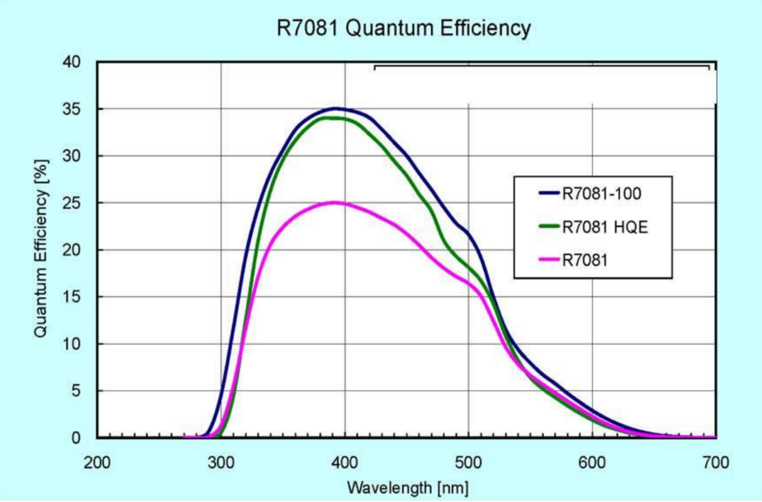

Figure 2.5: Quantum efficiency of selected types of PMTs given as a function of the wavelength. Taken from [52].

2.1.2 Section

A section consists of 12 OMs and a Central Module (CeM), see Fig. 2.6, mounted on vertical load-carrying cable. The architecture of the CeM is similar to the OM. The components of the CeM are enclosed in the pressure-resistant sphere VITROVEX. The sphere is covered in the black tape to eliminate influence of artificial light from LED diodes inside the CeM on surrounding OMs, see Fig. 2.7.

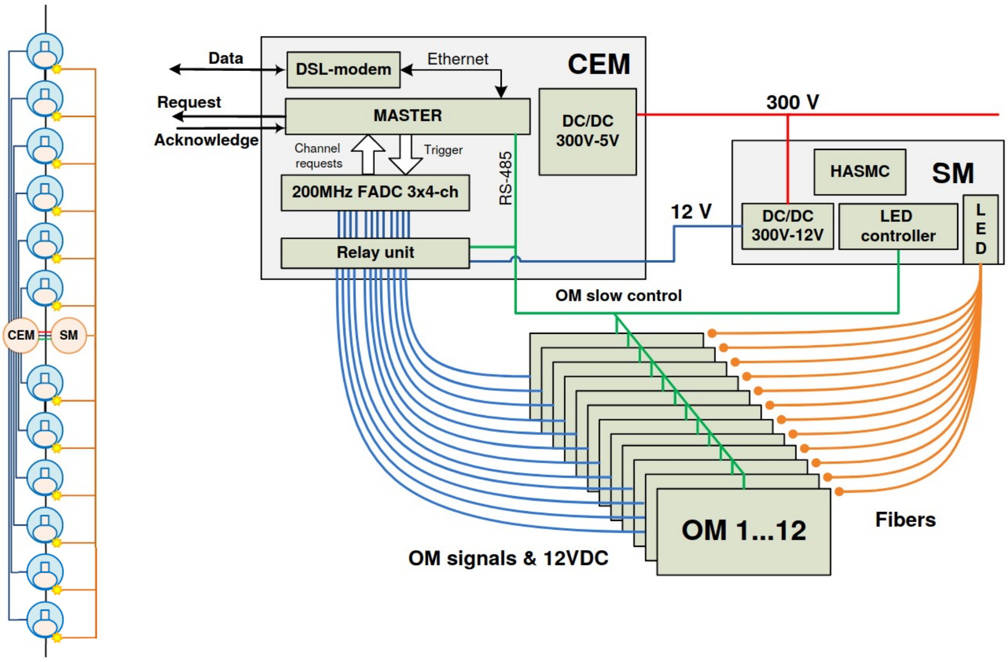

Figure 2.6: A block scheme of a section. Taken from [4].

Figure 2.7: Central module attached to a string. There are 12 copper cables in orange coating that connects each OM with the CeM. Image credit: Baikal-GVD Collaboration.

The analog signals collected by the OMs are sent to CeM through 92 m long coaxial cables. Digitization of the analog signals in CeM is provided by 12-channel 12-bit FADC with 200 MHz sampling frequency and 5 μs memory. The CeM is also responsible for providing of triggering logic. If detected signal exceeds high and low threshold on neighboring OMs within one section in time window of 100 ns, trigger request is created. Then, the request signal is sent to the cluster center, where the global trigger for all sections is created. This acknowledge signal initiates readout of the data from all FADC memories. The pulses with amplitude above 0.5 photoelectrons and the samples in their vicinity are transferred to the Data Acquisition Center (DAQ-center) for subsequent processing. This set of pulses – amplitudes and times of their detection, saved after the trigger condition is fulfilled, is defined as an event in the Baikal-GVD detector.

2.1.3 String

A string is composed of three sections and a Communication Module (CoM) attached to the same backbone cable, see Fig. 2.8a. On one string there are 36 OMs with 15 m vertical spacing. The lowest OM is installed at the depth of 1 275 m, the highest OM is deployed at the level of 750 m. To reduce movement and keep the string stretched, heavy anchor is attached to the bottom of the string, see Fig. 2.9a, and approximately

30 m below water surface the buoys are connected to the top of the string, see Fig. 2.9b.

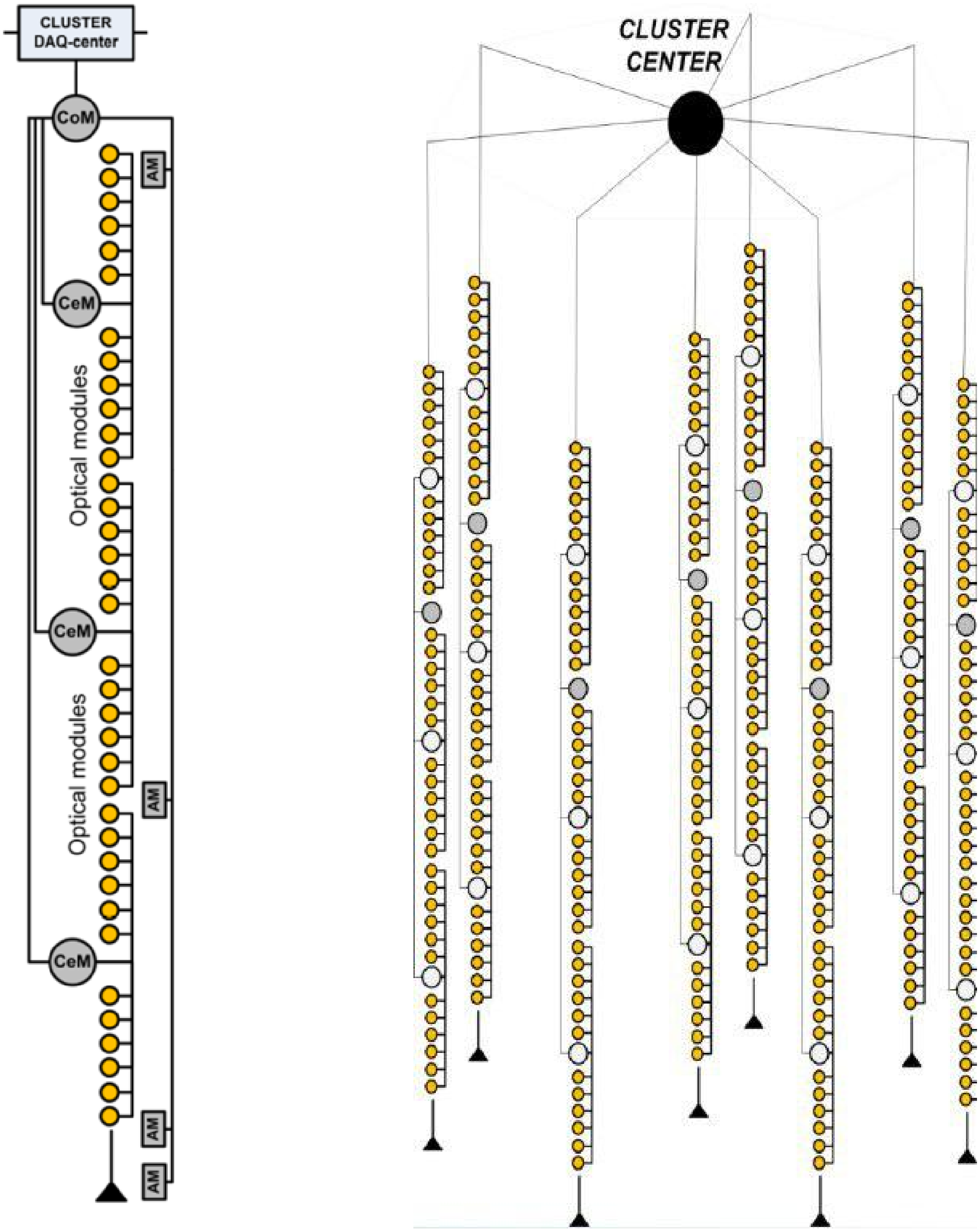

(a) (b)

Figure 2.8: Illustration of the components of the Baikal-GVD telescope. a) Scheme of a central string. Adapted from [50]. b) Illustration of the Baikal-GVD cluster. Taken from [51].

The CoM provides power supply for the sections and it is also responsible for the data transfer between the sections and the DAQ-center of the cluster. It collects trigger request signals from the sections and branches acknowledge signal from the DAQ-center to them.

(a) (b)

Figure 2.9: a) Photo of the anchor of the Baikal-GVD string. b) Photo of the buoys attached to the top of the Baikal-GVD string. Image credit: Baikal-GVD Collaboration.

2.1.4 Cluster

An independently working unit of Baikal-GVD is called cluster, see Fig. 2.8b. The cluster consists of the DAQ-center and 8 strings – one central string and seven peripheral strings. Spacing between the central and peripheral strings is approximately 60 m.

The DAQ-center is deployed approximately 30 m below water surface. It is composed of three parts – a cluster communication center, an optical cable clutch, and a PC-sphere. Strings and the DAQ-center are connected through $\sim$ 1.2 km long cables. These cables are used for transfer of data, power supply, and also synchronization of the sections. For the data transfer from the DAQ-center to the shore station, approximately 6 km long electro-optical cable is used, see Fig. 2.10. This cable also provides power supply for the cluster.

Figure 2.10: Photo of the electro-optical cable used in Baikal-GVD, that connects the DAQ cluster center with the shore station. Image credit: Baikal-GVD Collaboration.

2.1.5 Shore data acquisition and control center

The purpose of the shore station, see Fig. 2.11 is to collect, process and deposit data from the clusters as well as to provide power supply for the clusters. The shore station is also used for monitoring of functionality of the detector.

Figure 2.11: Photo of the shore station. Image credit: Baikal-GVD Collaboration.

2.1.6 Acoustic positioning system

Due to the water currents in Lake Baikal, OMs can be shifted from their initial positions. Therefore, for determining precise actual positions of the OMs, the acoustic modems are installed on every string [53], see Fig. 2.12.

The node is installed nearby string anchor, its position is known with high precision. For determination of the coordinates of other beacons installed along the strings, acoustic trilateration is used. On every string there are 3 - 4 beacons. One at the top and the bottom of the string and two between sections, see Fig. 2.12b. The positions of individual components of the string are determined from linear interpolation of the measured positions of the beacons. The measurement of the beacons positions is repeated every 100 - 200 seconds. The mean error on the position estimations of OMs is below 15 cm.

To determine tilt of the OM and orientation of the OM with respect to the string, the compass, accelerometer and gyroscope are installed in every OM.

2.2 KM3NeT neutrino telescope

The Cubic Kilometre Neutrino Telescope (KM3NeT) [54] is a water Cherenkov neutrino telescope under construction in the Mediterranean Sea. It consists of two main

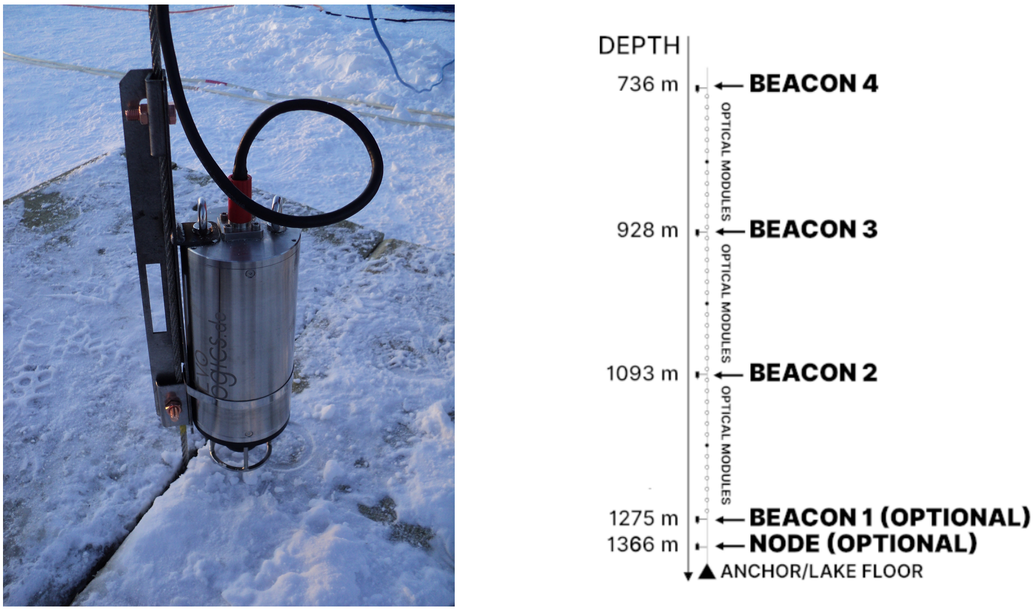

(a) (b)

Figure 2.12: a) EvoLogics acoustic modem. Image credit: Baikal-GVD Collaboration. b) Layout of acoustic modems on string. Taken from [53].

parts – Astroparticle Research with Cosmics in the Abyss (KM3NeT/ARCA) and Oscillation Research with Cosmics in the Abyss (KM3NeT/ORCA). KM3NeT/ARCA detector is located $\sim$ 100 km offshore of Portopalo di Capo Passero, Sicily, Italy, where the sea reaches depths of 3500 m. The main aim is to study high-energy astrophysical neutrinos (with TeV energies and above) and their sources. The second detector – KM3NeT/ORCA is focused on neutrino oscillation analysis and determination of neutrino mass hierarchy. KM3NeT/ORCA is optimized for detection of atmospheric neutrinos with energies at the level of few GeV. It is positioned in distance of approximately 40 km from French coast, close to Toulon. The sea depth at the KM3NeT/ORCA site is approximately 2500 m.

Besides astrophysical and atmospheric neutrino analyses, KM3NeT data can be used for cosmic rays research, dark matter studies, and also they provide unique opportunity for marine sciences due to location of the telescope at the seabed.

Properties of the seawater are shown in Fig. 2.13. The dependence of the phase refractive index on wavelength of the light is displayed in Fig. 2.13a with black color. The phase refractive index is related to the angle of emission of the Cherenkov light. The scattering and absorption length distributions as functions of light wavelength are shown in Fig. 2.13b.

Both detectors KM3NeT/ARCA and KM3NeT/ORCA consist of detection units – vertical strings equipped with digital optical modules. Detection units are arranged into the building blocks. One building block will consist of 115 detection units af-

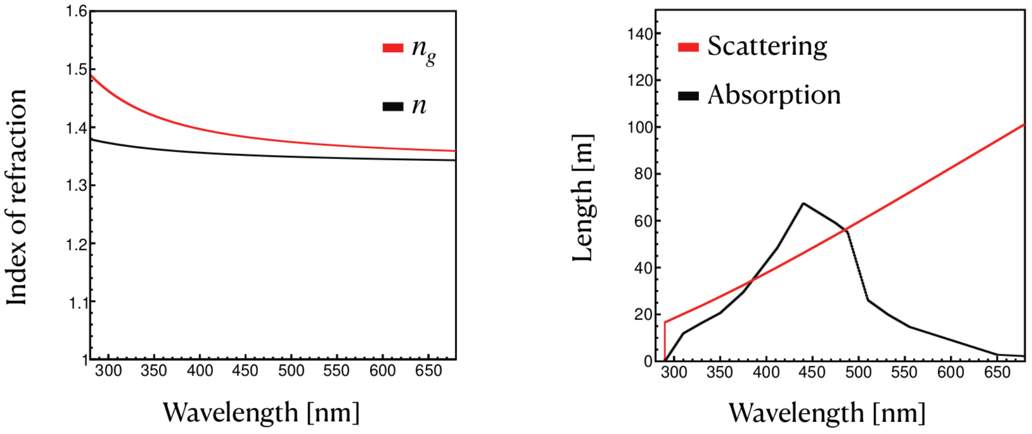

(a) (b)

Figure 2.13: Distributions of the attributes of the seawater as functions of light wavelength. a) Group (red) and phase (black) refraction indices. b) Scattering (red) and absorption (black) lengths. Taken from [55].

ter finalizing the detector construction. Both detectors are still under construction, for KM3NeT/ARCA 2 building blocks are planed to be built, while final size of KM3NeT/ORCA is 1 building block. The illustration of design of the building blocks for KM3NeT/ARCA and KM3NeT/ORCA is displayed in Fig. 2.14. As of November 2024, KM3NeT/ARCA consists of 33 detection units and 24 detection units are installed in KM3NeT/ORCA detector.

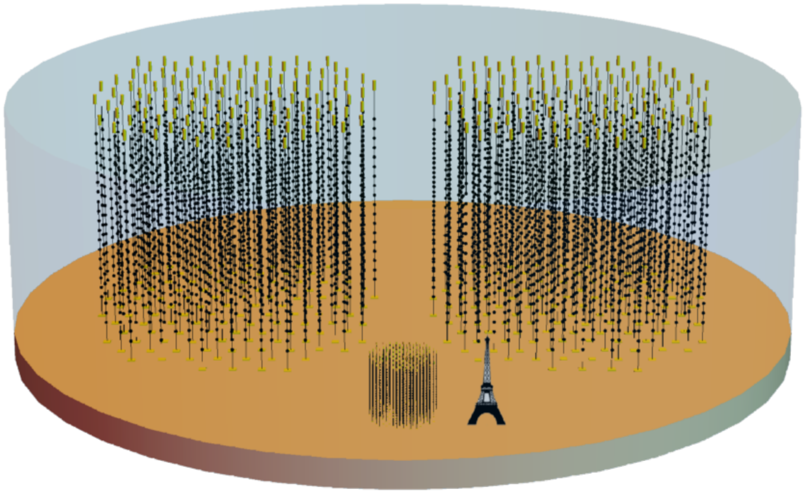

Figure 2.14: Layout of the KM3NeT telescope. Vertical lines represent detection units. Two building blocks with larger distance between digital optical modules correspond to KM3NeT/ARCA, one building block with denser layout of digital optical modules represents KM3NeT/ORCA detector. Size comparison with Eiffel tower with height of 330 m is given. Taken from [56].

2.2.1 Detector design

Digital optical module

The basic detection unit of KM3NeT is called Digital Optical Module (DOM), see Fig. 2.15. It is a pressure resistant glass sphere with a diameter of 17 inches. One DOM houses 31 photomultiplier tubes with 3 inches photocathode. For the first phase of the KM3NeT detector, the Hamamatsu R12199-02 PMT was chosen. For next batches, the Hamamatsu R14374 was adopted. The projected photocathode area of such DOM is equivalent to $\sim$ 1300 cm^2 which corresponds to approximately three 10 inches PMTs. Moreover segmented photocathode area provides more information on direction of incoming photons. To enhance photon detection, there is a reflector ring around each PMT. It increases photon acceptance by 20 - 40 % [57].

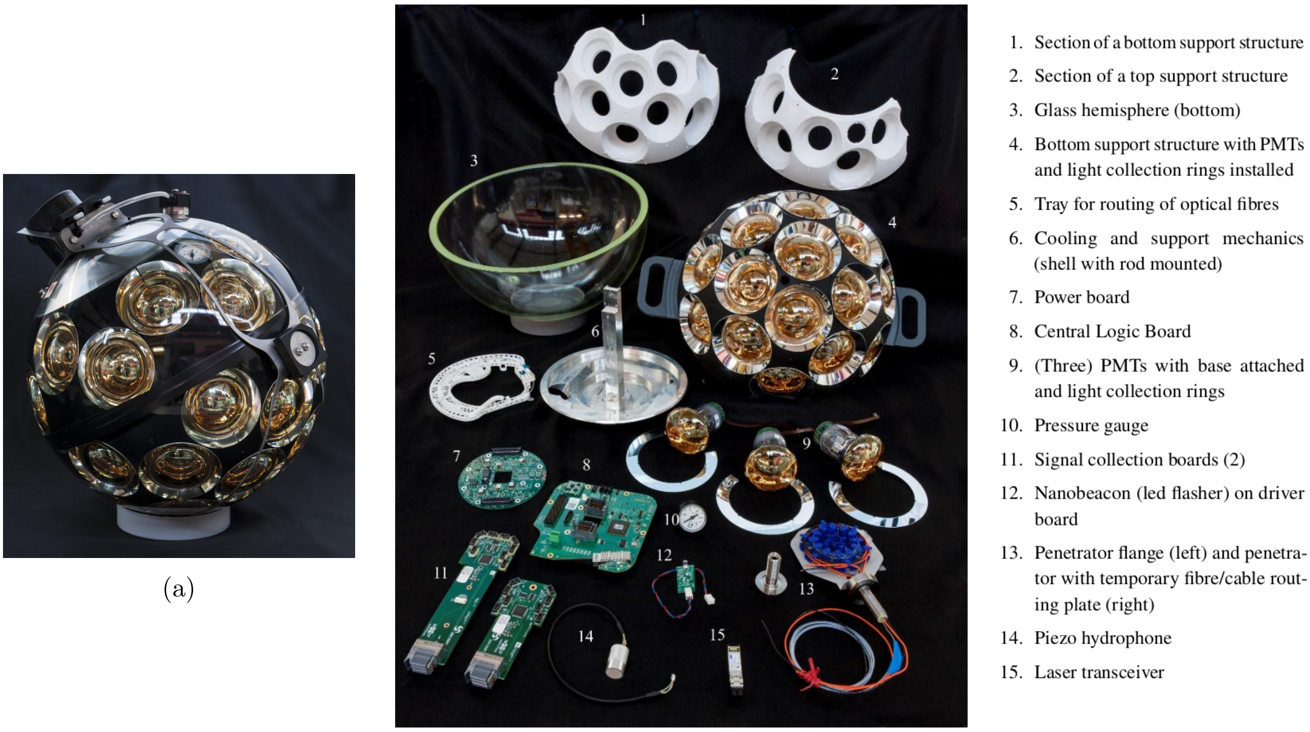

(a)

(b)

Figure 2.15: Digital optical module of the KM3NeT neutrino telescope. a) Photo of the digital optical module. Taken from the KM3NeT official website https://www.km3net.org/. b) Components of the KM3NeT digital optical module. Taken from [57].

The time between a photon hitting photocathode and resulting electrons reaching anode is called transit time. For KM3NeT PMTs (Hamamatsu R12199-02) it is around 30 ns. The transit time spread – spread on the mean value of the transit time is at the level of 2 ns [58, 59]. The probability of the photoelectron emission from the photocathode initiated by the photon hitting the photocathode is called quantum efficiency.

The quantum efficiency of the PMTs used in KM3NeT (Hamamatsu R12199-02) as a function of the wavelength is displayed in Fig. 2.16 [59].

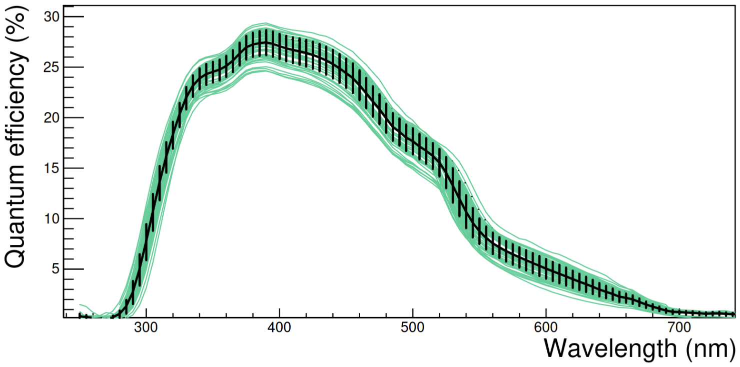

Figure 2.16: Dependence of quantum efficiency of photocathode on the wavelength. Green lines depict measurements for 56 individual PMTs (Hamamatsu R12199-02). Black line shows mean with one standard deviation. Taken from [59].

At the back of each PMT, a PMT base board is attached, see Fig. 2.17. In the PMT base, analogue pulse from PMT is digitized. It also contains Cockroft-Walton circuit, which provides possibility to adjust high-voltage from 3.3 V input for each PMT separately. The high-voltage is set according to the required gain of the PMTs. The PMT gain is an average number of electrons reaching the anode induced by the single photoelectron emitted from the photocathode. To reduce aging effect of PMTs, relatively low nominal gain was chosen 3×10^6. This value was defined according to PMT counting rates in seawater at the KM3NeT sites. The PMT base power usage in operation is at the level of 36 mW [57].


(a) (b)

Figure 2.17: a) The Hamamatsu R12199-02 PMT of the KM3NeT neutrino telescope with a PMT base mounted at its back. b) PMT base board. Taken from [57].

Signals from PMTs are transferred to Central Logic Board (CLB) through two signal collection boards so called Octopus boards, each corresponding to the PMTs in different hemispheres [60]. In CLB, these signals are further processed, and subsequently transmitted to shore.

The information about signal detected on PMTs is compressed into PMT identification, arrival time, and width of the pulse. This set of information about PMT signal is called hit. Arrival time corresponds to the time at which the pulse surpassed the predefined threshold. This threshold is set to the value corresponding to 0.3 photoelectron equivalent [61]. Width of the pulse, called Time over Threshold (ToT) is defined as the time interval in which the signal was above the threshold, see Fig. 2.18. Compression of signal from PMTs to arrival time and ToT reduces the required bandwidth while sufficient information about the PMT signal is still provided.

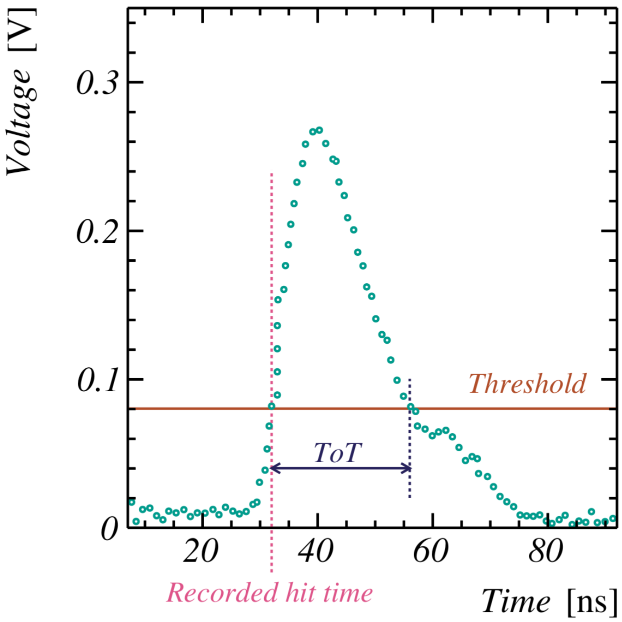

Figure 2.18: Pulse detected with KM3NeT PMT during laboratory measurements. Two quantities characterizing pulse in KM3NeT data – hit time and time over threshold (ToT) are illustrated. Taken from [58].

For data acquisition in KM3NeT, the all-data-to-shore concept is used [57]. It means that all collected data are digitized and sent to shore without reduction. This allows to apply various triggers on the data according to the analysis request during offline data processing. The highest possible rate for one PMT is 20 kHz, if detected rates exceed this value, the data acquisition electronics reject such signal [58].

The synchronization of DOMs in KM3NeT within 1 ns precision is provided by White Rabbit Protocol. Conversion of power from 12 V input voltage is provided by Power board. Transfer of heat from the electronics enclosed in DOM is realized through aluminum piece placed at the top of DOM called mushroom [60].

In the DOM, there are also devices for monitoring and calibration like nanobeacon, piezo sensor, compass, tiltmeter, humidity and temperature sensors and pressure gauge, see Fig. 2.15b.

Detection unit

A Detection Unit (DU) [62] is a structure of 18 DOMs attached to two Dyneema ropes through titanium collar mounted on each DOM. To keep the ropes parallel, there are additional spacers between DOMs. The data transfer and power supply is provided by vertical electro-optical cable (VEOC). It is a plastic tube filled with oil containing copper wires and optical fibres.

Spacing of the DOMs and DUs differs between KM3NeT/ARCA and KM3NeT/ORCA, because of the different purposes of the detectors. For KM3NeT/ARCA detector that aims for higher energies spacing between DOMs on DU is 36 m and inter-DU horizontal spacing is 90 m. In KM3NeT/ORCA, detector, the distance between DOMs on DU is 9 m and distance between neighboring DUs is 20 m. The illustration of KM3NeT/ARCA and KM3NeT/ORCA DU is displayed in Fig. 2.19.

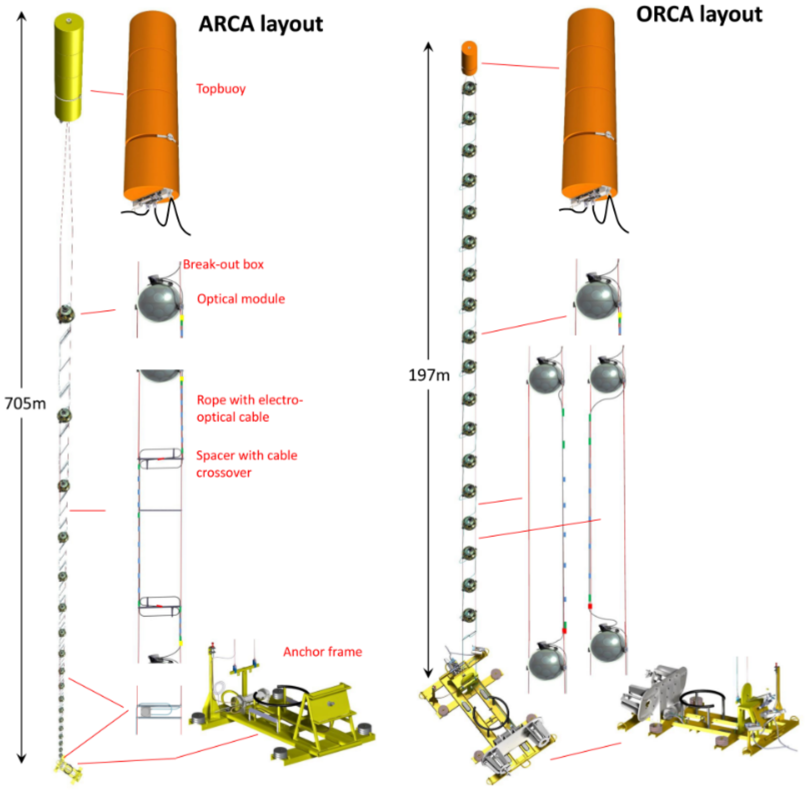

Figure 2.19: Illustration of the layout of the KM3NeT/ARCA and KM3NeT/ORCA detetion units. Taken from [63].

To minimize the movement of DUs caused by the sea currents, the DUs are attached to the anchor at the seafloor and at top of the DUs there are buoys to provide stretching of DUs. Moreover, each DOM provides buoyancy of 11 kg. At the anchor of the DU, there is a base module which provides connection to electro-optical seafloor cable network. This network connects DUs with shore station and ensure detector control and data transfer [63].

Deployment of the detection units

For the deployment of the KM3NeT DUs a Launcher of Optical Modules (LOM) is used [64]. It is a spherical device that can hold DOMs, corresponding cables and it also contains buoyancy spheres, see Fig. 2.20.

Fully integrated DU is loaded into the LOM and attached to the anchor-frame. This structure is deployed to the sea from the ship. Firstly, the LOM with anchor is positioned on the seabed. Next, a remotely operated underwater vehicle connects it to the seafloor network and activates the releasing mechanism. The LOM is then released from the anchor and it starts to rotate in upward direction, untangling the DU along its way. The LOM is designed to be reusable. Empty LOM structure floats on the water surface. Therefore, after the whole DU is uncoiled, the empty LOM is retrieved from the sea to be used for next DU deployment.

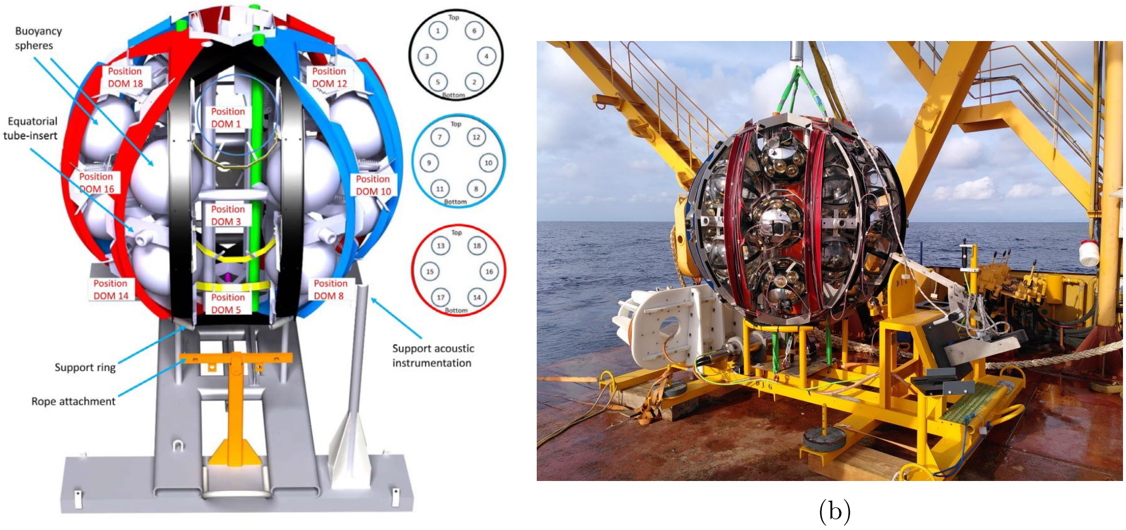

(a)

(b)

Figure 2.20: Launcher of optical modules of the KM3NeT neutrino telescope. a) Illustration of the launcher of optical modules with the anchor-frame. b) Fully loaded launcher of optical modules with the anchor-frame prepared for deployment. Taken from [64].

2.2.2 Neutrino detection background

In addition to signal produced in interaction of neutrinos, there are also other sources of light which create signal on the KM3NeT PMTs and therefore contribute to background to the neutrino studies. Among the sources of background hits in KM3NeT belong decays of the radioactive isotopes contained in seawater and in the DOM glass, bioluminescence, dark noise of PMTs, and atmospheric muons.

Potassium 40 decay

The main source of background hits in the KM3NeT neutrino telescope is decay of ^{40}K contained in seawater. It has two main decay channels:

- β^- decay with branching ratio $\sim$ 89.25 %

$$^{40}K \rightarrow ^{40} Ca + e^- + \overline{\nu}_e, \tag{2.1}$$

- electron capture with branching ratio $\sim$ 10.55 %

$$^{40}K + e^- \rightarrow ^{40} Ar^* + \nu_e \rightarrow ^{40} Ar + \gamma + \nu_e. \tag{2.2}$$

In these processes, electrons with sufficient energy for Cherenkov radiation emission can be produced. Either directly from β^- decay, because maximal energy of electrons from these decays is $\sim$1.31 MeV or they can originate in Compton scattering of γ from electron capture channel. These γ have energy at the level of 1.46 MeV. The decay scheme of ^{40}K is shown in Fig. 2.21. The expected rate of hits from ^{40}K decays per PMT is at the level of 4.7 kHz for KM3NeT/ARCA detector [58].

Bioluminescence

Bioluminescence is a phenomenon of emission of light by living organisms. Contribution of the bioluminescence to hit rates varies in time and space – it exhibits seasonal changes and depends also on sea currents. There is also possibility that bursts of bioluminescent activity occur. To suppress these hits produced by bioluminescence, a high rate veto is used [66]. If the signal detected on the PMT exceeds 20 kHz, the data from this PMT are removed [58].

Dark noise of photomultiplier tubes

Even when PMTs are in complete darkness there is a probability of detection of signal on the PMT anode. The main source of this signal is spontaneous thermionic electron emission from the photocathode. The rates are dependent on photocathode material and proportional to the photocathode area. The charge of such hits is mainly at the

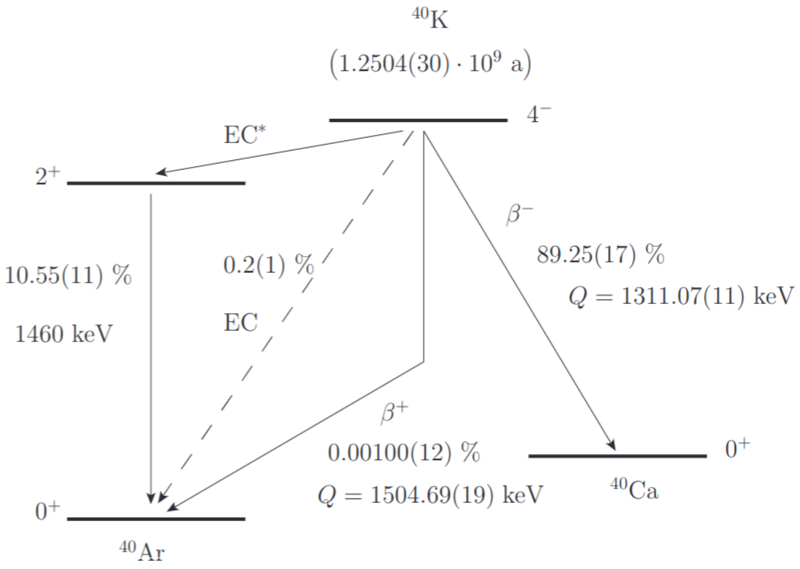

Figure 2.21: Decay scheme of ^{40}K. Taken from [65].

level of single photoelectron. The contribution of the dark count rate was measured on sample of approximately 7000 PMTs, the results are displayed in Fig. 2.22. The average value is about 1.3 kHz, for good PMTs the average dark count rate is about 0.7 kHz [59].

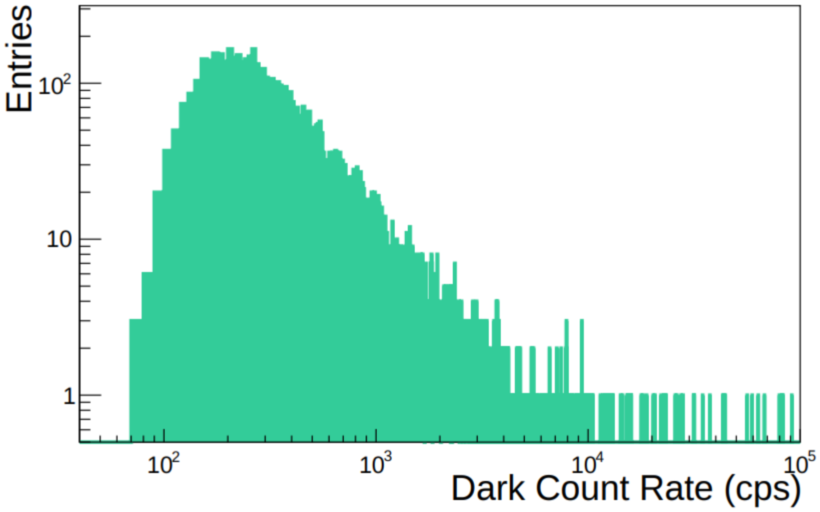

Figure 2.22: The results of the measurement of dark count rate of PMTs. The sample of approximately 7000 PMTs was analyzed. Dark count rate is given in counts per seconds. Taken from [59].

Atmospheric muons

Significant source of background for neutrino studies are atmospheric muons. These muons are produced in the interaction of cosmic rays with atmosphere. Even though the water overburden provide suppression of these muons, non-negligible part of them reach the KM3NeT detectors. The dependence of mean free path of muons in water on their energy is displayed in Fig. 2.23.

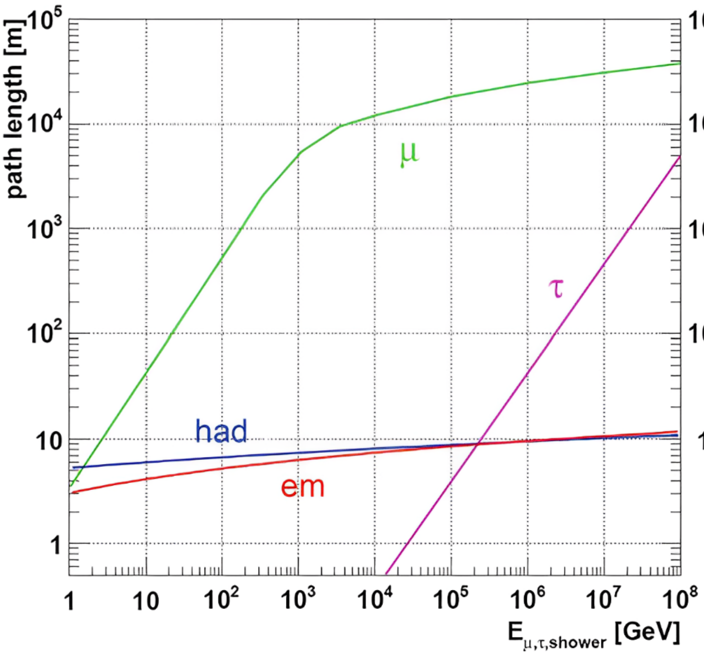

Figure 2.23: Path length of different particles in water given as a function of their energy. Green color represents muons, purple line tau leptons. Blue and red lines display hadronic and electromagnetic showers, respectively. Taken from [67].

These muons produce the same signature as muons created in charged current interaction of muon neutrinos, therefore their proper identification and suppression is crucial. Since atmospheric muons can not propagate through the Earth, the rejection of down-going muons for neutrino analyses is efficient tool to suppress atmospheric muons.

In neutrino studies atmospheric muons are contributing to background, but they are considered to be a signal for other type of studies, since KM3NeT are multi-purpose detector. Detection of the atmospheric muons provide a way to study cosmic rays and they are also used for calibrations of KM3NeT telescope.

2.2.3 Calibration

Since the KM3NeT neutrino telescope is installed in the depths of the Mediterranean sea it is exposed to influences of sea currents. Due to these currents, positions of DOMs can change. To perform precise analyses with KM3NeT data, the accurate position, orientation and time calibration is crucial. The expected precision of position calibration for DOM is < 20 cm which corresponds to the hit time uncertainty of 1 ns [54].

Position calibration

To obtain precise positions of DOMs, the acoustic positioning system is used. This positioning system is composed of acoustic emitters placed on the seabed at known positions, at the bases of DUs there are hydrophones, and in each DOM acoustic piezo sensor is installed.

For orientation calibration, compass and accelerometer are mounted inside the DOM. The measurements are performed every second, and subsequently transformed to roll, yaw, and pitch of the DOM [57].

Time calibration

In order to calibrate detector in time, beside measurements performed in laboratory, several in-situ time calibrations methods are used:

- nanobeacon calibration
  In every DOM, a nanobeacon is installed [68]. It is LED pulser with wavelength of 470 nm that is able to illuminate neighboring DOMs in order to obtain inter-DOM time offsets. Such calibrations are performed during dedicated runs. Furthermore, the data collected during these runs can be used to study properties of seawater like absorption and scattering length [57].

- atmospheric muons
  To obtain inter-DOM and inter-DU time offsets, atmospheric muons can be used. The advantage of this calibration method is that it does not require dedicated calibration runs. It uses muon reconstruction – firstly muon tracks are reconstructed using positions of the DOMs obtained from position calibrations, then the reconstruction quality is improved by tuning time offsets between DOMs and between DUs [58, 69].

- decays of potassium 40
  Potassium-40 is homogeneously spread in the water and the products of its decay can produce Cherenkov radiation, see Sec. 2.2.2. The signals from decays of

> potassium-40 can be used for inter-PMT calibrations within the DOM. The time offsets between PMTs can be obtained by studying the coincident hits from ^{40}K decays. Since the ^{40}K decay rate is almost constant over time, this calibration method provides a way how to calibrate and monitor performance of the detector over long time periods. Moreover, this calibration procedure does not require specific calibration runs.

Except estimation of time offsets between PMTs, decays of ^{40}K are also used to determine other PMT parameters such as transit time spread – spread on the mean time between photon hitting the photocathode and electrons arriving to the anode, and relative PMT efficiency – ratio of the PMT efficiency to the efficiency of a PMT with nominal characteristics. These PMT parameters are used as an input for the simulations of the detector [58].

For the calibrations with decays of ^{40}K, the distributions of time difference between detection of hits on two PMTs are used. Simulation of such distribution for arbitrary PMT pair is shown in Fig. 2.24. It shows that the time difference is zero on average, which is caused by homogeneous distribution of ^{40}K in water surrounding DOM. The effect of the addition of detector response to simulations – simulations of PMT efficiency and transit time, is displayed with brown color.

The dependence of coincidence rates for particular PMT pair $(i,\ j)$ on time difference Δt between detection of hits can be modeled as Gaussian distribution:

$$R_{i,j}(\Delta t) = \frac{\epsilon_i \cdot \epsilon_j \cdot R(\theta_{i,j})}{\sqrt{2\pi}\sigma_{i,j}} \cdot exp\left(-\frac{(\Delta t - \mu_{i,j})^2}{2\sigma_{i,j}^2}\right), \tag{2.3}$$

where ϵ_i and ϵ_j are efficiencies of PMTs i and j, $R(\theta_{i,j})$ is dependence of total coincidence rates on the opening angle $\theta_{i,j}$ between studied PMTs, which can be written as:

$$R(\theta_{i,j}) = \text{Rate}_{\text{Hz}} \cdot e^{-(p_1+p_2+p_3+p_4)} \cdot e^{(p_1\cos(\theta_{i,j})+p_2\cos^2(\theta_{i,j})+p_3\cos^3(\theta_{i,j})+p_4\cos^4(\theta_{i,j}))}, \tag{2.4}$$

where $\text{Rate}_{\text{Hz}} = 18.46$, $p_1 = 3.08$, $p_2 = -1.21$, $p_3 = 0.99$, and $p_4 = 0.94$ [70]. $\sigma_{i,j}$ is parameter related to transit time spread TTS as:

$$\sigma_{i,j}^2 = TTS_i^2 + TTS_j^2 + 0.54^2, \tag{2.5}$$

and $\mu_{i,j}$ is related to relative time offset t_0 between PMTs:

$$\mu_{i,j} = t_{0,i} - t_{0,j}. \tag{2.6}$$

To determine the PMT parameters – relative time offsets t_0, transit time spreads TTS, and relative PMT efficiencies ϵ, the distributions of hit time difference for all $\binom{31}{2} = 465$ PMT pairs are fit with the model given in Eq. 2.3. This fit has 92 free parameters –

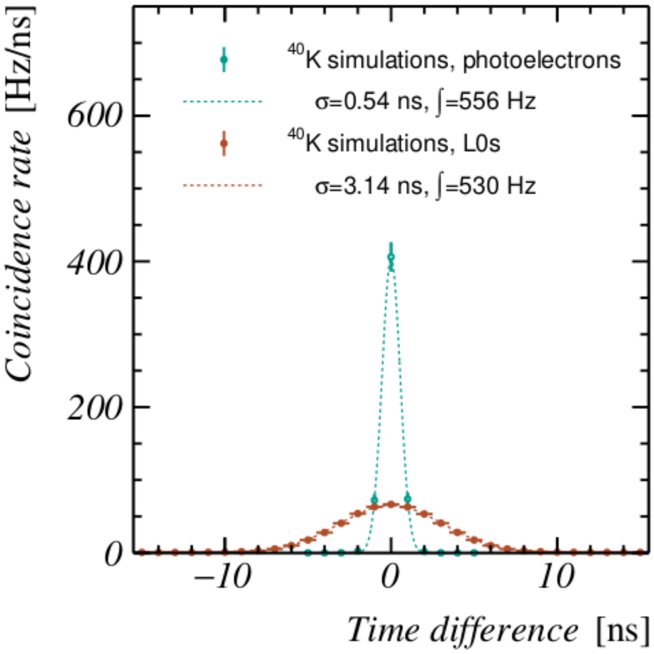

Figure 2.24: Distribution of time difference between signal detection on arbitrary PMT pair. Simulation of distribution of the time difference between detection of photons from one decay of ^{40}K is displayed with green color. Brown color represents distribution of the time difference between detection of the hits after simulation of the detector response (simulations of transit time and PMT efficiency). Taken from [58].

31 ϵ, 31 TTS, and 30 t_0, the last time offset is constrained by condition that average of the relative time offsets is equal to zero by definition.

In Fig. 2.25, hit time difference distributions before and after application of the inter-PMT calibration for one arbitrarily chosen PMT pair are shown. The data before and after calibration (after subtraction of the PMT time offsets determined from the inter-PMT calibration from raw times) are shown with the green and brown dots, respectively. With black line ^{40}K model fit is displayed. Pink line and area mark the random coincidences [58].

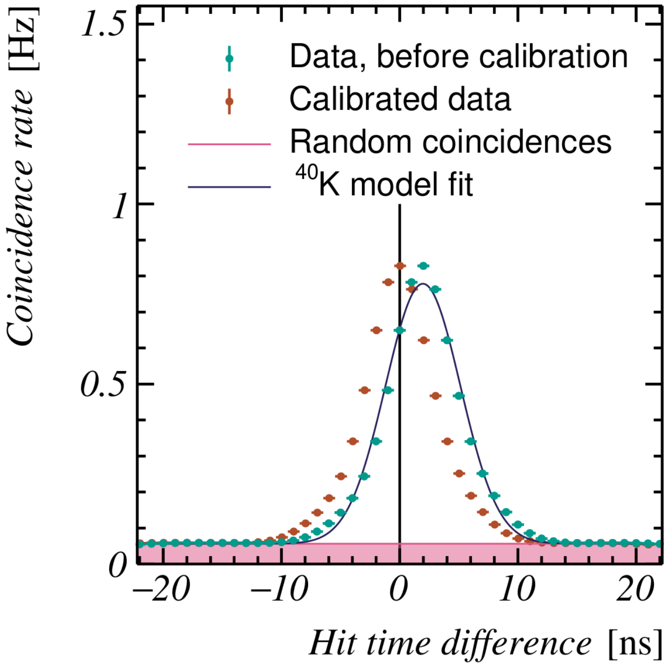

Figure 2.25: Distribution of time difference between detection of pulses on arbitrarily selected pair of PMTs. Data before calibration are displayed with green dots and brown dots represent calibrated data. Random coincidences are displayed with pink area. Taken from [58].

Chapter 3

Study of the KM3NeT digital optical module properties

A digital optical module is fundamental part of the KM3NeT neutrino telescope. It is a basic building element of both KM3NeT detectors KM3NeT/ARCA and KM3NeT/ORCA – they are three-dimensional arrays of DOMs. In consequence, understanding of properties of DOM is of crucial importance.

One of the characteristic attribute of the DOM is its internal noise i.e. signals that would be measured without any external source present. Internal noise of the DOM is composed of signals from e.g. radioactive isotopes contained in the DOM glass, dark noise of PMTs (mostly thermal emission of photoelectrons), and signals from other DOM components. Typically, it is impossible task to measure this attribute directly on the Earth surface, considering all of the particles, most significantly muons, contributing continuously to signals acquired by the DOM. As a result, to suppress signal from atmospheric muons, the measurements have to be either performed with dedicated detector setup e.g. detector with muon veto or such measurements require software for muon rejection. However, the most straightforward way to eliminate muons is to perform measurements in environments where muons are naturally suppressed. Among these places belong underground laboratories above which the overburden of rocks is thick enough to significantly suppress atmospheric muon flux.

In this chapter, the first measurements with the KM3NeT DOM in the Modane underground laboratory are presented. The description of the experimental setup is given. Furthermore, dedicated simulations for these measurements and corresponding experimental results are compared and discussed in detail.

3.1 Modane underground laboratory

The Modane underground laboratory (Laboratoire Souterrain de Modane (LSM)) is an underground laboratory located in the Alps in the road tunnel under Fréjus peak. Layout of the Fréjus road tunnel with location of LSM is shown in Fig. 3.1.

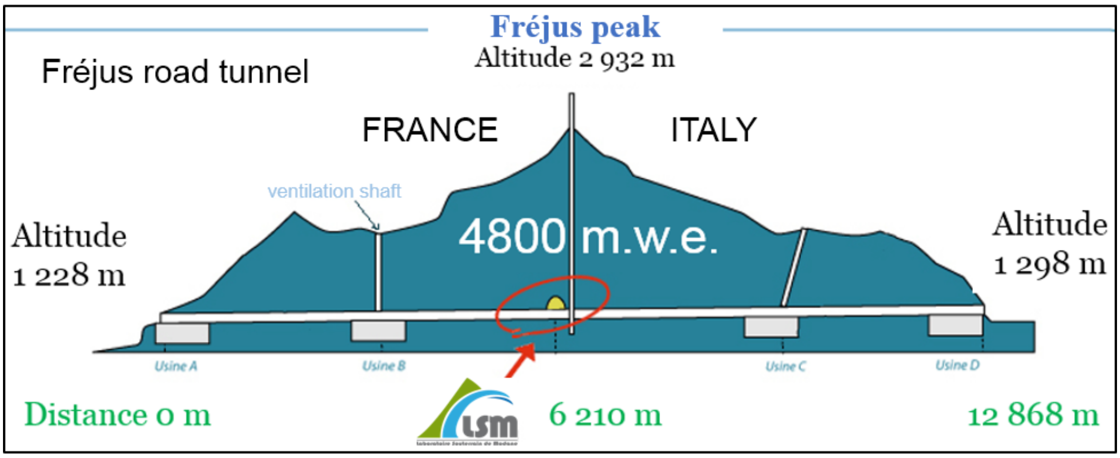

Figure 3.1: Scheme of Fréjus road tunnel with the Modane underground laboratory.

The LSM is located approximately in the middle of this tunnel where the overburden of rock reaches around 1750 m, which corresponds to $\sim$ 4800 meter water equivalent. This location provides unique environment for measurements – muon flux is at the level of 5 muons/m^2/day in comparison with $\sim 10^7$ muons/m^2/day at sea level [71]. Hence, the measurements performed in the LSM are unique and the data can be used in various analyses.

The main advantage of measurements with the KM3NeT DOM in the Modane underground laboratory is ability to measure directly DOM's internal noise. It means that the contribution to signal from all DOM components can be estimated more precisely and thus suppressed more effectively in data analysis. Moreover, detailed understanding of the DOM can improve precision of calibrations and various analyses. Furthermore, the possibility to obtain data practically without muons provides opportunity for development of algorithm to identify and reconstruct muons by comparing data collected in environment with muons and in almost muon-free environment hence directly analyzing muon patterns in detector.

3.2 Experimental setup

The basic setup used for measurements with the KM3NeT DOM in the Modane underground laboratory is displayed in Figs. 3.2 and 3.3. The data acquisition system is a simplified version of the full KM3NeT system used at KM3NeT/ORCA and

KM3NeT/ARCA sites. The output data measured in the LSM setup are in the same format as for the main detectors.

The main part of the setup is the dark box, see Fig. 3.2a, inside which the DOM is situated, see Fig. 3.2b. The author of this thesis participated in development and construction of this dark box. Corresponding electronics are shown in Fig. 3.3. The electronic setup consists of power supply, laser transceiver, media converter, and computer for data acquisition.

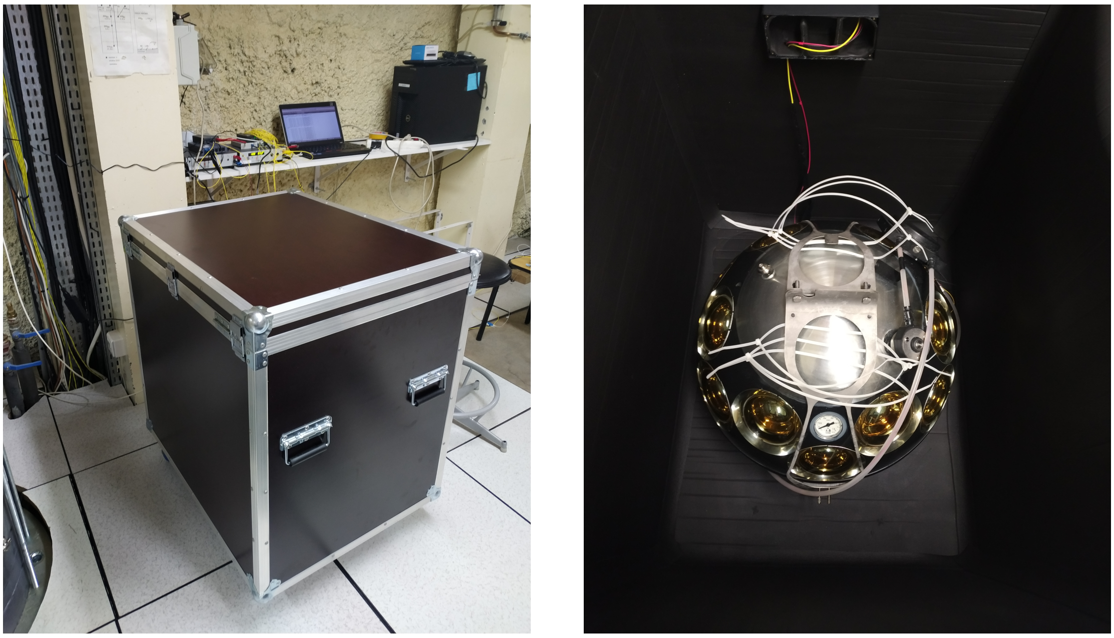
(a)

(b)

Figure 3.2: a) Setup for the measurements with DOM in the Modane underground laboratory. b) DOM situated in the dark box.

The power supply provides voltage of 12 V. To achieve required high voltage for PMTs, there is the Cockroft-Walton circuit situated at each PMT base board inside the DOM. Appropriate value of high voltage is specific for each PMT and it was set according to the calibrations of the PMT gains performed before the measurements. Media converter ensures the conversion of the signal transmitted through optic fibers to Ethernet cable and therefore enables communication with PC through standard Ethernet port for data acquisition.

3.3 Monte Carlo simulations

OMGsim [72] is a software package that provides dedicated detailed Monte Carlo (MC) simulations of the KM3NeT DOM based on Geant4 [73, 74, 75]. With OMGsim package it is possible to simulate primary particle propagation as well as decay of radioactive isotopes and subsequent production and propagation of secondary particles. Photons

Figure 3.3: Photo of the electronics used for the single DOM measurements in the Modane underground laboratory.

are simulated until they reach photocathode and produce photoelectrons. Detector response simulation was performed using JPP software [70].

The first analysis of the DOM internal noise in the Modane underground laboratory was focused on the study of the coincidences detected by PMTs in one DOM produced by the signals originated from the DOM components themselves, mainly from the radioactive isotopes contained in the DOM glass. Coincidence rates are important because they are used in the inter-PMT calibrations to obtain particular PMT parameters (description of the calibrations is given in Sec. 2.2.3).

For purposes of simulations of experimental setup described in Sec. 3.2, default simulation setup – DOM placed in seawater, was reconfigured and adjusted. In this configuration, it is expected that decays of ^{40}K contained in the glass of the DOM produce the highest contribution to coincident signal. In addition to ^{40}K decays, decays of the ^{232}Th and ^{238}U contained in the DOM glass are simulated. Visualization of the Modane setup simulated in OMGsim is shown in Fig. 3.4. This visualization is produced with Java Analysis Studio 3 (Jas3) [76].

In Fig. 3.5, the visualization of one ^{40}K decay in the DOM glass is shown. Fig. 3.5a displays general view of the decay of ^{40}K. In Fig. 3.5b, detailed view of ^{40}K decay vertex is given. It shows production of electron and electron anti-neutrino in ^{40}K β^- decay.

The visualizations of decays of ^{238}U and ^{232}Th are shown in Fig. 3.6a and Fig. 3.6b, respectively.

In Fig. 3.7, coincidence rates for all 465 PMT pairs obtained from the OMGsim

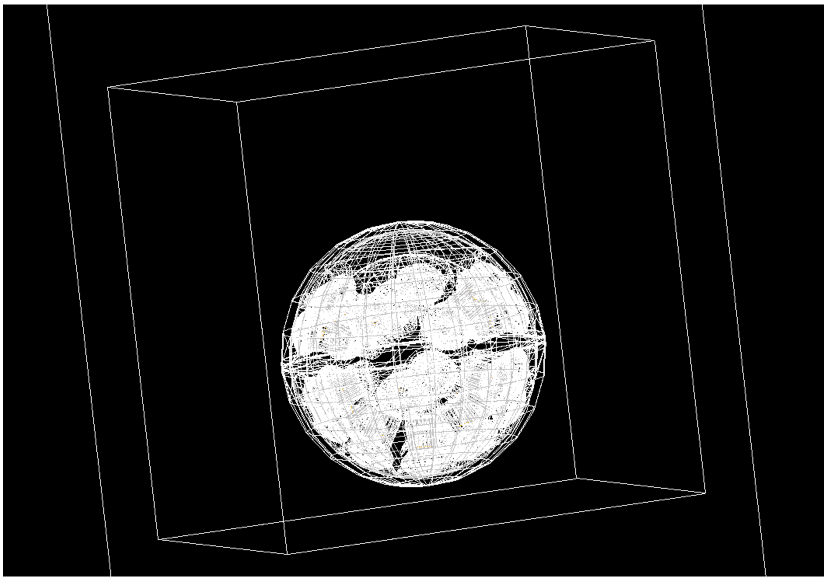

Figure 3.4: Visualization of the experimental setup used during the measurements with the KM3NeT DOM in the Modane underground laboratory generated with the OMGsim simulation package. The visualization is produced with Jas3 software.

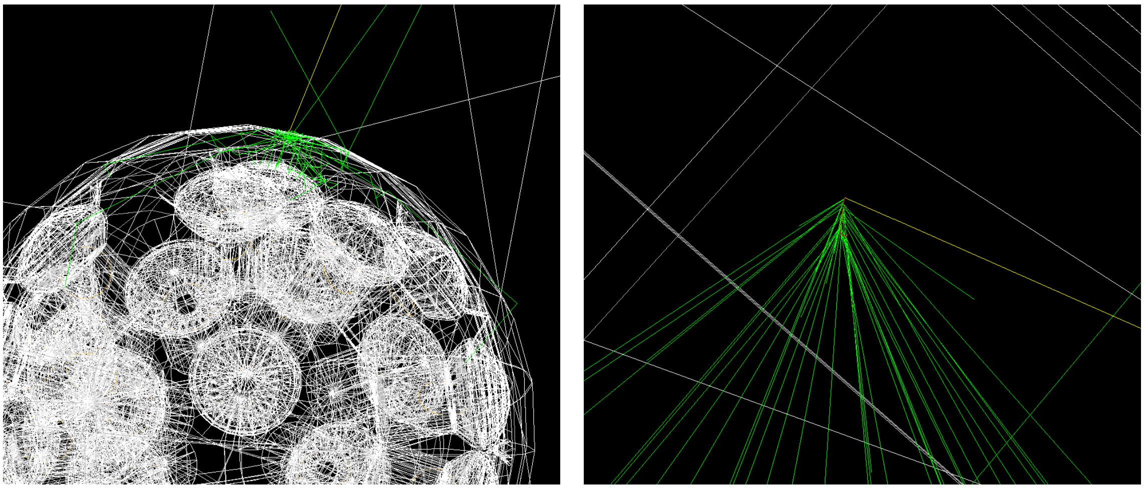

(a) (b)

Figure 3.5: Visualization of ^{40}K decay in the DOM glass simulated with OMGsim and visualized in Jas3. Green lines correspond to optical photons, red lines display electrons and yellow lines neutrinos and anti-neutrinos. a) Overview visualization. b) Zoom on the ^{40}K decay vertex.

simulations corresponding to the Modane setup are shown. Values of mass-specific activities of radioactive isotopes contained in the DOM glass used in these simulations are as follows [77]:

- ^{40}K: 60 Bq/kg,

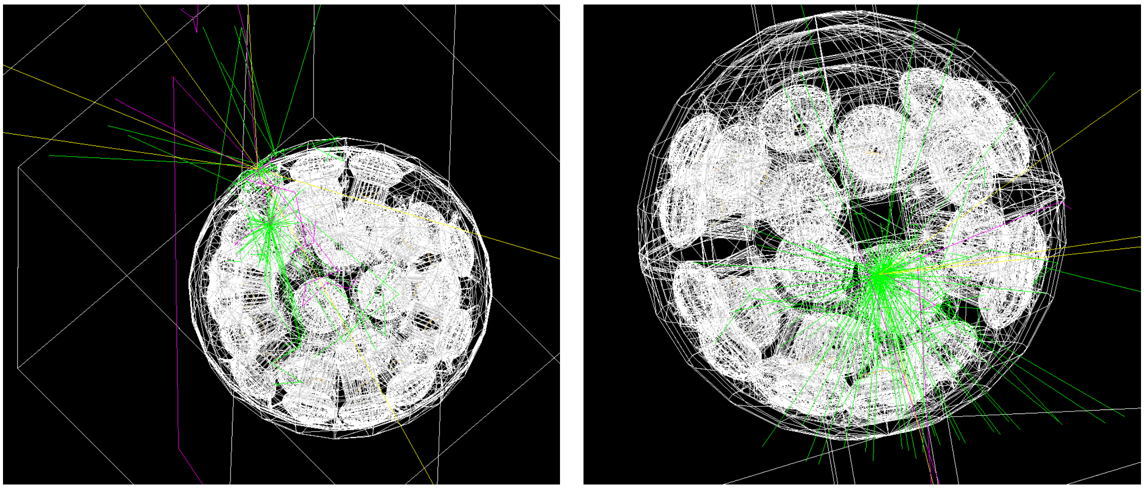

(a) (b)

Figure 3.6: Visualizations of the decays of the radioactive isotopes contained in the KM3NeT DOM glass simulated with OMGsim and visualized in Jas3. Optical photons are displayed with green lines, purple lines correspond to gammas, and yellow lines display neutrinos and anti-neutrinos. a) Decay of ^{238}U. b) Decay of ^{232}Th.

- ^{232}Th: 1.35 Bq/kg,
- ^{238}U: 5 Bq/kg.

PMT pairs are sorted according to the opening angle between PMTs. The lowest PMT pair ID corresponds to the PMT pair with the largest opening angle ($\sim 163.46°$), the highest ID represents PMT pair with the smallest angle between PMTs ($\sim 30.50°$). Coincidence rates are decreasing with increasing opening angle between PMTs – there is a higher probability of producing signal on neighboring PMTs because in order to obtain coincidences on PMT pairs with large opening angles particles have to propagate over larger distances.

For PMT pairs with small opening angles, signal from ^{40}K decays is dominating, while for PMT pairs with large opening angles, majority of the coincidences are produced by ^{238}U. It might be explained by the fact that in comparison with ^{40}K which decays mainly into the stable isotope ^{40}Ca, both of these radioactive isotopes – ^{238}U and ^{232}Th are the initial isotopes of the decay chains. The decays of the daughter isotopes are also included in the OMGsim simulations. In general, it might result in the signal with higher multiplicities – more than two PMTs in the coincidence and also more coincidences for PMT pairs with larger opening angles.

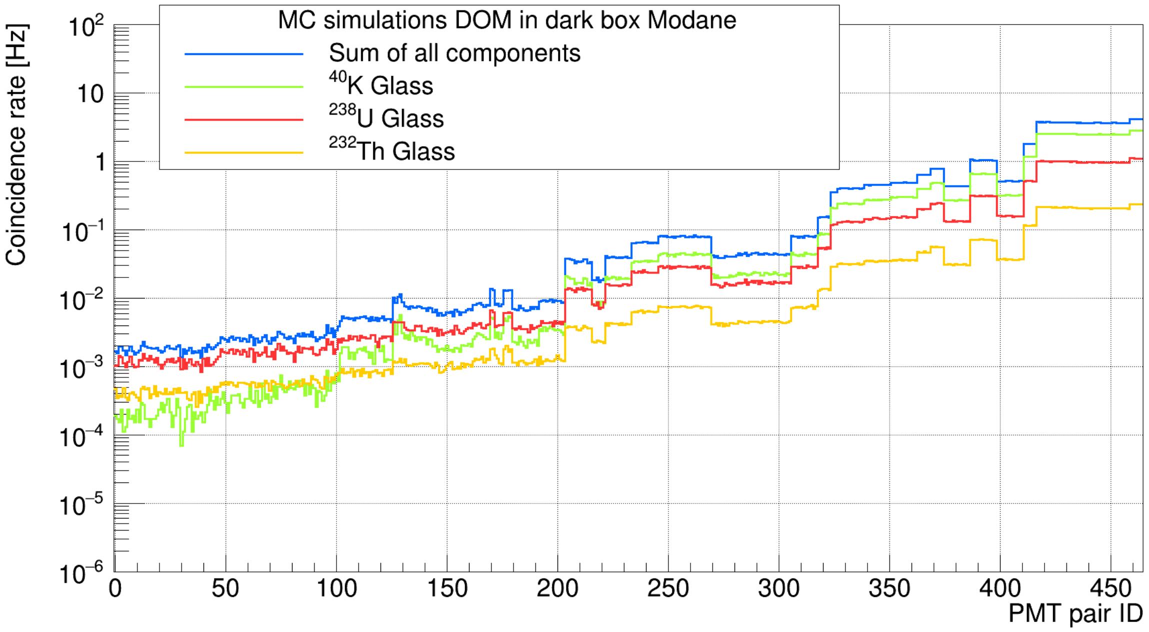

Figure 3.7: Coincidence rates for all 465 PMT pairs in the DOM estimated from MC simulations. PMT pairs are sorted according to the opening angle – the opening angle is decreasing with increasing PMT pair ID. Blue line corresponds to the sum of the contributions to coincidence rates from all simulated radioactive decays. Other lines display contributions from individual radioactive isotopes.

3.4 Data & Monte Carlo simulations comparison

The first step in realization of this project is to estimate precision of MC simulations of the measurements with the KM3NeT DOM placed in the dark box filled with air in the Modane underground laboratory.

In Fig. 3.8, the comparison between coincidence rates obtained from data and from MC simulations for all possible PMT pairs is shown. Coincidence rate for one PMT pair is defined as an integral of the distribution of time difference between pulses detected on the PMTs in particular pair after subtraction of the random background coincidences, see Fig. 2.25. PMT pairs are organized according to the opening angles between PMTs – from the largest angles (low PMT pair IDs) to the smallest opening angles (high PMT pair IDs). Empty bins in this histogram for data are caused by one PMT which was not working.

The best agreement between data and MC simulations is achieved for the PMT pairs with the smallest opening angles. These PMT pairs are expected to detect mainly coincident signals from one decay of ^{40}K, ^{232}Th or ^{238}U directly and therefore the best agreement is predicted. The better agreement can be reached by more precise esti-

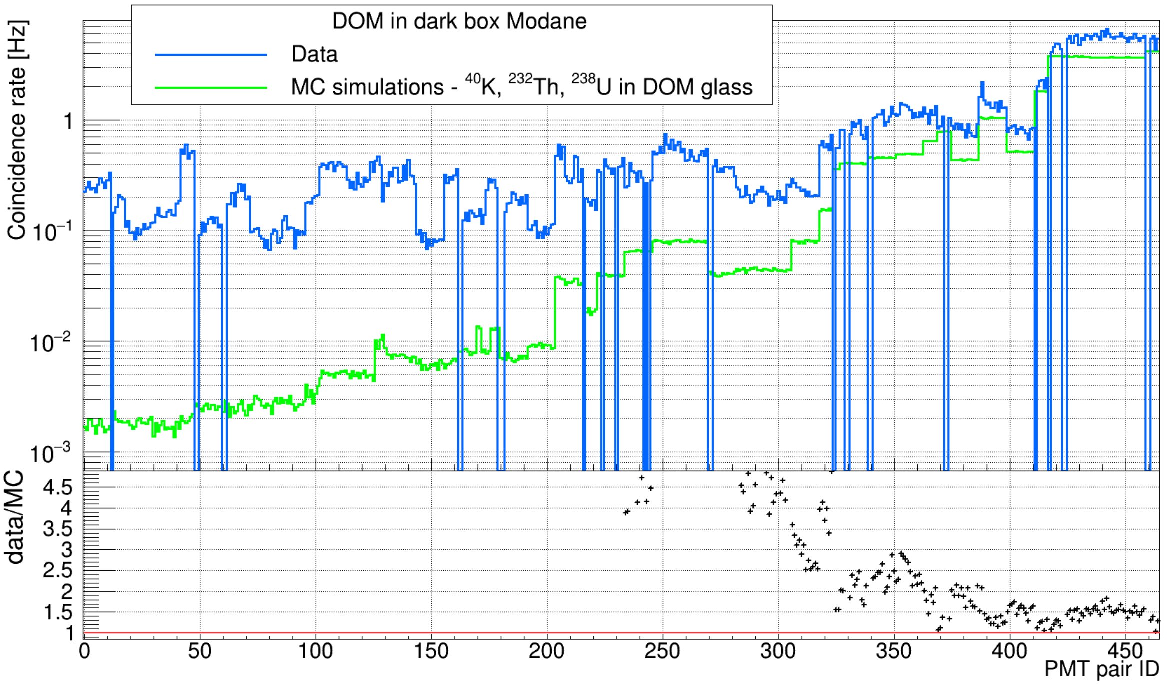

Figure 3.8: Coincidence rates for all 465 PMT pairs in DOM from data (blue) and from MC simulations (green). PMT pairs are sorted according to the opening angle – the opening angle is decreasing with increasing PMT pair ID. The ratio of the coincidence rates from data to the rates obtained from MC simulations is shown in the lower panel.

mation of mass-specific activities of radioactive isotopes contained in the DOM glass. Coincidences measured on the PMT pairs with large opening angles can be produced by detection of the signal from one decay of a radioactive isotope but particles have to undergo multiple processes like scattering to reach PMT on the other side of the DOM. Therefore, for PMT pairs with large opening angles, there is larger discrepancy between data and MC simulations – proper simulation of these coincidence rates requires not only precise estimation of amount of radioactive isotopes in glass but also simulation of propagation of particles is of crucial importance.

Coincidences can also be caused by coincident signals from two different decays. However, in current version of the simulations, these coincidences of the signals from multiple decays are not taken into account. Furthermore, coincident signal on PMTs can also be caused by combination of the PMT dark noise pulses and signal from the decay of radioactive isotope or there can also be pure PMT noise coincidences. Thus, proper estimation and accurate simulation of PMT noise rates can possibly have non-negligible impact on coincidence rates. Moreover, the DOM glass can contain other radioactive isotopes than isotopes currently included in simulations – ^{40}K, ^{232}Th or ^{238}U, which can also be possible sources of the signal. Additionally, other components of the DOM (see Fig. 2.15b) like electronic boards, compass, and PMT glass can also contribute to the DOM internal noise. To investigate this hypothesis, signal from all components of the DOM have to be studied separately and it needs to be implemented to the current MC simulations. Further, in the current version of simulations, the afterpulses simulations are not included. It can also contribute to the disagreement between data and MC simulations.

Afterpulses are spurious pulses which appear after the signal pulse. They can be created by elastic scattering of the electrons on the first dynode. Typical time delay between main pulse and afterpulse for this kind of afterpulses is at the level of several nanoseconds to several tens of nanoseconds. The second type of the afterpulses – afterpulses with a longer delay after signal pulse in the range from hundreds of nanoseconds to several microseconds originate in ionization of residual gases in the PMT. In the process of ionization, positive ions are created, these ions return to the photocathode and create photoelectrons. These photoelectrons subsequently create signal in PMT [78].

3.4.1 Digital optical module glass radioactivity

To study and potentially decrease the discrepancy between coincidence rates obtained from data and MC simulations, the impact of the new more precise values of mass-specific activities of the radioactive isotopes contained in the DOM glass was studied. The default values for activity per mass of radioactive isotopes contained in the DOM glass used in simulations are based on the IceCube measurements published in [77]. To obtain precise measurements of the glass radioactivity directly for KM3NeT DOMs, glass hemispheres before their integration into DOMs were sent to the National Radiation Protection Institute (NRPI) in Czech Republic. The glass hemisphere composition was evaluated using HPGe detectors, the setup for these measurements is shown in Fig. 3.9.

The results of the NRPI measurements together with default values are summarized in Tab. 3.1.

Table 3.1: The mass-specific activity for the different radioactive isotopes contained in VITROVEX glass. Default values and values from the measurements of the KM3NeT DOM glass in NRPI are shown.

Mass-specific activities	^{40}K [Bq/kg]	^{232}Th [Bq/kg]	^{238}U [Bq/kg]
default	60.00	1.35	5.00
NRPI	68.46	1.58	5.70

The comparison of the coincidence rates simulated for dark box setup with different amounts of radioactive isotopes in the DOM glass is displayed in Fig. 3.10. For the

Figure 3.9: Experimental setup for measurements of the DOM glass radioactivity in National Radiation Protection Institute in Czech Republic. For estimation of the radioactive isotopes contribution HPGe detector was used.

simulations performed with mass-specific activities of radioactive isotopes obtained from the NRPI measurements, the coincidence rates for PMT pairs with small opening angles increase by around 15 % in comparison with the simulations with default values for mass-specific activities.

In Fig. 3.11, the comparison of the coincidence rates from data and MC simulations with mass-specific activities of radioactive isotopes in the DOM glass measured in NRPI is shown. For majority of PMT pairs with small opening angles, ratio between data and MC simulations is under approximately 1.4, in the case of MC simulations with default mass-specific activities this ratio is around 1.5, see Fig. 3.8. In following sections, values of mass-specific activities of radioactive isotopes contained in the DOM glass measured in NRPI are used in MC simulations.

3.4.2 Random coincidence background estimation methods

Calculation of the coincidence rates is dependent on the estimation of the random background coincidence level. Therefore, the method used for the estimation of random background coincidences has influence on the final estimates of the coincidence rates and it is essential to analyze performance of the background estimation methods.

The pattern of the signal and random background coincidences may vary for dif-

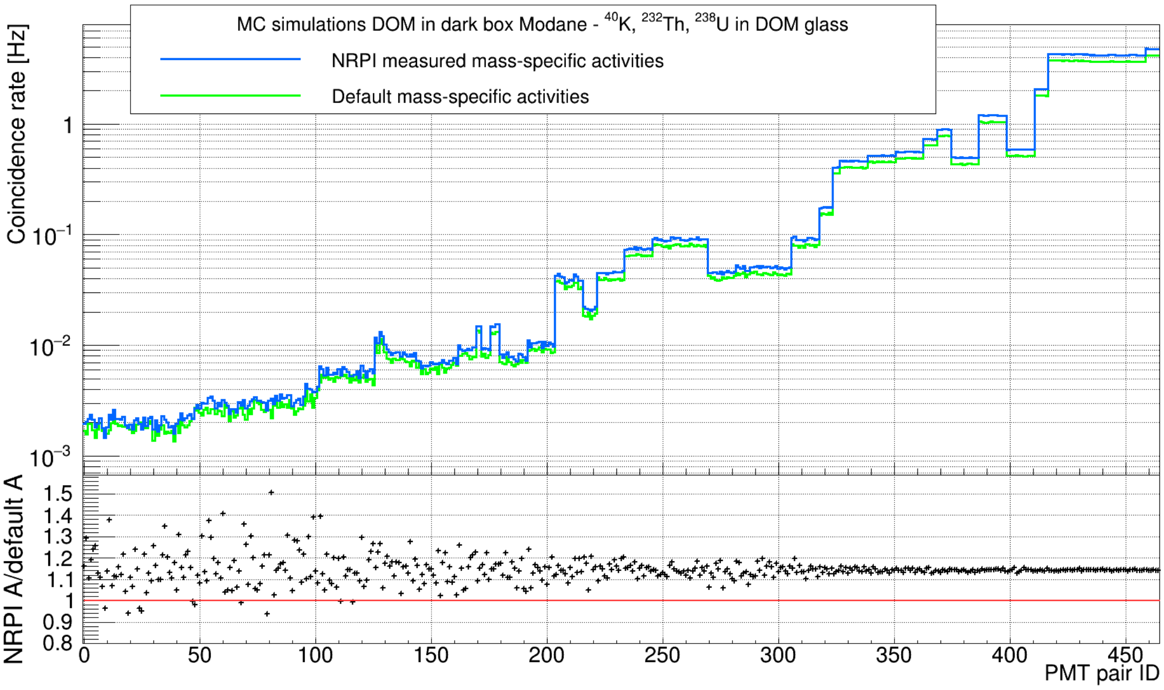

Figure 3.10: Comparison of the coincidence rates for all 465 PMT pairs in the DOM from MC simulations for different values of mass-specific activities of radioactive isotopes contained in the DOM glass. Blue (green) line corresponds to the coincidence rates obtained from MC simulations for NRPI (default) mass-specific activities. PMT pairs are sorted according to the opening angle – opening angle is decreasing with increasing PMT pair ID. The ratio between coincidence rates obtained from MC simulations for NRPI and default mass-specific activities is shown in the lower panel of the figure.

ferent experimental setups (seawater, air), hence it is important to adjust background estimation method according to the specifications of the collected data and corresponding MC simulations. The purpose of the background estimation method is to remove random coincidences in order to obtain the purest set of the real coincidences possible – in our case correlated signals originating from the decays of radioactive isotopes. This process is illustrated in Fig. 2.25, where the distribution of time difference between detection of pulses on two arbitrary PMTs is shown. Estimation of coincidence rates corresponds to integral of this distribution after subtraction of random coincidences (plateau displayed with pink area). In KM3NeT, there are two main background estimation methods for data collected in regime all-data-to-shore (L0 data) called *counts* and *tails* [70].

In the case of *counts* background estimation method, the probability for random

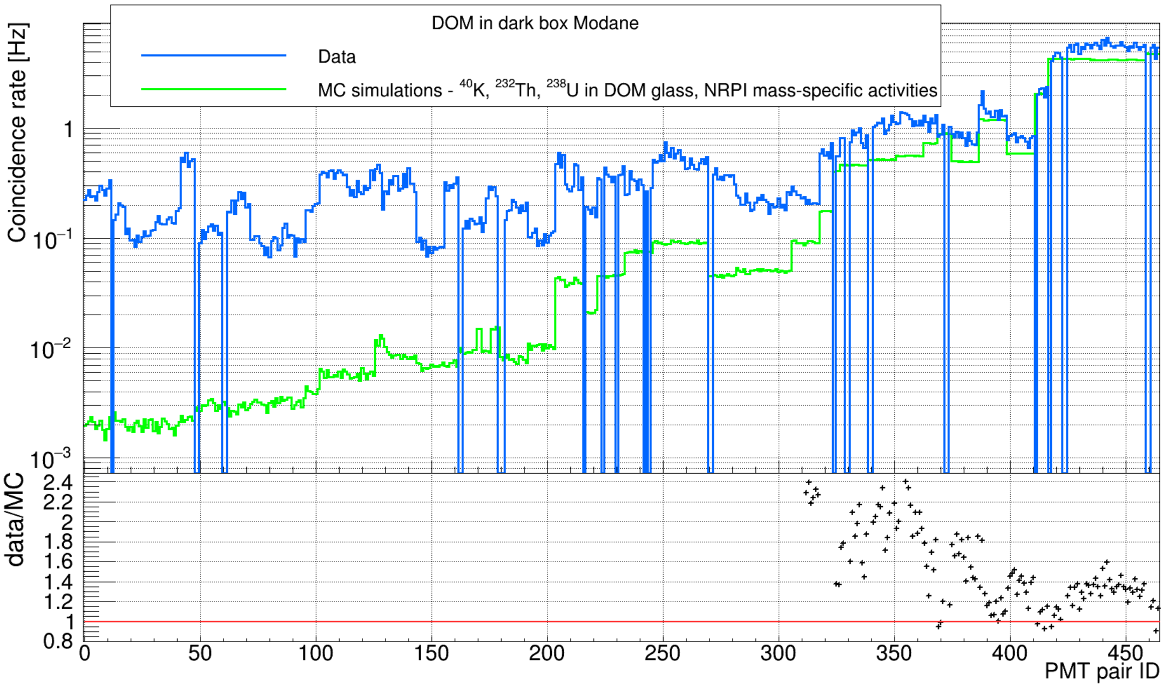

Figure 3.11: Comparison of coincidence rates for all 465 PMT pairs in the DOM obtained from data collected in the Modane laboratory (blue line) and MC simulations made with mass-specific activities measured in NRPI (green line). The lowest PMT pair ID corresponds to the PMT pair with the largest angle between PMTs and the highest PMT pair ID is assigned to the PMT pair with the smallest opening angle. The ratio of the coincidence rates from data to the coincidence rates from MC simulations is displayed in lower panel.

coincidences for PMT pairs is estimated from the overall PMT rates from L0 data. The *tails* method estimates rates of random background coincidences from the bins in the tails of time difference between pulse detection histograms for PMT pairs (usually 15 ns $< \mid \Delta t \mid <$ 20 ns). This method is dependent on statistics in the corresponding bins in the tails of the hit time difference distribution. Insufficient statistics can lead to larger statistical uncertainty.

In coincidence histograms presented in previous sections, background estimation method *counts* was applied. The performance of background estimation methods *tails* and *counts* is analyzed in following paragraphs.

The comparison between the performance of background estimation method *tails* and *counts* for data measured in the Modane underground laboratory is shown in Fig. 3.12. For *counts* background estimation method, final estimated values of coincidence rates are approximately 20 - 30 % higher for majority of the PMT pairs than in the case of application of the *tails* method. For PMT pairs with the smallest opening angle it reaches ~ 30 - 35 %.

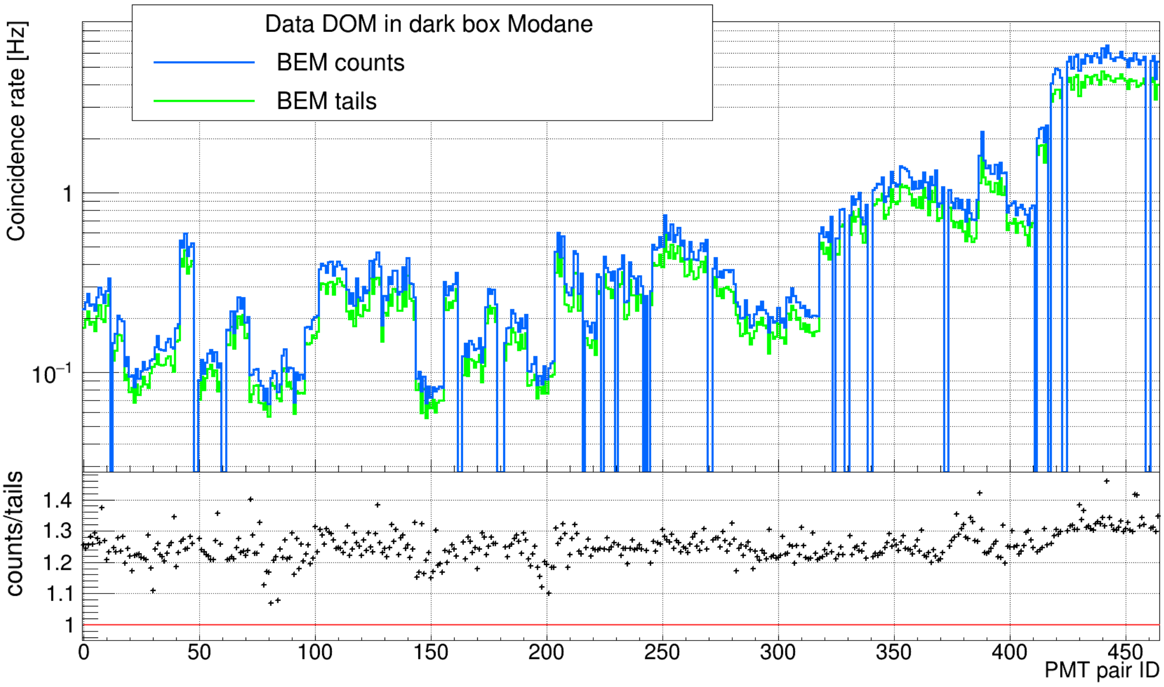

Figure 3.12: Comparison between performance of background estimation method (BEM) *counts* and *tails* for data collected in air dark box in the LSM. For all PMT pairs in the DOM sorted from the largest opening angles (low PMT pair ID) to the smallest opening angle (high PMT pair ID) coincidence rates are shown. Blue line displays estimation of coincidence rates obtained after application of *counts* background estimation method, green line corresponds to the coincidence rates obtained after using *tails* method. The ratio between them is given with black crosses in lower part of the figure.

The performance comparison of *counts* and *tails* for two arbitrary PMT pairs is given in Fig. 3.13. In both cases, value of background coincidence level is underestimated when *counts* method is used. This might be caused by the fact that *counts* method, which uses for the random background coincidence level calculation overall PMT rates, was developed for seawater measurements where the signal is dominated by ^{40}K in water. Hence the PMT rates are higher and also the ratio of the signal (peak) and random background coincidence region (plateau) might be different than in the air measurements. In conclusion, it is more suitable to use *tails* background estimation method for data collected in air environment in dark box in the Modane laboratory.

In Fig. 3.14, the comparison of the usage of the background estimation methods *counts* and *tails* for MC simulations for the LSM measurements is given. Overall behavior is similar as in the case of measured data – usage of the *counts* method leads in general to higher final estimation of coincidence rates. However, in MC simulations case, the relative difference between estimation of coincidence rates after application

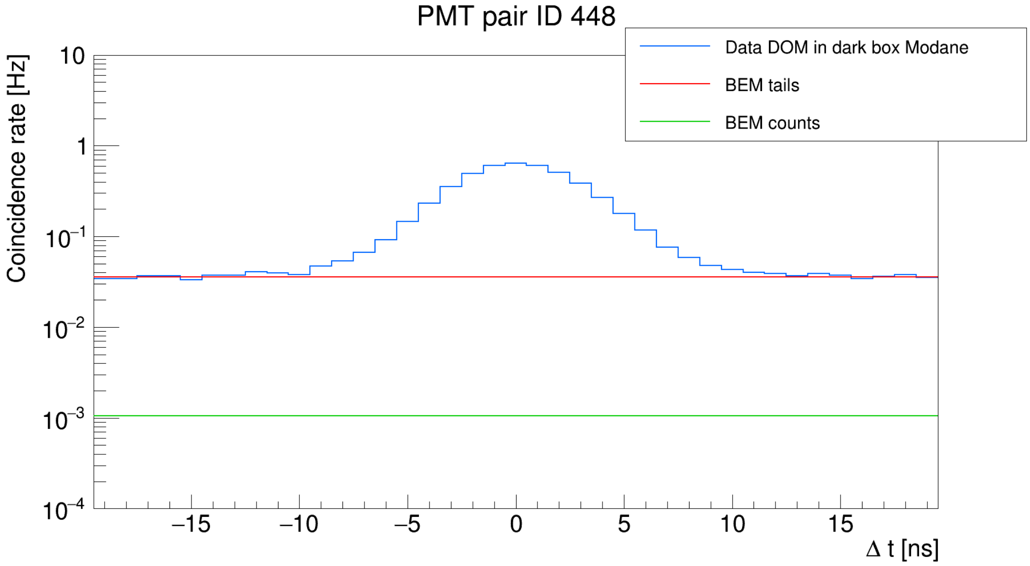

(a)

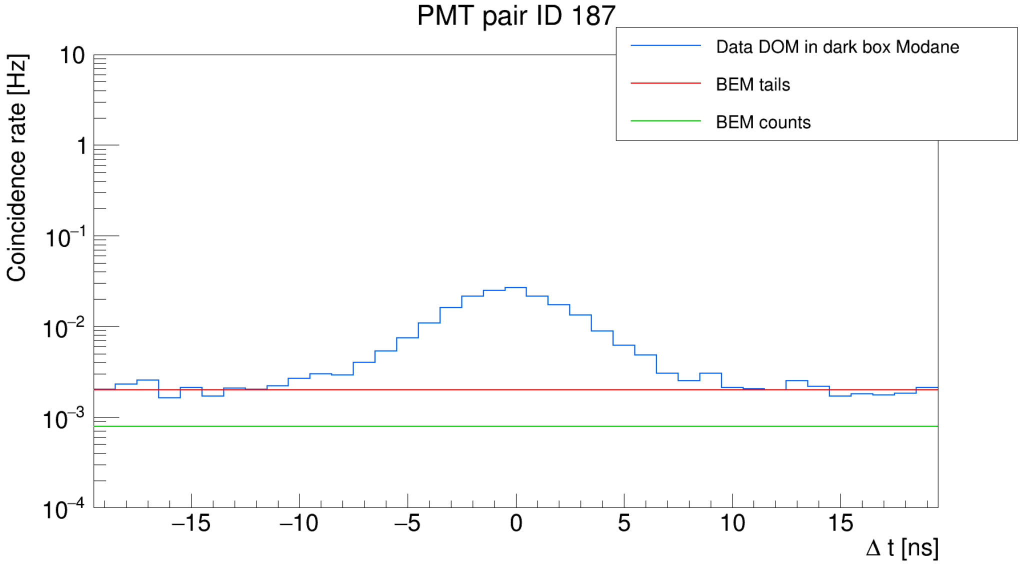

(b)

Figure 3.13: Hit time difference distributions (blue line) for two arbitrary PMT pairs for data measured in the Modane laboratory. Comparison of background estimation methods performance for L0 data – *tails* (red line) and *counts* (green line) is given. a) PMT pair No. 448, opening angle ∼ 31.57°. b) PMT pair No. 187, opening angle ∼ 104.52°.

of the *counts* method and *tails* method is smaller. After application of *counts* method, the estimated coincidence rates are approximately 3 % higher for PMT pairs with small opening angles than in the case of usage of *tails* method. Smaller effect of the choice of the background estimation method might be explained by the fact, that in the MC simulations only signal from the decays of radioactive isotopes contained in glass – ^{40}K, ^{232}Th, and ^{238}U are taken into account, therefore smaller amount of the random background coincidence rates is expected.

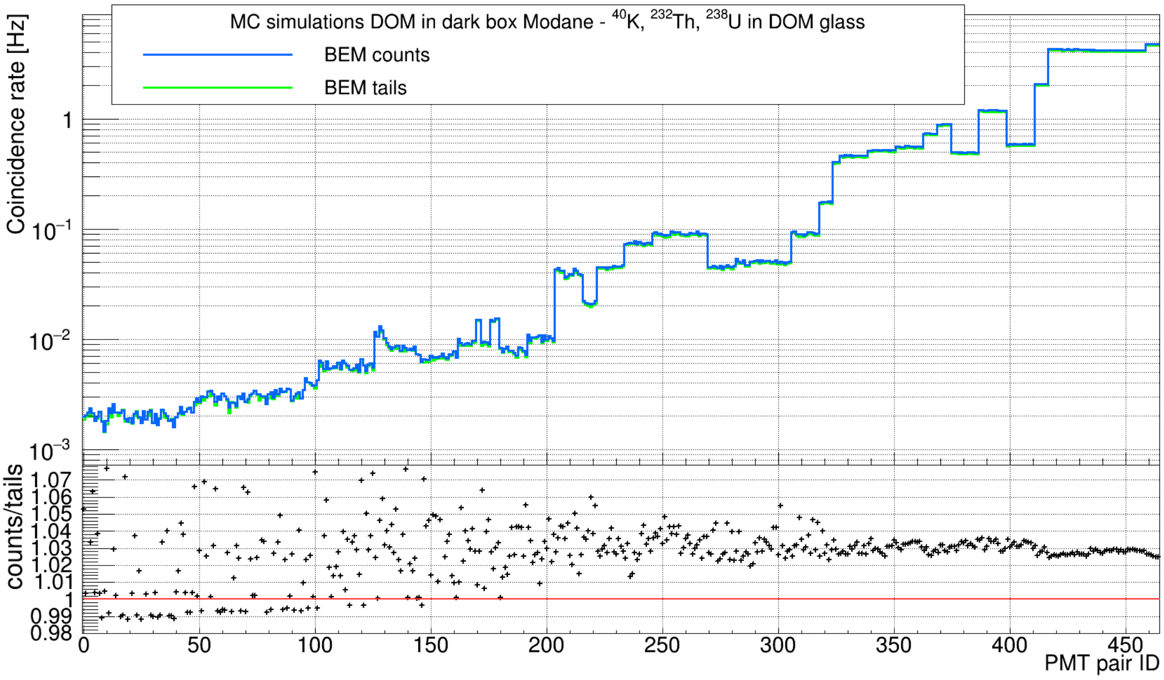

Figure 3.14: Estimations of coincidence rates obtained from MC simulations of the DOM Modane measurements. The comparison between coincidence rates estimation after application of different background estimation methods – *counts* (blue line) and *tails* (green line) is given. The coincidence rates are displayed for all PMT pairs in the DOM (465) and sorted according to the opening angle between two PMTs in the pair from the highest (small PMT pair ID) to the smallest (large PMT pair ID). The ratio of coincidence rates estimation after application of *counts* method to coincidence rates obtained after using *tails* method is shown in the lower panel.

More detailed view on performance of background estimation methods *counts* and *tails* for MC simulations is given in Fig. 3.15, where distributions of the time difference between detection of pulses on two PMTs are shown for two arbitrary PMT pairs. For both PMT pairs, negligible amount of random coincidence rates can be seen, leading to the similar performance of *counts* and *tails* in comparison with data.

The comparison between coincidence rates obtained from data and MC simulations is displayed in Fig. 3.11 for *counts* method and in Fig. 3.16 for *tails* method. The difference between coincidence rates from MC simulations and data after application of the *counts* method for the majority of the PMT pairs with small opening angles is from 20 to 40 %, after using *tails* method this difference is under 20 %, for the majority of these PMT pairs even under 10 %.

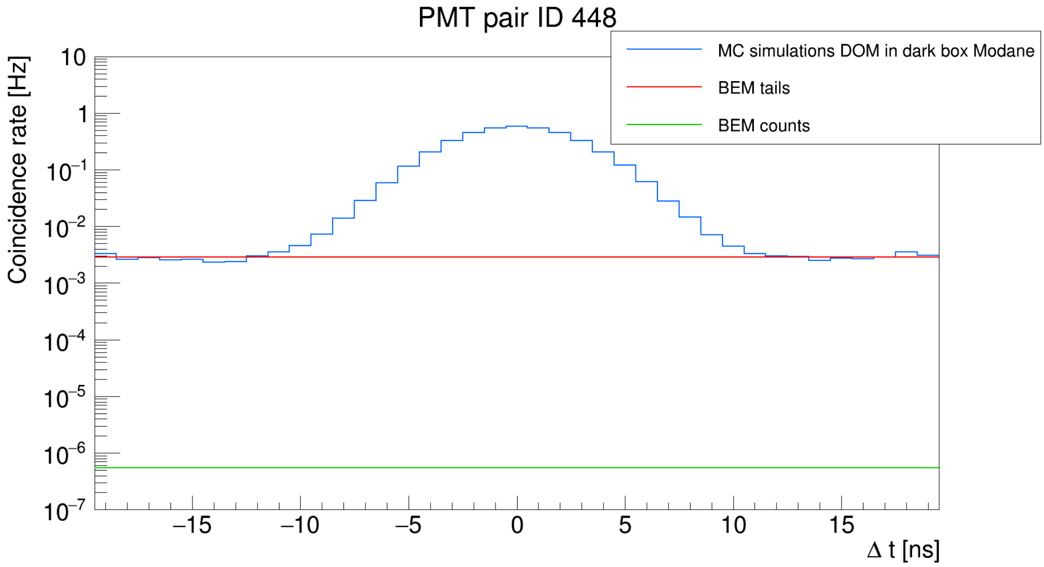

(a)

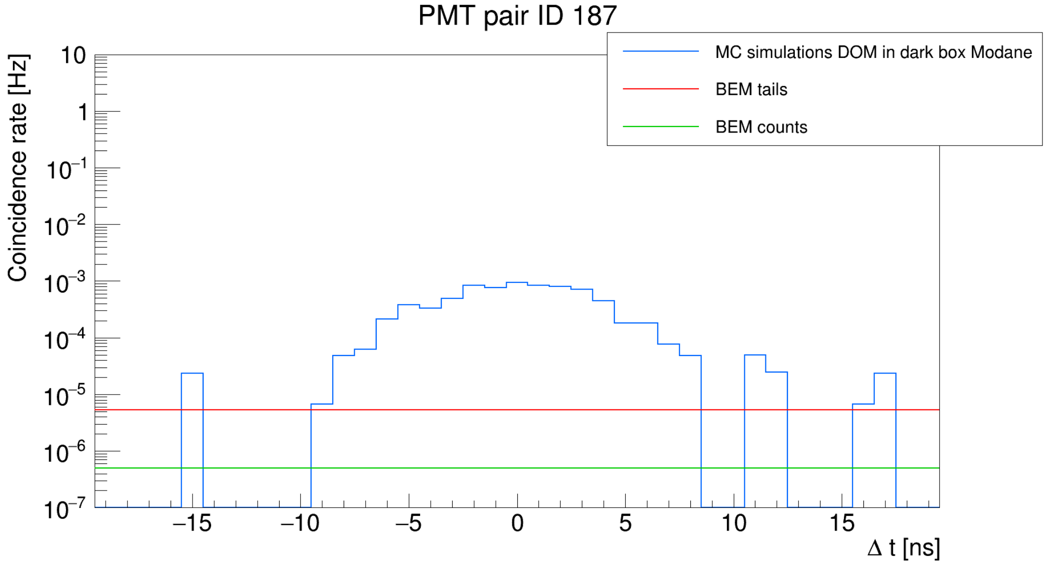

(b)

Figure 3.15: The performance of the background estimation methods *counts* and *tails* for MC simulations for the DOM Modane measurements. The hit time difference distributions (blue line) for two particular PMT pairs with different opening angles are given. Background estimated with *tails* method is shown with red line, green line corresponds to the *counts* method. a) PMT pair No. 448, opening angle ∼ 31.57°. b) PMT pair No. 187, opening angle ∼ 104.52°.

3.4.3 PMT noise rates estimation and simulations

The next effect that can contribute to the discrepancy between coincidence rates obtained from data and MC simulations presented in Fig. 3.8, is simulation of PMT noise rates. In the basic MC simulations, PMT noise rates are not included, the signal simulated on PMTs originates from the decays of radioactive isotopes contained in the

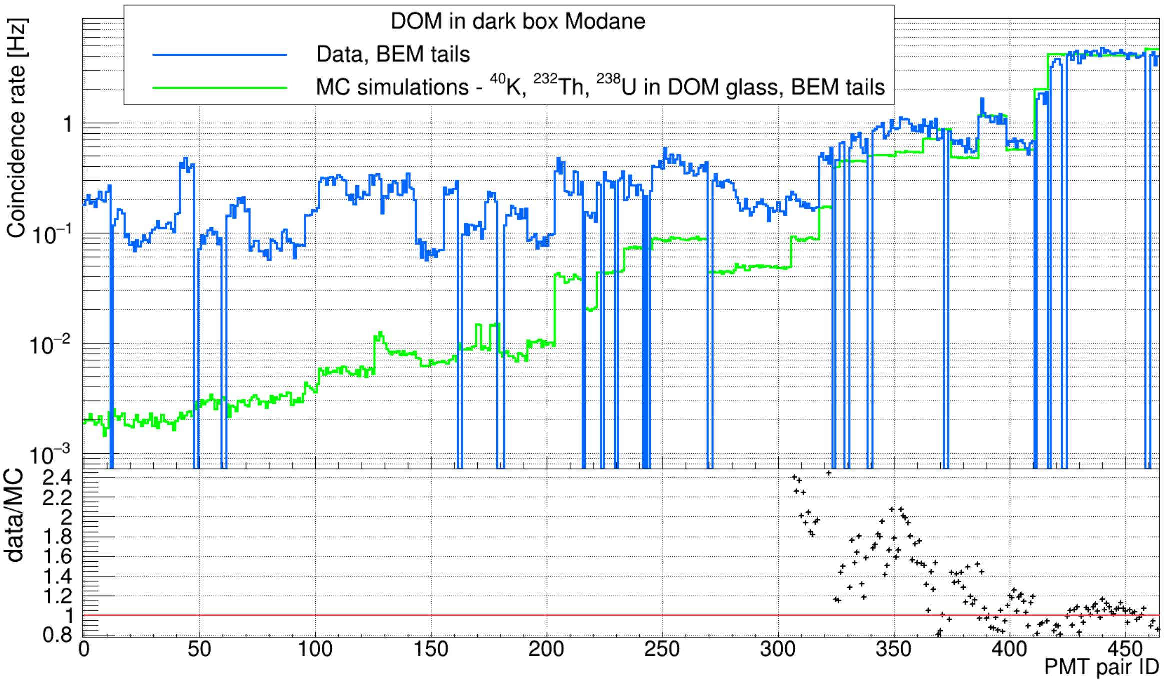

Figure 3.16: Comparison between estimations of coincidence rates obtained from data and MC simulations for 465 PMT pairs in the DOM after application of background estimation method (BEM) *tails*. Ratio of the estimated coincidence rates from data to estimated coincidence rates from MC simulations is shown in lower panel.

DOM glass (^{40}K, ^{232}Th, and ^{238}U) only. In air measurements performed in the Modane laboratory in comparison with seawater measurements, contribution to PMT rates from ^{40}K and ^{238}U from water and from muons are missing. Hence, rates measured in air in the underground laboratory are lower and therefore noise rates from PMTs can be at non-negligible levels. Therefore, it might lead to non-negligible increase of the coincidence rates.

The estimation of the proper value of PMT noise rates that should be added to MC simulations is not straightforward. During measurements with the DOM, the PMT noise rates are summed with the signal from other sources. Secondly, noise rates depend on PMT – every PMT has dark noise rates at different level and therefore these rates can not be estimated from an arbitrary PMT. Obtaining precise rates requires measurements of these rates for particular PMTs before their integration into the DOM and then repeat measurements in the Modane underground laboratory with this particular DOM. Conclusively, in the following study, only approximations will be given and for all PMTs in DOM same noise rates will be simulated.

The approximate level of the noise rates required to be added to the simulations can be estimated from the histogram of the PMT rates from dark box measurements in the Modane laboratory, see Fig. 3.17. It displays rates for all 31 PMTs in one DOM (PMT number 14 is not working). This figure shows that the rates are PMT dependent, the most significant deviations exhibit PMTs with number 3 and 11. On average the rates are at the level of 750 Hz. However, they can reach also approximately 7.5 kHz.

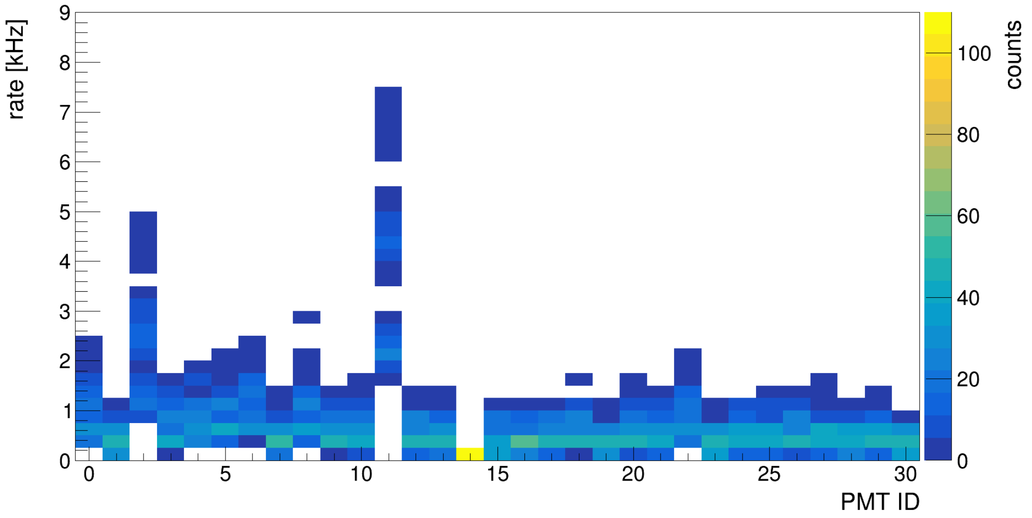

Figure 3.17: Rates of all 31 PMTs in the DOM from measurements in dark box in the underground laboratory in Modane.

The influence of the addition of different random PMT noise rates to the MC simulations of the measurements with the DOM in the Modane underground laboratory for two arbitrary PMT pairs is illustrated in Fig. 3.18. For simulations of the noise rates KM3NeT internal software was used [70]. Fig. 3.18a shows distributions of time difference between pulses detected on two PMTs in the selected pair with opening angle $\sim 31.57^\circ$ for data and MC simulations with different levels of noise rates simulated. Fig. 3.18b displays the same distributions for PMT pair with opening angle $\sim 104.52^\circ$.

It can be seen that data and MC simulations discrepancies vary with different rates of simulated noise pulses. Signal in the main peak should be dominated with correlated signals from simulated decays of ^{40}K, ^{232}Th or ^{238}U with smaller contribution of coincidences of signals from radioactive isotopes decays with noise pulses or two noise pulses coincidences. Interesting feature is the absence of the significant peak in the -5 to 5 ns region for MC simulations for the PMT pair with larger opening angle, see Fig. 3.18b. The suppression of this peak indicates that some processes involved in particle propagation e.g. scattering or absorption of light in DOM glass are not simulated correctly, since in order to obtain coincidences on PMT pairs with larger opening angles, particles have to propagate over larger distances than in the case of PMT pairs with smaller opening angles. To support this hypothesis, more detailed study of the MC simulations is needed.

As it was demonstrated in Fig. 3.18, it is not straightforward to estimate proper

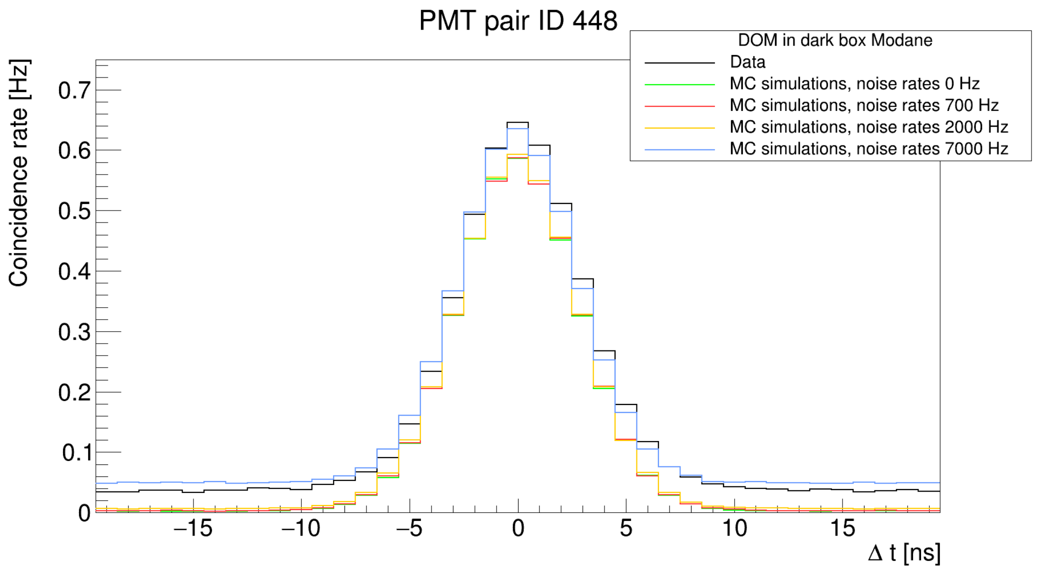

(a)

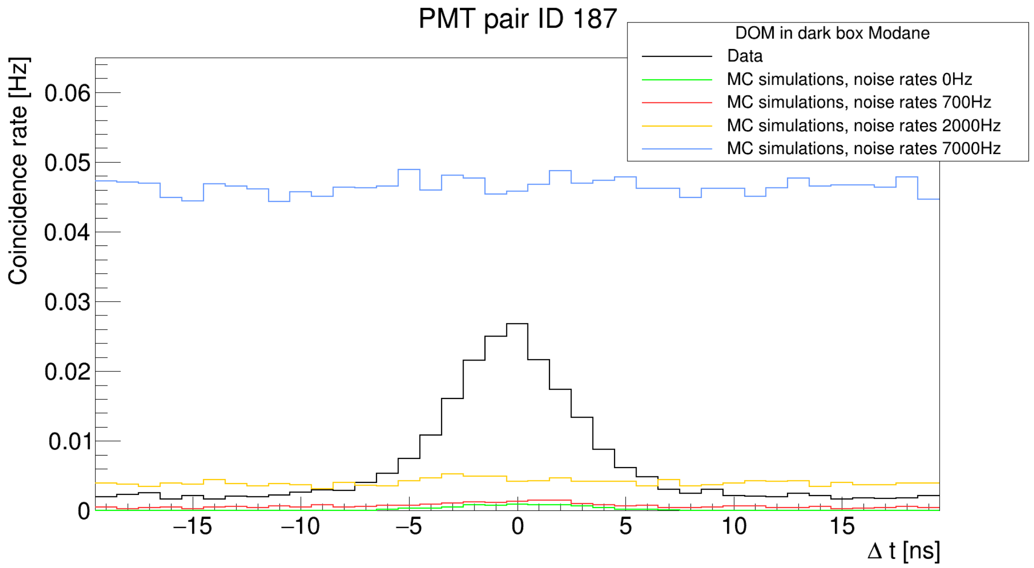

(b)

Figure 3.18: Distributions of difference between detection of pulses on PMTs for the particular PMT pairs for data and MC simulations with different amount of the PMT noise pulses included in the MC simulations. a) PMT pair No. 448, opening angle ∼ 31.57°. b) PMT pair No. 187, opening angle ∼ 104.52°.

level of PMT noise rates (the same for all PMTs in the DOM) that should be included in MC simulations to obtain optimal agreement between data and MC simulations in distributions of time difference between detection of pulses for PMT pairs. There are several possible reasons – dark noise is PMT dependent and also in the MC simulations of the air measurements without generated noise rates, there are additional discrepancies between coincidence rates from data and MC simulations. These issues of MC simulations of air setup propagate to the simulations with additional noise rates and it can result in the requirement of the improper level of noise rates in the MC simulations to obtain sufficient agreement between data and MC simulations. Therefore, in following preliminary analysis the frequency of PMT noise pulses 700 Hz was chosen according to the previous study of dark noise of the KM3NeT PMTs, see Sec. 2.2.2.

The impact of the simulations of the PMT noise rates on the final estimation of coincidence rates is also dependent on the performance of the background estimation method. In ideal situation, majority of simulated coincidences caused by PMT noise rates should be removed after subtraction of random background coincidences. Hence, the final coincidence rates should not be significantly dependent on the PMT noise rates. Nevertheless, proper simulations of the PMT noise rates make the MC simulations more precise and such simulations provide the way to study the influence of the PMT noise rates on final coincidence rates. Moreover, addition of the PMT noise rates to the MC simulations might cause the change in the performance of the background estimation methods. Therefore, it is important to estimate combination of influence of the PMT noise rates simulations and usage of the different background estimation methods on the MC simulations.

So far the performance of the background estimation methods *counts* and *tails* was studied on the MC simulations containing only decays of the radioactive isotopes in the DOM glass. In following analysis, the performance of these methods applied on the MC simulations including also PMT noise rates is given.

The comparison of the performance of the background estimation methods *counts* and *tails* for MC simulations with additionally simulated random background noise at the level of 700 Hz for all PMT pairs is shown in Fig. 3.19. The relative difference between coincidence rates estimation after application of the *counts* method and the *tails* method for PMT pairs with small opening angles is at 3 % level, similar as in the case of MC simulations without additional random pulses simulated, see Fig. 3.14.

However, for the PMT pairs with larger opening angles performance of the background estimation methods starts to differ. This difference is exhibited in Fig. 3.20 in more detail. For the PMT pairs with small opening angles there is a significant difference between number of genuine coincidences (peak) and random coincidences (plateau), see Fig. 3.20a. Therefore, the difference between performance of background estimation methods in the integral plot (Fig. 3.19) is less significant. For the PMT pairs with larger opening angles, difference between genuine and random coincidences is smaller, see Fig. 3.20b which leads to the oscillating behavior in the integral coincidence plot.

In addition, it is important to evaluate change in the estimation of the coincidence rates after adding random rates to the MC simulation. Ratio between coincidence rates estimation for MC simulations with additional 700 Hz of random PMT noise rates and without simulation of random PMT noise for two background estimation

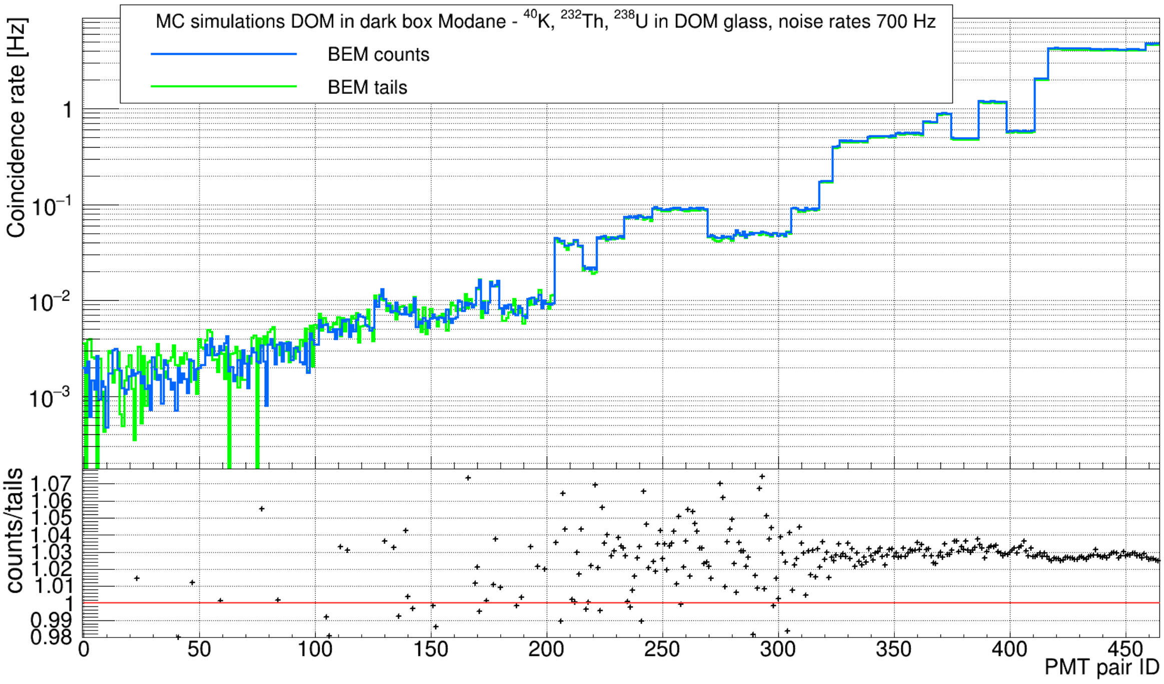

Figure 3.19: The performance of the background estimation methods *counts* and *tails* for MC simulations of the LSM measurements with the single DOM positioned in air dark box with additional simulations of PMT noise rates at the level of 700 Hz. For all PMT pairs in the DOM, sorted according to the opening angle between PMTs – with increasing PMT pair ID, the opening angle is decreasing, estimation of coincidence rates is given. Blue line corresponds to the coincidence rates estimations for *counts* method, green line to the *tails* method. Their ratio is given in lower panel with black crosses.

methods *counts* and *tails* is shown in Fig. 3.21. For both background estimation methods the relative change in the coincidence rates estimation for the PMT pairs with small opening angles is under 1 %, for the smallest opening angles even under 0.5 %.

In Fig. 3.22 the comparison between coincidence rates from data and from MC simulations with PMT noise simulated at the level of 700 Hz for two background estimation methods *counts* anf *tails* is shown.

The comparison of the histograms in the Figs. 3.11, 3.16, and 3.22 shows that the choice of background estimation method has larger impact on discrepancy between coincidence rates estimations obtained from data and MC simulations than simulations of noise pulses. In the case of usage of background estimation method *counts* the difference between data and MC simulations, both without simulated PMT noise and with PMT noise simulated at the level of 700 Hz is under approximately 40 % for the PMT pairs with the smallest opening angles and for *tails* method this difference is

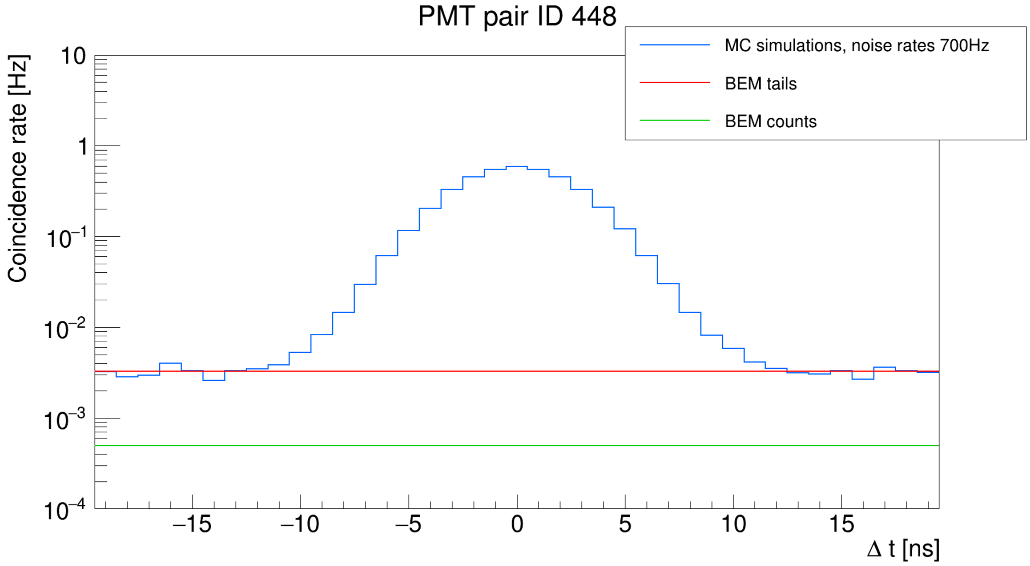

(a)

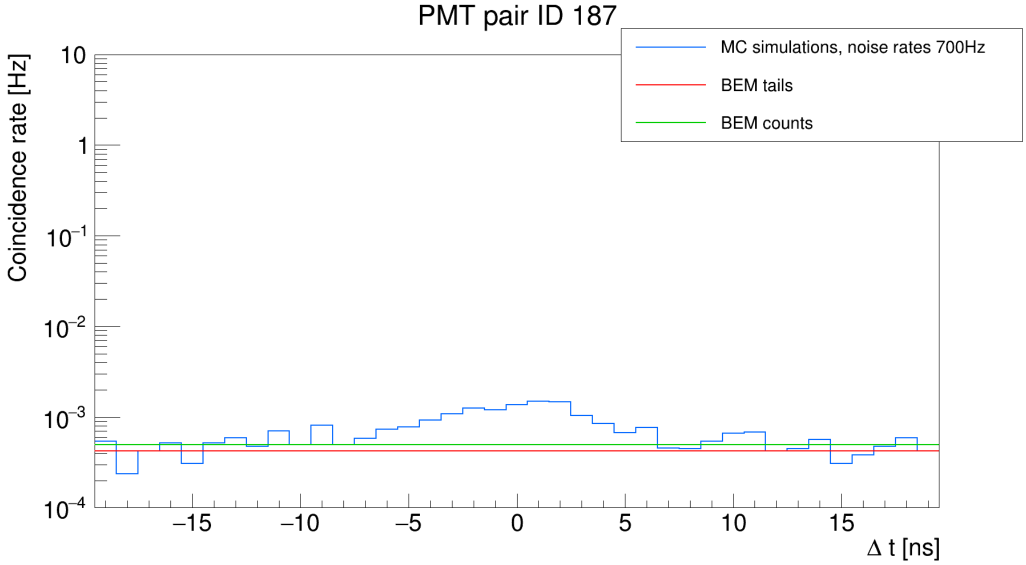

(b)

Figure 3.20: Comparison of background estimation methods *counts* and *tails* performance for two arbitrary PMT pairs for MC simulations of decays of radioactive isotopes in the DOM glass for the LSM measurements with additional 700 Hz of PMT noise rates simulated. Hit time difference distribution is displayed with blue line. Red line depicts background level estimated with method *tails* and green line shows results of application of the *counts* method. a) PMT pair No. 450, opening angle ∼ 31.57°. b) PMT pair No. 187, opening angle ∼ 104.52°.

under around 10 - 20 %. In combination with the results of performance testing of both background estimation methods for individual PMT pairs, for further analysis of data measured in dark box filled with air in the LSM, application of the background estimation method *tails* is recommended.

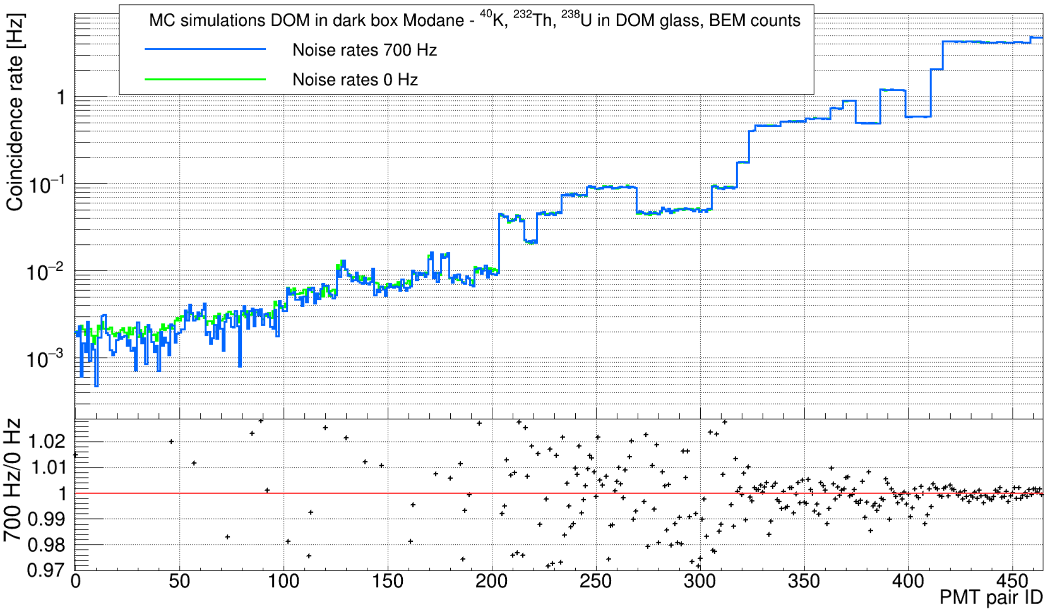

(a)

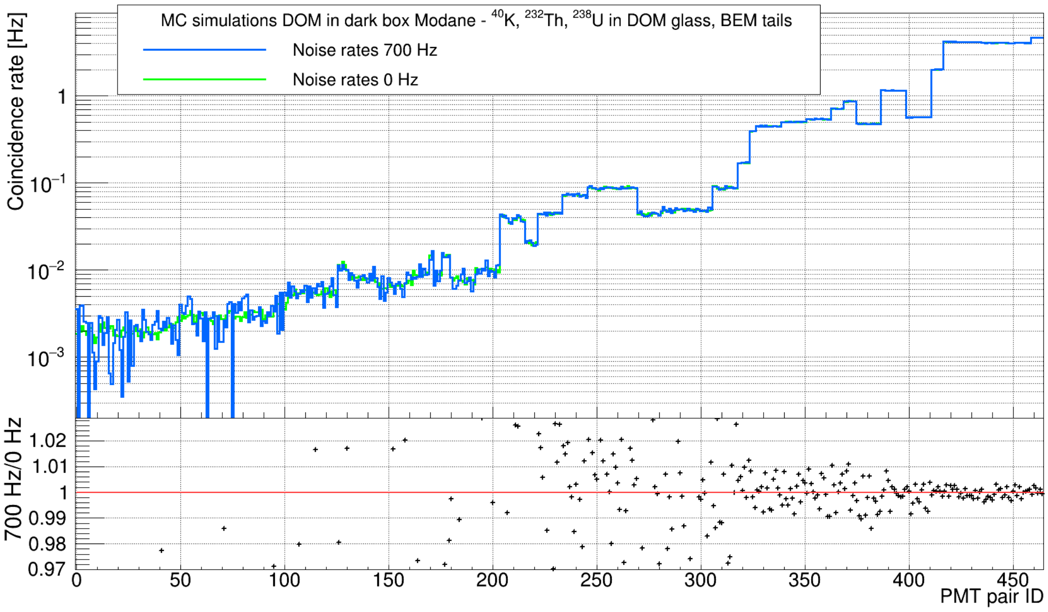

(b)

Figure 3.21: The evaluation of the influence of the additionally simulated PMT noise rates at the level of 700 Hz in MC simulations on the coincidence rates estimation. Blue line shows coincidence rates for MC simulations with additional 700 Hz of noise rates, green line corresponds to the basic MC simulations without additional noise rates simulated. Their ratio is displayed in the lower panel with black crosses. The coincidence rates and their ratio are given for all PMT pairs in the DOM lined up according to the angle between two PMTs in pair – increasing PMT pair ID corresponds to the decreasing opening angle between PMTs. a) Background estimation method *counts*. a) Background estimation method *tails*.

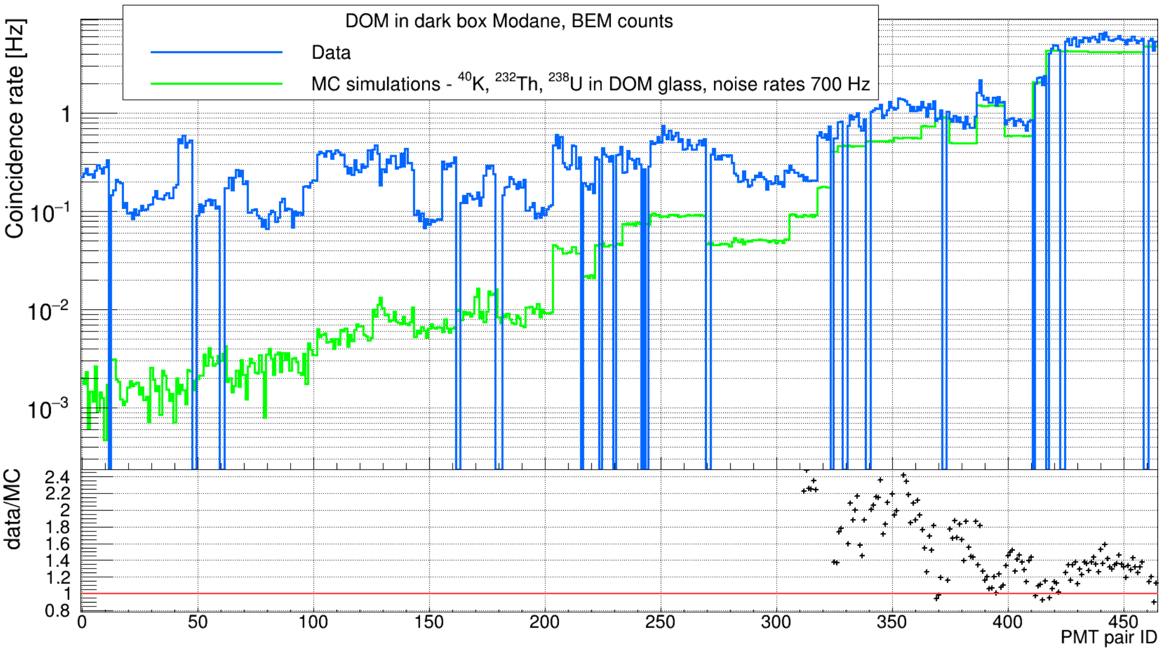

(a)

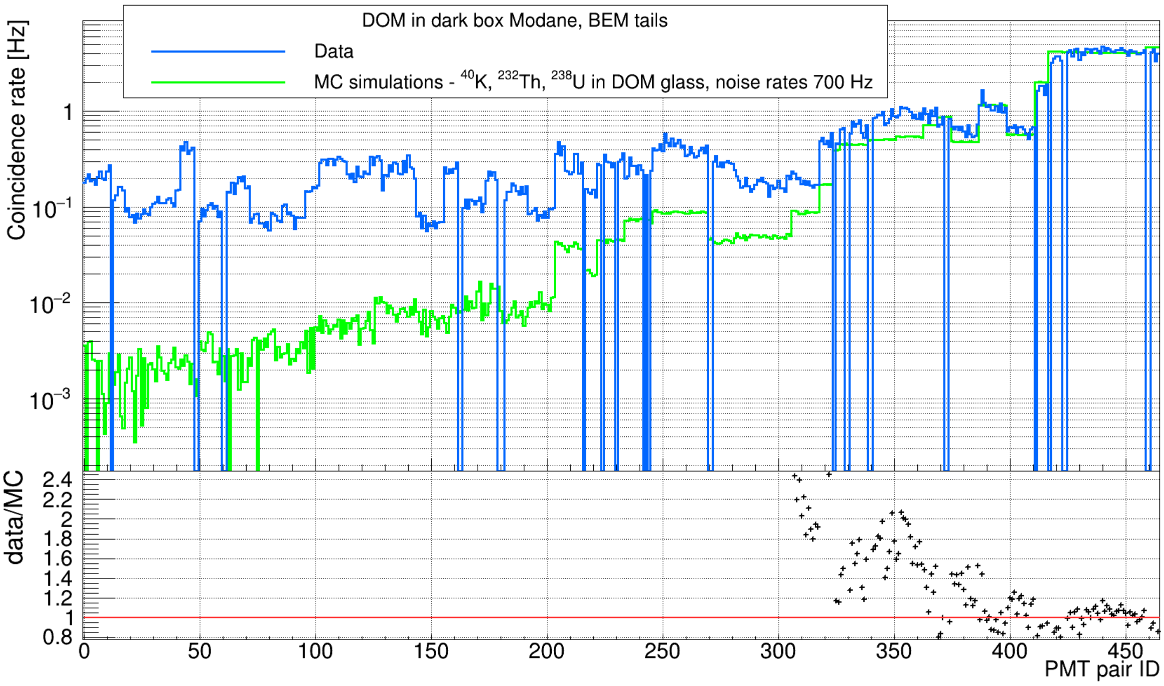

(b)

Figure 3.22: Comparison between the estimations of the coincidence rates from data and MC simulations with additional noise pulses simulated at the level of 700 Hz for 465 PMT pairs in the DOM for different background estimation methods applied. Ratio of the coincidence rates estimation from data to the estimation from MC simulations is shown in panel below. a) Background estimation method *counts*. b) Background estimation method *tails*.

3.4.4 Environment correction

In previous sections, only decays of radioactive isotopes (^{40}K, ^{232}Th, and ^{238}U) in the DOM glass and PMT noise rates were taken into account in the MC simulations. However, in the environment of the Modane underground laboratory, there are other possible sources of background [79] that need to be studied, and their contribution to the measured data have to be estimated. Among them belong natural radionuclides in the rock of the Fréjus peak or elements contained in the concrete used to built the Modane underground laboratory. Moreover also radon contained in the air can contribute to the DOM data. In following section, the influence of ^{222}Rn contained in the air in the dark box will be analyzed.

^{222}Rn is part of the ^{238}U decay chain, see Fig. 3.23. It is chemically inert noble gas and due to its relatively long half-life ∼ 3.8 days in comparison with other radon isotopes occurring in nature, ^{222}Rn can be released from the rock and soil where it is created. Subsequently, it decays to ^{218}Po through alpha decay with almost 100 % branching ratio.

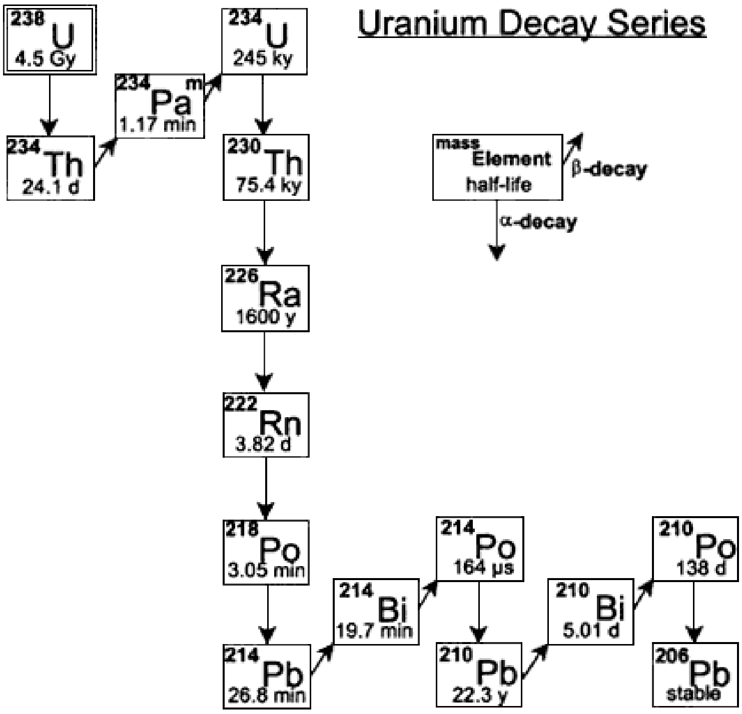

Figure 3.23: ^{238}U decay chain. Taken from [80].

In the simulations, the activity per volume of the ^{222}Rn from the radon detector placed in the DOM measurements room was used. It was estimated as 41 Bq/m^3.

Fig. 3.24 shows coincidence rates obtained from MC simulations of decays of radioactive isotopes in the DOM glass – ^{40}K, ^{232}Th, and ^{238}U together with the expected contribution from ^{222}Rn. For all PMT pairs, the contribution from ^{222}Rn is approximately one order lower than the lowest contributing component for that PMT pair.

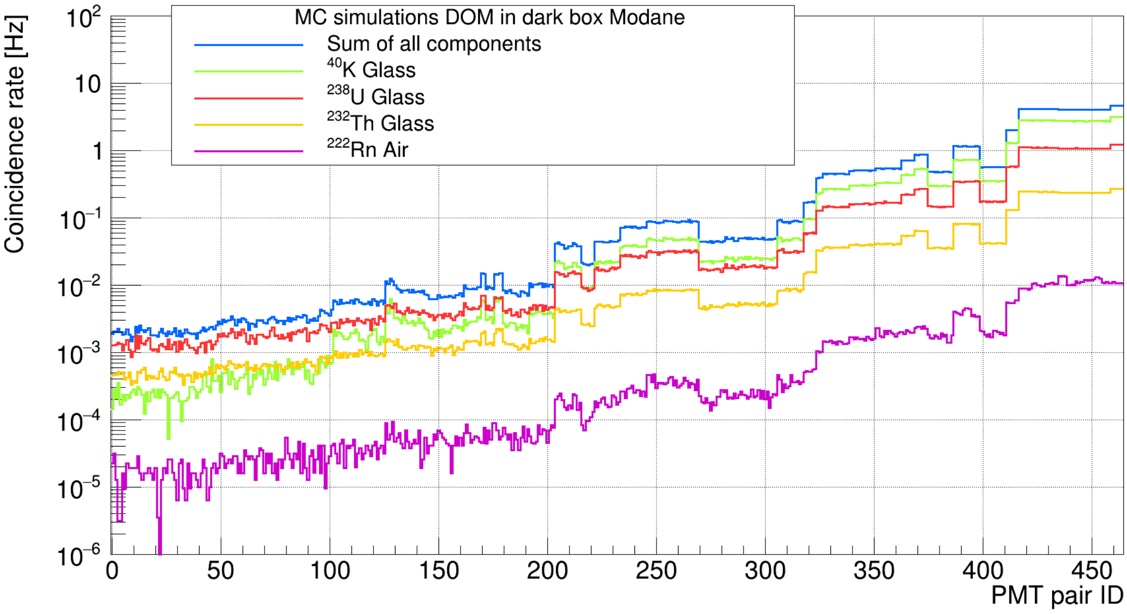

Figure 3.24: Distribution of coincidence rates from MC simulations for all 465 PMT pairs in the DOM sorted according to the angle between PMTs in the pair. The highest PMT pair IDs correspond to the PMT pair with the smallest angle between PMTs. With decreasing PMT pair ID, this angle is increasing. Blue color shows sum of the coincidence rates obtained from all radioactive isotopes in MC simulations – ^{40}K, ^{232}Th, and ^{238}U contained in the DOM glass, and ^{222}Rn contained in air in the dark box. With other colors contributions from individual isotopes are given.

Since the radon detector was placed outside of the dark box, obtaining more precise estimation of the contribution from the ^{222}Rn in the air inside the dark box requires the measurements of the radon content in the air directly inside the dark box. However, this first study indicates that the contribution to the coincidence rates from ^{222}Rn contained in the air is negligible in comparison with the contributions from the radioactive isotopes contained in the DOM glass.

3.4.5 Measurements in reflective box

To study MC simulations of the measurements with the DOM in the Modane underground laboratory in more detail, in addition to the dark box (Fig. 3.2), the box with walls covered in mylar foil was constructed, see Fig. 3.25. Data collected in two different setups have potential to contribute to better understanding of MC simulations.

The most important difference between pure dark box and aluminum box is the reflection of light on the walls of the box. With this setup it is possible to collect data with the same sources – radioactive isotopes contained in the DOM glass, but with different processes that have to be taken into account like reflection of the light from the box walls. Therefore, the analysis of the discrepancy between data and MC simulations of such measurements can reveal potential issues of the MC simulations.


(a) (b)

Figure 3.25: a,b) Dark box with walls covered with mylar foil used during the DOM measurements in the LSM.

In Fig. 3.26, the comparison between coincidence rates estimations from data measured in box with walls covered with mylar foil and basic dark box is shown. For the PMT pairs with small opening angles, there is approximately 2 times increase in coincidence rates estimation for aluminum box, while for PMT pairs with larger opening angles this difference is at the level of one order.

Fig. 3.27 displays comparison between data and MC simulations of coincidence rates estimation for aluminum box. The difference between data and MC simulations for the PMT pairs with the smallest opening angles is under approximately 20 %. This result is comparable with the outcome from the dark box measurements, see Fig. 3.16. For the PMT pairs with larger opening angles, the discrepancy between data and MC simulations is approximately 50 - 60 %, while for dark box measurements, the ratio between coincidence rates from data and MC simulations reaches several orders of magnitude, see Fig. 3.16. These attributes of the coincidence rates histograms indicate

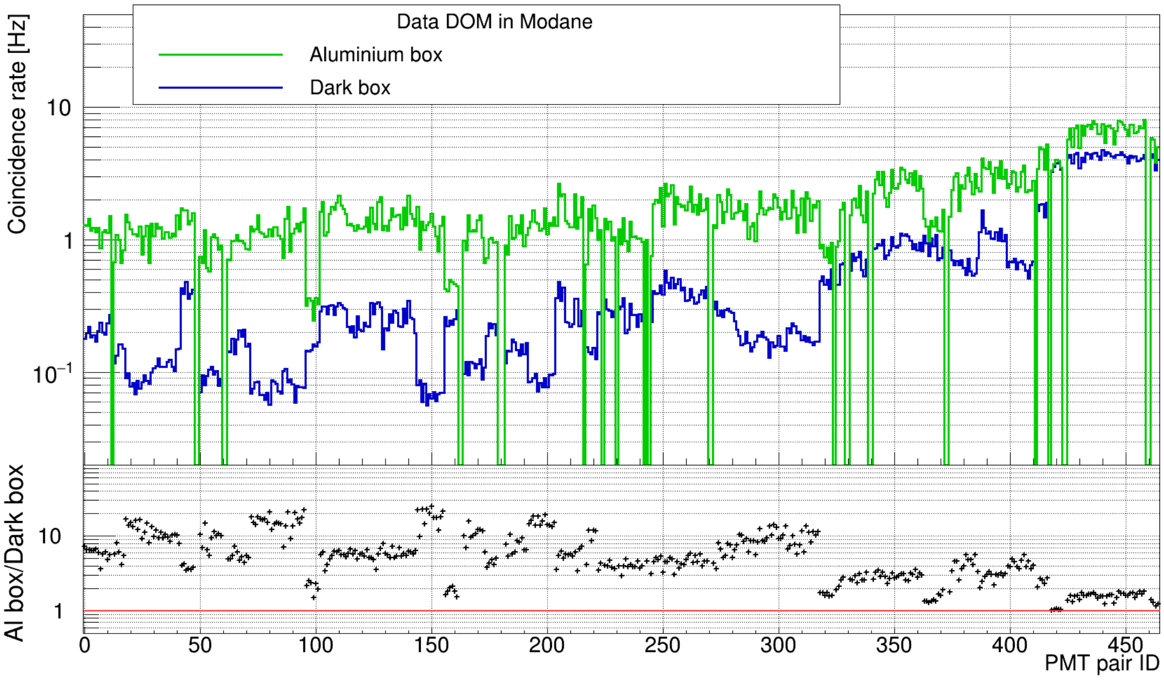

Figure 3.26: Comparison of the coincidence rates given as a function of the PMT pairs in the DOM (sorted according to the opening angle between PMTs from the highest angle to the smallest angle) obtained from data measured in two different setups – dark box and aluminum box in the Modane underground laboratory. The ratio of the coincidence rates between dark box data and aluminum box data is displayed in the lower panel.

that the disagreement between MC simulations and data for PMT pairs with larger opening angles can be caused by improper simulation of light propagation in glass, since in the mylar box effect of the light propagation in the glass is expected to be negligible in comparison with the reflection of the light from the walls.

More detailed view on these aspects is given in Fig. 3.28, where the hit time difference distributions for data and MC simulations for the basic dark box and the aluminum box are displayed. The coincidence rates in the main peak for aluminum box are higher and also the main peak is wider for aluminum box in comparison with dark box. Both of these features might be explained by the effect of the reflection of the light on the walls of the box. Since light is not absorbed, it is increasing coincidence rates and due to the time delay caused by the distance from the DOM to the box walls, the peak in Δt distribution is widened. From the Fig. 3.28b follows, that this effect also creates correlated coincidences in MC simulations for the PMT pairs with large opening angles – agreement between data and MC simulations is significantly improved in comparison with dark box measurements. This can indicate that the discrepancy between data and MC simulations for the dark box measurements for PMTs with large

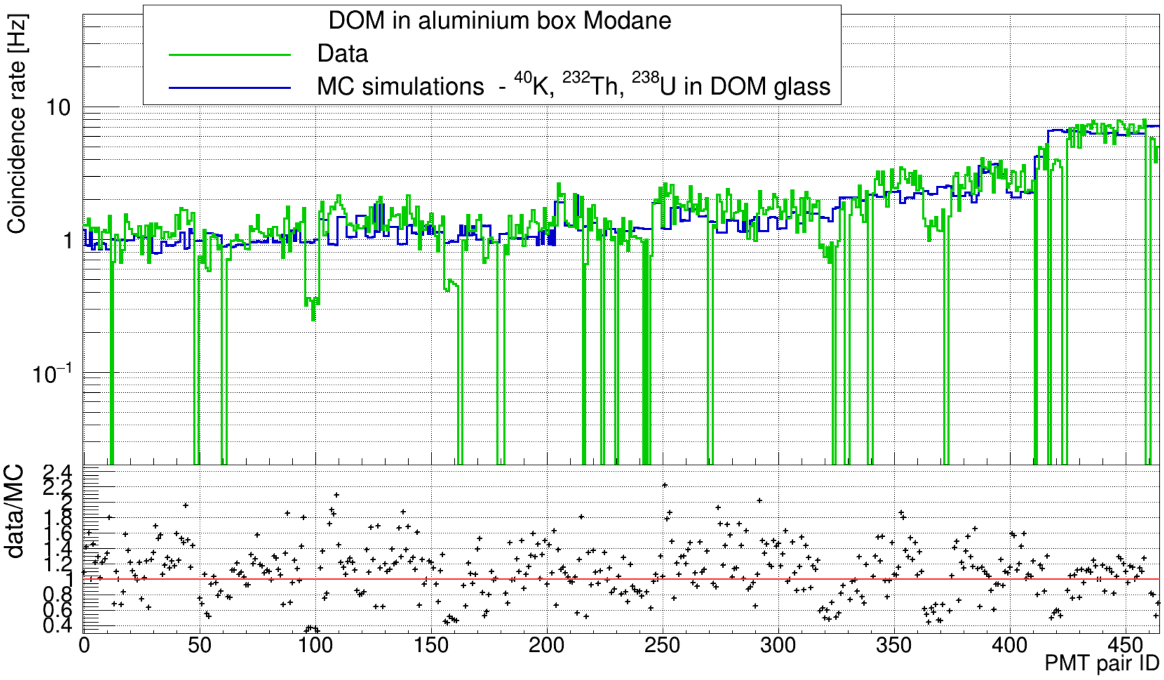

Figure 3.27: Comparison of the estimation of the coincidence rates from data and MC simulations for all PMT pairs in the DOM for the aluminum box setup. PMT pairs are sorted according to the angle between PMTs in pair – the angle decreases with increasing PMT pair ID. The ratio between estimation of the coincidence rates from data and MC simulations is given with black crosses.

opening angles (see Fig. 3.16) is caused by improper simulations of some processes, e.g. propagation of light in glass, rather than missing source of signal from decays of the radioactive isotopes – for PMTs with small opening angles where direct signal from decays of radioactive elements should dominate, satisfactory agreement is achieved.

3.5 Sea data

Calibrations with ^{40}K decays described in Sec 2.2.3 are performed in-situ with the data collected with DOMs deployed in sea. This type of calibrations provides a way how to monitor and calibrate detector during operation. In this section, the preliminary analysis of the impact of the results from the first analysis of the Modane underground laboratory data on the coincidence rates estimation used in calibration of the KM3NeT detectors with ^{40}K decays is described.

In addition to the decays of the radioactive isotopes contained in the DOM glass (^{40}K, ^{232}Th, and ^{238}U) which were taken into account in MC simulations of measurements in the Modane underground laboratory, for the data measured in seawater environment, decays of the radioactive isotopes contained in seawater (^{40}K and ^{238}U)

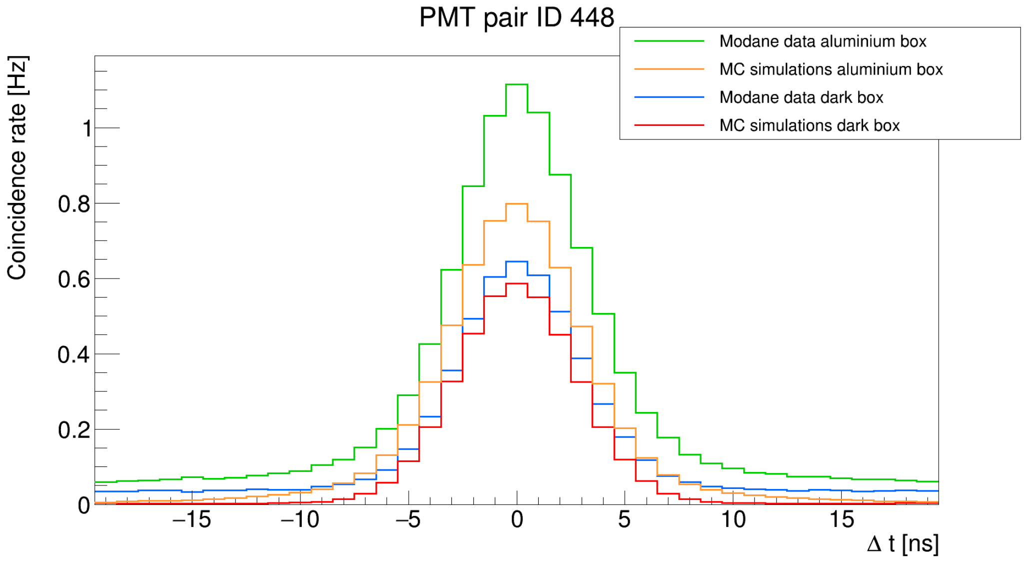

(a)

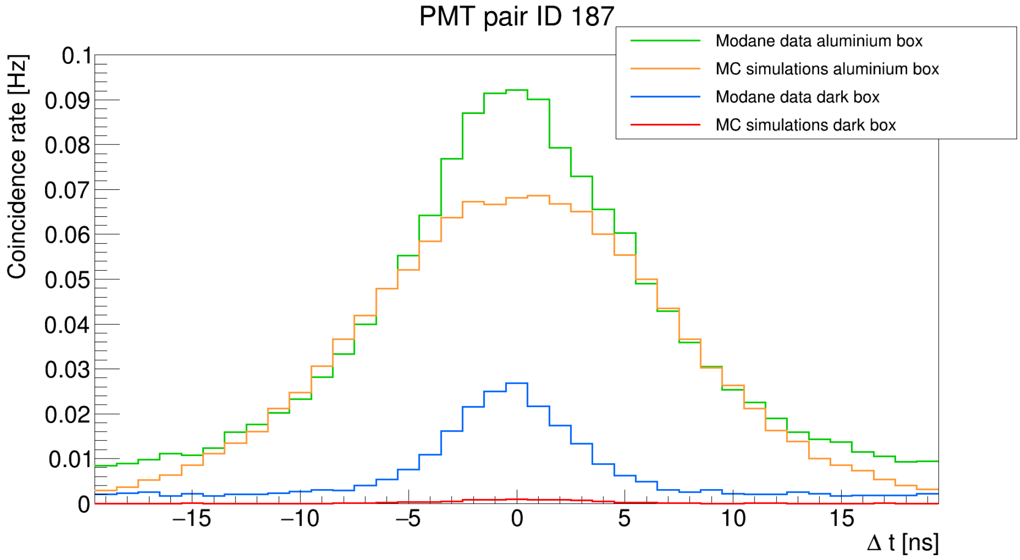

(b)

Figure 3.28: Hit time difference distributions for the particular PMT pairs for data and MC simulations for measurements with the DOM in the dark box and aluminum box. a) PMT pair No. 448, opening angle $\sim 31.57°$. b) PMT pair No. 187, opening angle $\sim 104.52°$.

have to be included. The activity per volume for ^{40}K contained in seawater used in MC simulations is 13 750 Bq/m^3 and for ^{238}U in seawater it is 40 Bq/m^3.

In the case of the data measured in the air dark box in the Modane laboratory, all hits registered on the PMTs were saved, there was no selection algorithm applied. This type of data is called L0 data. However, for the analysis of the data collected in sea presented in following paragraphs, L1 hits were used. The condition for the L1 hit selection is the coincidence of two or more L0 level hits detected in the same DOM in a specified time window. This time window can be adjusted according to the analysis, in following study time window of 25 ns was used.

For L1 data, there are two background coincidence estimation methods *rates* (equivalent of the L0 data method *counts*) and *tails*. The working principle of these methods is given in Sec. 3.4.2. However, in the case of L1 hits only selected hits are available, hence it is not possible to obtain the overall rates detected on PMTs purely by counting L1 level hits. That is the reason why the background estimation method for L0 data *counts* is not applicable on L1 data. It is overcome by saving so called summary data where the overall rates are stored, and these summary rates are input for the *rates* background estimation method.

In following paragraphs, change in the coincidence rates estimation for seawater MC simulations and data caused by using different values of mass-specific activities of radioactive isotopes contained in the DOM glass and also influence of the choice of the background estimation method is presented.

In Fig. 3.29, the comparison of the coincidence rates estimation from MC simulations for all PMT pairs in one DOM for default mass-specific activities of radioactive isotopes contained in DOM glass and NRPI measured mass-specific activities is given. Fig. 3.29a shows the comparison of coincidence rates estimation after application of background estimation method *rates* and Fig. 3.29b after application of *tails* method. For the PMT pairs with the smallest opening angles, the behavior for both background estimation methods *rates* and *tails* is similar, the increase in estimated coincidence rates with NRPI measured mass-specific activities in comparison with default mass-specific activities is at the level of 3 - 4 %. It is approximately 5 times lower relative increase in comparison with MC simulations of the measurements with the DOM in the dark box filled with air in the Modane laboratory, see Fig. 3.10. Estimation of coincidence rates in Fig. 3.10 was obtained with *counts* background estimation method, but the application of *tails* method leads to similar relative increase, therefore figure for *tails* method is not included. The reason of the smaller impact of the changes in the glass composition for MC simulations of the DOM placed in seawater is that in seawater there is also contribution to the signal from radioactive isotopes contained in seawater. With increasing opening angle between PMTs, the change in coincidence rates estimation is under approximately 1 - 2 %. Comparison between Fig. 3.29a and Fig.3.29b also indicates that in the case of MC simulations of the DOM placed in seawater, the background estimation method *rates* gives more stable results for the final coincidence rates for the PMT pairs with the largest opening angles for the statistics chosen in this study.

The comparison between performance of *rates* and *tails* methods for MC simulations and data from sea is displayed in Fig. 3.30 and Fig 3.31, respectively. In the case of data, this comparison is given for two DOMs – one DOM with PMTs with older design – Hamamatsu R12199-02 (Fig. 3.31a) and one DOM in which PMTs with new design

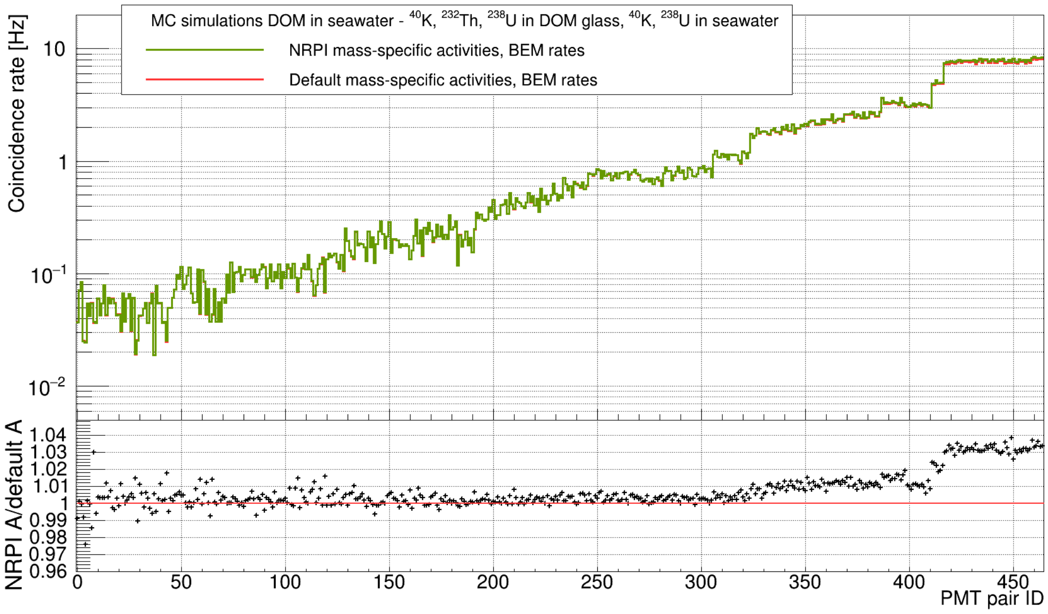

(a)

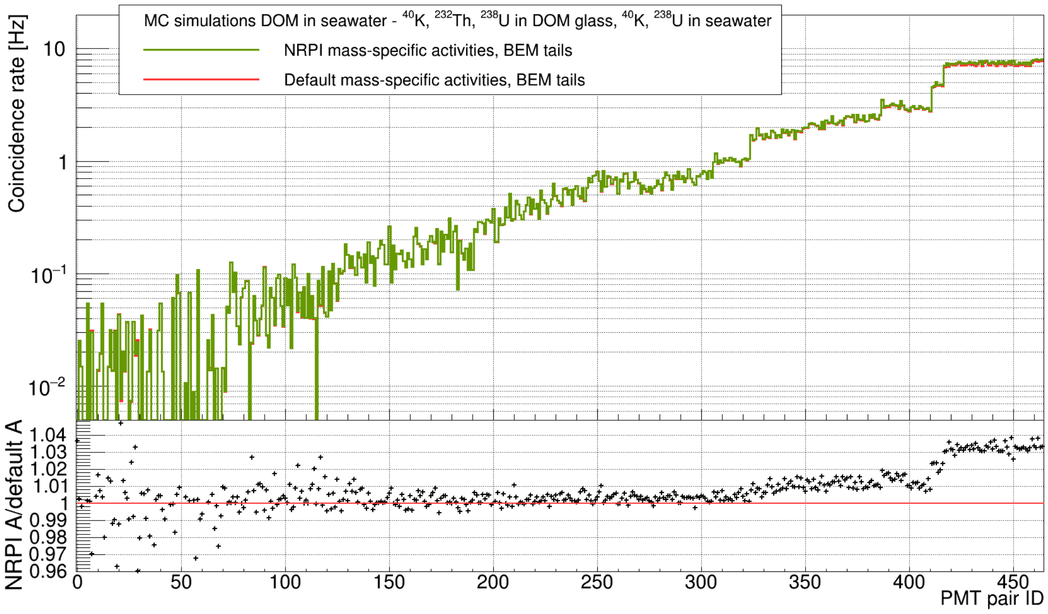

(b)

Figure 3.29: Comparison of the influence of different values of mass-specific activities for radioactive isotopes in DOM glass used in MC simulations of DOM situated in seawater on coincidence rates estimation. For all PMT pairs in the DOM, coincidence rates estimation is given. PMT pairs are aligned according to the opening angle between PMTs participating in particular pair. The lowest (highest) IDs correspond to the largest (smallest) opening angles. Ratio between coincidence rates obtained with different mass-specific activities of the radioactive isotopes in the DOM glass is given in lower panel. a) Background estimation method *rates*. b) Background estimation method *tails*.

– Hamamatsu R14374 are installed (Fig. 3.31b). For MC simulations, the difference between the resulting coincidence rates for *rates* and *tails* methods is at the level of 5 % for the PMT pairs with the smallest opening angles. In the case of sea data, this difference is approximately from 5 to 10 %. This ratio may differ according to the chosen DOM. For more precise estimation of this effect, larger statistics have to be considered. For the DOM with old type PMTs, the difference between coincidence rates for the PMT pairs with the smallest opening angles after application of *rates* and *tails* method is at the level of 5 - 10 %, for new type PMTs DOM it is slightly lower at the level of 5 %. The same comparison for data and MC simulations for the Modane laboratory measurements (data – Fig. 3.12, MC simulations – Fig. 3.14) leads to the larger relative differences ∼ 30 - 35 % for data and ∼ 3 % for MC simulations. This can indicate that for seawater data and corresponding MC simulations, the background estimation methods are more compatible, and since *rates* method performance is for statistic chosen for this study more stable for all PMT pairs, in the following preliminary analysis the background estimation method *rates* is used.

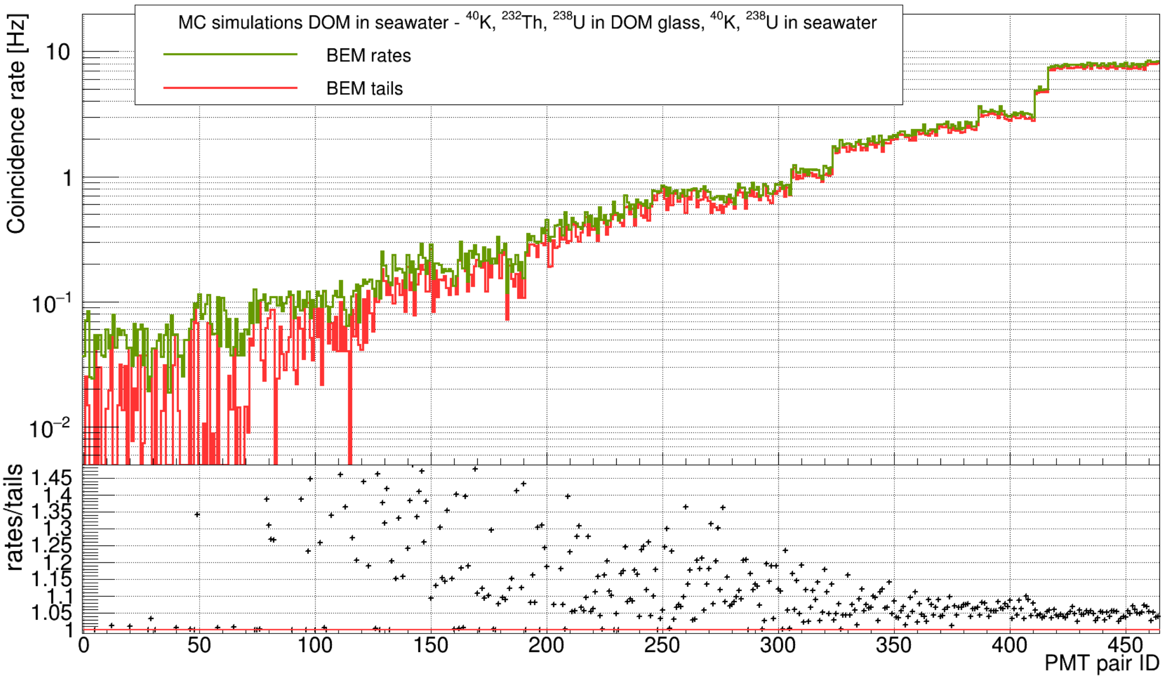

Figure 3.30: The comparison of the performance of the background estimation methods *rates* and *tails* for MC simulations of the DOM measurements in seawater. For all PMT pairs in the DOM, estimation of the coincidence rates is given. PMT pairs are arranged from the highest to the lowest opening angles between PMTs. Ratio of the coincidence rates obtained with background estimation method *rates* to the coincidence rates acquired with *tails* method is given with black crosses.

In Fig. 3.32, the contributions to the coincidence rates of the individual radioactive

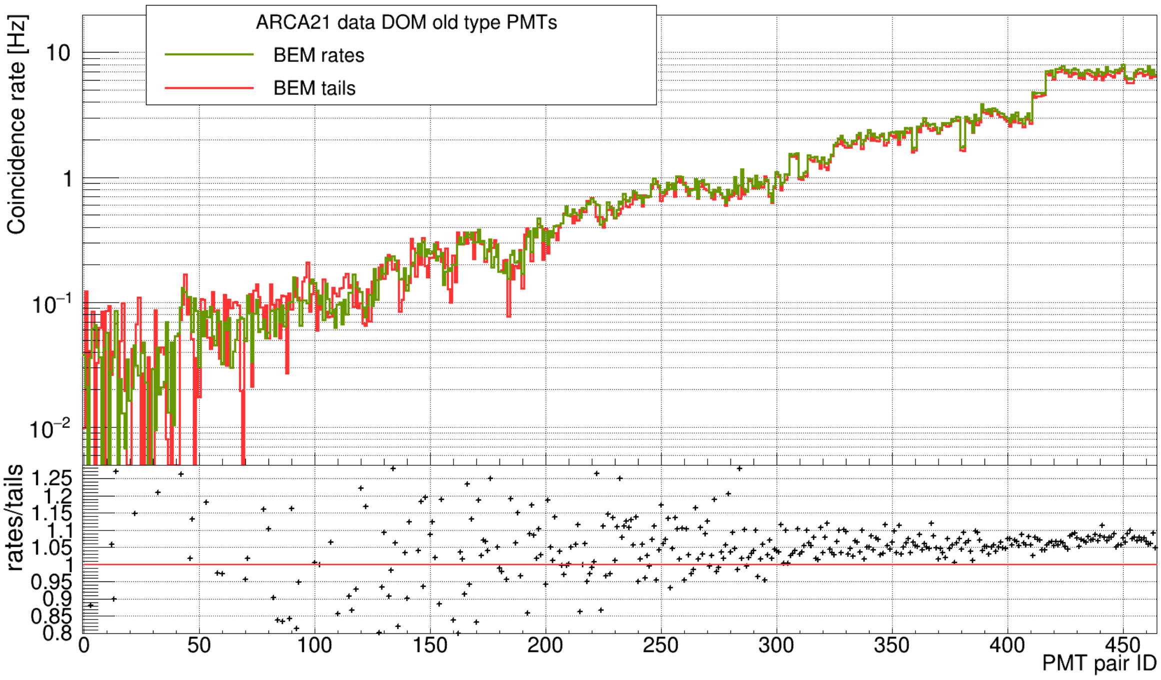

(a)

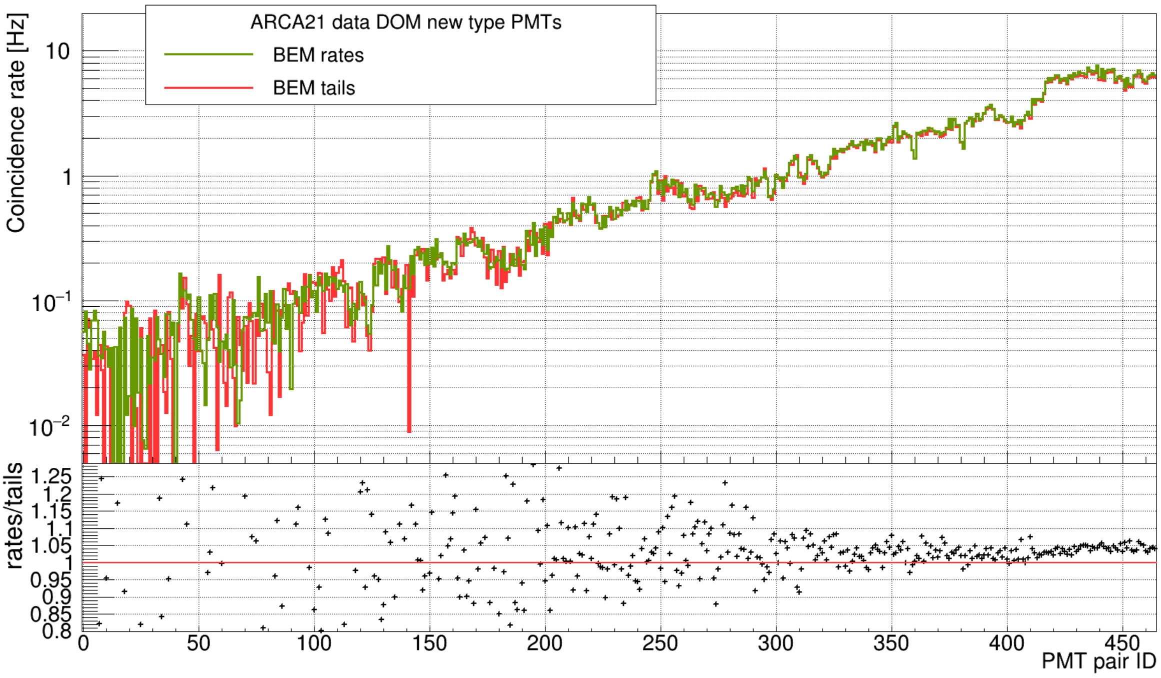

(b)

Figure 3.31: The performance of the background estimation methods *rates* and *tails* for the data measured with the DOMs deployed in seawater. Coincidence rates and their ratio are given for all PMT pairs in the DOM sorted according to the opening angle from the highest to the lowest with increasing PMT pair ID. a) DOM with older type of the PMTs. b) DOM with newer design of KM3NeT PMTs.

isotopes contained in the DOM glass and seawater estimated from MC simulations are given. For all PMT pairs the contribution from ^{40}K in water is dominating. For the

PMT pairs with the smallest opening angles, the second biggest contribution is from ^{40}K in glass. With increasing opening angle, ^{238}U in water starts to dominate over ^{40}K in glass. For the PMT pairs with the largest opening angles contribution from ^{238}U in glass prevails ^{238}U in water. The fact, that the largest contribution to the coincidence rates is from ^{40}K in water is compatible with the smaller impact of the change of the glass radioactivity for coincidence rates estimation for seawater simulations (Fig. 3.29) than in the case of simulations of air Modane measurements (Fig. 3.10). However, for the PMT pairs with the smallest opening angles, the contribution from the ^{40}K decays in glass is at the same order as the contribution from the ^{40}K decays in seawater. For the PMT pairs with larger opening angles, the difference between the contribution from the ^{40}K decays in seawater and the highest contributor from glass is higher than one order. Behavior observed in Fig. 3.32 is compatible with the fact, that the change in the final coincidence rates for MC simulations of the DOM placed in seawater with NRPI measured mass-specific activities for the radioactive isotopes contained in the DOM glass and default values of these activities is the most significant for the PMT pairs with the smallest opening angles, see Fig. 3.29.

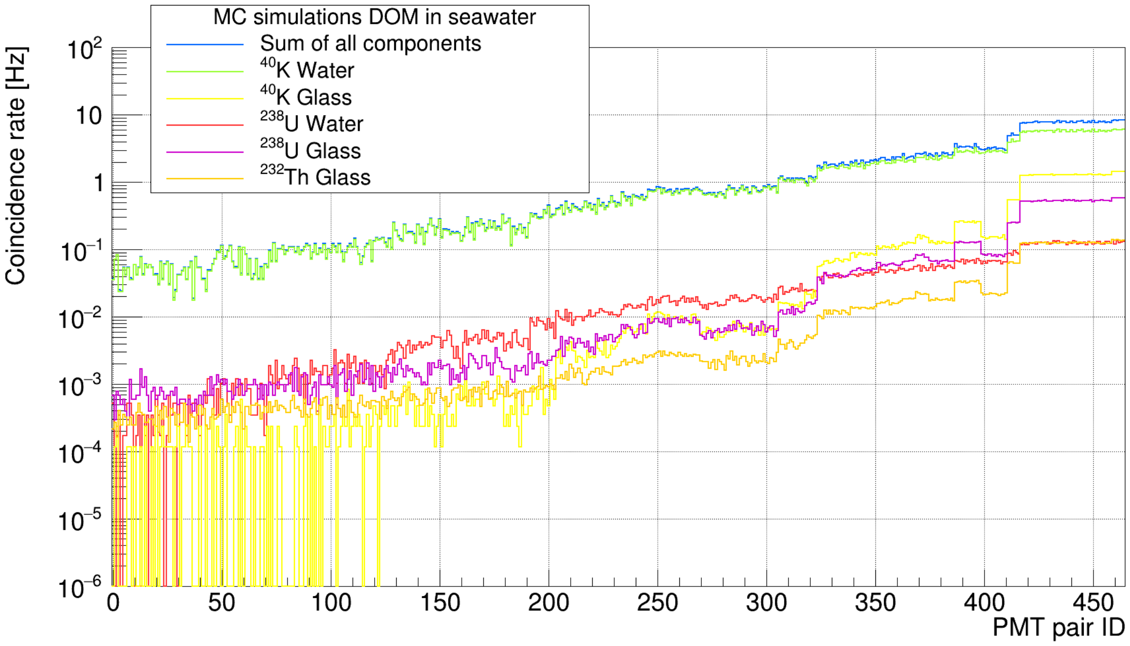

Figure 3.32: Distribution of the coincidence rates for all possible PMT pairs in the DOM for MC simulations of the DOM in the seawater. Sum of the contributions to the coincidence rates from all simulated decays of radioactive isotopes – ^{40}K and ^{238}U contained in seawater, and ^{40}K, ^{232}Th, and ^{238}U contained in the DOM glass together with the individual contributions are shown. PMT pairs are arranged according to the angle between PMTs in the pair from the highest to the lowest.

In Fig. 3.33, the comparison between data and MC simulations of coincidence rates for all PMT pairs in the DOM is given. Fig. 3.33a shows this comparison for the DOM with old type of PMTs. Fig. 3.33b corresponds to the DOM with new type of PMTs. These figures show that the data and MC simulations agreement is DOM dependent. The ratio between coincidence rates estimation from data and MC simulations can differ according to the DOM position on the DU, time of the deployment (sedimentation) or type of PMTs installed in the DOM. Therefore, for the proper analysis of the comparison between data and MC simulations, larger statistics have to be taken into account. For selected DOM with old type of PMTs, for the PMT pairs with the smallest opening angles the difference between data and MC simulations is under ~ 20 %, for the selected DOM with new type of PMTs it is under ~ 30 %. Larger relative discrepancy for the DOM with new type of PMTs can by partly caused by the fact that in the MC simulations that were used in this study old type PMTs are used. To study this effect, it is essential to study comparison between data and MC simulations for larger number of the DOMs with old and new types of PMTs and analyze the influence of the change of the type of the PMTs from the old to the new design on MC simulations. Moreover, the discrepancy between data and MC simulations in these measurements might be partially caused by the improper simulation of light propagation in glass as was indicated in the result from the Modane laboratory measurements.

The interesting aspect of the coincidence rates distributions in Fig. 3.33 is that for the majority of the PMT pairs with the smallest opening angles, MC simulations give higher estimations of coincidence rates than the coincidence rates estimated from data for the selected DOMs. However, it is important to analyze this behavior for more DOMs to estimate the significance of this effect. The reason of this behavior can be partly explained by the fact that in the MC simulations used in this study, nominal values of PMT efficiencies are applied.

The preliminary study of the effect of the updated efficiencies for PMTs in MC simulations is given in following paragraphs. PMT efficiencies can be estimated from the fit of the hit time difference distributions for PMT pairs for data with Eq. 2.3. With new values of the mass-specific activities measured in the NRPI, it is possible to update the model used in this fit. Hence, in this study, the parameters in the Eq. 2.4, updated using MC simulations with the NRPI measured values of the mass-specific activities of the radioactive isotopes contained in the DOM glass were used. To obtain the PMT efficiencies corresponding to the efficiencies of the PMTs deployed in the sea, the data were fitted with the updated function from Eq. 2.3. As the first approach, the average of the efficiencies of 31 PMTs for the selected DOMs was applied for all PMTs in these DOMs. The change in the MC simulations with updated PMT efficiencies is given in Fig. 3.34.

Since the same value of PMT efficiency was applied for all PMTs in the DOM,

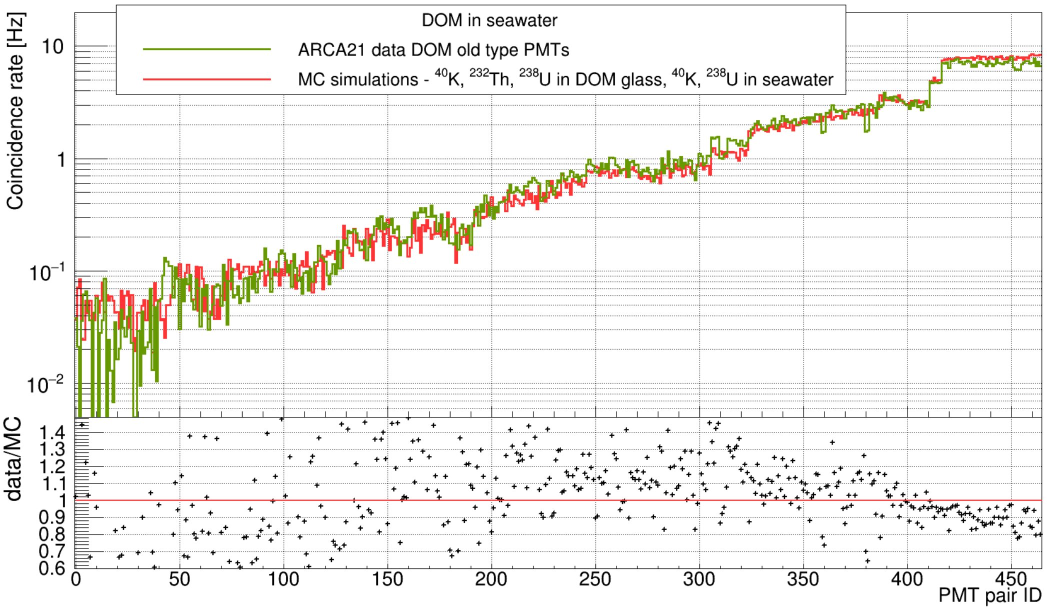

(a)

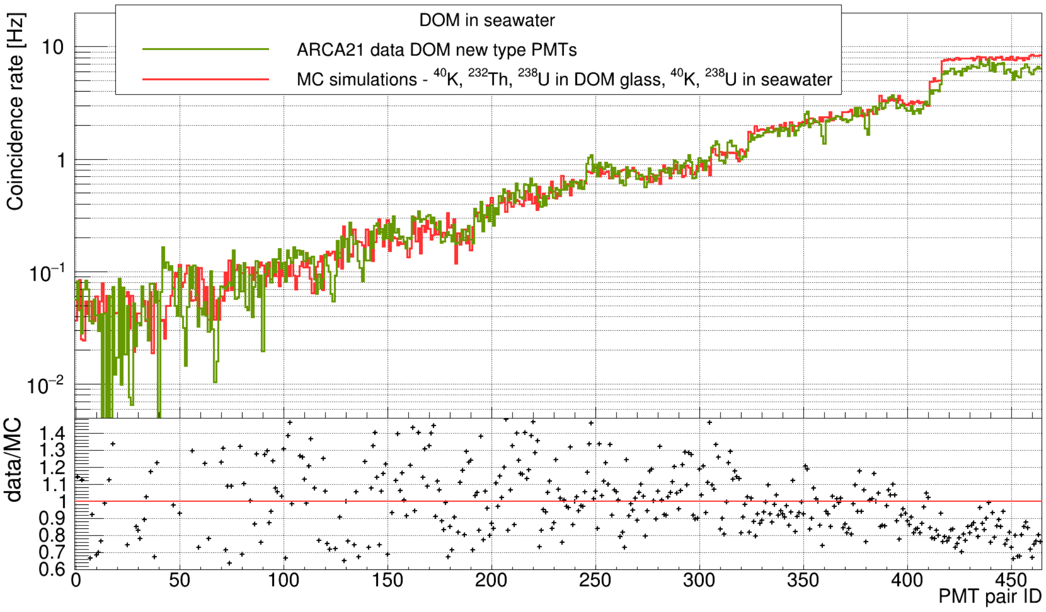

(b)

Figure 3.33: The comparison of the coincidence rates estimation from data and MC simulations for seawater measurements given for all PMT pairs in the DOM. The smallest PMT pair IDs correspond to the the highest opening angles between PMTs in the pair, the highest IDs are assigned to the pairs with the smallest opening angles. Ratio of coincidence rates obtained from data to the coincidence rates from MC simulations is shown with black crosses. a) Data collected with the DOM with PMTs with older design. b) Data measured with the DOM with new type of PMTs installed.

the change in the coincidence rates estimations with updated values for efficiencies of PMTs was evaluated using sum of the coincidence rates estimations for all PMT pairs in the DOM. The ratio between this integral for data and MC simulations for the selected DOM with PMTs with old design is approximately 0.972, for the selected DOM with new design PMTs installed ~ 0.881. After update of the PMT efficiencies this ratio is about 0.998 for the DOM with PMTs with older design and 0.988 for the DOM with PMTs with new design. Conclusively, the agreement between coincidence rates estimation from data and MC simulations improved with updated efficiency for PMTs in MC simulations. To obtain better data MC simulations agreement even from the point of view of the individual PMT pairs it is necessary to set efficiencies for all PMTs individually since these values vary among them.

The change of PMT efficiencies changes estimation of the detector efficiency simulation thus affecting all high level analyses. The usage of the new PMT efficiencies is expected to provide significant improvements, for example for the neutrino flux measurement.

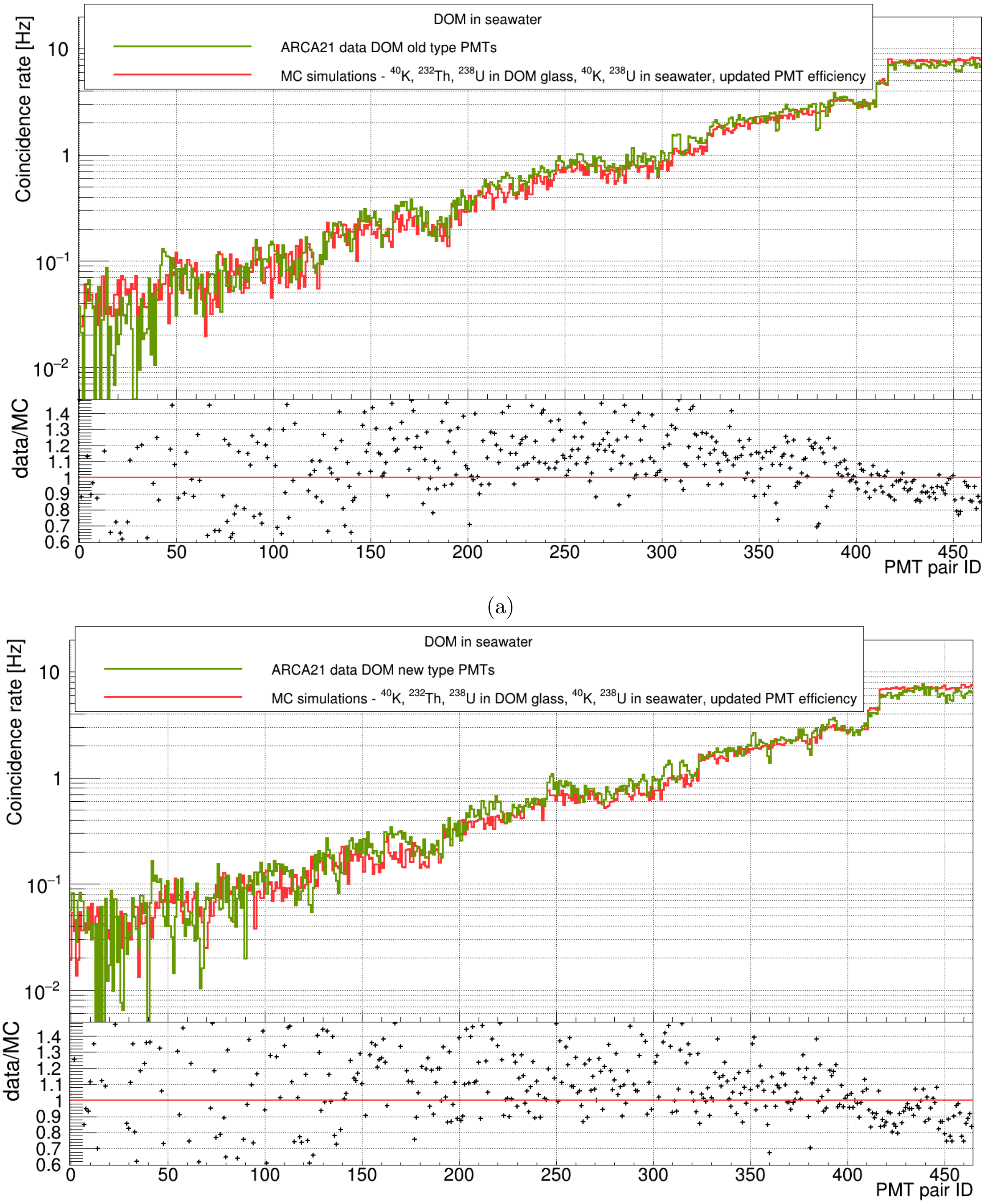

(a)

(b)

Figure 3.34: The comparison of data and MC simulations with updated efficiencies of PMTs for seawater measurements. The comparison is given as the dependence of coincidence rates on all PMT pairs in the DOM. The smallest PMT pair IDs is assigned to the the smallest opening angles between PMTs in the pair, the highest IDs are appointed to the PMT pairs with the smallest opening angles. Ratio between data and MC simulations is displayed in the lower panel with black crosses. a) Data obtained with the DOM containing PMTs with older design. b) Data collected with the DOM enclosing PMTs with new design.

Chapter 4

Ambient light in Lake Baikal

The main aim of the Baikal-GVD neutrino telescope is to detect Cherenkov radiation of the charged particles that originates in neutrino interactions. Even though Baikal-GVD is constructed for the Cherenkov light registration, ambient light is also detected. It creates unavoidable background for the performed analyses, see Fig. 4.1. Therefore, the analysis of ambient light field in Lake Baikal is of great importance.

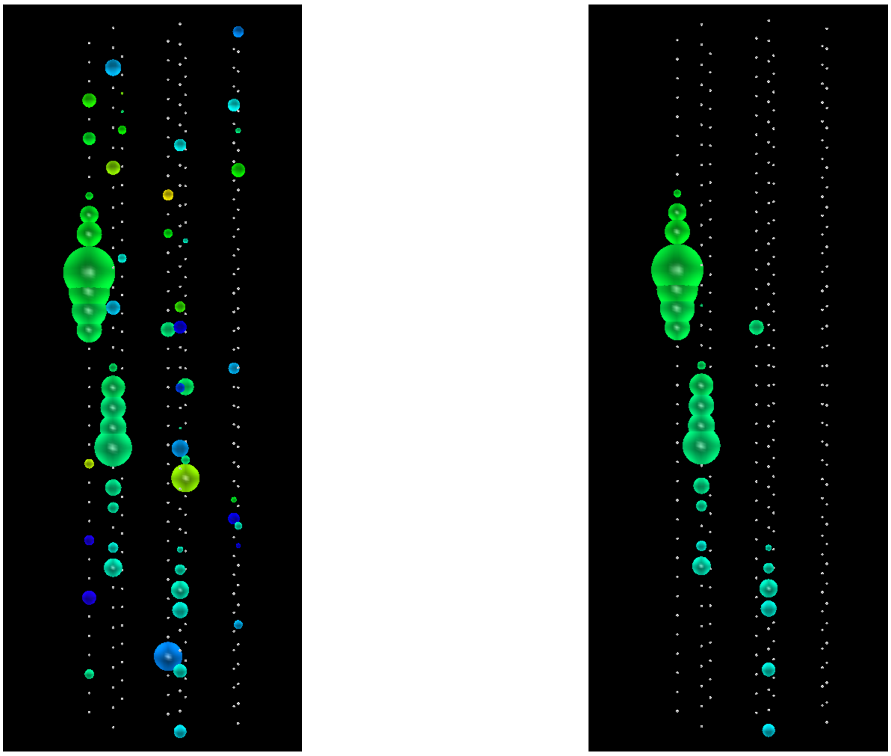
(a)

(b)

Figure 4.1: Visualization of event detected in one cluster in the Baikal-GVD. Small white dots depict OMs. The size of the sphere displays amount of charge detected on particular OM. The color of the sphere represents time of the detection (from red to green/blue). a) Visualization with noise hits. b) Visualization without noise hits.

Since Lake Baikal is a freshwater lake, the contribution to ambient light from ^{40}K is negligible. The contribution from sunlight in the depths below $\sim$ 400 m is less than contribution from water luminescence photon flux, see Fig. 4.2. In the depths below approximately 800 m is the sunlight contribution lower than one photon/(cm^{2}s) [81].

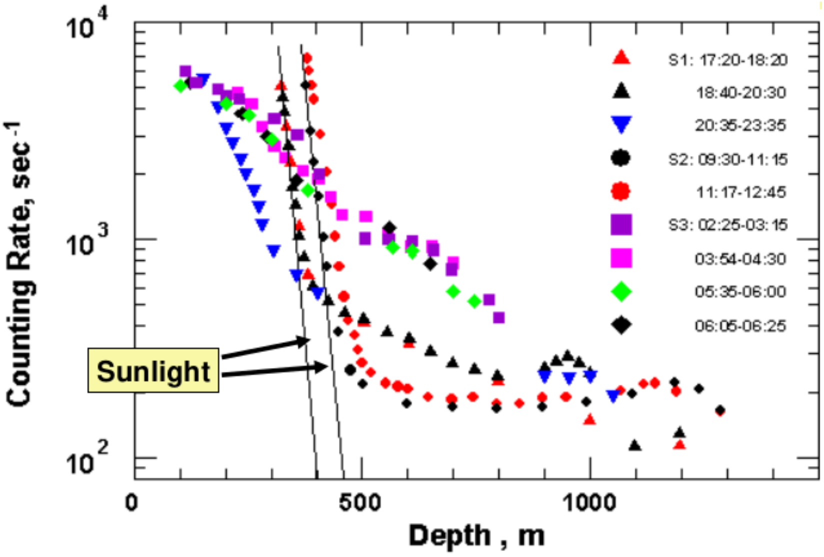

Figure 4.2: The dependence of the counting rate of photomultiplier tubes single photoelectron pulses on the depth. Taken from [81].

The ambient light in Lake Baikal is primarily associated with chemiluminescence [82]. The other contribution to background light is from dark noise of photomultiplier tubes and electronics. It was measured in laboratories in Dubna and its contribution was established to 8-12 kHz.

The analysis of ambient light in Lake Baikal is not beneficial only for the neutrino analyses but it can contribute also to earth and sea sciences and to understanding of the hydrodynamics of lakes. The data for analysis of background light were collected with the standard trigger system. The typical rate of the trigger system is 40 Hz [83]. After fulfilling the trigger condition, data from the 5 μs window are stored, see Sec. 2.1.2. For ambient light analysis, signals from the first 2 μs of the window were used, see Fig. 4.3. The PMT rates are averaged over 5 min windows, therefore, the data are acquired almost continuously.

4.1 General features of ambient light field

In general, periods of various amplitudes of noise rates are alternating. Three years time evolution of the noise rates for OMs deployed at different depths are depicted in Fig. 4.4.

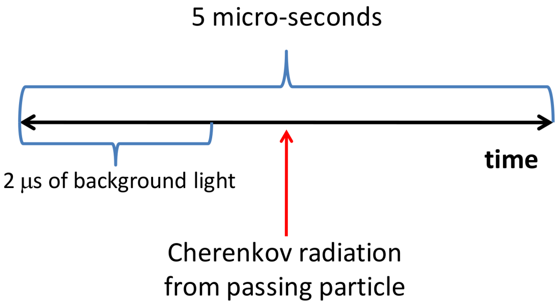

Figure 4.3: Illustration of the 5 μs window of the FADC buffer.

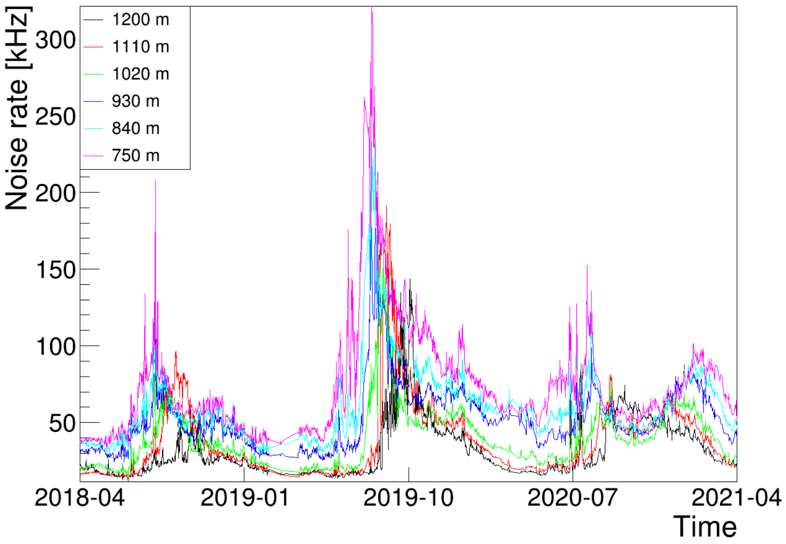

Figure 4.4: Time evolution of the noise rates during three years 2018-2020. The noise rates for OMs installed at different depths are displayed.

One year period can be in general divided into three noise periods. In the spring and early summer there is stable noise rates period. Usually, high noise rates period takes place in summer and so called calm noise rates period in the autumn and winter, see Fig. 4.5.

4.2 Charge distribution of ambient light field

The charge distribution of noise pulses for different noise rates time periods is displayed in Fig. 4.6. From comparison of the distributions in high and low noise rates periods follows that the charge distribution of the noise pulses remains the same in different noise rates periods.

The analysis of noise pulses was performed with a threshold set on one fifth of a

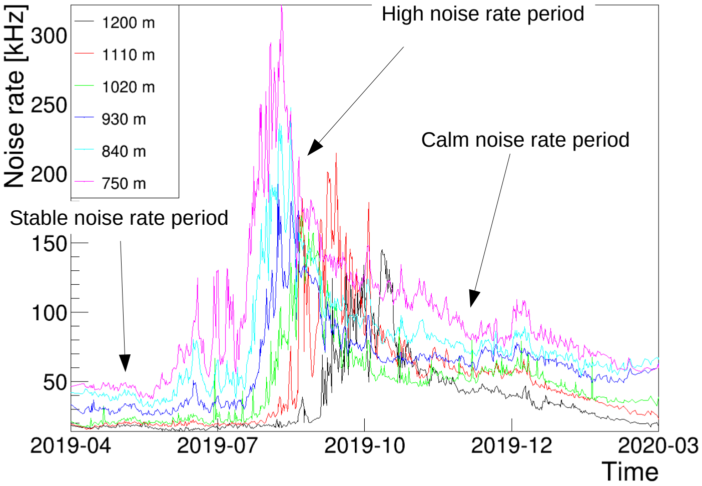

Figure 4.5: General features of ambient light field. The noise rates time evolution during year 2019 for OMs installed at different is shown.

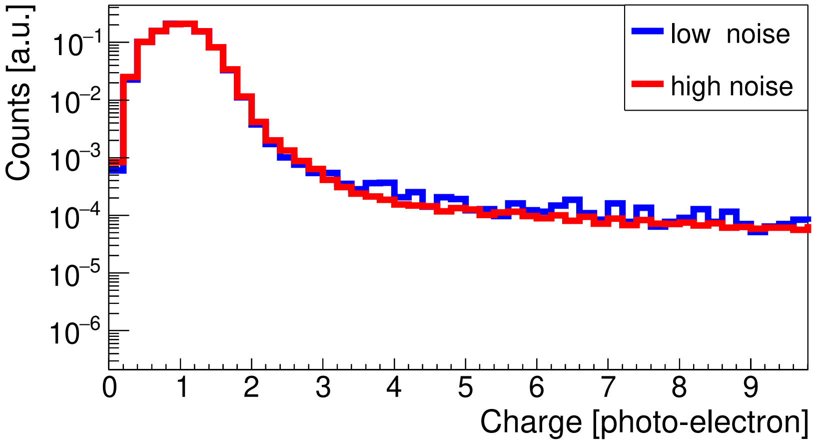

Figure 4.6: Charge distribution of noise pulses for high and low noise rates periods. Taken from [84].

single photo-electron charge. The threshold set at this level ensures significant suppression of the dark noise of PMTs and electronics. The majority of the noise pulses have charge approximately one photo-electron. By setting threshold on single photo-electron the noise rates are reduced by a factor of two [84].

4.3 High noise rates time periods

In Fig. 4.7, the time evolution of noise rates in year 2018 is shown. The highly optically active layer propagating from the top to the bottom of the lake can be observed. The vertical velocity of this layer can be obtained by comparing of maximal values of the noise rates for OMs installed at different depths. In August 2018 this velocity was approximately evaluated as 16 m/day, in September 2018 it reached ∼ 5 m/day.

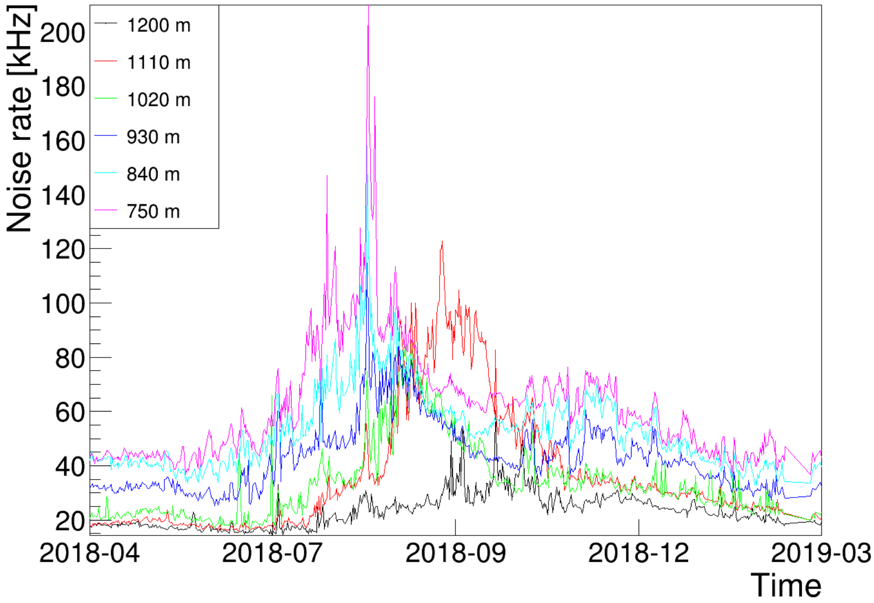

(a)

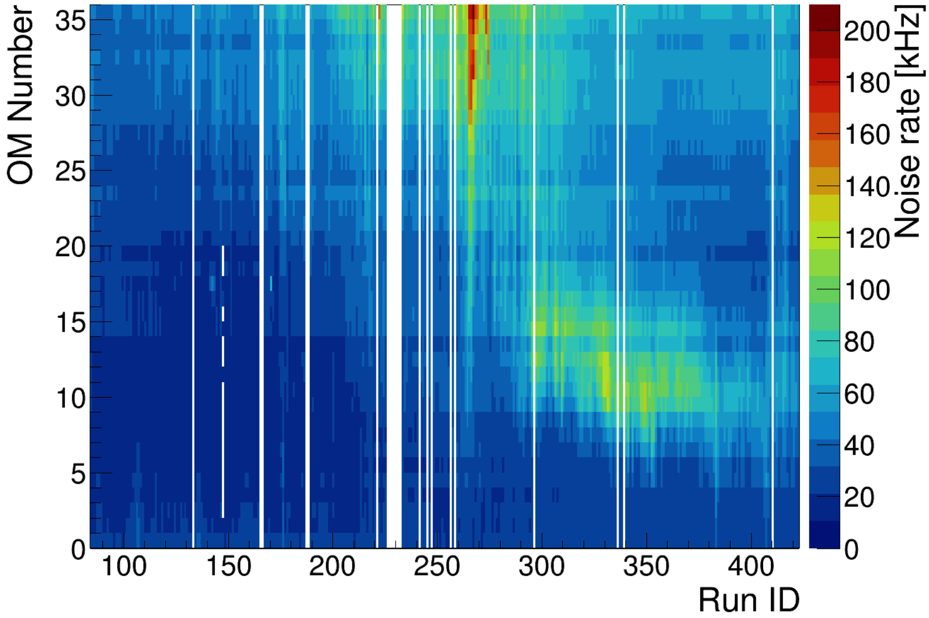

(b)

Figure 4.7: a) Time evolution of the noise rates in year 2018 for OMs installed at different depths. b) The dependence of noise rates in year 2018 on Run ID and OM number. OM number 0 (35) marks OM deployed at the bottom (top) of the string. Run ID corresponds to the time of the measurements.

The dependence of noise rates on time for year 2020 is displayed in Fig. 4.8. For the first time, highly optically active layer was observed to move upwards. In January 2021 the vertical velocity in the upwards direction reached ~ 28 m/day.

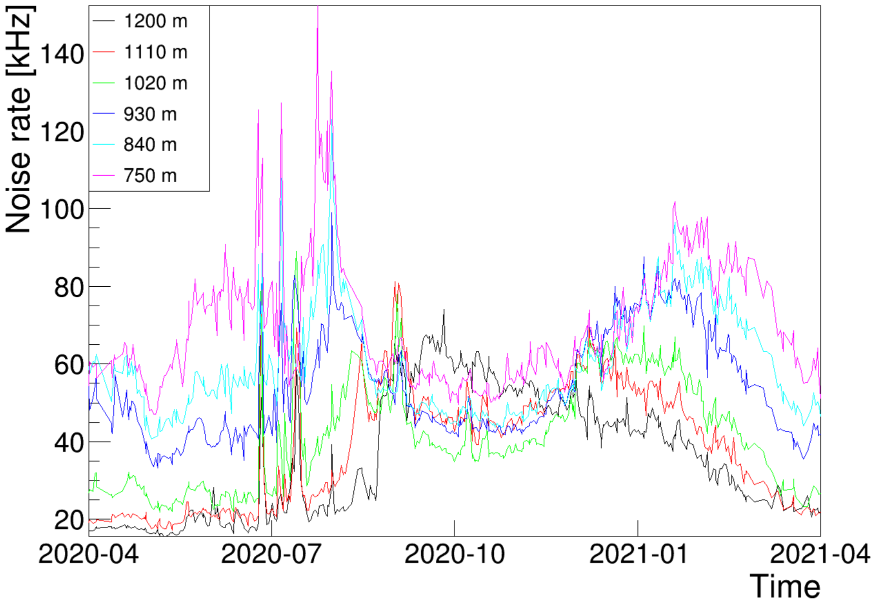

(a)

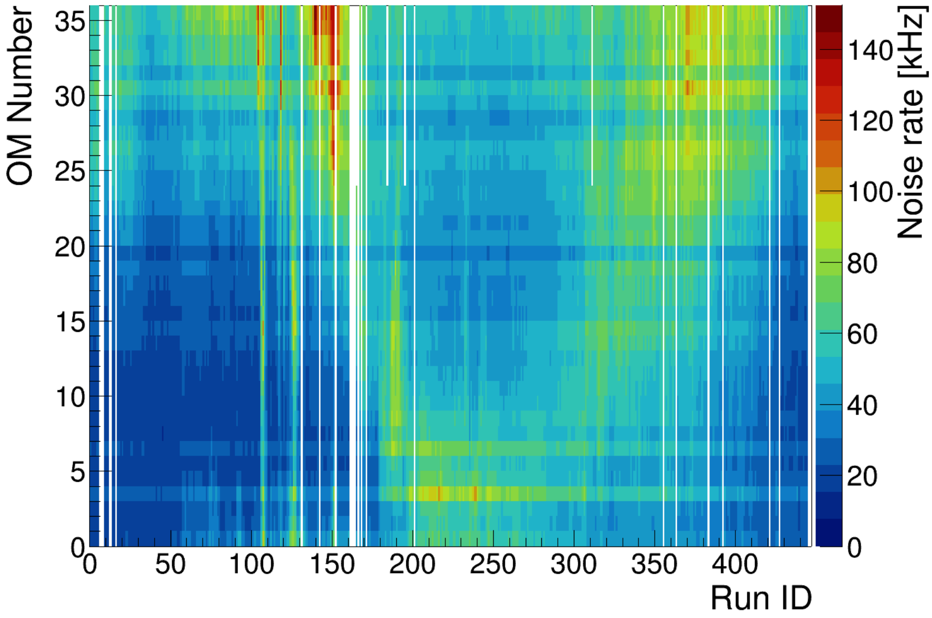

(b)

Figure 4.8: a) Noise rates time evolution in year 2020 for OMs deployed at different depths. b) The distribution of noise rates in year 2020 plotted with respected to Run ID and OM number. OM number 0 (35) corresponds to the OM installed at the bottom (top) of the string. Run ID correlates with the time of the measurements.

During the high noise rates time periods, the sharp changes of noise rates can be observed, see Fig. 4.9. The time duration of these changes can reach from several hours to a few days.

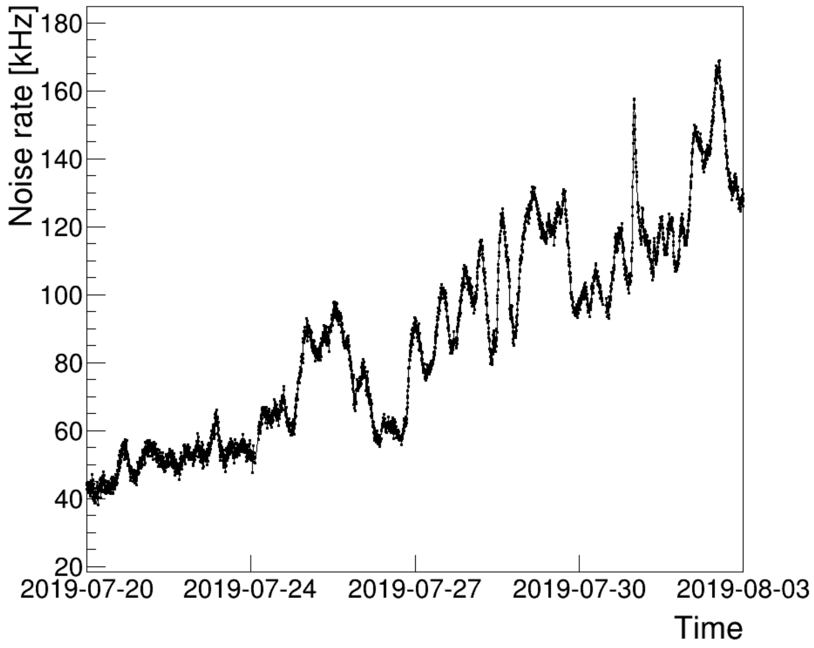

(a)

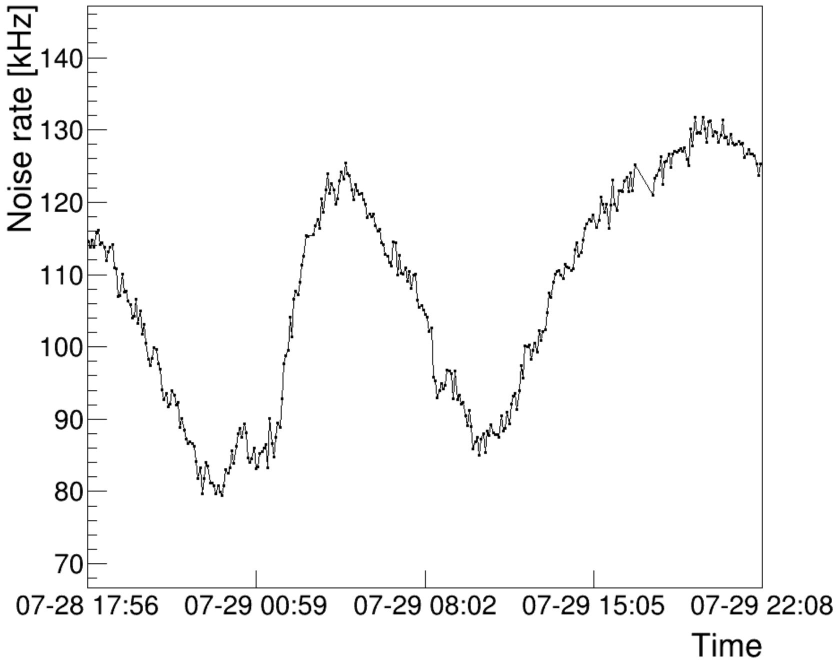

(b)

Figure 4.9: a,b) Time evolution of noise rates for OM located at the depth of 870 m.

4.4 Calm noise rates time periods

In the calm noise rates periods (autumn-winter) the regular changes in noise rates can be seen, see Fig. 4.10. The period of these variations is several hours.

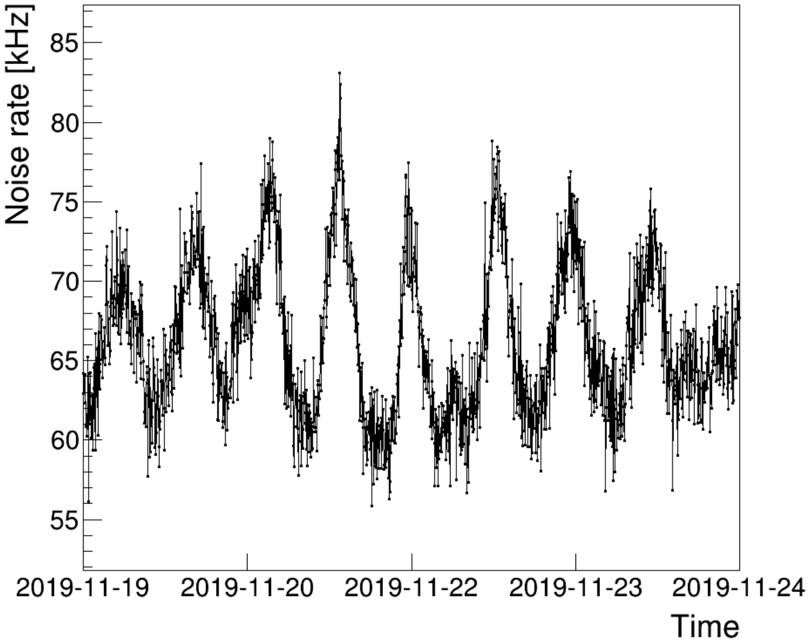

Figure 4.10: The dependence of noise rates on time for particular OM installed at the depth of 975 m.

4.5 Stable noise rates time periods

During the periods of stable noise activity, there is exponential dependence of noise rates on depth:

$$f(H) \approx e^{-\frac{H}{H_0}}, \tag{4.1}$$

where $f(H)$ means average noise rates, H is depth in meters, and H_0 is parameter obtained from the fit of the data [81, 85]. In Fig. 4.11, the dependence of average noise rates on depth is shown. The values of average noise rates were calculated by averaging of noise rates for all eight OMs located at the same depth in one cluster. From the fit of distributions displayed in Fig. 4.11 with Eq. 4.1 the value of parameter H_0 equals to 461 m, 312 m, and 292 m for years 2018, 2019, and 2020, respectively.

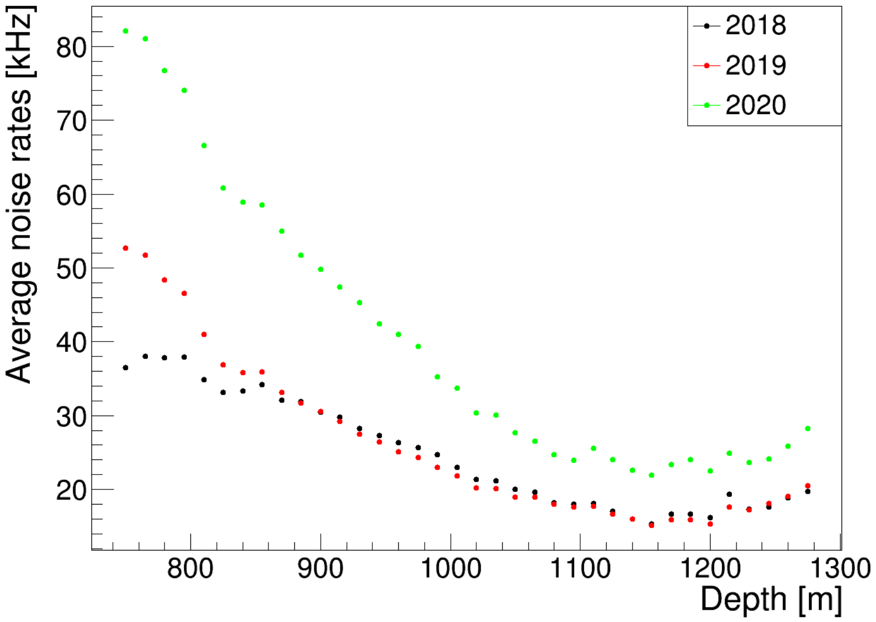

Figure 4.11: Distribution of average noise rates with respect to the depth.

Chapter 5

Double cascade reconstruction in Baikal-GVD

High-energy astrophysical neutrinos were observed for the first time by the IceCube experiment in year 2013 [17]. One of the most promising methods of the astrophysical neutrinos identification is the detection of the high-energy ν_τ, because the probability of the production of high-energy ν_τ in the atmosphere is negligible [12]. ν_τ can also be created in oscillation of atmospheric ν_e or ν_μ. Oscillation length is defined as [86]:

$$L_{osc} \simeq 2.47 \frac{E}{\Delta m^2} [\mathrm{m}], \tag{5.1}$$

where E denotes the energy of neutrino given in MeV and Δm^2 represents the squared difference between the masses of oscillating neutrinos in eV^2. Neutrino oscillations are negligible if the oscillation length is significantly larger than the distance which neutrino travels before reaching detector. Oscillation length for neutrinos with energy at the level of TeV and $\Delta m^2 \sim 2.4 \cdot 10^{-3}$ eV^2 [21] is approximately 10^6 km while the length of atmospheric neutrinos trajectory is at the level 10^4 km. Hence, the probability of the oscillation of atmospheric ν_e or ν_μ to ν_τ is negligible for high-energy neutrinos considered in this thesis. Therefore, the identification of the high-energy ν_τ event in the data would be a strong hint of the detection of the neutrino with the astrophysical origin.

In the CC interaction of ν_τ, τ lepton is created. Subsequently, it decays either into hadrons or leptons [21]. There are two types of light signatures created by CC interaction of ν_τ according to the τ decay mode:

- τ decays into $\mu \Rightarrow$ *single cascade + μ track* (branching ratio $\sim$ 17.4 %),
- τ decays into e or hadrons $\Rightarrow$ *double cascade* (branching ratio $\sim$ 82.6 %).

Illustrations of these two signatures are shown in Fig. 5.1.

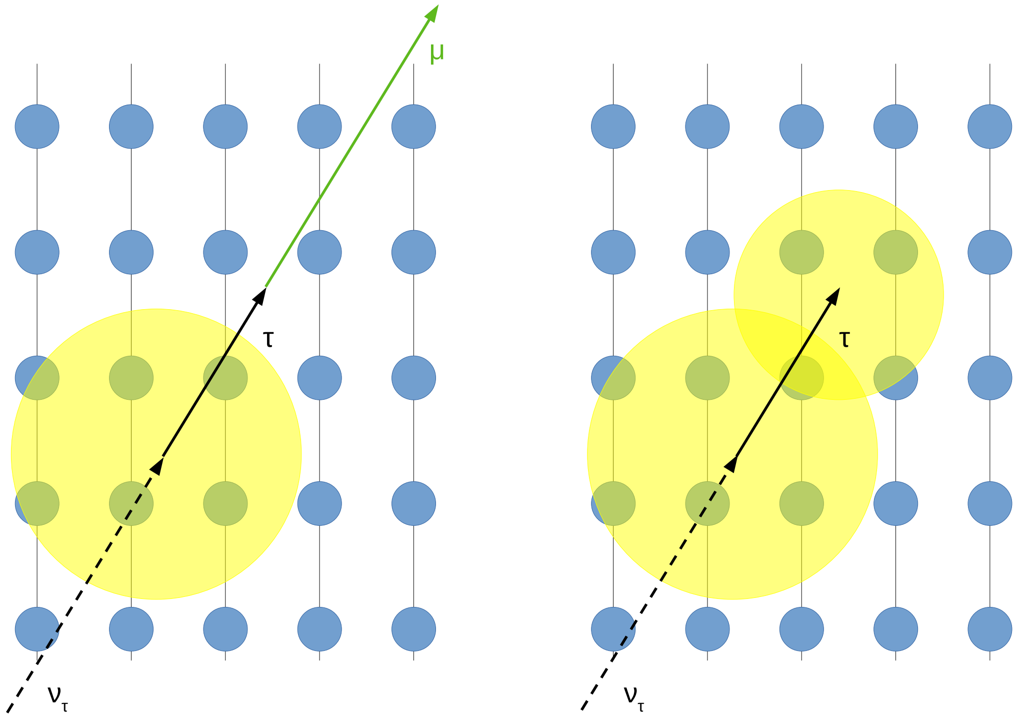

(a)

(b)

Figure 5.1: Illustration of two signatures that can originate in the charged current interaction of ν_τ. a) Tau lepton decays into muon, which results in single cascade signature with muon track. b) Tau lepton decays into electron or hadrons, this process produces double cascade signature.

The reconstruction of double cascade signature is of great importance for the registration of astrophysical ν_τ in the Baikal-GVD detector. In the following chapter the development of the very first double cascade reconstruction algorithm for the Baikal-GVD neutrino telescope is described.

5.1 Monte Carlo simulations of ν_τ double cascades

For development of the double cascade reconstruction algorithm, Monte Carlo simulations of ν_τ double cascades from the All Neutrino Interactions Simulation (ANIS) [87] were used. The ANIS is a neutrino event generator capable of simulating CC and NC neutrino interactions including the Glashow resonance. The input parameters that needed to be specified to obtain simulations of required type of ν interactions are energy range, spectral index of energy distribution, flavor of interacting ν and $\bar{\nu}$, range of zenith angle, and the size of the detection volume.

In the case of the ν_τ interactions, the events are simulated in energy range from 10 TeV to 10 PeV according to distribution E^{-1}. There is a specific MC weight assigned to each event in order to obtain the expected astrophysical flux given by the following formula [88]:

$$\phi(E) = 2 \cdot 10^{-8} \cdot \left(\frac{E}{\mathrm{GeV}}\right)^{-2} [\mathrm{GeV}^{-1}\mathrm{s}^{-1}\mathrm{sr}^{-1}\mathrm{cm}^{-2}]. \tag{5.2}$$

This flux corresponds to single flavor neutrino flux and equal ratio of neutrinos and antineutrinos.

The direction of incoming ν_τ is simulated uniformly over full 4π angle. The effect of the neutrino propagation through the Earth is taken into account by means of Earth's Preliminary Model [89]. The events are simulated in the cylinder with dimensions adjusted to properly cover cylindrical shape of the Baikal-GVD cluster. The radius of this cylinder is 320 m and its height is 820 m. During simulations this cylinder is rotating to cover whole solid angle in order to generate the direction of the events over full 4π angle.

The events simulated with ANIS were subsequently processed with algorithm simulating detector response developed by the Baikal-GVD Collaboration. For the development of the double cascade reconstruction algorithm only single cluster events were used. The MC trigger condition is fulfilled if at least one of the cascades produces enough light to generate response on at least 4 OMs located on at least 3 strings. Given this trigger condition and using flux defined in Eq. 5.2, approximately 0.6662 ν_τ double cascade events (CC interaction of ν_τ, τ lepton decays into electron or hadrons) are expected to be registered in the Baikal-GVD per year per one cluster. In the detector response algorithm, the cascades are simulated separately but afterwards the pulses detected in time window of 50 ns registered on one OM are merged together, and in further processing are considered as one pulse. The reason is that in the experimental data, there is high probability that pulses detected in such time window on one OM would be overlapped. There is also additionally generated noise with constant frequency of 50 kHz.

There are two types of ν_τ double cascade events in Baikal-GVD:

- *single-cascade-like* – two cascades are very close to each other and hence they are overlapped so the resulting signature is single cascade or only one cascade is in the sensitive volume of the detector,
- *double-cascade-like* – both cascades are in the sensitive volume of the detector and they are separated by the sufficient distance so they are not overlapped.

The aim of the first double cascade reconstruction algorithm in Baikal-GVD is to reconstruct double cascade events in which cascades are not completely overlapped – double-cascade-like events. It is caused by the fact that this version of the reconstruction algorithm does not study events on the pulse shape level. The pulses from overlapped cascades are more likely to be merged and without the information about shape of the pulse, the origin of these pulses can not be determined correctly. Conclusively, the merged pulse is assigned only to the one of the cascades and the information of its double cascade origin is lost. Therefore, for development of the double cascade reconstruction algorithm only a subset of simulated ν_τ double cascade events was used. An event is tagged as double-cascade-like when it fulfills set of conditions:

- both cascade vertices are simulated within the cluster volume + 40 m,
- the distance between them is larger than 10 m,
- the energy of interacting ν_τ is higher than 100 TeV,
- each of the cascades produces response on at least 10 OMs.

The expected rate of events fulfilling these requirements is around 0.0405 per year per cluster. It is approximately 6.08 % from all events that fulfilled MC trigger condition. This rate is considered as the reference rate for the calculations of efficiency of the double cascade reconstruction algorithm. The distribution of the energy of interacting ν_τ and the distribution of the simulated distances between cascade vertices for the triggered double cascade events and selected double-cascade-like events are shown in Fig. 5.2.

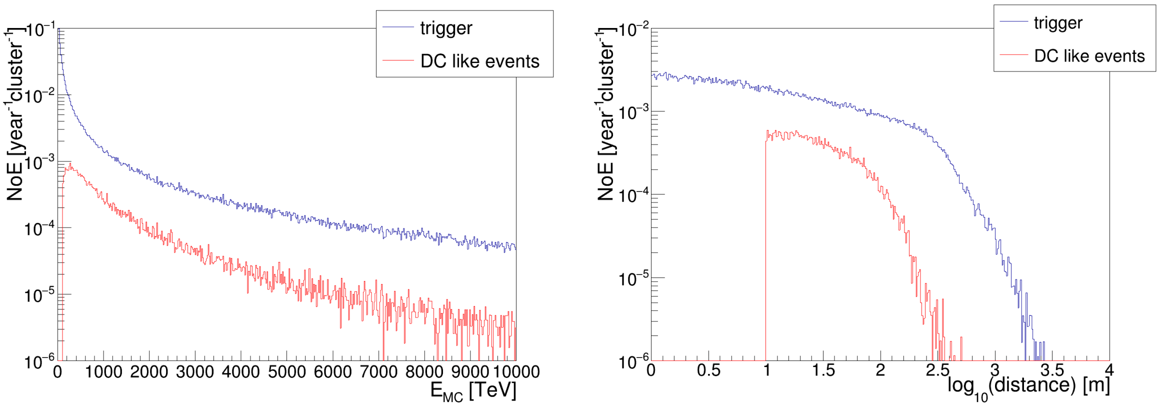

(a)

(b)

Figure 5.2: a) Energy of interacting ν_τ for double cascade events that passed MC trigger condition (blue) and for selected double-cascade-like events (red). b) Distance between ν_τ and τ cascade vertices for events that passed MC trigger condition (blue) and for selected double-cascade-like events (red).

5.2 Double cascade reconstruction algorithm

The main aim of the double cascade reconstruction algorithm is to reconstruct positions, energies and direction of the two cascades in case of the double cascade event.

Input to this algorithm is set of pulses (hits) detected on the OMs. Pulses are represented by their charges, times of the detection, and IDs of the OMs which detected them. Since in the energy range considered in this work ν_τ is relativistic, both cascades have the same direction, therefore, there is no need to define directions for the cascades separately. This effect was studied using ANIS MC simulations, and the deviation from the prediction that cascade directions are parallel is negligible.

Basically, there are three types of pulses in MC simulations of the ν_τ double cascade events – pulses produced by ν_τ cascade, pulses originated in τ cascade, and noise hits. The reconstruction algorithm consists of four main parts:

- *hit selection* – selection of pulses originating from both cascades;
- *hit sorting* – dividing the set of hits into two subsets according to hits origin - either ν_τ or τ cascade;
- *position and time reconstruction*
- *energy reconstruction*

The flowchart for the double cascade reconstruction is shown in Fig. 5.3. Since in the hit sorting step of the algorithm there is no control over decision which cascade pulses (belonging either to ν_τ or τ cascade) are selected first, the new tags for cascades were introduced. In the description of the algorithm, the cascade whose pulses are selected first in the hits sorting procedure is defined as cascade A. The remaining cascade is tagged as cascade B.

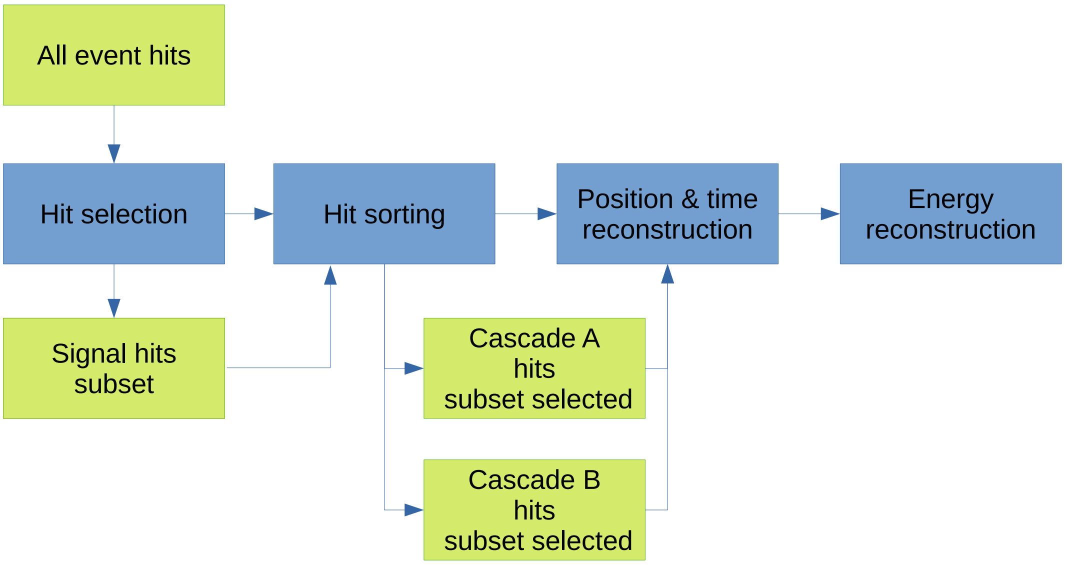

Figure 5.3: Simplified flowchart of the double cascade reconstruction algorithm.

As a baseline for development of the first double cascade reconstruction algorithm in the Baikal-GVD neutrino telescope, single cascade reconstruction algorithms described in [90, 91] were used. In the following sections, description of the individual steps of the double cascade reconstruction algorithm is given together with comparison of the performance of the first and the second version of this reconstruction method. The second version is an update to the first one. Both versions were developed as a part of this PhD work.

5.2.1 Hit selection – Causality filter

The first step of the double cascade reconstruction algorithm is to suppress noise hits and select hits that were produced by cascades.

Hits need to have higher charge than 1.5 photoelectrons and fulfill two conditions to be selected for the reconstruction of double cascade event. The first condition is causality criterion. Pulses are firstly sorted according to their charge. Hit with the highest charge is assumed to be detected by the OM that is the closest to the either one of cascade vertices or this OM can lie between them and register merged pulse – pulse composed from hits from the both cascades detected in the specific time window. This pulse is tagged as a reference pulse. Every other hit is then compared with this reference pulse, namely, whether it fulfills a condition:

$$\mid T^{ref} - T_i^{meas} \mid < d_i/v + \delta t, \tag{5.3}$$

where T^{ref} is the time of the detection of the reference pulse, T_i^{meas} is the detection time of the studied pulse, d_i is the distance between OMs on which these pulses were registered and v is the speed of light in water. Parameter δt determines stringency of the causality condition.

For more effective suppression of the noise pulses, there is an additional criterion on neighboring OMs [90]. As a result, the pulse is tagged as a signal pulse if it passed causality condition and if at least one of the neighboring OMs – two upper and two lower OMs, detected hit in a required time window (typically at the level of 100 ns).

The selected subset of hits passes hit selection procedure and the event is accepted for further reconstruction, only if the selected subset of hits contains at least 6 hits detected on at least 3 strings. Otherwise, the event is rejected. This requirement on the spatial distribution of the hits is necessary for non-ambiguous reconstruction of cascade vertices in the following steps of the algorithm.

The mean efficiency of signal pulse selection, percentage of cascade pulses that passed criteria of causality filter in all cascade pulses, is approximately 79.4 %. The mean purity of signal pulse selection, i.e. percentage of chosen pulses created by cascades in all chosen pulses in hit selection procedure is $\sim$ 99.35 %.

Update of Hit selection

The causality filter is designed to select all signal pulses from both cascades and reject noise hits. However, in the first version of the reconstruction algorithm there is an asymmetry in hit selection depending on whether the reference pulse is from ν_τ cascade or τ cascade. For analysis of this effect, new variable called relative direction of hits has been established. It is defined as an angle between the MC simulated direction of the double cascade event and the vector that connects the OM that detects particular hit and the MC simulated vertex of the cascade from which this hit originates, see Fig. 5.4.

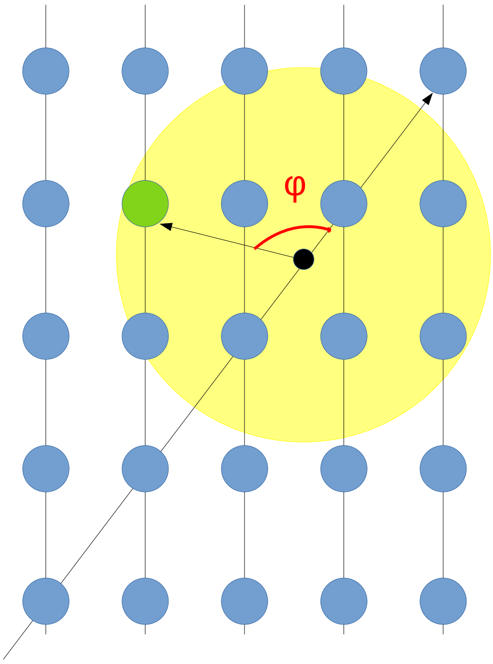

Figure 5.4: Illustration of the relative direction definition. The blue circles represent OMs. The black dot corresponds to the MC simulated cascade vertex. The green OM represents OM that registered studied pulse. The angle φ corresponds to the relative direction and is defined as an angle between MC simulated direction of the double cascade event and vector that connects MC simulated cascade vertex and OM that recorded studied pulse.

The asymmetry effect is explained in what follows. If the reference pulse originates in ν_τ cascade, there is an angular dependence in selection of pulses from τ cascade – the hits from τ cascade spreading in the opposite direction as the τ lepton are selected for reconstruction with lower efficiency, see Fig. 5.5a. In the case of the reference pulse from the τ cascade, see Fig. 5.5b no significant angular dependence for pulses originated from both cascades is observed.

To reduce the angular dependence of the hit selection in the second version of the

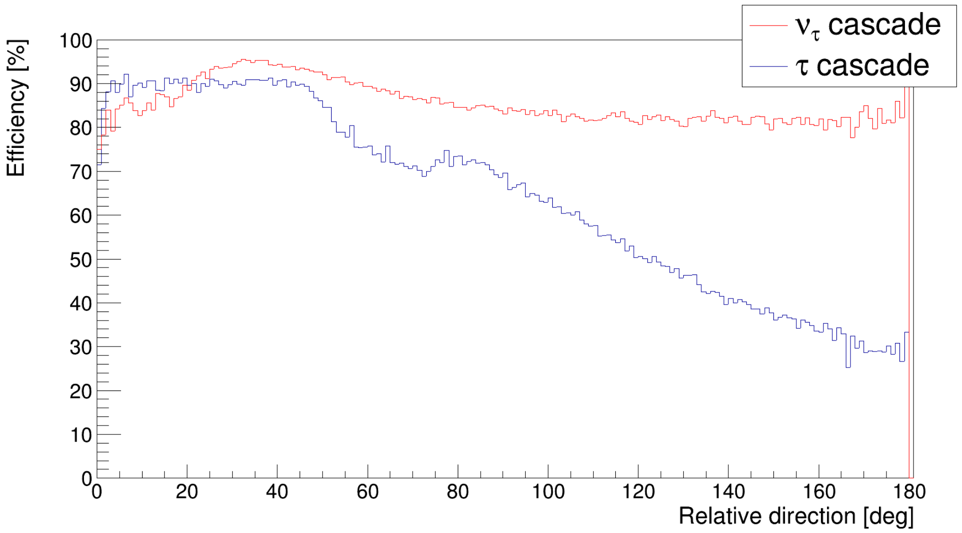

(a)

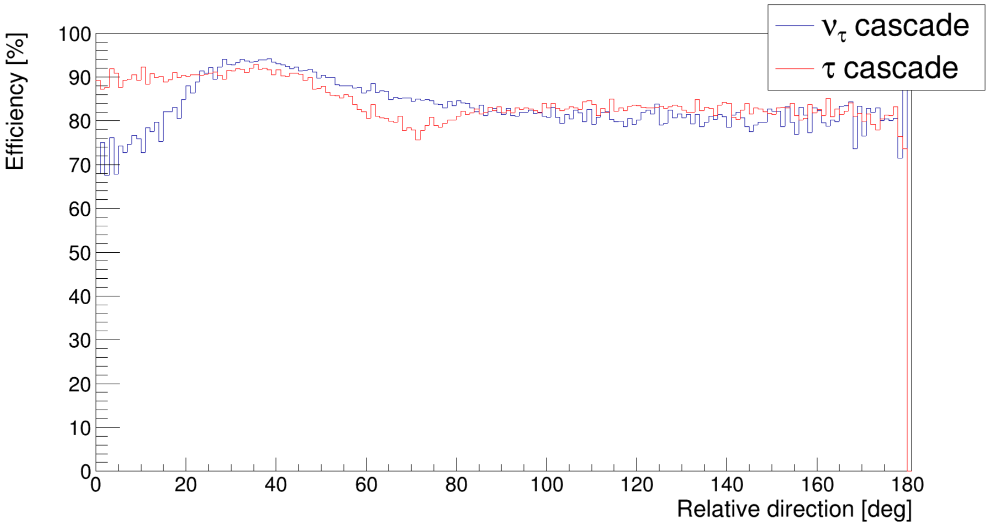

(b)

Figure 5.5: Dependence of the hit selection efficiency on the relative direction of the hits. a) The reference pulse is from ν_τ cascade. b) The reference pulse is from τ cascade.

double cascade reconstruction algorithm the condition given in Eq. 5.3 was loosened. The hit is chosen if it fulfills criterion from Eq. 5.3 with respect to the one of the 5 hits with the highest charges. It means that in the updated version of the hit selection part of the algorithm there are 5 reference pulses instead of 1, which was used in the first version of the hit selection. The updated criterion increased the mean efficiency of the hit selection to the level of 82.82 % while mean purity remains satisfactory $\sim$ 99.31 %. It also reduces the angular dependence of the hit selection, see Fig. 5.6. Possible explanation is that there is a higher chance that among the 5 pulses with highest charges there are pulses from both ν_τ and τ cascades.

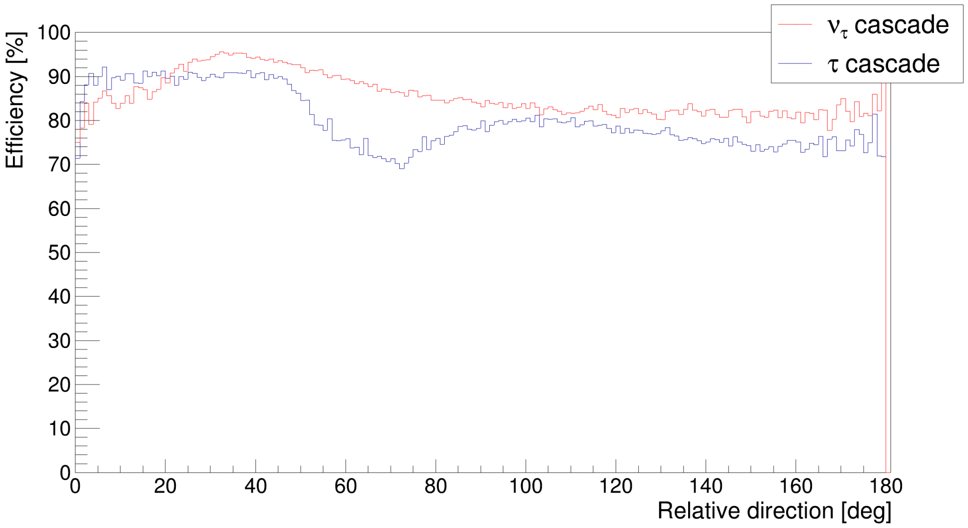

(a)

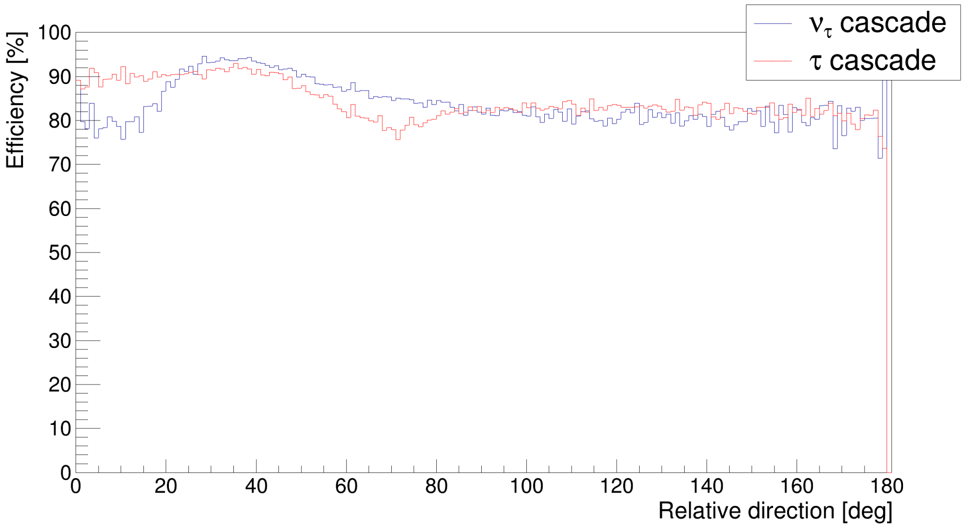

(b)

Figure 5.6: The efficiency of the hit selection with respect to the relative direction of the hits for the second version of the double cascade reconstruction algorithm. a) The reference pulse with the highest charge is from ν_τ cascade. b) The reference pulse with the highest charge is from τ cascade.

5.2.2 Hit sorting – ν_τ and τ cascade hits identification

The next step of the algorithm is to categorize the set of the selected signal pulses into two subsets, each corresponding to one of the cascades – cascade produced in the ν_τ interaction and the second cascade created in τ lepton decay. The aim of the hit sorting procedure is to estimate positions and times of both cascades ($\vec{R_1}$, T_1 and $\vec{R_2}$, T_2) and subsequently select pulses that correspond to each of them.

Selection of the pulses to the subsets is performed according to the criterion:

$$\mid T_i^{meas} - T_i^{exp}(\vec{R}, T) \mid \leq \delta T, \tag{5.4}$$

where T_i^{meas} is the time of the detection of the hit, $T_i^{exp}(\vec{R}, T)$ is the expected time of the detection of the pulse given that position of the cascade vertex is $\vec{R}$ and time of the cascade is T, and δT determines stringency of the criterion. This process is repeated twice, for selection of the pulses corresponding to ν_τ and τ cascade hence each time with different cascade vertex ($\vec{R}_1$, T_1 and $\vec{R}_2$, T_2). In this step cascades are labeled – a cascade is tagged as a cascade A when its hits are chosen to the first subset, the remaining cascade is labeled as a cascade B.

The first estimation of positions and times of the cascade vertices ($\vec{R}_1$, T_1 and $\vec{R}_2$, T_2) which are required in Eq. 5.4 for selection of pulses into cascade A and cascade B pulses subsets, are determined from the scan of the space-time with several estimations of the positions and times of the cascade vertices (($\vec{R}$, T)-space).

Each position and time estimation of the cascade vertex – points from which the ($\vec{R}$, T)-space is constructed, is obtained from the groups of the 5 pulses by solving a set of equations for the distance d_i between position of the cascade vertex and the OMs that recorded selected pulses:

$$d_i = \sqrt{(x - x_i)^2 + (y - y_i)^2 + (z - z_i)^2} = c/n(t - t_i), \tag{5.5}$$

where $\mathbf{x} = (x, y, z, t)$ is the space-time vector of the cascade vertex, $\mathbf{x}_i = (x_i, y_i, z_i, t_i)$ is the space-time vector of the OM that detected particular pulse, and c/n is speed of light in water. This method assumes that cascade is a point-like source of light in comparison with the distance among OMs. The number of pulses in the group (five) used for the cascade vertex position and time estimation was chosen because it is the lowest number of hits required to determine $\mathbf{x}$ unambiguously with this procedure [42]. These five pulses are required to be detected on different OMs and at least on three different strings. The lowest possible number of hits was selected because it increases probability that the selected group contains pulses from the one cascade only. Using pure set of pulses to obtain cascade vertex coordinates is expected to result in the relatively precise position and time estimation of the cascade vertex, see Fig 5.7a. However, if the set of five pulses consists of pulses from both cascades or noise pulses, position and time of the cascade are estimated inaccurately, see Fig. 5.7b.

It is expected that in the vicinity of the real vertices of the cascades there is an excess in the number of position and time estimations in ($\vec{R}$, T)-space. To localize these excesses for both cascade vertices, the ($\vec{R}$, T)-space scan is used. To perform the scan of the ($\vec{R}$, T)-space, the vector that stores time and position estimations was introduced. Every new position and time estimation is compared with all previous estimates and if the required number of them is in defined area of the space-time

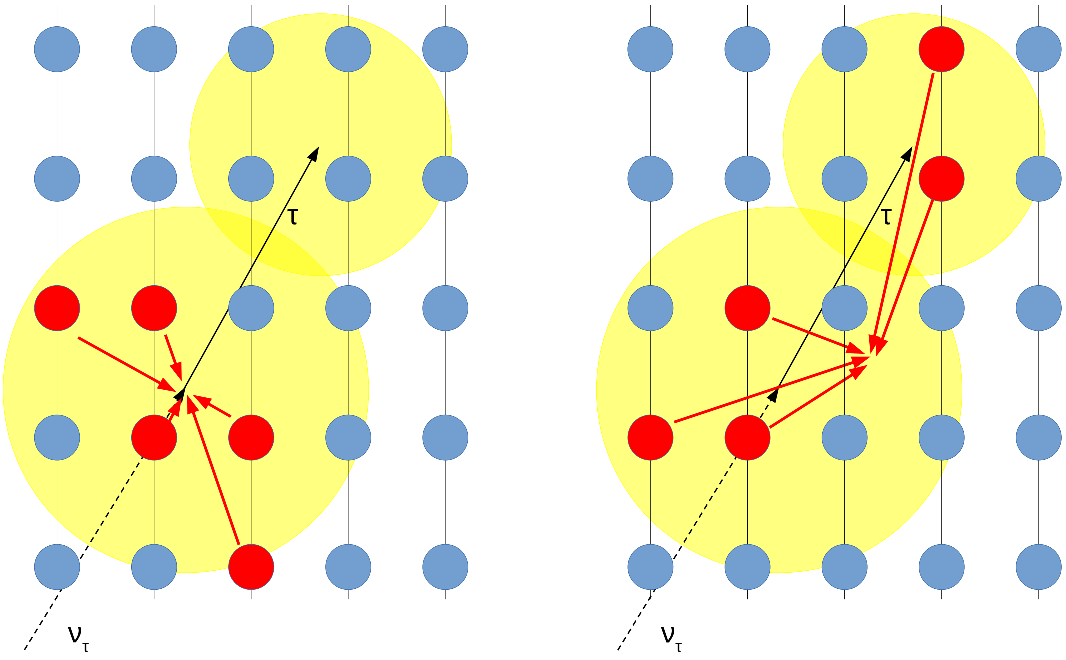

(a) (b)

Figure 5.7: Illustration of the estimation of cascade position. a) All five pulses corresponds to one cascade, resulting in an accurate position estimation. b) The set of five pulses is a mixture of pulses from both cascades, that results in an inaccurate estimation of cascade position.

around the newest estimate, the average value of all estimates in that area is selected for further processing and estimation of the new position and time of the cascade vertex is ceased. The illustration of this procedure is shown in Fig. 5.8.

In Figs. 5.9 and 5.10, the demonstration of this method on the MC simulations of the double cascade events is shown. For all possible combinations of sets of five pulses for one double cascade event, position and time of the cascade were estimated using Eq. 5.5. These estimates are displayed in Figs. 5.9 and 5.10, specifically – XZ plane in Fig. 5.9a, XY plane in Fig. 5.9b, and time in Fig. 5.10. In all of these figures, two peaks corresponding to the simulated positions and times of both cascades can be observed. Subsequently, above described scan procedure illustrated in Fig. 5.8 is able to identify these peaks and determine the first positions and times estimations of the cascade vertices.

Taking into account all combinations of five pulses for position and time estimation of the cascade is computationally very extensive and the number of all possible sets of five pulses grows approximately as a factorial of number of hits. Therefore, the set of requirements were introduced to get the most accurate position and time of the cascades with the minimal number of sets of five pulses possible – the $(\vec{R},\ T)$-

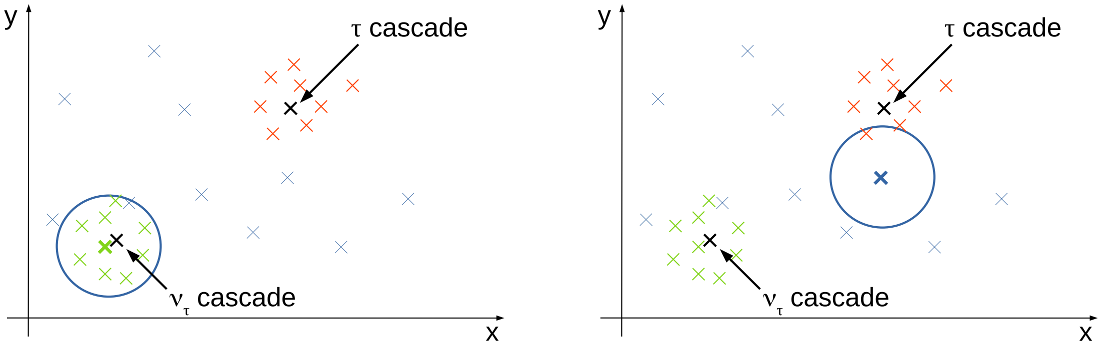

(a) (b)

Figure 5.8: Illustration of the selection of the first estimate of the cascade vertex position in XY plane. The black crosses represent MC simulated cascade vertices. The blue crosses correspond to the estimations of the cascade positions obtained from the mixture of the pulses from the both cascades or noise. The green (red) crosses represent estimations of the cascade positions if only pulses produced by ν_τ (τ) cascade were taken into account. a) New estimate (bold green cross) is in the vicinity of the cascade vertex therefore space region around it contains sufficient previous position estimates. b) New estimate (bold blue cross) is far from the cascade vertices hence space region around it contains insufficient previous position estimates.

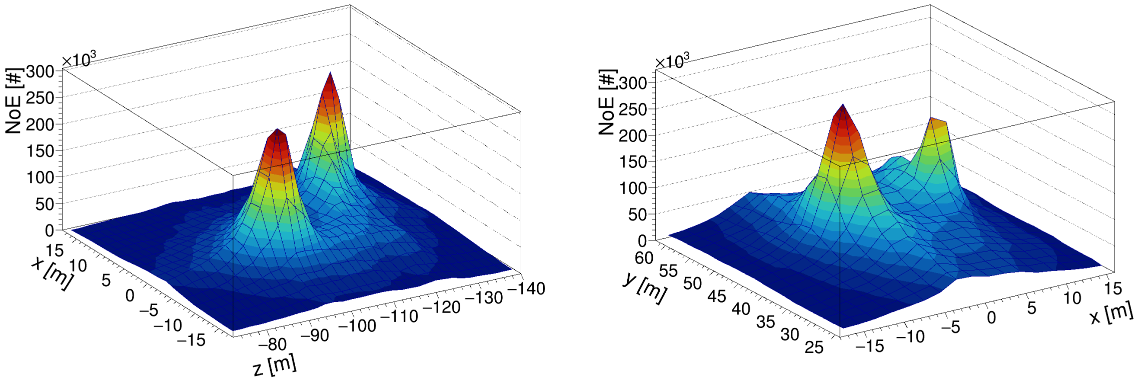

(a) (b)

Figure 5.9: Demonstration of the estimation of the cascades positions for one MC simulated double cascade event, considering all sets of five pulses. The MC simulated position of ν_τ cascade vertex is [9, 47, -126], τ cascade vertex position is simulated at [-3, 45, -100]. The positions are in meters. Two peaks that coincide with MC simulated positions of both cascades are created. a) XZ plane of the $(\vec{R}, T)$-space. b) XY plane of the $(\vec{R}, T)$-space.

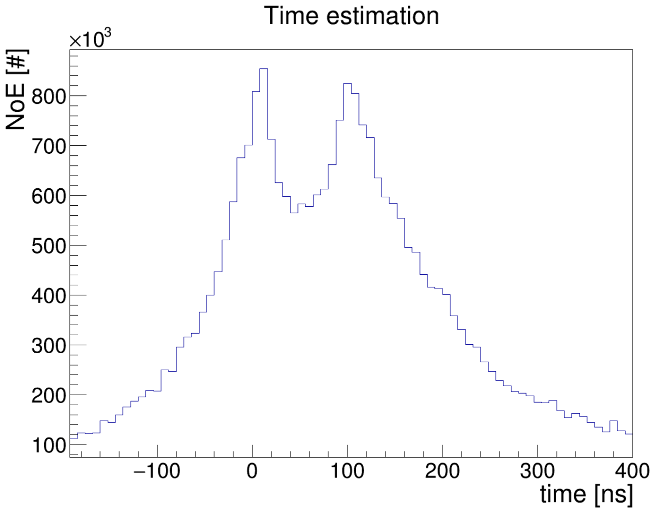

Figure 5.10: Demonstration of the time estimation for one MC simulated double cascade event, considering all combinations of five pulses. Two peaks corresponding to the times of the two cascades are created. The MC simulated distance between cascades is ∼ 28 m, the difference in the time estimation for both cascades is approximately 100 ns that corresponds to ∼ 30 m.

space scan. Additionally, in the process of the selection of groups of five pulses, hits are sorted according to their charge (from the highest to the lowest). This ordering increases probability that the pulses from the cascades are selected preferentially over noise pulses. Hence, it is expected that smaller number of groups of five pulses is required for the successful ($\vec{R}$, T)-space scan. Naturally, in other types of events different than cascades, the scan of the ($\vec{R}$, T)-space is less likely to be successful even if all combination of five pulses would be considered. Therefore, the limit on maximal number of sets of five pulses was added to ensure reasonable processing time of all types of events.

The subset of hits selected according to Eq. 5.4 is accepted for the further processing if it contains at least 6 hits detected on at least 3 strings. The last requirement that the subsets have to fulfill is that they have to contain at least 80 % of the signal hits selected in causality filter together.

To summarize the description of the hit sorting step of the double cascade reconstruction algorithm, the simplified flowchart of this part of the algorithm is given in Fig. 5.11. The procedure starts with selection of 5 pulses, which are used for estimation of the position and time of the cascade vertex satisfying condition given in Eq. 5.5. This procedure is repeated until the ($\vec{R}$, T)-space scan is able to identify two peaks created from the time and position estimations of cascade vertices in the ($\vec{R}$, T)-space or until maximal number of groups of pulses is reached. The last step is to choose the pulses that correspond to the first estimations of the cascade vertices coordinates ($\vec{R}_1$,

T_1 and $\vec{R}_2$, T_2) using Eq. 5.4. The advantage of the hit sorting procedure, developed specifically for the reconstruction of the double cascade events, is its universality – it might be adjusted for different types of events with cascade signatures – single cascades or multiple cascades.

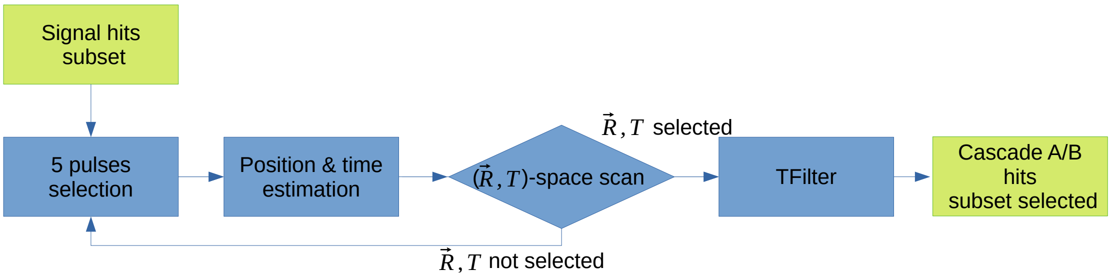

Figure 5.11: Simplified flowchart of the hit sorting part of the double cascade reconstruction algorithm. TFilter marks pulse selection procedure given in Eq. 5.4.

In the first version of the double cascade reconstruction algorithm, the mean efficiency of the selection of cascade A pulses obtained after hit sorting procedure is approximately 90.99 % and mean purity is around 81.4 %. For cascade B the mean efficiency of pulse selection is at the level of 66.29 % and the mean purity is approximately 92.74 %.

5.2.3 Cascade position and time reconstruction

For the final reconstruction of the positions and times of the both cascades, the minimization of χ^2 for the double cascade hypothesis is used. It is assumed that cascade is a point-like light source. There are 7 free parameters in the minimization – positions of the both cascades and the time of the cascade A. The time of the cascade B is linked to the time of the cascade A by assuming tau lepton traveling between the two vertices $(\vec{R}_1, \vec{R}_2)$ at the speed of light in vacuum c. The formula for χ^2 takes the following form:

$$\chi^2 = \frac{1}{N_{hit1} + N_{hit2} - 7} \left(\sum_{i=1}^{N_{hit1}} \frac{(T_{1i}^{meas} - T_{1i}^{exp}(\vec{R}_1, T_1))^2}{\sigma_t^2} + \sum_{i=1}^{N_{hit2}} \frac{(T_{2i}^{meas} - T_{2i}^{exp}(\vec{R}_2, T_2))^2}{\sigma_t^2} \right) \tag{5.6}$$

where N_{hit1}, N_{hit2} are, respectively, number of hits in the first and the second subset of hits, 7 stands for number of free parameters in the fit, T_{1i}^{meas}, T_{2i}^{meas} are the measured times of the pulses from the first and the second subset of pulses detected on particular OMs, σ_t^2 is the uncertainty in measurement of detection time of pulses, and T_{1i}^{exp}, T_{2i}^{exp} are the expected times of detection of pulses on particular OMs with respect to the cascade positions $\vec{R}_1$ and $\vec{R}_2$ and times T_1 and T_2 [91].

As initial values for times and positions of the cascades for the χ^2 minimization, the estimates from hit sorting procedure are used. χ^2 minimization is repeated three times, each time initial values for estimations of coordinates of cascades and subsets of hits are redefined according to the result of the previous minimization. The events with high value of χ^2 are excluded from further reconstruction.

After the last iteration of the χ^2 minimization, the final estimations of times and positions of the cascades are obtained. The direction of the double cascade event is calculated from these estimations of the cascade vertices.

5.2.4 Energy reconstruction

In the last step of the reconstruction algorithm, the energies of both cascades are estimated. For the energy reconstruction, minimization of the sum of the hit and non-hit likelihood function is used:

$$L = -\sum_{i=1}^{hitOM} log(P_i(q_i \mid Q_i)) - \sum_{i=1}^{unhitOM} log(P_i(q_i = 0 \mid Q_i)), \tag{5.7}$$

where P_i denotes the Poisson probability of i^{th} OM to detect charge q_i while charge Q_i is expected:

$$P_i(q_i \mid Q_i) = \frac{Q_i^{q_i} e^{-Q_i}}{q_i!}. \tag{5.8}$$

The expected charge is calculated as a sum of the charges expected from both cascades:

$$Q_i = Q(\vec{r_{1i}}, \theta, \phi, E_1) + Q(\vec{r_{2i}}, \theta, \phi, E_2). \tag{5.9}$$

Calculation of the charge takes into account energies of the cascades, positions of the cascades, direction of the cascades, and position and orientation of the OM. Moreover, it also considers light propagation in water and detector response simulation [91]. The minimization of the likelihood is performed 16 times with different combinations of initial energies: 1, 100, 1000, 10 000 TeV to ensure that true global minimum is found. Subsequently, the events with high likelihood value are rejected.

Update of Energy reconstruction

The double cascade energy reconstruction method described above used in the first version of the reconstruction algorithm has several issues. They can be illustrated using 2-dimensional distribution of ratios between reconstructed and simulated energies for the cascade A and B, see Fig. 5.12. Firstly, there is a shift of the peak of the well reconstructed events, which should be situated at [1,1] coordinates in the 2-dimensional plot of the ratios between reconstructed and simulated energies, see Fig. 5.12a. The second issue is the underestimation of the energy of the cascade B – the peak in the histogram in Fig. 5.12b with very low energy estimation of cascade B. Possible explanation of this peak is that the charge detected on the OM is summed before the

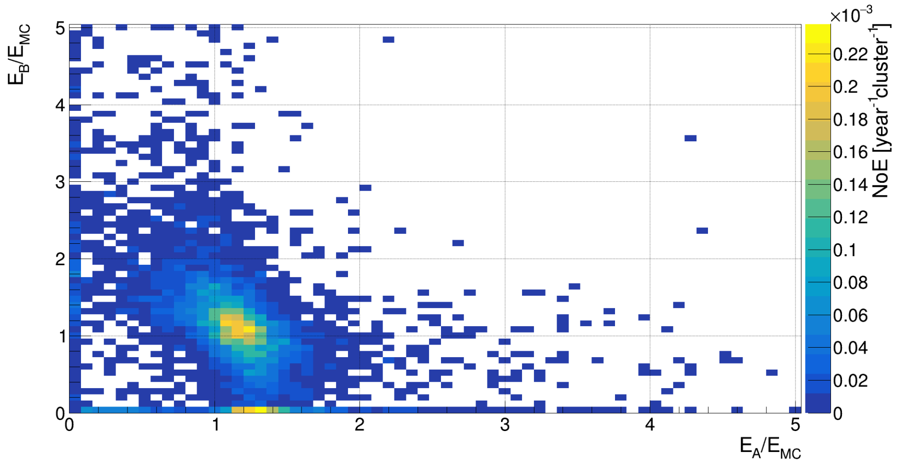

(a)

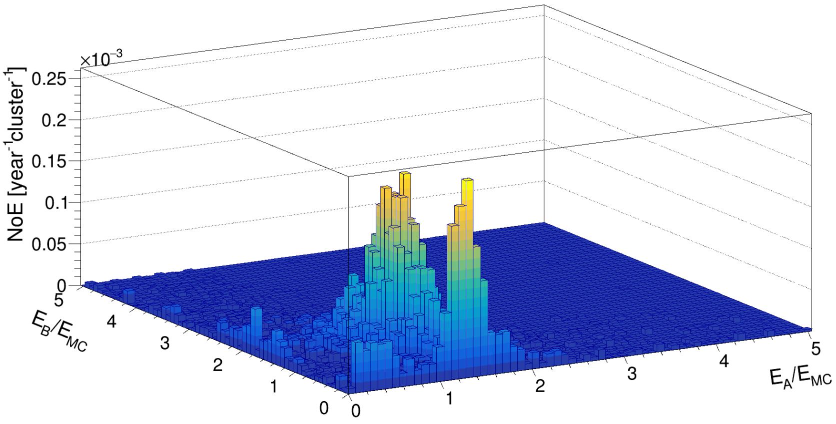

(b)

Figure 5.12: Performance of the energy reconstruction for the first version of the double cascade reconstruction algorithm given as two-dimensional distribution of the ratios of reconstructed to simulated energies of cascades A and B. Panels (a) and (b) show the same distributions from different points of view.

energy reconstruction step of the algorithm and therefore the information about the amount of the charge from individual cascades is lost.

Events that belong to the peak where energy of the cascade B is underestimated were analyzed in detail. It was observed that the common feature of these events is that the one subset of hits contains more pulses that the other subset of hits. Therefore, the criterion on the ratio between number of hits in subsets was introduced. After application of this criterion – rejection of the events with the ratio between number of hits in the two subsets higher than 1.5, the problematic peak was reduced, see Fig. 5.13. However, non-negligible number of events were excluded by imposing such requirement therefore additional adjustments were required.

To improve efficiency and precision of the energy reconstruction, an energy pre-

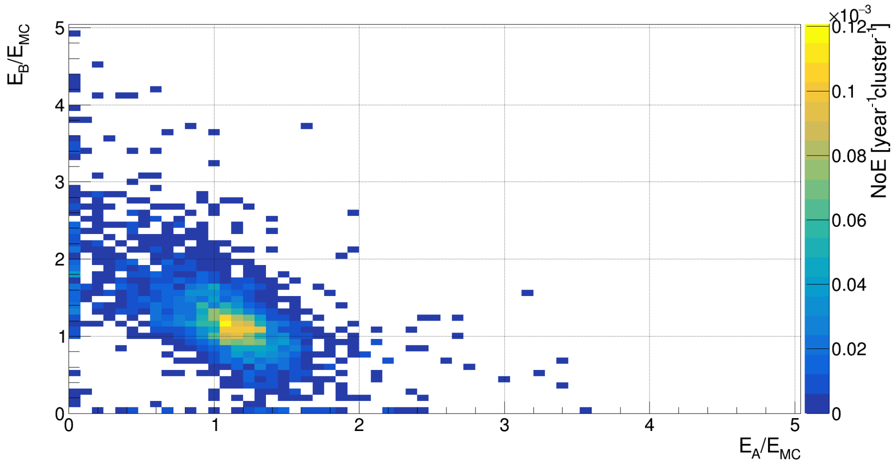

Figure 5.13: Two dimensional distribution of ratios between reconstructed and simulated energies for A and B cascades for selected events – events with high ratio between number of pulses in subsets are removed.

fit was introduced. The energy prefit is a procedure in which cascade energies are estimated from selected pulse(s) from the position and orientation of the OMs that detected particular pulse(s), their charge and also from already estimated position and direction of cascade. In current version of the double cascade reconstruction algorithm, pulse with median value of the charge from the each subset of hits is used in the energy prefit. The precision of the estimation of the energies of both cascades obtained from the energy prefit is shown in Fig. 5.14.

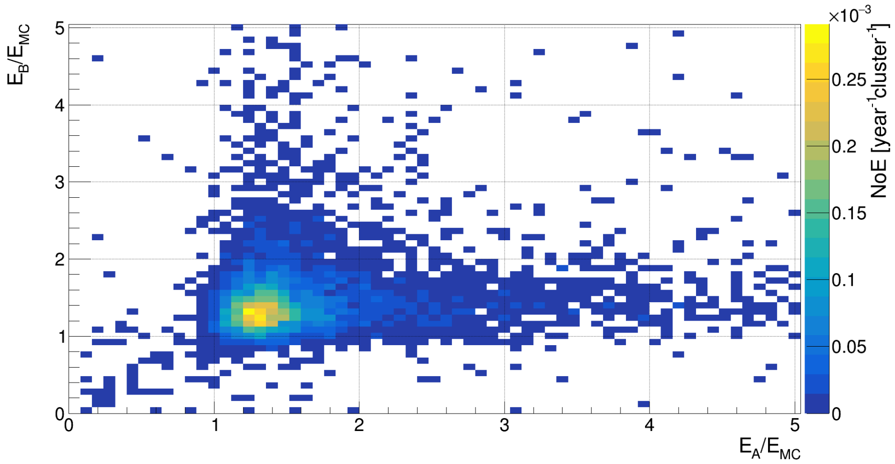

Figure 5.14: Performance of the energy prefit shown as ratios of reconstructed to simulated energies for A and B cascades.

The most important feature is that the peak with underestimated energy of cascade B is suppressed. As a conclusion, two step energy reconstruction procedure was designed. As the first step energy prefit is performed for all events. The second step is minimization of the log-likelihood for the events which are not excluded by the criterion on the ratio between number of hits in the cascade subsets. Moreover, the log-likelihood minimization is performed only once with the initial energies from the energy prefit which makes it less time consuming than in the first version.

The other issue of the first version of the reconstruction algorithm was the overall overestimation of the energies of both cascades, see Fig. 5.12a. In Fig 5.15a, the distribution of the ratios between reconstructed and simulated energy of the cascade A is given. The same ratios for cascade B is shown in Fig. 5.15b. Both of these histograms were fit with Gaussian functions. In the case of the cascade A, the mean of the Gaussian function from the fit is approximately 1.29, for the cascade B it is around 1.34.

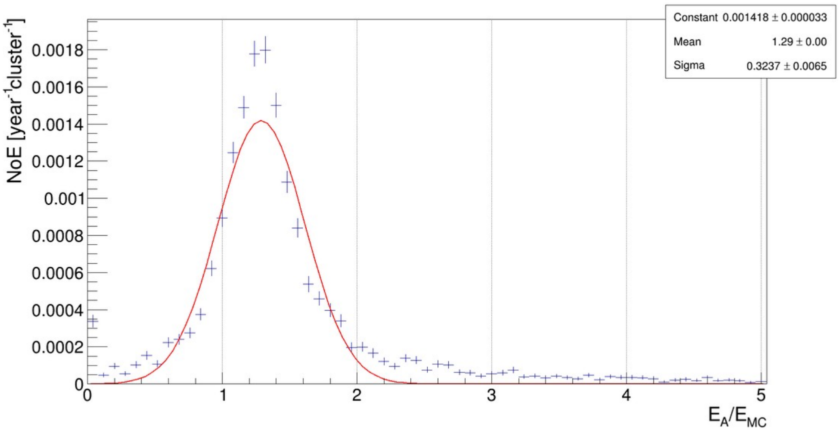

(a)

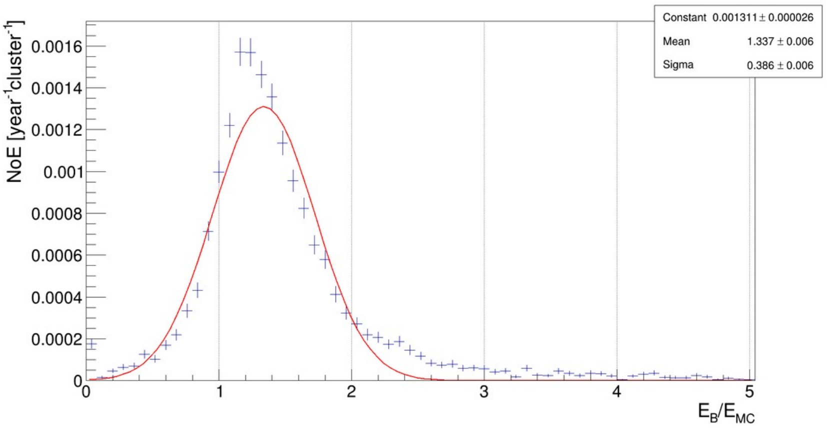

(b)

Figure 5.15: Distribution of the ratios of reconstructed to simulated energies with the Gaussian fit. a) Cascade A. b) Cascade B.

To eliminate energy overestimation, the correction factor on the reconstructed energy was introduced. In Fig. 5.16, the performance of energy reconstruction after application of the correction factor is shown. The mean of the Gaussian fit for the cascade A is at the level of 1.02 and for cascade B it is approximately 1.05.

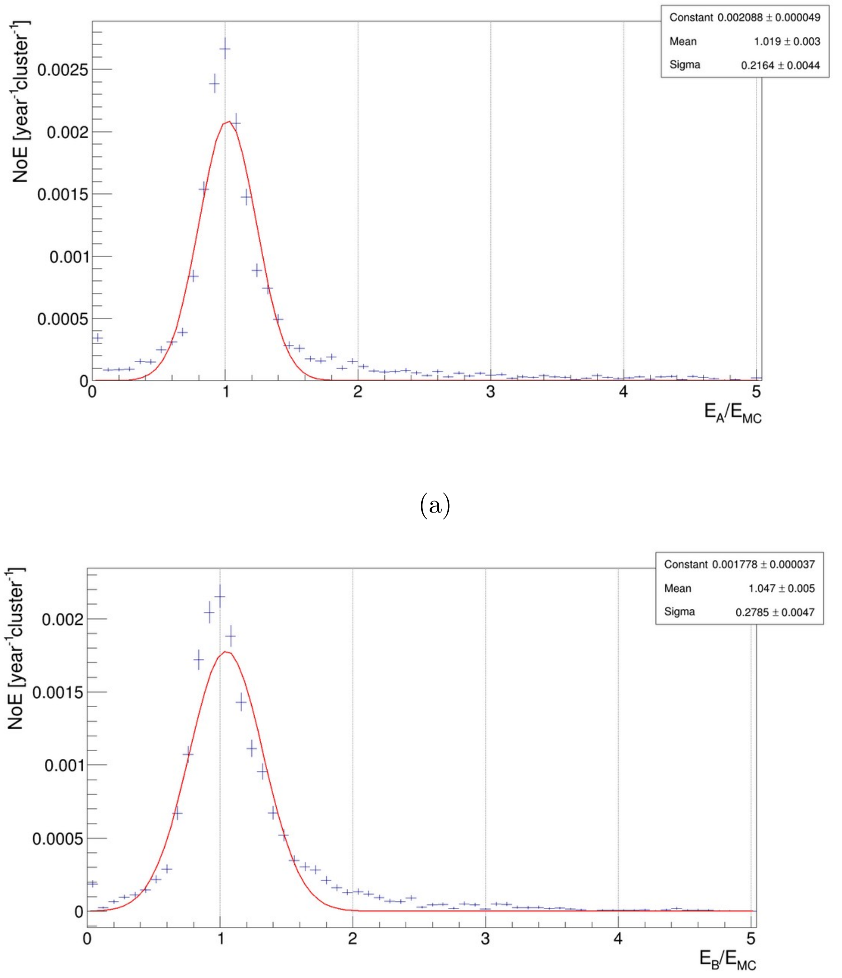

(a)

(b)

Figure 5.16: Distribution of the ratios between reconstructed and simulated energies shown together with Gaussian fit after application of the energy reconstruction correction factor. a) Cascade A. b) Cascade B.

In Fig. 5.17, the performance of the energy reconstruction of the second version of the double cascade reconstruction algorithm is given as the distribution of the ratios between reconstructed and simulated energies for both cascades A and B. In comparison with the same distribution for the first version of the energy reconstruction (Fig. 5.12), both studied issues – underestimation of the cascade B energy for non-negligible number of events and overall overestimation of the energy of both cascades were reduced.

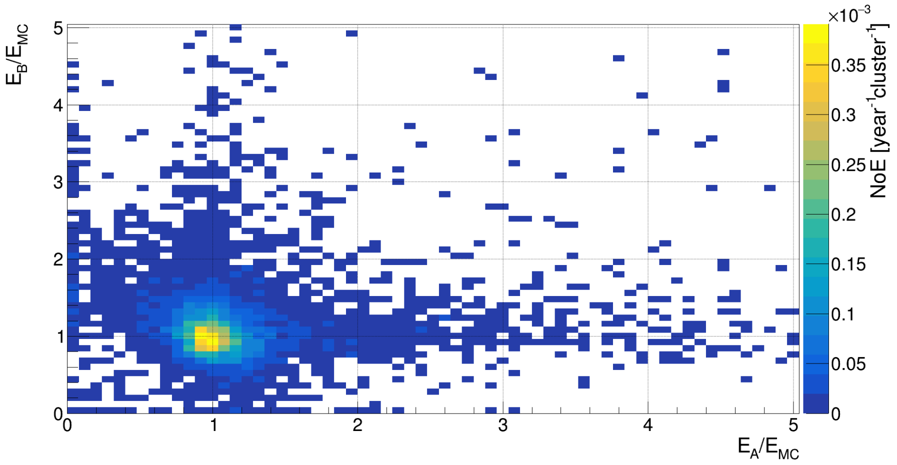

(a)

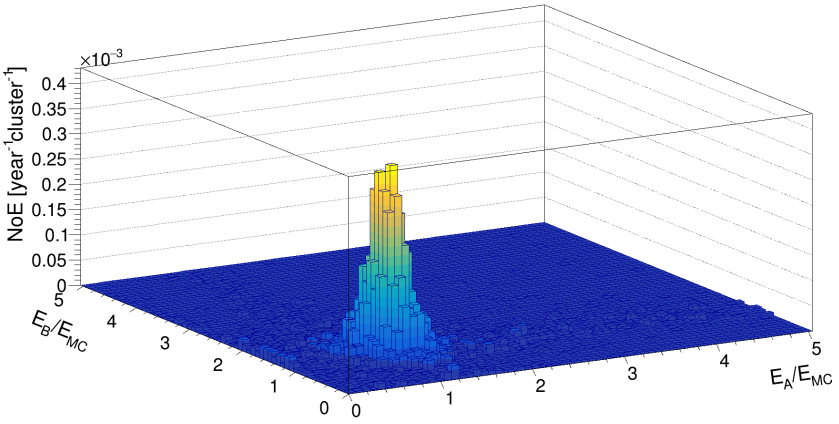

(b)

Figure 5.17: Performance of the energy reconstruction for the second version of the double cascade reconstruction algorithm given as two-dimensional distribution of the ratios between reconstructed and simulated energies for both cascades A and B. Figures (a) and (b) display the same distributions from different points of view.

5.3 Performance of the double cascade reconstruction algorithm

The main goal of the double cascade reconstruction algorithm is identification of the double cascade event and determination of its parameters. In the following section, the efficiency and the precision of the newly developed reconstruction algorithm with the preliminary criteria imposed (e.g. criteria on χ^2 and likelihood values) will be discussed. Moreover, the comparison of the efficiency and the performance of the first version of the algorithm (version 1) and updated version of the reconstruction algorithm (version 2) is given.

5.3.1 Precision of the algorithm

In Tab. 5.1, the evaluation of the reconstruction precision of the double cascade parameters is summarized. For parameters of the double cascade event – positions of both cascades, distance between cascade vertices and direction of the double cascade event, mean and median of the distributions showing difference between their simulated and reconstructed values are given.

Table 5.1: The reconstruction precision evaluation of the particular parameters of double cascade events. Mean and median of distributions of the difference between simulated and reconstructed parameters of the double cascade events for two versions of the reconstruction algorithm are given.

Double cascade parameter	version 1 $\lvert x_{sim} - x_{reco}\rvert$ mean	median	version 2 $\lvert x_{sim} - x_{reco}\rvert$ mean	median
cascade A position [m]	3.09	2.27	2.82	2.25
cascade B position [m]	5.03	2.46	4.01	2.45
distance between vertices [m]	2.83	0.75	1.94	0.71
direction [deg]	9.96	2.67	7.87	2.43

Position reconstruction performance

The median value of the final distribution of the difference between simulated and reconstructed position of cascade A is approximately 2.27 m and for cascade B it is about 2.46 m for the first version of the algorithm. In the second version, final median values are approximately 2.25 m for cascade A and 2.45 m for cascade B. For the first version of the algorithm the mean value of the distribution of difference between reconstructed and simulated position of the cascade A is at the level of 3.09 m and for cascade B it is approximately 5.03 m, for the second version this mean for cascade A is $\sim$ 2.82 m and for cascade B it is approximately 4.01 m.

The final mean value of the distribution of difference between simulated and reconstructed distance between cascade vertices is $\sim$ 1.94 m (2.83 m for the first version of the algorithm) and the median is approximately 0.71 m (0.75 m for the first version).

Direction reconstruction performance

The mean value of the distribution of angle between simulated and estimated direction of the double cascade events after final reconstruction of cascade vertices positions is approximately 7.87° (in the first version of the algorithm 9.96°) and the median 2.43°

(2.67° for the first version of the algorithm). The direction of the double cascade event is determined from the reconstructed positions and times of the cascades. Possible improvement of the direction reconstruction that can be implemented to the next version of the reconstruction algorithm is to add the direction of the double cascade event as a free parameter to the likelihood minimization.

5.3.2 Efficiency of the algorithm

The efficiency of the algorithm is defined as a ratio of events that passed certain step and corresponding criteria in the reconstruction procedure to all preselected double-cascade-like events from all simulated ν_τ double cascade events. The efficiency after whole reconstruction algorithm is $\sim$ 45.39 % (41.31 % for the first algorithm version). Using neutrino flux parametrization defined in Eq. 5.2, it corresponds to approximately 0.0184 (0.0167 for the first version) reconstructed ν_τ double cascade events per one cluster per one year. In Tab. 5.2, the efficiencies of the double cascade reconstruction algorithm after particular algorithm steps are shown.

Table 5.2: The efficiency of the double cascade reconstruction algorithm after particular procedures of the reconstruction algorithm. The efficiency is calculated with respect to selected double-cascade-like events (DC like events). The comparison of the two versions of the double cascade reconstruction algorithm is given.

algorithm step	version 1		version 2	
	NoE [10^{-2} y^{-1} cl^{-1}]	efficiency [%]	NoE [10^{-2} y^{-1} cl^{-1}]	efficiency [%]
selection DC like events	4.049	100	4.049	100
hit selection	4.019	99.26	4.032	99.59
hit sorting	1.970	48.67	2.133	52.69
position & time reconstruction	1.676	41.40	1.840	45.45
energy reconstruction	1.673	41.31	1.838	45.39
well reconstructed events	1.431	35.35	1.614	39.85

However, after double cascade reconstruction, there are some events that passed criteria set in the reconstruction algorithm although their parameters are not reconstructed precisely. Therefore, the efficiency of the double cascade reconstruction algorithm was additionally evaluated with respect to the well reconstructed events. They are defined as the events in which both positions of cascade vertices were reconstructed with maximal difference between simulated and reconstructed value at the level of 5 m. With this criterion applied, the efficiency of the reconstruction algorithm is approximately 39.85 %. It means that around 0.0161 ν_τ double cascade events are expected to be well reconstructed per one cluster per one year. The comparison of the first and updated version of the reconstruction algorithm shows the increase in the number of well reconstructed events. This increase is more significant approximately 4.5 %, in comparison of the increase in number of events after the last step of the reconstruction algorithm – around 4 %. This can indicate that updates in the reconstruction algorithm enhanced both – the precision and the efficiency of the double cascade reconstruction algorithm.

Fig. 5.18 displays dependence of the efficiency of the double cascade reconstruction algorithm for the first version of the algorithm for well reconstructed events on different attributes of double cascade events.

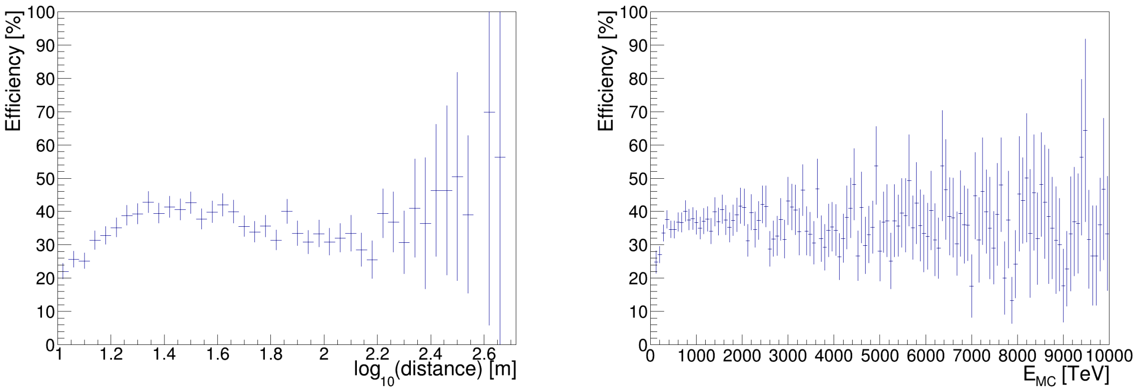

(a)

(b)

Figure 5.18: The dependence of the algorithm efficiency for the well reconstructed cascades (both cascade vertices are reconstructed with 5 m maximal mismatch between simulated and reconstructed vertex position) on a) MC simulated distance between cascade vertices, b) MC simulated energy of incoming ν_τ.

In Fig. 5.18a, the dependence of this efficiency on the MC simulated distance between cascade vertices is shown. This distribution shows that the double cascade reconstruction algorithm has lower efficiency of reconstruction of the events with relatively low distance between cascade vertices. This efficiency can be increased by addition of the pulse shape analysis and pulse separation to the reconstruction algorithm. Analysis of the shapes of pulses enables identification of merged pulses – overlapped pulses originating from both cascades registered by one OM. For larger distances between cascade vertices this efficiency is relatively uniform at the level of 30 % - 40 %, and for the largest possible distances for double-cascade-like events the efficiency is rising. It is likely caused by the fact that in such range of the cascade vertices distances, two cascades are almost completely separated and therefore their reconstruction is easier. Fig. 5.2b shows that the double cascade events with distances higher than approximately 500 m do not fulfill the initial criteria for double-cascade-like events selection. The possible reason is the cluster geometry – for such double cascade events both cascades do not fit in a single cluster detection volume. Therefore, the efficiency of the reconstruction algorithm can be increased by including multi-cluster events in the reconstruction.

In Fig. 5.18b, the distribution of the efficiency of the algorithm (the first version) for well reconstructed events with respect to the MC simulated energy of the incoming ν_τ is shown. In this case, there is no significant dependence, the efficiency is approximately 35 % for whole simulated energy range of the ν_τ.

The visualization of one reconstructed ν_τ event from MC simulations is displayed in Fig. 5.19. Hits from the both cascades – ν_τ (black dots) and τ (purple dots) lying in the expected regions (green and dark green lines) calculated with respect to the reconstructed positions of the cascades (red and dark red dots), indicate properly reconstructed double cascade event.

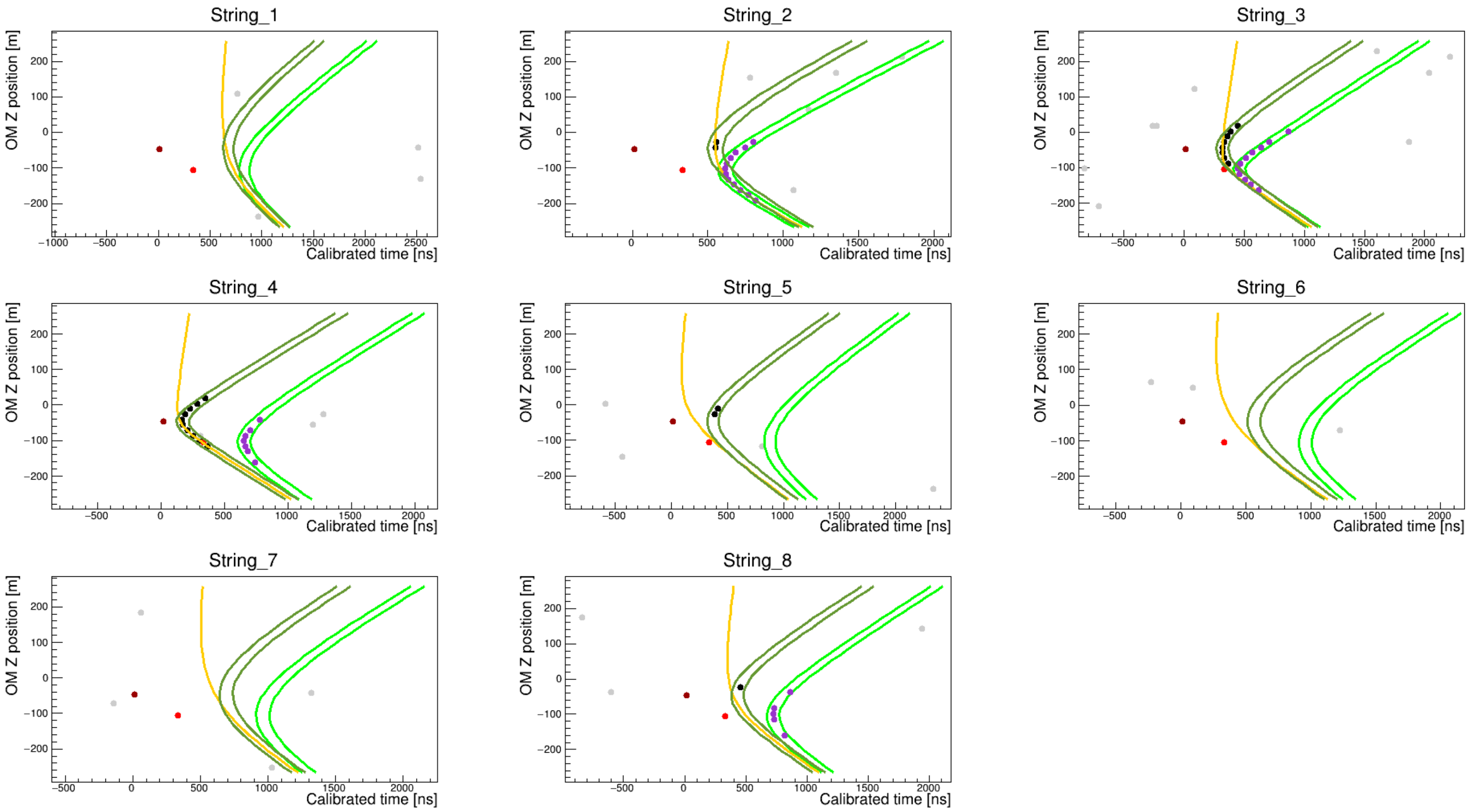

Figure 5.19: The visualization of the reconstructed ν_τ double cascade event from MC simulations. The dependence of the Z coordinate of the OM on the time of the pulse detection is shown for all 8 strings in the cluster. The red (dark red) dot represents the reconstructed position of the cascade A (B). The green (dark green) lines define region where pulses originating from the cascade A (B) should be, they are calculated with respect to the reconstructed vertex position of the cascade A (B). The orange line marks region where hits created by potential μ track calculated with respect to the reconstructed position and direction of hypothetical ν_τ cascade are expected to be detected. The black (purple) dots correspond to the hits produced by ν_τ (τ) cascade. The gray dots represent noise hits.

5.4 Tau neutrino background

The ν_τ double cascade events are not the only events that pass the criteria in the double cascade reconstruction procedure. The ν_τ double cascade signature can be mimicked for example by the signatures created by muon events. Two cascades can be produced along a muon track by stochastic energy losses (bremsstrahlung, pair production, nuclear interactions). If these two cascades are created in the cluster volume, the double cascade signature in combination with muon track is produced, see Fig. 5.20. Also some other type of events might possibly pass the current preliminary reconstruction criteria. Therefore, to determine expected rate of the events in ν_τ search in the experimental data, MC simulations of various ν_τ double cascade background events were processed.

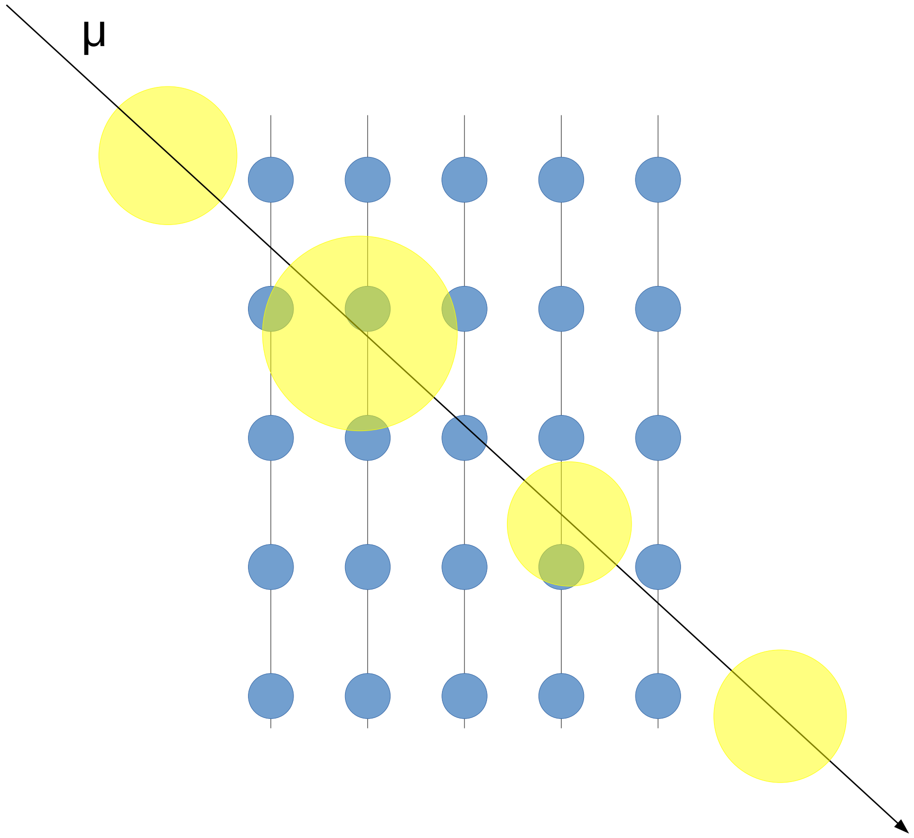

Figure 5.20: Illustration of the muon track event in the detector. Cascades that are created by stochastic energy losses along the muon track can resemble double cascade signature.

MC simulations of atmospheric ν_e and ν_μ CC and NC interactions as well as astrophysical ν_e and ν_μ CC and NC interactions were generated by ANIS. Atmospheric ν_e and ν_μ are simulated in the energy range from 1 TeV to 310 TeV according to the Volkova flux [92]. Astrophysical ν_e and ν_μ are generated in energy range from 1 TeV to 40 PeV according to the expected rate given in Eq. 5.2. In the case of the CC interaction of ν_μ, only the primary cascade is simulated, the μ track is not included. This can have non-negligible impact on the expected rates, since the primary cascade in combination with cascades created along muon track can mimic double cascade signature. Hence, it is crucial to update MC simulations of ν_μ CC interactions to obtain more precise results.

Atmospheric μ bundle events were simulated in two different energy regions. In the first one, energies of primary particles from cosmic rays are in the interval from 240 GeV to 20 PeV. These MC simulations take into account the masked OMs, therefore they are different for every cluster. The second energy region is from 20 PeV to 100 PeV. These MC simulations are the same for every cluster assuming all OMs are working. For simulations of cosmic rays interactions and propagation of the secondary particles the CORSIKA is used [93] in both energy regions. The hadronic interactions are simulated according to the QGSJET model [94]. The summary of the expected rates from MC simulations of different events is shown in Tab. 5.3. The expected rate of atmospheric μ bundle events is obtained from the combination of MC simulations in two energy regions.

Table 5.3: Expected rates of ν_τ interaction background events from MC simulations detected by one cluster in one year. Moreover, the rates of signal events – ν_τ double-cascade-like (DC-like) events are given. NoE means number of events that passed particular trigger condition. NoE_{DCreco} corresponds to the number of events that passed criteria in the double cascade reconstruction algorithm. In addition, there is an efficiency of the double cascade reconstruction algorithm shown. The comparison of these values for the first and updated version of the double cascade reconstruction algorithm is given.

type of MC simulations	NoE [y^{-1} cl^{-1}]	version 1		version 2	
		NoE_{DCreco} [y^{-1} cl^{-1}]	efficiency [%]	NoE_{DCreco} [y^{-1} cl^{-1}]	efficiency [%]
ν_τ astrophysical (DC-like)	$4.05 \cdot 10^{-2}$	$1.67 \cdot 10^{-2}$	41.31	$1.84 \cdot 10^{-2}$	45.39
atmospheric μ bundles	$5.38 \cdot 10^{8}$	38.1	$7.09 \cdot 10^{-6}$	37.62	$6.99 \cdot 10^{-6}$
ν_e atmospheric	9.34	$1.42 \cdot 10^{-3}$	$1.52 \cdot 10^{-2}$	$1.40 \cdot 10^{-3}$	$1.50 \cdot 10^{-2}$
ν_μ atmospheric	87.4	$1.31 \cdot 10^{-2}$	$1.50 \cdot 10^{-2}$	$1.29 \cdot 10^{-2}$	$1.48 \cdot 10^{-2}$
ν_e astrophysical	1.71	$3.82 \cdot 10^{-2}$	2.24	$3.92 \cdot 10^{-2}$	2.29
ν_μ astrophysical	$9.86 \cdot 10^{-1}$	$1.23 \cdot 10^{-2}$	1.25	$1.24 \cdot 10^{-2}$	1.26

In Tab. 5.3, the efficiency of the double cascade reconstruction algorithm for different types of MC simulated events is given. This efficiency is defined as the ratio between events that passed all steps of the double cascade reconstruction algorithm and all simulated events. Values in Tab. 5.3 indicate that the events obtained from the experimental data after processing with the double cascade reconstruction algorithm should be dominated by the atmospheric μ bundle events.

5.5 Experimental data processing

To identify potential double cascade events, experimental data from year 2019 were processed with the double cascade reconstruction algorithm. Firstly, the comparison between expected rates from the MC simulations and rates obtained after processing of the data with the reconstruction algorithm was studied. The results of the processing of the MC simulations with the double cascade reconstruction algorithm shown in Tab. 5.3 indicate that the set of events obtained after processing of the data with the double cascade reconstruction algorithm should mostly contain muon bundles events. Therefore, to study the agreement between the rate of potential double cascade events from experimental data and MC simulations, a reasonable approximation is to take into account only the MC simulations of the atmospheric μ bundles – the ratio of the rate of the atmospheric μ bundles to the rate of the detected events in experimental data should be equal to ~ 1. In Tab. 5.4, the ratio of the rate of atmospheric μ bundles that passed criteria in the double cascade reconstruction algorithm to number of potential double cascade events identified in experimental data collected in year 2019 for different clusters is shown. Since the noise pulses in the MC simulations of the atmospheric μ bundles are generated with values for the part of the year where noise rates are relatively stable, only data from that part of the year are taken into account in evaluation of the comparison between MC simulations and data. Corresponding exposition times for each cluster are given in the Tab. 5.4.

The deviation from expected value of the ratio might be caused by several factors – only low statistics was taken into account in this first study, masked OMs are not taken into account in both MC simulations of atmospheric μ used in this analysis and even in stable noise rates periods the noise levels can fluctuate (see Chap. 4) which might possibly affect the reconstruction procedure. To improve precision of this comparison, the MC simulations generated specifically for each run should be used.

Visualizations of two potential double cascade events identified in experimental data are shown in Figs. 5.21, 5.22. Comparison of these figures with Fig. 5.19 shows, that in both displayed events identified in experimental data, the double cascade pattern of hits can be seen on several strings. However, according to the values in Tab. 5.3,

Table 5.4: The summary of experimental data processing with the double cascade reconstruction algorithm for 5 clusters in part of year 2019, when the noise rates are relatively stable. $N_{MC\,\mu\,bundles}$ corresponds to the rate of μ bundle events that fulfilled double cascade reconstruction criteria. It is normalized according to the exposition time for each cluster. N_{data} means number of reconstructed double cascade events from experimental data corresponding to the same exposition time.

version 1	cluster 1	cluster 2	cluster 3	cluster 4	cluster 5
Exposition time [days]	77.58	71.70	61.25	78.70	64.02
$N_{MC\,\mu\,bundles}$	6.20	3.65	7.19	8.86	10.35
N_{data}	10	11	7	22	13
$N_{MC\,\mu\,bundles}/N_{data}$	0.62	0.33	1.03	0.40	0.80

version 2	cluster 1	cluster 2	cluster 3	cluster 4	cluster 5
Exposition time [days]	77.58	71.70	61.25	78.70	64.02
$N_{MC\,\mu\,bundles}$	5.64	3.68	6.76	8.88	10.86
N_{data}	8	9	7	18	15
$N_{MC\,\mu\,bundles}/N_{data}$	0.71	0.41	0.97	0.49	0.72

the most probable interpretation is that these events were produced by atmospheric μ bundles. This hypothesis is also supported by the fact that for both events, several pulses are detected in the region where the pulses from the μ track are expected to be registered. However, more detailed analysis is needed to determine the origin of these events.

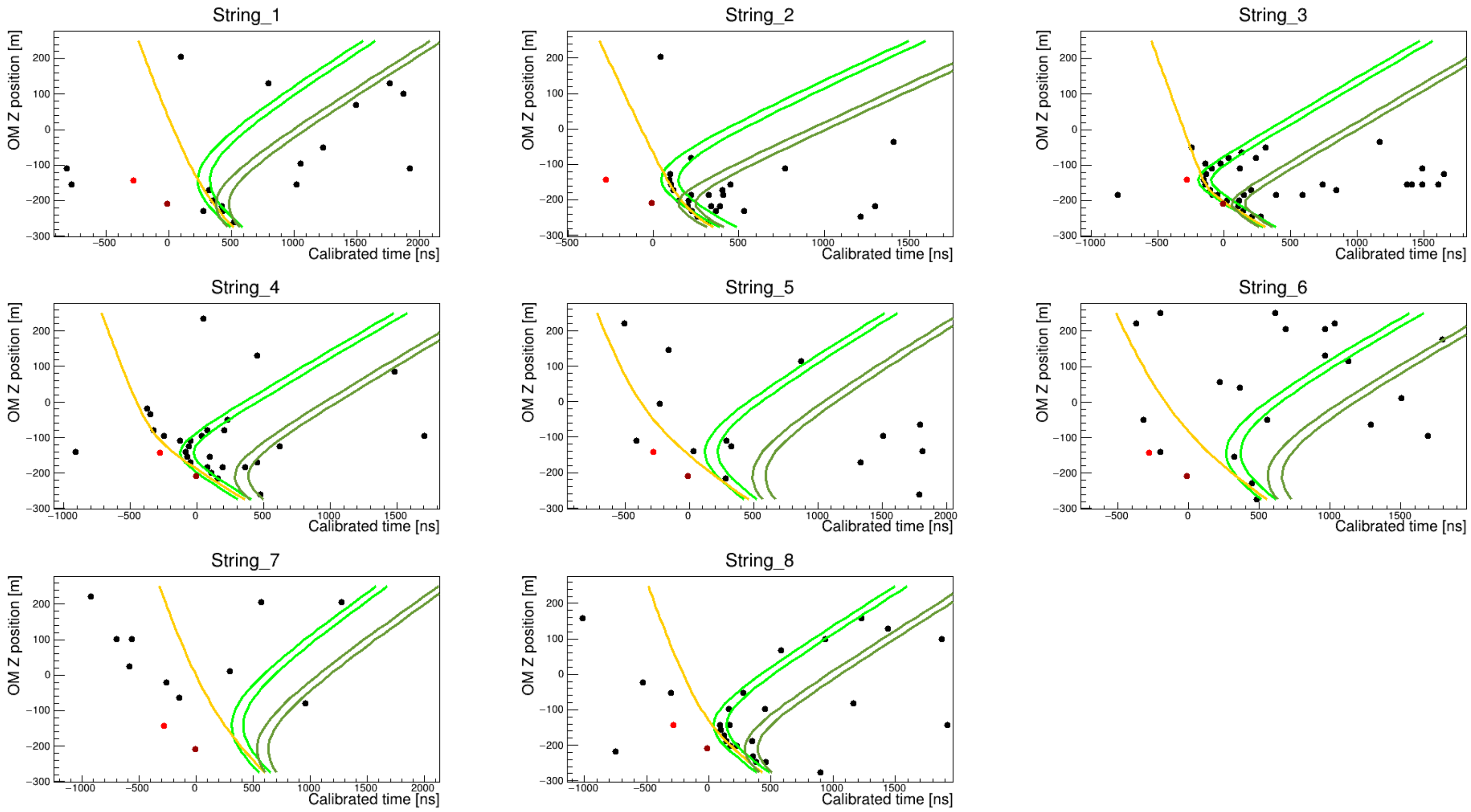

Figure 5.21: The visualization of potential double cascade event identified in data collected in 2019. The dependence of the Z coordinate of the OM on the time of the pulse detection is shown for all 8 strings in the cluster. The red (dark red) dot represents the reconstructed position of the cascade A (B). The green (dark green) lines define region where pulses originating from the cascade A (B) should be, they are calculated with respect to the reconstructed vertex position of the cascade A (B). The orange line marks region where hits created by potential μ track calculated with respect to the reconstructed position and direction of hypothetical ν_τ cascade are expected to be detected. The black dots represent hits registered by OMs. Event detected by cluster 2.

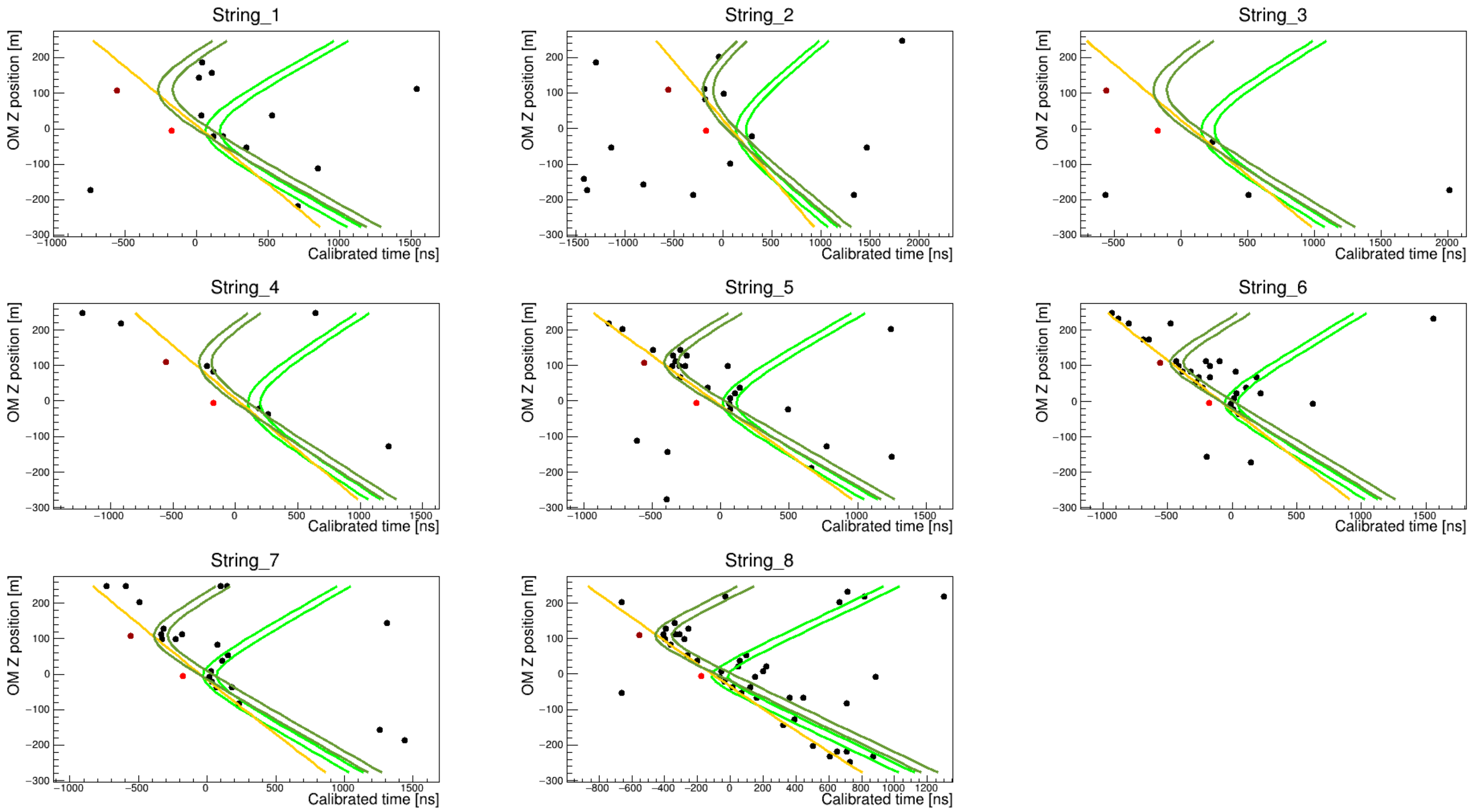

Figure 5.22: The visualization of potential double cascade event identified in data collected in 2019. The dependence of the Z coordinate of the OM on the time of the pulse detection is shown for all 8 strings in the cluster. The red (dark red) dot represents the reconstructed position of the cascade A (B). The green (dark green) lines define region where pulses originating from the cascade A (B) should be, they are calculated with respect to the reconstructed vertex position of the cascade A (B). The orange line marks region where hits created by potential μ track calculated with respect to the reconstructed position and direction of hypothetical ν_τ cascade are expected to be detected. The black dots represent hits registered by OMs. Event detected by cluster 5.

5.6 Performance of the double cascade reconstruction algorithm with the first results on Baikal-GVD astrophysical neutrino flux

In previous sections, the efficiency and precision of the double cascade reconstruction algorithm were evaluated using MC simulations with event weights calculated according to the flux given in Eq. 5.2. In the following section, the precision of this algorithm is determined using Baikal-GVD parametrization of astrophysical neutrino flux [20]:

$$\phi(E) = 2.41 \cdot 10^{-5} \cdot \left(\frac{E}{\text{GeV}}\right)^{-2.58} [\text{GeV}^{-1}\text{s}^{-1}\text{sr}^{-1}\text{cm}^{-2}], \tag{5.10}$$

which corresponds to the single flavor neutrino flux, assuming equal number of neutrinos and antineutrinos.

Tab. 5.5 displays the precision of the reconstruction of the double cascade event parameters. Means and medians of the distributions of the difference between simulated and reconstructed values of the double cascade event parameters are given. Even though new parametrization of the astrophysical neutrino flux decreases the expected number of higher energy neutrino events, the precision of the algorithm remains at the same level, see Tab. 5.1.

Table 5.5: The reconstruction precision of selected parameters of the double cascade event. The mean and median values of distributions of difference between simulated x_{sim} and reconstructed x_{reco} values of parameters of double cascade events are presented.

Double cascade parameter	$\lvert x_{sim} - x_{reco}\rvert$ mean	median
cascade A position [m]	2.76	2.21
cascade B position [m]	4.11	2.44
distance between vertices [m]	1.96	0.71

In Fig. 5.23, the performance of the reconstruction of the direction of the double cascade events is given. It displays dependence of the angle between simulated and reconstructed direction of the double cascade events with respect to the simulated distance between cascade vertices. Green line represents median of this distribution, green belt shows 68 % containment region of this dependence. The accuracy of the reconstruction is improving with increasing distance between cascade vertices due to the elongation of the event. Due to this effect, it is possible to obtain better precision of the identification of possible ν sources with the double cascade events with larger distance between cascade vertices than in the case of the single cascades. The median of the direction deviation distribution under $\sim 1^\circ$ is achieved for the double cascade events with distance between cascade vertices higher than approximately 50 m.

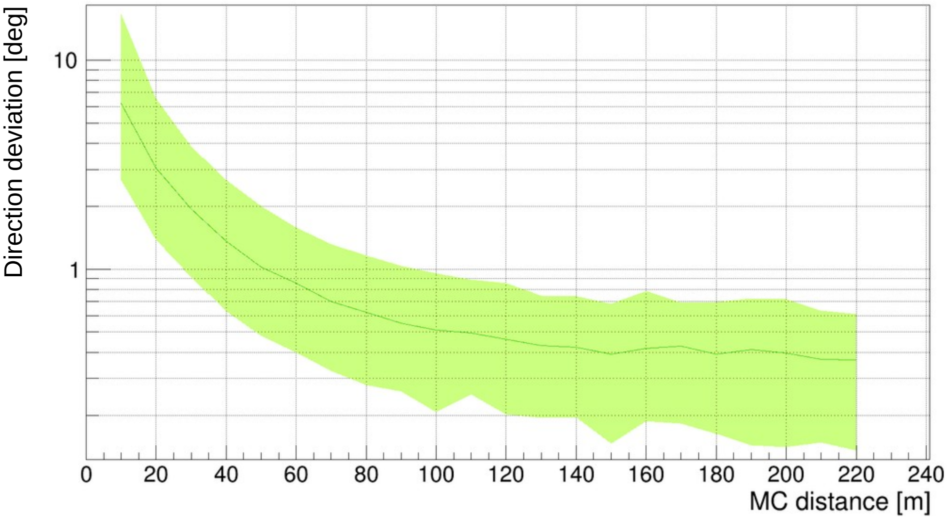

Figure 5.23: Performance of the reconstruction of the double cascade event direction given as the dependence of the angle between simulated and reconstructed direction of ν_τ double cascade event on true distance between cascade vertices. Green line displays median value and 68% containment region is shown with green belt.

The performance of the reconstruction of the energy is presented in Fig. 5.24. This figure displays two-dimensional distribution of ratios between reconstructed and simulated energy of A and B cascade. To obtain precision of energy reconstruction, this dependence was fitted with two-dimensional Gaussian function given as:

$$f(x,y) = A \cdot e^{-\frac{(x-\mu_A)^2}{2\sigma_A^2} - \frac{(y-\mu_B)^2}{2\sigma_B^2}}\,. \tag{5.11}$$

The parameters of the two-dimensional Gaussian function determined from the fit are $\mu_A = 1.02$, $\mu_B = 1.04$, $\sigma_A = 0.18$, and $\sigma_B = 0.24$.

5.7 Multi-cluster double cascade reconstruction

One of the means how to improve the efficiency of the double cascade reconstruction algorithm is to include reconstruction of the multi-cluster double cascade events. Due to the restriction of the detection of the both cascades in one cluster, there is a cutoff of the events entering the reconstruction for large distances, see Fig. 5.2b. This limit can be moved to higher distances by including multi-cluster events in the reconstruction.

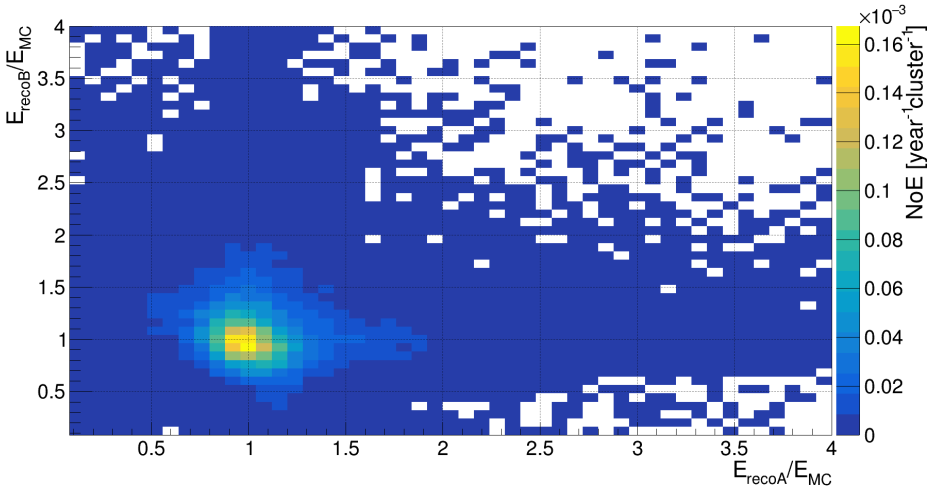

(a)

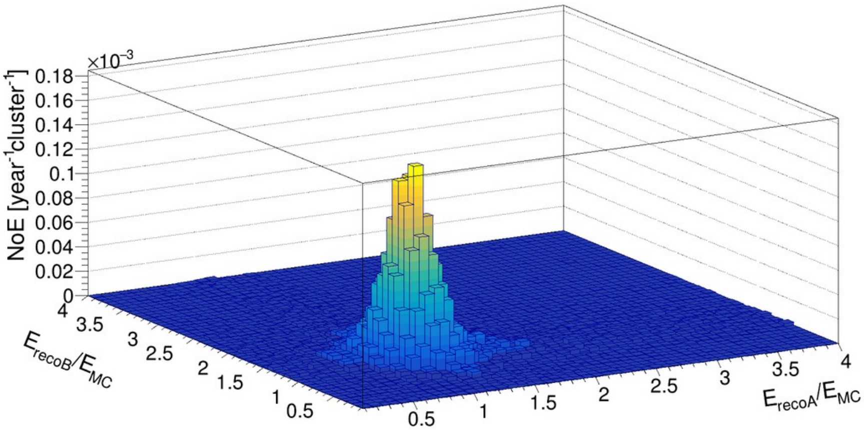

(b)

Figure 5.24: The two-dimensional distribution of ratios between reconstructed and simulated energy for cascades A and B. Figures (a) and (b) display the same distributions from different points of view.

In the following section, the preliminary analysis of the reconstruction of the multi-cluster double cascade events for Baikal-GVD geometry of the year 2019 (5 clusters) is presented.

Firstly, the MC simulations were studied. Using flux given in Eq. 5.10 and energies of ν_τ in range from 10 TeV to 10 PeV, it is expected to register 2.997 ν_τ double cascade events per year per 5 clusters (MC trigger condition – pulses detected on at least 4 OMs located on at least 3 strings). However the single cluster events are dominating, around 97.17 % of all simulated events which corresponds to the approximately 2.913 events per year are purely single cluster events. Remaining 2.83 %, which corresponds to approximately $8.47{\cdot}10^{-2}$ per year, are multi-cluster events, see Fig. 5.25.

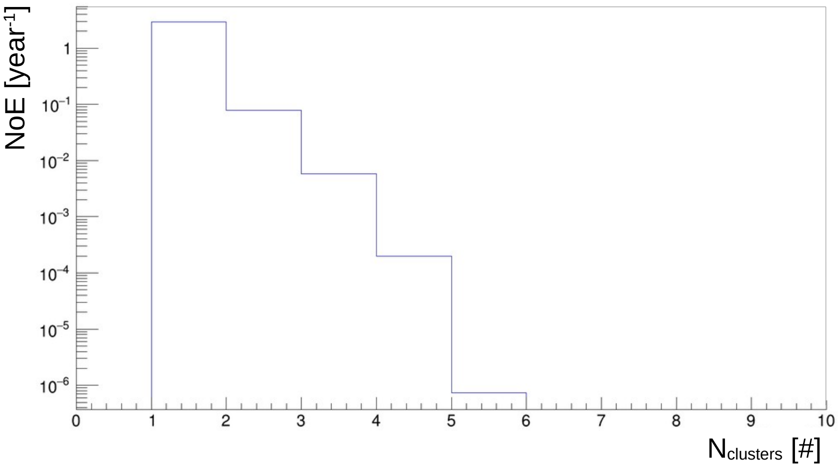

Figure 5.25: Number of clusters that detected hits from the ν_τ double cascade event for the 2019 geometry.

Possible explanation is that the mean distance between centers of the clusters is at the level of 300 m. For the double cascade events with such distance between cascade vertices, interaction of very-high energy ν_τ is required, see Eq. 1.14. The flux of such neutrinos is suppressed in comparison with lower energetic neutrinos, see Eq. 5.10. In addition to requirement of high-energy ν_τ to increase the probability of sufficient distance between cascade vertices, there are supplementary conditions that have to be fulfilled to detect ν_τ double cascade multi-cluster event – there has to be CC interaction of ν_τ, τ lepton originating in this interaction has to decay into electron or hadrons and also the position and direction of such event has to align to hit two or more clusters.

Next, the types of the multi-cluster double cascade events were studied in detail. Firstly, the fraction of the double-cascade-like events was determined. The conditions are the same as in the case of single cluster double-cascade-like events described in Sec. 5.1. Such conditions can also lead to both vertices contained in one cluster or in its vicinity but the signal has to be detected in two or more clusters, see Fig. 5.26. Around 15.98 % of the all multi-cluster ν_τ double cascade events ($\sim 8.47{\cdot}10^{-2}$ per year) which corresponds to the approximately $1.35{\cdot}10^{-2}$ per year passed these criteria.

When the stricter condition on the positions of the vertices is applied – requirement that both cascade vertices have to be contained in the different clusters, see Fig. 5.27, approximately $1.39{\cdot}10^{-4}$ events are expected to be detected per year, which corresponds to around 0.16 % of all simulated multi-cluster ν_τ double cascade events.

The evaluation of precision of the direction reconstruction for double-cascade-like events for 2019 geometry (single cluster and multi-cluster events) is shown in Fig. 5.28. It is given as a dependence of angle between simulated and reconstructed direction of the double cascade events on simulated distance between cascade vertices. Blue band

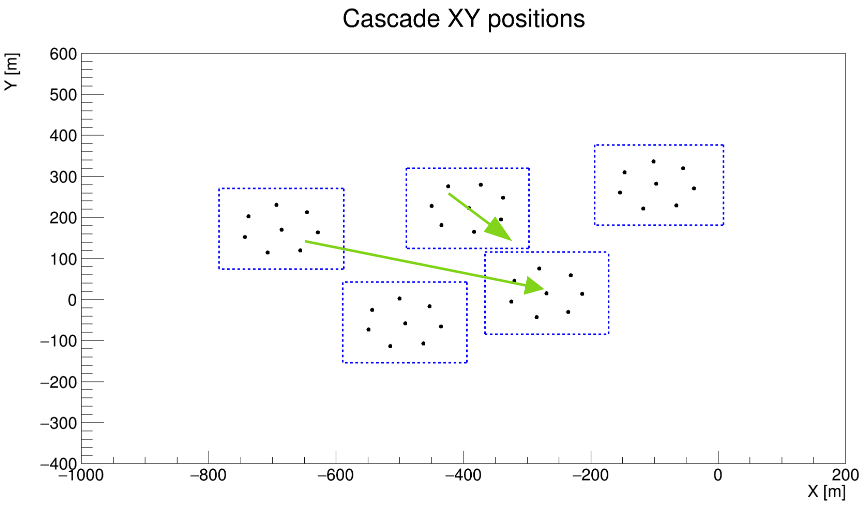

Figure 5.26: Illustration of the criteria imposed on the vertices positions for double-cascade-like events selection for multi-cluster geometry in year 2019 in planar view. Black dots represent string positions, dashed blue lines mark the region where the position of the cascade vertex is allowed to be situated, and with the arrows allowed double cascade events are displayed.

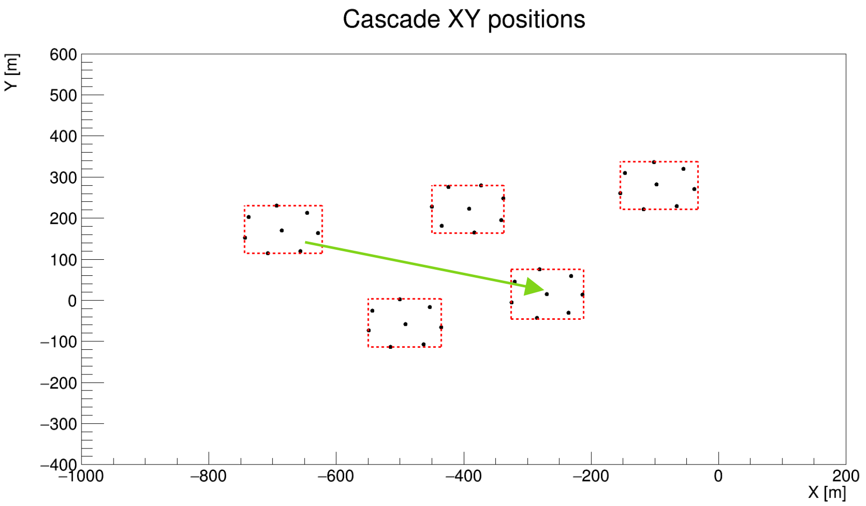

Figure 5.27: Illustration of the allowed positions of the vertices of selected multi-cluster double cascade events for 2019 year geometry with 5 clusters in planar view for different sets of criteria. With black dots string positions are shown. Dashed red lines display regions where the cascade vertex is allowed to be placed. Green arrows illustrate double cascade events that pass event selection.

depicts 68 % containment region, with blue line median of this distribution is displayed.

The addition of the multi-cluster events allows to study the performance of the

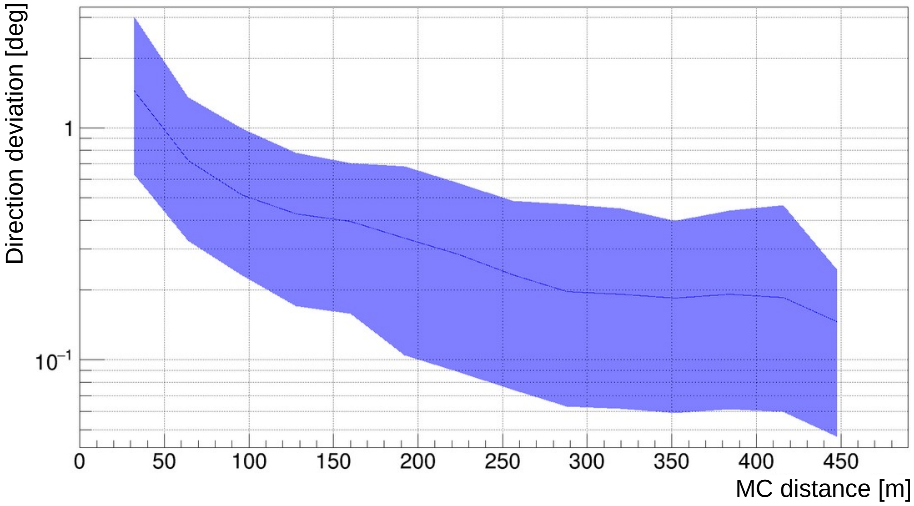

Figure 5.28: The distribution of angle between simulated and reconstructed direction of ν_τ double cascade event as a function of true distance between cascade vertices for combined dataset of single cluster and multi-cluster ν_τ double cascade events for 2019 geometry which corresponds to 5 clusters. Median value of this distribution is displayed with blue line, blue belt shows 68% containment region of this distribution.

double cascade reconstruction algorithm for events with higher distance between cascade vertices in comparison with pure single cluster events study, see Fig. 5.23. For the double cascade events with distance between cascade vertices higher than $\sim$ 100 m the median of this distribution is lower than approximately 0.5° and for events with distance between cascade vertices larger than $\sim$ 285 m the median is lower than approximately 0.2°.

Precision of the energy reconstruction was evaluated using same procedure as described in Sec. 5.6. Two dimensional distribution of the ratios of reconstructed energy to simulated energy of cascades A and B was fit with two-dimensional Gaussian function, see Eq. 5.11. Parameters $\mu_A = 1.01$, $\mu_B = 1.03$, $\sigma_A = 0.15$, and $\sigma_B = 0.20$ were obtained from the fit.

5.8 Tau neutrino search

There are various approaches how to perform identification of the potential ν_τ events. The most straightforward one is based on processing of the experimental data with the double cascade reconstruction algorithm and subsequent evaluation of the probability of the ν_τ origin for tagged events. Another method is to take the sample of already reconstructed single cascade events with potential astrophysical origin and process them with the double cascade reconstruction algorithm. Since in the astrophysical flux, the neutrino flavor ratio $\nu_e : \nu_\mu : \nu_\tau$ = 1:1:1 is expected at the Earth, ν_τ events are also anticipated among selected potential astrophysical neutrino events.

This method assumes that at least some types of double cascade events can pass the single cascade reconstruction algorithm criteria, for example events in which there is sufficient distance between two cascades and therefore one of them can be reconstructed separately with single cascade reconstruction algorithm or double cascade events in which two cascades are completely overlapped. To verify this assumption, MC simulations of ν_τ double cascade events have to be processed with the single cascade reconstruction algorithm and the efficiency of this algorithm for different types of ν_τ double cascade events has to be evaluated.

The selection of 11 potential astrophysical events used in this analysis was published in [20] and it is shown in Tab. 5.6. These events were processed with the double cascade reconstruction algorithm.

Table 5.6: The list of parameters of 11 reconstructed single cascade events – observation date given as modified Julian date – MJD, E_{sh} is reconstructed energy, θ denotes zenith angle, l and b corresponds to the Galactic longitude and latitude, RA is right ascension, Dec means declination, 50 % and 90 % unc. deg. display containment angular uncertainty regions and ρ is distance between central string of the cluster and cascade vertex. In the name of the event in the first column the date of the event detection is given in yymmdd format. Taken from [20].

Event name	MJD	E_{sh} TeV	θ deg.	l deg.	b deg.	RA deg.	Dec deg.	50% unc. deg.	90% unc. deg.	ρ meter
GVD180504CA	58242.5739004	25.1	111.7	299.1	3.6	185.4	−59.0	3.9	6.9	28
GVD190523CA	58626.44462963	91.0	109.0	200.4	−58.4	45.1	−16.7	2.2	4.5	49
GVD200614CA	59014.27202546	39.8	144.1	359.3	10.6	256.2	−23.6	3.4	6.8	108
GVD201112CA	59165.01353009	24.5	136.1	305.0	−15.1	202.2	−77.8	5.4	11.8	66
GVD210418CA	59322.94855324	224	115.5	196.8	−14.6	82.4	7.1	3.0	5.8	70
GVD210501CA	59335.45576389	64.6	112.3	223.4	−67.7	38.1	−28.9	2.6	12.6	109
GVD210506CA	59340.34252315	21.9	114.2	5.9	46.7	230.6	3.1	2.8	6.6	30
GVD210710CA	59405.56907407	24.5	115.5	139.8	−54.2	22.7	7.4	3.6	8.6	83
GVD210803CA	59429.58071759	20.9	136.9	321.0	−50.3	347.0	−63.0	1.9	4.1	41
GVD220121CA	59600.45934028	30.9	110.5	241.3	10.4	126.2	−19.5	3.4	7.1	49
GVD220308CA	59646.14655093	36.3	105.0	203.2	−35.2	67.3	−8.0	2.5	5.6	37

However, in this case none of these events passed hit sorting step of the double cascade reconstruction algorithm. The possible reasons are:

- low statistics in selected sample of events and therefore no ν_τ interaction,
- there is ν_τ interaction but it was NC interaction,
- there is ν_τ CC interaction but resulting signature is single cascade,
- there is ν_τ CC interaction with double cascade signature, but the distance between cascade vertices was insufficient to be reconstructed with current version of the

double cascade reconstruction algorithm (dependence of mean distance that tau lepton travels before it decays on its energy is given in Eq. 1.14).

To study the hypothesis of the ν_τ double cascade signature with insufficient distance between cascade vertices, it is crucial to extend the current version of the double cascade reconstruction algorithm to reconstruct single-cascade-like double cascade events.

The visualization of one of the events from Tab. 5.6 with the highest reconstructed energy is shown in Fig. 5.29. With blue dots hits that were chosen for the cascade A subset of hits are shown. Comparison with the visualizations of the potential double cascade events from experimental data in Figs. 5.21, 5.22 implies, that in the case of the event with the highest reconstructed energy from the selection shown in Tab. 5.6, there was insufficient number of hits for the second cascade reconstruction.

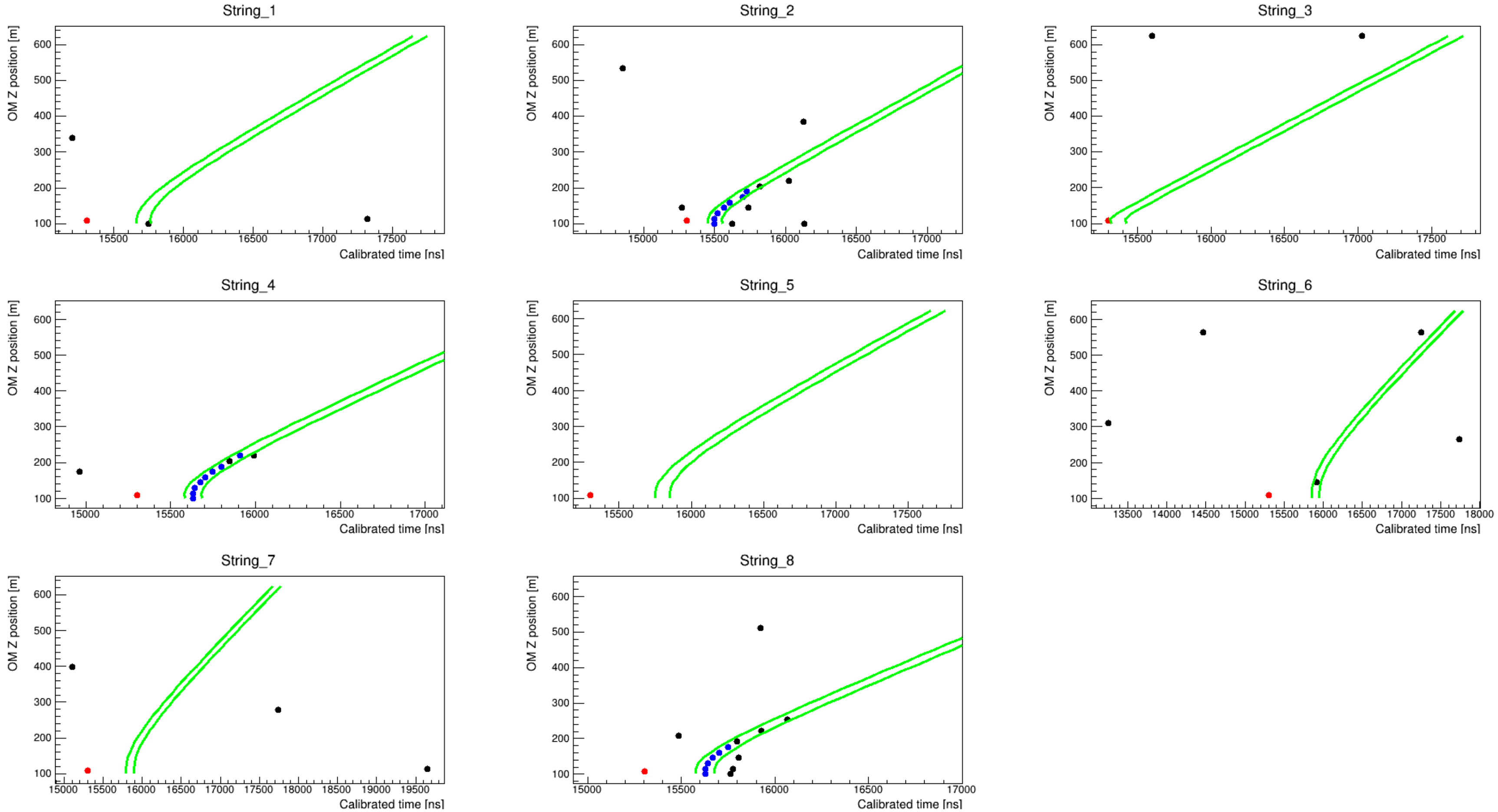

Figure 5.29: The visualization of the event with the highest energy from the list given in Tab. 5.6. The dependence of the Z coordinate of the OM on the time of the pulse detection is shown for all 8 strings in the cluster. The red dot displays the reconstructed position of the cascade. The green lines define region where pulses originating from the cascade should be, they are calculated with respect to the reconstructed vertex position of the cascade. The dots correspond to the hits detected in the event. Blue dots represent hits selected to the subset of hits for the reconstruction of cascade A.

Conclusion

This work is dedicated to the two of the main neutrino telescopes in the world – Baikal-GVD and KM3NeT. It is focused on three main topics: development of the double cascade reconstruction algorithm for Baikal-GVD, study of the ambient light field in Lake Baikal, and analysis of the properties of the KM3NeT digital optical module.

Development of the double cascade reconstruction algorithm for the Baikal-GVD neutrino telescope

The main goal of the Baikal-GVD part of this thesis is the development of the first double cascade reconstruction algorithm for the detection of astrophysical ν_τ in the Baikal-GVD neutrino telescope. The developed algorithm consists of four main parts – hit selection, hit sorting, position and time reconstruction, and energy reconstruction.

The precision of the reconstruction of the double cascade event parameters (positions of cascade vertices, their distance, direction of double cascade event and energies of cascades) was evaluated using Monte Carlo (MC) simulations of ν_τ double cascade events with approximation of the astrophysical neutrino flux parametrization and parametrization of astrophysical neutrino flux obtained by Baikal-GVD. When applying the Baikal-GVD astrophysical neutrino flux parametrization, the median of the dependence of direction deviation on true distance between cascade vertices is under $\sim 1^\circ$ for the double cascade events with distance between vertices larger than approximately 50 m.

This version of the double cascade reconstruction algorithm was designed to identify and to reconstruct selected ν_τ double cascade events so called double-cascade-like events. Using approximation of the astrophysical neutrino flux parametrization, the expected rate of such events is around 0.0405 per one cluster per one year. The rate of the reconstructed double-cascade-like events is approximately 0.0184 per one cluster per one year. With the condition that both cascade vertices have to be reconstructed with maximal difference between simulated and reconstructed vertex position 5 m, the rate of the reconstructed events is approximately 0.0161 per one cluster per one year.

The first study of the reconstruction of the multi-cluster ν_τ double cascade events is presented. Using MC simulations with Baikal-GVD astrophysical neutrino flux parametrization, the expected rate of double-cascade-like multi-cluster events for the Baikal-GVD 2019 geometry (5 clusters) is approximately 0.0135 per year per this geometry. The median of the dependence of the direction deviation on MC simulated distance between cascade vertices for the double-cascade-like events (2019 geometry, single cluster and multi-cluster together) is under approximately 0.5° for events with distance between vertices larger than ~ 100 m and under around 0.2° for events with cascade vertices distance larger than ~ 285 m.

The expected rates of ν_τ double cascade background events after double cascade reconstruction were estimated. The results from this study indicate that the rates of the background events should be dominated by atmospheric muon bundles. The experimental data collected by Baikal-GVD in year 2019 were processed with the double cascade reconstruction algorithm. The comparison of potential double cascade event rates from MC simulations (considering simulations of atmospheric muon bundles only since their rates should be dominating) and rates of potential double cascade events from experimental data collected in year 2019 is presented. The ratio between these expected rates from MC simulations and rates obtained from data was determined as 0.71, 0.41, 0.97, 0.49, and 0.72 for clusters 1 - 5, respectively.

Study of the ambient light field in Lake Baikal

The second subject of this thesis related to the Baikal-GVD neutrino telescope deals with the study of ambient light field in Lake Baikal. The noise rates levels in years 2018 - 2020 are presented. The study of the optical noise showed the periods of the increased luminescent activity alternating with periods of the stable optical noise in studied years. Highly optically active layer was observed to move upwards in years 2020 and 2021. The maximal velocity of this layer reached a value 28 m/day in January 2021. In stable noise rates periods, the depth (H) dependence of the average noise rates follows exponential law $\sim e^{-\frac{H}{H_0}}$. The values of the parameter of exponential decrease H_0 for years 2018, 2019, and 2020 were determined as 461 m, 312 m, and 292 m, respectively. In calm noise rates period the regular modulations of noise levels were observed, in high noise rates period the sharp changes in noise rates were registered.

Analysis of the properties of the KM3NeT digital optical module

The KM3NeT part of this thesis is focused on the characterization of the properties of the Digital Optical Module (DOM) which is the main detection unit of the KM3NeT neutrino telescope. Understanding of the DOM attributes is essential for precision of data analyses as well as calibration of the detector. The analysis is focused on the study of the internal noise of the DOM – signal which is measured when no external sources are present. For the first time, the measurements with the KM3NeT DOM were performed in nearly muon free environment in the Modane underground laboratory. The experimental setup used for these measurements consists of custom built dark box for the DOM and corresponding electronics which enable to collect data from a single DOM. Standard KM3NeT MC simulations were adjusted for this custom setup. The first analysis of data measured in Modane is focused on study of the coincidences among PMTs in the DOM. These coincidences are used in inter-PMT calibrations. Particularly, the results presented in this thesis are connected with study of the agreement between coincidence rates estimation from data and MC simulations and influence of the various phenomena on the comparison between data and MC simulations.

In MC simulations of the measurements with DOM in air box in the Modane underground laboratory, decays of the radioactive isotopes – ^{40}K, ^{232}Th, and ^{238}U contained in the DOM glass were simulated. The influence of the new values of the mass-specific activity of these radioactive isotopes measured in the National Radiation Protection Institute (NRPI) in Czech Republic on coincidence rates estimation from MC simulations is presented. For the PMT pairs with the smallest opening angles, the increase of the coincidence rates estimation is at the level of 15 % in comparison with MC simulations with default values of mass-specific activities. The agreement between data measured in the Modane underground laboratory and MC simulations was improved by using NRPI measured values of mass-specific activities.

Secondly, the impact of the choice of the random coincidence background estimation method on the coincidence rates estimation was analyzed. Two background estimation methods were studied – *counts* and *tails*. In the case of application of the *counts* background estimation method the coincidence rates estimated from data for all PMT pairs are higher than in the case of the *tails* method, for the PMT pairs with the smallest opening angles, the increase is at the level of approximately 30 to 35 %. In the case of the MC simulations, the usage of the *counts* method also leads to higher estimation of the coincidence rates but the increase is at the level of 3 % for the PMT pairs with small opening angles. The difference between coincidence rates obtained from the data and MC simulations is under $\sim$ 40 % for PMT pairs with small opening angles for *counts* method, in the case of application of *tails* method, this difference is under approximately 10 - 20 % for these PMT pairs. The performance of both background estimation methods was also studied directly on coincidence rates distributions for particular PMT pairs. Consequently, for data collected in our experimental setup in the Modane underground laboratory, application of *tails* method is recommended.

Further, the influence of the simulation of the PMT noise rates and radon contained in the air in the dark box on the coincidence rates was evaluated. The first analysis of these effects indicates that the change in the estimation of the coincidence rates is negligible in comparison with the change caused by the new values for mass-specific activities of radioactive isotopes contained in the DOM glass from NRPI measurements or choice of the background coincidence estimation method.

The precision of the MC simulations of the Modane experimental setup was tested with additional measurements with modified dark box – box with walls covered with mylar foil i.e. reflective box. In such setup, measurements with the same source of signal – DOM itself, but in environment with different light propagation properties are possible. The agreement between data and MC simulations was improved in comparison with dark box measurements. The most significant improvement can be observed for the PMT pairs with large opening angles, the difference between coincidence rates from MC simulations and data is at the level of ~ 50 %, while for the dark box measurements, this difference was at the level of orders of magnitude. These results indicate that the possible cause of the discrepancy for these PMT pairs in the case of the dark box measurements is that the particle propagation in glass is not specified correctly in the MC simulations. To support this statement, further detailed analysis is required.

In the last part of the section related to the KM3NeT neutrino telescope, data collected by the DOMs deployed in the sea at KM3NeT/ARCA site and corresponding MC simulations were analyzed. Coincidence rates estimation obtained from MC simulations with the new values of the mass-specific activities of radioactive isotopes comprised in the DOM glass measured by NRPI was increased by 3 - 4 % for PMT pairs with small opening angles in comparison with the coincidence rates from MC simulations with default values of the mass-specific activities. The smaller influence of the modification of these values for the MC simulations of the DOM in seawater in comparison with simulations of the DOM in air dark box is caused by the additional signal from the radioactive isotopes (^{40}K and ^{238}U) contained in seawater. More precise estimation of the mass-specific activities of the radioactive isotopes contained in the DOM glass enables update of the model of the expected coincidence rates used in the inter-PMT calibrations of the KM3NeT neutrino telescope and therefore it can increase the precision of these calibrations.

List of publications

Corresponding author

1. E. Eckerová et al., Baikal-GVD Collaboration, *Development of the Double Cascade Reconstruction Techniques in the Baikal-GVD Neutrino Telescope*, PoS ICRC 2021 (2022) 1167, doi: 10.22323/1.395.1167, arXiv:2108.00333 [astro-ph.IM].
2. E. Eckerová, et al., Baikal-GVD Collaboration, *Luminescence of Baikal water as a dynamic background of the Baikal-GVD Neutrino Telescope*, Journal of Instrumentation 16 (2021) no.11, C11011, doi: 10.1088/1748-0221/16/11/C11011.
3. E. Eckerová et al., Baikal-GVD Collaboration, *Development of the Double Cascade Reconstruction Technique in the Baikal-GVD Neutrino Telescope*, PoS ECRS 2022 (2023) 099, doi: 10.22323/1.423.0099.
4. E. Eckerová et al., Baikal-GVD Collaboration, *Double cascade reconstruction in the Baikal-GVD neutrino telescope*, PoS ICRC 2023 (2024) 1016, doi: 10.22323/1.444.1016, arXiv:2309.17118 [astro-ph.IM].
5. E. Eckerová et al., Baikal-GVD Collaboration, *Reconstruction of double cascades in the Baikal-GVD neutrino telescope*, PoS TAUP 2023 (2024) 258, doi: 10.22323/1.441.0258.

Popularization of science

1. Z. Bardačová, R. Dvornický, E. Eckerová, F. Šimkovic, *Okno do vesmíru*, the main article in Slovak magazine about science and technology Quark, 2024, ISSN 1335-4000.

List of conferences

1. Cosmic Rays and Neutrinos in the Multi-Messenger Era conference, Paris, France 2020 – **poster** *Double Cascade Detection Techniques in the Baikal-GVD Neutrino Telescope*
2. Very Large Volume Neutrino Telescope Workshop, Valencia, Spain 2021 – **talk** *Luminescence of Baikal water as a dynamic background of the Baikal-GVD Neutrino Telescope*
3. The 37th International Cosmic Rays Conference, Berlin, Germany 2021 – **panel discussion poster** *Development of the Double Cascade Reconstruction Techniques in the Baikal-GVD Neutrino Telescope*
4. The 27th European Cosmic Ray Symposium, Nijmegen, the Netherlands 2022 – **poster** *Development of the Double Cascade Reconstruction Technique in the Baikal-GVD Neutrino Telescope*
5. The 38th International Cosmic Rays Conference, Nagoya, Japan 2023 – **talk** *Diffuse neutrino flux measurements with the Baikal-GVD neutrino telescope* & **poster** *Double cascade reconstruction in the Baikal-GVD neutrino telescope*
6. The 18th International Conference on Topics in Astroparticle and Underground Physics, Vienna, Austria 2023 – **poster** *Reconstruction of double cascades in the Baikal-GVD neutrino telescope*

Bibliography

[1] M. A. Markov, *On high energy neutrino physics*, Proceedings 10th International Conference on High Energy Physics, Rochester, NY, USA (1960) 578-581.

[2] C. Spiering, *History of high-energy neutrino astronomy*, International Conference on History of the Neutrino, Paris, France, 2018, (2019), arXiv:1903.11481v1 [astro-ph.HE].

[3] K. D. Hoffman, *High Energy Neutrino Telescopes*, New Journal of Physics, 11:055006, 2009, arXiv:0812.3809v1 [astro-ph].

[4] Baikal-GVD Collaboration, *BAIKAL-GVD, Gigaton Volume Detector in Lake Baikal (Scientific-Technical Report)*, Moscow (2012).

[5] KM3NeT Collaboration, *KM3NeT: Technical Design Report for a Deep-Sea Research Infrastructure in the Mediterranean Sea Incorporating a Very Large Volume Neutrino Telescope*, (2009).

[6] ANTARES Collaboration, *ANTARES: the first undersea neutrino telescope*, Nuclear Instruments and Methods in Physics Research Section A **656** (2011), 11-38, doi: 10.1016/j.nima.2011.06.103, arXiv:1104.1607 [astro-ph.IM].

[7] M G. Aartsen et al., IceCube Collaboration, *The IceCube Neutrino Observatory: Instrumentation and Online Systems*, Journal of Instrumentation 19 (2024) 05, E05001, doi: 10.1088/1748-0221/19/05/E05001, arXiv:1612.05093 [astro-ph.IM].

[8] M. Agostini et al., P-ONE Collaboration, *The Pacific Ocean Neutrino Experiment*, Nature Astronomy 4 (2020) 10, 913-915, doi: 10.1038/s41550-020-1182-4.

[9] Z. P. Ye, F. Hu, W. Tian, et al., TRIDENT Collaboration, *A multi-cubic-kilometer neutrino telescope in the Western Pacific Ocean*, arXiv:2207.04519 [astro-ph.HE].

[10] T. Q. Huang et al., *Proposal for the High Energy Neutrino Telescope*, PoS ICRC2023 1080, doi: 10.22323/1.444.1080.

[11] S. Lin, L. Yang et al., *A proposed deep sea Neutrino Observatory in the Nanhai*, arXiv:2408.05122v2 [astro-ph.HE].

[12] A. Palladino, C. Mascaretti, F. Vissani, *The importance of observing astrophysical tau neutrinos*, Journal of Cosmology and Astroparticle Physics, 08:004, 2018, arXiv:1804.04965v2 [astro-ph.HE].

[13] R. Davis, D. S. Harmer, K. C. Hoffman, *Search for Neutrinos from the Sun*, Physical Review Letters 20 (1968) 1205-1209, doi: 10.1103/PhysRevLett.20.1205.

[14] K. Hirata et al., Kamiokande-II Collaboration, *Observation of a Neutrino Burst from the Supernova SN1987*, Physical Review Letters 58 (1987) 1490-1493, doi: 10.1103/PhysRevLett.58.1490.

[15] R. M. Bionta et al., *Observation of a neutrino burst in coincidence with supernova 1987A in the Large Magellanic Cloud*, Physical Review Letters 58 (1987) 1494, doi: 10.1103/PhysRevLett.58.1494.

[16] E. N. Alekseev, L. N. Alekseeva, V. I. Volchenko, I. V. Krivosheina, *Possible Detection of a Neutrino Signal on 23 February 1987 at the Baksan Underground Scintillation Telescope of the Institute of Nuclear Research*, JETP Lett. 45 (1987) 589-592, Pisma Zh.Eksp.Teor.Fiz. 45 (1987) 461-464.

[17] M. G. Aartsen et al., IceCube Collaboration, *Evidence for High-Energy Extraterrestrial Neutrinos at the IceCube Detector*, Science 342 (2013), 1242856, doi: 10.1126/science.1242856, arXiv:1311.5238 [astro-ph.HE].

[18] M. G. Aartsen et al., IceCube Collaboration, *Observation of High-Energy Astrophysical Neutrinos in Three Years of IceCube Data*, Physical Review Letters 113 (2014) 101101, doi: 10.1103/PhysRevLett.113.101101, arXiv:1405.5303 [astro-ph.HE].

[19] M. G. Aartsen et al., IceCube Collaboration, *Observation and Characterization of a Cosmic Muon Neutrino Flux from the Northern Hemisphere using six years of IceCube data*, The Astrophysical Journal 833 (2016) 1, 3, doi: 10.3847/0004-637X/833/1/3, arXiv:1607.08006 [astro-ph.HE].

[20] Baikal-GVD Collaboration et al., *Diffuse neutrino flux measurements with the Baikal-GVD neutrino telescope*, Physical Review D 107 (2023) 4, 4, doi: 10.1103/PhysRevD.107.042005.

[21] S. Navas et al., Particle Data Group Collaboration, *Review of Particle Physics*, Physical Review D 110, 030001 (2024).

[22] J. Coelho et al., KM3NeT Collaboration, *Latest results from KM3NeT*, Plenary talk at the Neutrino 2024 conference, Zenodo, 18 June 2024, Milan, Italy. doi: 10.5281/zenodo.12706075.

[23] D. Castelvecchi, *'Fantastic' particle could be most energetic neutrino ever detected*, Nature, 2024, 631(8019):18. doi: 10.1038/d41586-024-02074-5.

[24] IceCube Collaboration et al., *Multi-messenger observations of a flaring blazar coincident with high-energy neutrino IceCube-170922A*, Science 361 (2018) 6398, eaat1378, doi: 10.1126/science.aat1378, arXiv:1807.08816 [astro-ph.HE].

[25] M. G. Aartsen et al., IceCube Collaboration, *Neutrino emission from the direction of the blazar TXS 0506+056 prior to the IceCube-170922A alert*, Science 361 (2018) 6398, 147-151, doi: 10.1126/science.aat2890, arXiv:1807.08794 [astro-ph.HE].

[26] Baikal-GVD Collaboration et al., *High-energy neutrino-induced cascade from the direction of the flaring radio blazar TXS 0506+056 observed by Baikal-GVD in 2021*, Monthly Notices of the Royal Astronomical Society 527 (2023) 3, 8784-8792, doi: 10.1093/mnras/stad3653, arXiv:2210.01650 [astro-ph.HE].

[27] R. Abbasi et al., IceCube Collaboration, *Evidence for neutrino emission from the nearby active galaxy NGC 1068*, Science 378 (2022) 6619, 538-543, doi: 10.1126/science.abg3395, arXiv:2211.09972 [astro-ph.HE].

[28] R. Abbasi et al., IceCube Collaboration, *Observation of high-energy neutrinos from the Galactic plane*, Science 380 (2023) 6652, adc9818, doi: 10.1126/science.adc9818, arXiv:2307.04427 [astro-ph.HE].

[29] U. F. Katz, C. Spiering, *High-Energy Neutrino Astrophysics: Status and Perspectives*, Progress in Particle and Nuclear Physics 67 (2012) 651-704 doi: 10.1016/j.ppnp.2011.12.001.

[30] K. Greisen, *End to the cosmic ray spectrum?*, Physical Review Letters 16(17):748-750, 1966, doi: 10.1103/PhysRevLett.16.748.

[31] G. T. Zatsepin, V. A. Kuzmin, *Upper limit of the spectrum of cosmic rays*, JETP Letters 4 (1966) 78-80, Pisma Zh.Eksp.Teor.Fiz. 4 (1966) 114-117.

[32] A. M. Hillas, *The Origin of Ultrahigh-Energy Cosmic Rays*, Annual Review of Astronomy and Astrophysics 22 (1984) 425-444 doi: 10.1146/annurev.aa.22.090184.002233.

[33] T. Kajita, *Atmospheric neutrinos*, Advances in High Energy Physics 2012 (2012) 504715, doi: 10.1155/2012/504715.

[34] S. L. Glashow, *Resonant Scattering of Antineutrinos*, Physical Review 118(1):316-317, 1960, doi: 10.1103/PhysRev.118.316.

[35] M. G. Aartsen et al., IceCube Collaboration, *Detection of a particle shower at the Glashow resonance with IceCube*, Nature 591 (2021) 7849, 220-224, doi: 10.1038/s41586-021-03256-1, arXiv:2110.15051 [hep-ex].

[36] J. A. Formaggio, G. P. Zeller, *From eV to EeV: Neutrino Cross Sections Across Energy Scales*, Reviews of Modern Physics 84(3):1307-1341, 2012, doi: 10.1103/RevModPhys.84.1307, arXiv:1305.7513 [hep-ex].

[37] P. A. Čerenkov, *Visible Radiation Produced by Electrons Moving in a Medium with Velocities Exceeding that of Light*, Physical Review 52(4):378-379, 1937, doi: 10.1103/PhysRev.52.378.

[38] C. Bogazzi, *Search for cosmic neutrinos with ANTARES*, PhD thesis, Leiden University, The Netherlands, 2014.

[39] I. M. Frank, I. E. Tamm, *Coherent visible radiation of fast electrons passing through matter*, Compt.Rend.Acad.Sci.URSS 14 (1937) 3, 109-114, Dokl.Akad.Nauk SSSR 14 (1937) 3, 107-112, Usp.Fiz.Nauk 93 (1967) 2, 388-393, doi: 10.3367/UFNr.0093.196710o.0388.

[40] F. Halzen, S. R. Klein, *IceCube: An Instrument for Neutrino Astronomy*, Review of Scientific Instruments, vol. 81, p. 081101, 2010.

[41] P. Hallen, *On the Measurement of High-Energy Tau Neutrinos with IceCube*, Master's thesis, RWTH Aachen University, Germany, 2013.

[42] B. D. Hartmann, *Reconstruction of Neutrino-Induced Hadronic and Electromagnetic Showers with the ANTARES Experiment*, PhD thesis, University Erlangen, Germany, 2006, arXiv:astro-ph/0606697v1.

[43] Global Neutrino Network. GNN Web page, URL: https://www.globalneutrinonetwork.org/.

[44] E. Resconi et al., P-ONE Collaboration, *The Pacific Ocean Neutrino Experiment*, PoS ICRC2021 (2021), 024, doi: 10.22323/1.395.0024.

[45] V. M. Aynutdinov et al., Baikal-GVD Collaboration, *The Baikal-GVD Neutrino Telescope: Current Status and Development Prospects*, Physics of Atomic Nuclei 86 (2023) 6, 989-994, doi: 10.1134/S1063778824010101.

[46] K. Garrett, G. Duda, *Dark Matter: A Primer*, Advances in Astronomy, 2011, 968283 (2011). doi: 10.1155/2011/968283.

[47] P. A. M. Dirac, *Quantised singularities in the electromagnetic field*, Proceedings of the Royal Society London A 133 (1931) 60-72, doi: 10.1098/rspa.1931.0130.

[48] V. M. Aynutdinov et al., Baikal-GVD Collaboration, *Improving the efficiency of cascade detection by the Baikal-GVD neutrino telescope*, PoS ICRC2023 987, doi: 10.22323/1.444.0987, arXiv:2309.17069 [astro-ph.IM].

[49] R. Dvornický et al., Baikal-GVD Collaboration, *Baikal-GVD*, Plenary talk at the Neutrino 2024 conference, Zenodo, 19 June 2024, Milan, Italy. doi: 10.5281/zenodo.12726000.

[50] A. D. Avrorin et al., Baikal-GVD Collaboration, *The prototyping/early construction phase of the BAIKAL-GVD project* Proceedings, 4th Roma International Conference on Astro-Particle Physics, Rome, Italy, 2013, arXiv:1308.1833v1 [astro-ph.IM].

[51] L. Fajt, *Time Calibration and Pulse Processing of the Baikal-GVD Neutrino Telescope*, PhD thesis, Comenius University, Slovakia, 2019.

[52] Zh.-A. M. Dzhilkibaev, et al., Baikal-GVD Collaboration, *BAIKAL-GVD Project*, Talk at the VI International Pontecorvo Neutrino Physics School, 4 September 2015, Horny Smokovec, Slovakia.

[53] A. D. Avrorin et al., Baikal-GVD Collaboration, *Positioning system for Baikal-GVD*, PoS ICRC2021 1083, doi: 10.22323/1.395.1083, arXiv:2108.00212v1 [astro-ph.IM].

[54] S. Adrian-Martinez et al., KM3NeT Collaboration, *Letter of intent for KM3NeT 2.0*, Journal of Physics G: Nuclear and Particle Physics, 43 (2016) 8, 084001 , doi: 10.1088/0954-3899/43/8/084001, arXiv:1601.07459 [astro-ph.IM].

[55] T. J. van Eeden, *Neutrino astronomy with KM3NeT/ARCA*, PhD thesis, University of Amsterdam, The Netherlands, 2024.

[56] A. Romanov, *Cosmic ray studies with the KM3NeT neutrino telescope*, PhD thesis, University of Genoa, Italy, 2023.

[57] S. Aiello et al., KM3NeT Collaboration, *The KM3NeT multi-PMT optical module*, Journal of Instrumentation 17 (2022) P07038, doi: 10.1088/1748-0221/17/07/P07038, arXiv:2203.10048 [astro-ph.IM].

[58] K. Melis, *Studying the Universe from -3000m N.A.P.*, PhD thesis, University of Amsterdam, The Netherlands, 2021.

[59] S. Aiello et al., KM3NeT Collaboration, *Characterisation of the Hamamatsu photomultipliers for the KM3NeT Neutrino Telescope*, Journal of Instrumentation 13 (2018) 05, P05035, doi: 10.1088/1748-0221/13/05/P05035.

[60] D. Real et al., KM3NeT Collaboration, *KM3NeT Digital Optical Module electronics*, EPJ Web of Conferences 116 (2016) 05007, doi: 10.1051/epjconf/201611605007.

[61] S. Aiello et al., KM3NeT Collaboration, *Implementation and first results of the KM3NeT real-time core-collapse supernova neutrino search*, The European Physical Journal C 82 (2022) 4, 317, doi: 10.1140/epjc/s10052-022-10137-y, arXiv:2109.05890 [astro-ph.HE].

[62] R. Bruijn et al., KM3NeT Collaboration, *The KM3NeT Digital Optical Module and Detection Unit*, EPJ Web of Conferences 207 (2019) 06002, doi: 10.1051/epjconf/201920706002.

[63] S. Aiello et al., KM3NeT Collaboration, *KM3NeT Broadcast Optical Data Transport System*, Journal of Instrumentation 18 (2023) 02, T02001, doi: 10.1088/1748-0221/18/02/T02001, arXiv:2210.13328 [astro-ph.IM].

[64] S. Aiello et al., KM3NeT Collaboration, *Deep-sea deployment of the KM3NeT neutrino telescope detection units by self-unrolling*, Journal of Instrumentation 15 (2020) 11, P11027, doi: 10.1088/1748-0221/15/11/P11027, arXiv:2007.16090 [astro-ph.IM].

[65] J. Pradler et al., *On an unverified nuclear decay and its role in the DAMA experiment*, Physics Letters B720 (2013) 399-404, doi: 10.1016/j.physletb.2013.02.033, arXiv:1210.5501 [hep-ph].

[66] S. Adrián-Martínez et al., KM3NeT Collaboration, *Deep Sea Tests of a Prototype of the KM3NeT Digital Optical Module*, The European Physical Journal C 74 (2014) 9, 3056, doi: 10.1140/epjc/s10052-014-3056-3, arXiv: 1405.0839 [astro-ph.IM].

[67] M. Spurio, *Probes of Multimessenger Astrophysics. Charged cosmic rays, neutrinos, γ-rays and gravitational waves*, Astronomy and Astrophysics Library, Springer, 2018, doi: 10.1007/978-3-319-96854-4.

[68] S. Aiello et al., KM3NeT Collaboration, *Nanobeacon: A time calibration device for the KM3NeT neutrino telescope*, Nuclear Instruments and Methods in Physics Research 1040 (2022) 167132, doi: 10.1016/j.nima.2022.167132, arXiv: 2111.00223 [astro-ph.IM].

[69] R. Muller, *Getting to the point: First cosmic neutrino source search with the KM3NeT/ARCA detector*, PhD thesis, University of Amsterdam, The Netherlands, 2023.

[70] M. de Jong et al., KM3NeT Collaboration, *Documentation to JPP software*, URL: https://www.nikhef.nl/∼mjg/Jpp/public/index.html.

[71] P. P. Povinec et al., *New isotope technologies in environmental physics*, Acta Physica Slovaca 58 (2008) 1-154, doi: 10.2478/v10155-010-0088-6.

[72] M. Colomer, D. Dornic, V. Kulikovskiy, et al., KM3NeT Collaboration, *Detailed KM3NeT optical module simulation with Geant4 and supernova neutrino detection study*, PoS ICRC2017 983, doi: 10.22323/1.301.0983.

[73] J. Allison et al., *Recent developments in Geant4*, Nuclear Instruments and Methods in Physics Research Section A 835 (2016) 186-225, doi: 10.1016/j.nima.2016.06.125.

[74] J. Allison et al., *Geant4 developments and applications*, IEEE Transactions on Nuclear Science 53 (2006) 270, doi: 10.1109/TNS.2006.869826.

[75] S. Agostinelli et al., *GEANT4–a simulation toolkit*, Nuclear Instruments and Methods in Physics Research Section A 506 (2003) 250-303, doi: 10.1016/S0168-9002(03)01368-8.

[76] Jas3 – Java Analysis Studio, URL: https://jas.freehep.org/jas3/index.html.

[77] M. A. U. Elorrieta, *Studies on dark rates induced by radioactive decays of the multi-PMT digital optical module for future IceCube extensions*, Master's thesis, University of Münster, University of Seville, 2017.

[78] Hamamatsu Photonics, *Photomultiplier tubes, Basics and Applications, Fourth Edition*, 2017.

[79] V. Palušová et al., *Natural radionuclides as background sources in the Modane underground laboratory*, Journal of Environmental Radioactivity 216 (2020) 106185, doi: 10.1016/j.jenvrad.2020.106185.

[80] National Research Council, *Risk Assessment of Radon in Drinking Water*, Washington, DC: The National Academies Press, 1999, doi: 10.17226/6287.

[81] L. B. Bezrukov et al., *Luminescence of Baikal Water as an Instrument for Studying Lake Dynamics*, Izvestiya, Atmospheric and Oceanic Physics 34, 85 (1998).

[82] I. A. Belolaptikov et al., *On the Nonstationarity of Deep Baikal Water Flows as Derived from Neutrino Telescope Data*, Izvestiya, Atmospheric and Oceanic Physics 34, 78 (1998).

[83] A. D. Avrorin et al., Baikal-GVD Collaboration, *Data Quality Monitoring system in the Baikal-GVD experiment*, PoS ICRC2019 874, doi: 10.22323/1.358.0874, arXiv:1908.07270v1 [astro-ph.IM].

[84] R. Dvornický et al., Baikal-GVD Collaboration, *The optical noise monitoring systems of the Lake Baikal environment for the Baikal-GVD telescope*, PoS ICRC2019 875, doi: 10.22323/1.358.0875, arXiv:1908.06509v1 [astro-ph.HE].

[85] N. M. Budnev et al., Baikal-GVD Collaboration, *Environmental studies in Lake Baikal: basic facts and perspectives for interdisciplinary research*, EPJ Web Conferences 207 (2019) 09001.

[86] S. Bilenky, *Introduction to the Physics of Massive and Mixed Neutrinos*, Lecture Notes in Physics 817 (2010) 1-255, doi: 10.1007/978-3-642-14043-3.

[87] A. Gazizov, M. P. Kowalski, *ANIS: High Energy Neutrino Generator for Neutrino Telescopes*, Computer Physics Communications 172 (2005) 203–213, arXiv:astro-ph/0406439v1.

[88] E. Ganster, R. Naab, Z. Zhang, et al., IceCube Collaboration, *A Combined Fit of the Diffuse Neutrino Spectrum using IceCube Muon Tracks and Cascades*, PoS ICRC2021 1129, doi: 10.22323/1.395.1129, arXiv:2107.10003v1 [astro-ph.HE].

[89] A. M. Dziewonski, D. L. Anderson, *Physics of Earth and Planetary Interiors*, Physics of the Earth and Planetary Interiors, 25 (1981) 297-356.

[90] Z. Bardačová, *Neutrino Induced Cascade Reconstruction in the Baikal-GVD Neutrino Telescope*, Master's thesis, Comenius University, Slovakia, 2020.

[91] Zh.-A. M. Dzhilkibaev et al., Baikal-GVD Collaboration, *The Baikal-GVD neutrino telescope: search for high-energy cascades*, PoS ICRC2021 1144, doi: 10.22323/1.395.1144, arXiv:2108.01894 [astro-ph.HE].

[92] L. Volkova, *Energy spectra and angular distributions of atmospheric neutrinos*, Journal of Nuclear Physics, Vol.31, No. 6, 1980.

[93] D. Heck, J. Knapp, J. N. Capdevielle, G. Schatz, T. Thouw, *CORSIKA: a Monte Carlo code to simulate extensive air showers*, 1998.

[94] N. N. Kalmykov, S. S. Ostapchenko, *The nucleus-nucleus interaction, nuclear fragmentation, and fluctuations of extensive air showers*, Physics of Atomic Nuclei 56 (1993) 346-353.